University of Southampton

Faculty of Engineering and Physical science

Department of Engineering Material

Microstructure properties and fatigue behaviour of multiple materials fabricated by Laser Powder Bed Fusion process

by

Marie-Salomé Dani Duval-Chanéac

Supervision:

Dr. Nong Gao

Prof. Philippa Reed

Dr. Raja Khan

Thesis for the degree of Doctor of Philosophy

April, 2022

UNIVERSITY OF SOUTHAMPTON

Abstract

FACULTY OF PHYSICAL SCIENCE AND ENGINEERING

Department of Engineering Materials

Thesis for the degree of Doctor of Philosophy

MICROSTRUCTURE PROPERTIES AND FATIGUE BEHAVIOUR OF MULTIPLE MATERIALS MADE BY 3D PRINTING

by

Marie-Salomé Dani Duval-Chanéac

Multiple material additive manufacturing (MMAM) is a manufacturing technique that allows the fabrication in a single operation of components with different materials integrated into specific design locations. This technique allows the targeting of specific properties of materials and placing them into functional areas of a component, while reducing the number of manufacturing operations, the weight and costs of assemblies. The ability to produce components made of multiple materials in a single operation raises some challenges around the structural integrity of such components and the repeatability of the process. Considerable effort is made by the scientific community to understand and control the microstructure and mechanical properties of components fabricated by AM technologies. Standards are evolving and the transfer from "conventional" post treatment is also being investigated. The consequences on the microstructure properties and the effect on the mechanical response of these combinations will vary drastically from one combination couple to another. The overall objective of this work is to understand and try to enhance the structural integrity of multiple metallic materials produced by laser powder bed fusion (L-PBF) in a layered architecture. The alloys used in these studies are 316L Stainless Steel (SS) and Inconel 718 (IN718), both are widely employed in very demanding service environments where their oxidation resistance or ability to sustain high stress levels at elevated temperature are sought after. The fabrication of layered components has been chosen for crack propagation mitigation purposes, extending the fail-safe service lives of these components, a critical topic in structural integrity of key components. Layered architectures combining IN718 and 316L have been fabricated using the L-PBF process, and the effect of Heat Treatment (HT) on the microstructure and mechanical properties of these specimens has been studied. Single edge notched bend (SENB) specimens of bi-layer and four alternating layers were built horizontally, both IN718 and 316L layers were fabricated using the same set of process parameters (with an Energy ratio of 140J/mm2). A specific HT strategy including a solution treatment and a single stage ageing (1050°C/45min/FC + 620°C/4h/AC) was applied in order to allow precipitation strengthening to occur within the IN718 layer, while limiting the formation of detrimental phases within the 316L material and at the transition zone between the two alloys. The

microstructure and mechanical properties were studied by optical microscopy (OM), scanning electron microscopy (SEM), tensile testing, micro and nanohardness testing. The fatigue tests were performed on single edge notched bending (SENB) specimens to determine the crack propagation process through multi-layer specimens under 3 point bending cyclic loading. In the as-built (AB) condition, the yield strength of 316L alloy was 15% lower than that of IN718, but still 51 % superior to the value recommended by standard for conventionally manufactured 316L. This is an effect of the specific microstructure obtained from AM in the AB condition, where each grain is composed of subcellular structures (~0.5-1μm), that are usually formed due to the rapid cooling of the AM process and is due to the segregation of heavier elements also causing multiple dislocations to form around these cells. Whereas, IN718 produced by L-PBF in AB condition has a yield strength 34.3% lower compared to values expected from standard for conventionally manufactured and heat treated Inconel alloys, and displays an ultimate tensile strength (UTS) value 36.7 % lower than expected from standard for conventionally manufactured and heat treated Inconel alloys. These differences in strength are due to the lack of precipitation strengthening when the Inconel alloy is not thermally post treated. The crack propagation resistance mechanisms were differentiated in each alloy layer, and it was observed that grain misorientation has an effect on crack tortuosity within the 316L layer in the AB condition, while the fatigue crack propagation (FCP) in IN718 was observed to be transgranular and mostly dependent on the intrinsic strength of the alloy. The softer 316L layer (in AB condition) has been shown to release crack tip stress via substantial secondary crack opening, effectively shielding the crack propagation within the 4-layer specimen tested in AB condition, before the transition to the IN718 layer. The heat treatment of 316L/IN718 specimen caused a local inter-diffusion between the FCC(Fe) and the FCC(Ni) at the interface, leading to a region of 140μm depth where the local formation of Laves phases, locally enhanced decohesion with the matrix when subjected to FCP. The HT has improved tensile properties and supported the strengthening within the IN718 alloy leading to an increase of 11% in yield strength, 22% in UTS and 50% in Elongation. Meanwhile the 316L alloy saw a loss of 31% in YS and 5.2% UTS, although its tensile properties after HT remain superior to the values quoted for conventionally manufactured 316L. In the FCP test the heat treatment produced differences in da/dN versus ΔK, significantly improving IN718 resistance to crack propagation, whereas 316L has displayed a decrease in its crack propagation resistance. The effect of shielding/antishielding was also diminished by the effect of a weaker interface, where the local precipitation of Laves phases created an area more prone to decohesion. However, it was demonstrated that the shielding/antishielding effect of the interface transition is mostly effective when the ΔK at the crack tip is below 20MPa√m. Overall promising observations of the potential ability to produce multi-material components and heat treat them in order to create crack propagation resistant components have been made, however the design of such component should take into account the placement of such interfaces in order to take advantage of the shielding this transition in material can offer.

Table of Contents

Table of Tables

Table of Figures

Research Thesis: Declaration of Authorship

Print name: Marie-Salomé Dani Duval-Chanéac

Title of thesis: Microstructure properties and fatigue behaviour of multiple material made by 3D printing

I declare that this thesis and the work presented in it are my own and has been generated by me as the result of my own original research.

I confirm that:

1. This work was done wholly or mainly while in candidature for a research degree at this University;
2. Where any part of this thesis has previously been submitted for a degree or any other qualification at this University or any other institution, this has been clearly stated;
3. Where I have consulted the published work of others, this is always clearly attributed;
4. Where I have quoted from the work of others, the source is always given. With the exception of such quotations, this thesis is entirely my own work;
5. I have acknowledged all main sources of help;
6. Where the thesis is based on work done by myself jointly with others, I have made clear exactly what was done by others and what I have contributed myself;
7. Part of this work has been published as:

M.S. Duval-Chaneac, N. Gao, R.H.U. Khan, M. Giles, K. Georgilas, X. Zhao, P.A.S. Reed, Fatigue crack growth in IN718/316L multi-materials layered structures fabricated by laser powder bed fusion, **International Journal of Fatigue**, Volume 152, 2021, https://doi.org/10.1016/j.ijfatigue.2021.106454.

Duval-Chaneac, M-S., Gao, N., Khan, R.H.U, Giles, M., Georgilas, K., Zhao, X., Reed, P.A.S, Effect of heat treatment on fatigue crack growth in IN718/316L multiple-materials layered structures fabricated by laser powder bed fusion, **International Journal of Fatigue** (2022), doi: https://doi.org/10.1016/ j.ijfatigue.2022.106852

Signature: ..... Date:

Acknowledgements

This study was made possible by the sponsorship and support of the Engineering and Physical Science Research Council (EPSRC) and the Lloyds Register Foundation (LRF). The work was enabled through, and undertaken at both; the University of Southampton and The Welding Institute (TWI) of Cambridge, and the National Structural Integrity Research Centre (NSIRC): a postgraduate engineering facility for industry-led research into structural integrity, established and managed by TWI through a network of both national and international Universities.

This research was made possible thanks to the University of Southampton and the academic research team in the Engineering Materials Department from the Faculty of Physical Science and Engineering. Their support all along my learning process has allowed me to provide the following outcome.

I would like to address my personal deepest gratitude to my supervisor Professor Philippa Ann Sarah Reed for having followed me during my thesis, for her patience, her expert guidance and the quality of her suggestions and knowledge in her field. I would like to sincerely thank my supervisor Dr. Nong Gao, for his patience and wisdom, and the numerous good advices he gave me.

I would like also to thank Dr. Raja Khan, who always made sure that I was able to work in the best conditions, and assured the safe unfolding of this work.

I would like also to acknowledge the important contribution of all the other people I have met along the way, and whom have helped me to make progress around the different labs, and through this experience in general.

I send gratitude to: Angelos, Mike, Ben, Alvaro, Anqi, Diego, Saran, Kostas, Dr Xiao, Behrad, Andi and Geoff.

To all of you and from the bottom of my heart.

Thank you.

Definitions and Abbreviations

2D: Two Dimensional

3D: Three Dimensional

3DMP: Three Dimensional Metal Printing

AB: As-Built

AM: Additive Manufacturing

APB: Anti-Phase Boundary

BCC: Body Centre Cubic

BSE: Backscattered Secondary Electron

CAD: Computer Assisted Design

CCA: Complex Composition Alloy

CTE: Coefficient of Thermal Expansion

DDC: Ductility Dip Cracking

DLD: Direct Laser Deposition

DMD: Direct Metal Deposition

EBM: Electron Beam Melting

EBSD: Electron Backscattered Diffraction

EDM: Electrical Discharge Machining

EDS: Energy Dispersive Spectroscopy

FCC: Face Centre Cubic

FCP: Fatigue Crack Propagation

FDM: Fused Deposition Modeling

GCP: Geometrically Close Packed (atom structure)

HAGB: High Angle Grain Boundary

HAZ: Heat Affected Zone

HCF: High Cycle Fatigue

HEA: High Entropy Alloy

HIP: Hot Isostatic Pressing

HT: Heat Treated

HT: Heat Treated

IM: Intermetallic (phase)

IN718: Inconel 718

IPF: Inverse Pole Figure

LCF: Low Cycle Fatigue

LEFM: Linear Elastic Fracture Mechanics

LENS: Laser Engineered Net Shaping

LOM: Laminated Oject Manufacturing

L-PBF: Laser Powder Bed Fusion

LRO: Long Range Order

MMAM: Multiple Material (Metallic) Additive Manufacturing

MMC: Metal Matrix Composite

MPEAs: Multi-Principal Elements Alloys

NDT: Non-Destructive Detection Technique

OM: Optical Microscope

PMZ: Partially Melted Zone

PSB: Persistent Slip Band

RS: Residual Stresses

SE: Secondary Electron

SEM: Scanning Electron Microscopy

SFE: Stacking Fault Energy

SL: Stereolithography

SLM: Selective Laser Melting

SLS: Selective Laser Sintering

SRO: Short Range Order

SSS: Solid Solution Strengthening

SSY: Small Scale Yielding

TCP: Topologically Close Packed (atom structure)

TEM: Transmission Electron Microscope

TWIP: Twinning Induced Plasticity

WAAM: Wire Arc Additive Manufacturing

XRD: X-ray Diffraction

Nomenclature

$2c$: surface crack length

2θ: X-ray diffraction peak position

a : Depth of te fatigue crack (in sample width direction)

a/c : crack aspect ratio

a/W : ratio of the crack length to specimen width

da/dN: Fatigue crack growth rate

E: Young's Modulus (MPa)

K: Stress intensity factor (MPa$\sqrt{m}$)

K_I: Stress intensity factor in mode I fatigue

Nomenclature

K_{IC} : Plane strain fracture toughness

L_c : Profile filter value

L_r : Required evaluation length

n : An integer

N_f : Number of Cycles to Failure

P: Power (Watt, Mega Watt or Joules)

R_a : Arithmetical mean of vertical deviation of the linear roughness

R_z : Maximum height of the linear roughness profile

S_a : Arithmetical mean of vertical deviation of the roughness of a surface

S_z : Maximum height of the roughness for surface

T: Temperature (°C or K)

Z: Atomic number

$\Delta\varepsilon_p$: Plastic strain range

ΔK: Stress intensity factor range (MPa√m)

$\Delta\varepsilon$: Strain range

$\Delta\sigma$: Stress range

ε_a : Strain Amplitude

θ : Diffraction angle

λ : Wave length

σ_a : Stress Amplitude (MPa or Pascal)

σ_{uts} :Ultimate Tensile Strength (MPa)

σ_y : Yield Strength (MPa)

$\sigma_{y\,0.2\%}$: 0.2% Yield Strength (MPa)

Chapter 1 Introduction

1.1 Background

1.1.1 Additive manufacturing of metals

Additive Manufacturing (AM) processes are named in contrast to subtractive manufacturing techniques (or conventional manufacturing), and can also be referred to as 3D-printing, it refers to the wide variety of processes that allow the direct fabrication (usually by successive two dimensional (2D) layering) of components from a three-dimensional (3D) computer-aided design (CAD) model [1]. The scope of the term AM covers a variety of processes that are distinguished by the material feedstock type such as: liquid, solid or powder based. The processes considered in Figure 8-1 (appendix A) are: stereolithography (SL), Polyjet, fused deposition modeling (FDM), laminated object manufacturing (LOM), 3D printing (3DP), selective laser sintering (SLS), laminated engineered net shaping (LENS), and electron beam melting (EBM) [2].

Interest in AM technologies is fuelled by the many advantages, such as: a reduction in the number of manufacturing operations needed to produce parts with complex design, leading to a saving of energy and a reduction in time and cost within the production lines; AM also allows an optimal use of the material during production, hence optimising material waste. In addition, the overall weight of the final component can be minimised leading to a reduction in weight of the final part, thus saving energy during the service life of the component. AM also offers the ability to customise parts, and tailor production for very small run series or replacements [3].
3DMP (3 Dimensional Metal Printing) technologies are finding their applications in the production of high value components made of advanced materials such as high-performance heat exchangers and wear resistant coatings in the energy, oil and gas industries (see Figure 8-2 in appendix A). Application examples include critical products such as those certified for use in aerospace or for medical hardware, but also towards customized artistic designs and personalized items, and can also be extended to the repair and remanufacturing of components [4].

However in order to be employed in various industrial applications, metallic components fabricated by AM, need to be characterised in terms of strength and fatigue performance to be able to compete with conventionally manufactured alloys. So far many studies have been made on the effect of process parameters on the microstructure of metallic AM parts, because the thermal history during the AM process is the main factor affecting the chemical, physical and in turn, mechanical properties and fatigue behaviour of the final component [5].

1.1.2 Structural integrity and fatigue life of components

Structural integrity, repeatability and fatigue performance are essential characteristics to ensure safety of a component during its service life and avoid un-predicted failure or critical damage. The fatigue strength of metallic materials primarily depends on their microstructure, it often correlates to the area below the stress/strain curve of an isotropic material. However, it should be nuanced that in the case of AM components due to the anisotropic mechanical response of the specimens depending on their building orientation the fatigue strength may need to be referred to a specific orientation of the specimen [6]. However, process-inherent properties such as surface roughness and material defects strongly influence the mechanical performance of AM fabricated parts [7]. In order to introduce AM metallic components into demanding service environments (such as can be found in aerospace or oil and gas industries), not only a high density should be achieved, but both good static mechanical properties and cyclic properties are needed, as typically components are cyclically loaded during service. However, currently there have been only a few investigations into the cyclic mechanical behaviour of 3DMP components [8]. The appropriate use of principles of fracture mechanics and damage tolerance can effectively mitigate the risks against inherent material flaws, as well as manufacturing and service-induced defects [9]. Thus far the scientific community has begun to investigate the cyclic properties of some alloys fabricated by AM, but studies are still scarce. Meanwhile the field of mitigation of crack propagation by the use of multi-layer designs is more linked to studies on composites or dissimilar material joints (such as welds, diffusion bonding, or adhesive…) [10]. MMAM thus offers a new avenue for investigating potential improvements in fatigue crack propagation resistance of metallic parts.

1.1.3 Multi-Material Additive Manufacturing (MMAM)

By extension from AM, multi-material additive manufacturing (MMAM) techniques allows tailoring of combinations of different materials, thus choosing different types of microstructure with the intent to effectively control the resulting mechanical properties. Designing multi-material components means increasing the potential functionality with the downside of increasing the complexity to produce such components, and assess their performances [11][12].

The different types of AM processes are presented in Figure 8-3 (appendix A), and a detailed table of the different MMAM processes is presented in appendix B.

Led by the industrial interest in reducing the number of assemblies, limiting the machining time, the part weight and the additional costs of inventory, the idea of tailoring the material composition in different geometrical locations within a component in a single operation, has gained interest in the scientific community [13]. Two main types of multi-material structure can be found in the

literature: on one hand dissimilar discrete material joining [14], and on the other hand functionally graded material structures [15], [16]. However both techniques have limitations, such as: mixing of material powders inducing material waste for functionally graded material transitions, while discrete joins are more prone to cracking and weakness at the interface [17]. Powder bed technologies are limited in the process to create graded structures [18], but can use deposition nozzles to create discrete multi-material deposition [19], [20], [21].

Some studies have focused on discrete vacuum removal of powder allowing more complex 2D powder delivery and a schematic of this technique in shown is Figure 8-4 in appendix A [22], [23], [24]. However dissimilar material produced by MMAM has often caused issues such as cracking or defects at the interface due to the interdiffusion between the dissimilar materials, and this is almost solely dependent on the coupling of the material that is combined [25]–[27] . Combination possibilities are endless but this work will primarily focus on a two materials that have relevant properties to survive harsh environments and that are of interest to industry (discussed in section 2.3).

1.2 Aims and Objectives

1.2.1 Aims

This PhD research project aims to investigate the effect of the microstructure and material properties on fatigue behaviour of 316L/IN718 produced by MMAM.

The present study aims to establish a knowledge of the MMAM layered structure fabricated by L-PBF, and investigate the effect a heat treatment (HT) can have respectively; on each alloy (produced by L-PBF) separately and as a multi-material structure, then the investigation will aim to determine the potential for fatigue performance enhancement, by investigating the crack propagation resistance of these layered architectures.

The novelty of this work links to developing an in-depth understanding of the chemistry and metallurgy resulting from MMAM process, and HT of MMAM structure, and understanding the relation between the microstructure and the fatigue performance of these new types of components.

1.2.2 Objectives

Consequently, the objectives for the present work are as follows:

1/ To characterise the microstructure of 316L/IN718 fabricated by MMAM, before and after HT.
2/ To characterise the tensile properties of 316L and IN718 separately fabricated by L-PBF before and after HT.
3/ To investigate the fatigue crack propagation behaviour through layered 316L/IN718, and link the results to the microstructure and mechanical properties, before and after HT.
4/ To compare and conclude, on the effect of HT on layered architectures produced by MMAM in order to mitigate the crack propagation resistance of these new types of structures.

1.3 Scope of this work

The fabrication of 3D metal parts (3DMP) is the focus of this work, and will be referred to both as 3DMP and AM, with a preference for AM. For comparative purposes the studies used for the literature review of this work will focus on processes using metallic powder as precursors, hence excluding the AM processes using wire or sheet for material joining. Finally, in the powder based category, the scope of this work will cover technologies that involves concentrated energy sources excluding the binding category. Therefore reducing the scope of interest to three main types of AM technologies:

- Laser Powder Bed Fusion (L-PBF): such as Selective laser Melting (SLM) , and its variant Selective Laser Sintering (SLS) . These powder-bed technologies are known for their ability to produce complex shapes with very high precision, but often limited in size by the dimension of the building chamber.
- Direct laser Deposition (DLD): such as Laser Engineering Net Shaping (LENS) and Laser cladding. These technologies do not use powder-bed but powder jet/nozzle that allow the fabrication of larger parts, and can even be used directly onsite for repairs.
- Electron Beam Melting (EBM) technology uses a different energy source from the above mentioned categories, and requires a chamber atmosphere maintained under vacuum during the fabrication process, allowing reactive materials such as Titanium to be included in the fabrication of highly complex design.

An extensive number of materials have been investigated for use with AM processes, however this work will focus on two alloys: 316L stainless steel and Inconel 718 (IN718).
Additionally most work on post-thermal treatments of AM parts has focused on repeating treatment protocols developed for wrought and cast material [28]. But this work will have to cover the literature around conventional heat treatment (HT) for both 316L and IN718 alloy.

1.4 Thesis structure

After the introduction the present work is structured as follows:

- Chapter 2: will cover the literature review, including: basic knowledge of fatigue of metallic materials, knowledge on 316L stainless steel and Inconel 718 metallic alloys and comparing effects of additive manufacturing, to conventional manufacturing, on these alloys' microstructure, the different types of thermal post treatment will also be discussed and finally the effect of multi-material layers on the mitigation of crack propagation. A gap in the scientific knowledge will be identified and set the scene for the development of the work.
- Chapter 3: will present the different experimental techniques used throughout the rest of this work, along with a characterisation of the metallic powders used as precursor in this work. The choice of a specific heat treatment sequence will also be discussed in this chapter.
- Chapter 4: will present the fatigue crack propagation in layered 316L/IN718 fabricated by L-PBF in the as-built state, and discuss the relation between microstructure and fatigue behaviour.
- Chapter 5: will present fatigue crack propagation in layered 316L/IN718, and effect of heat treatment on fatigue performance. The effect of layered architecture on the crack propagation resistance will also be discussed in this section.
- Chapter 6: will present a discussion covering the results found in both chapter 4 and 5 and compare the effect of the HT on the mitigation of crack propagation through multi-layer specimens of 316L/IN718 produced by L-PBF.
- Chapter 7: will summarise the results obtained, and draw conclusions.
- Chapter 8: will propose potential directions for future work.

Chapter 2 Literature review

2.1 Fatigue behaviour of metallic materials

2.1.1 Introduction and terminologies

The term “Fatigue” in metallic materials, is commonly referred to as: progressive and localized structural damage occurring in materials due to a repeated application of stresses and strains, this term usually applies to changes leading to cracking and failure [29]. The whole fatigue process includes fatigue crack initiation, propagation and final fracture. It is estimated that approximately 90% of the failures of industrial components are caused by fatigue damage. Cyclic fatigue testing is usually carried out under a nominal maximum stress which is usually selected below the ultimate tensile strength (UTS) or even the yield strength (YS), which are monotonic properties, of the material tested. Fatigue failure can occur under different types of fatigue loading and these can also be combined with other service conditions: mechanical fatigue, thermomechanical fatigue, corrosion fatigue, sliding contact fatigue, rolling contact fatigue, and fretting fatigue.

Fatigue cracks usually initiate from an accumulation of damage within the material structure, induced by cyclic stresses and strains that will eventually cause a crack to initiate, then propagate, until the crack reaches a critical size leading to failure. When it comes to cyclic fatigue testing, parameters used are described in Table 2-1 and Figure 2-1 and also include the frequency *f*.

Table 2-1 : Cyclic parameters from [29]

	Stress	Strain
Mean	$\sigma_0 = \frac{\sigma_{max} + \sigma_{min}}{2}$	$\varepsilon_0 = \frac{\varepsilon_{max} + \varepsilon_{min}}{2}$
Amplitude	$\sigma_a = \frac{\sigma_{max} - \sigma_{min}}{2}$	$\varepsilon_a = \frac{\varepsilon_{max} - \varepsilon_{min}}{2}$
Range	$\sigma_r = \sigma_{max} - \sigma_{min}$	$\varepsilon_r = \varepsilon_{max} - \varepsilon_{min}$
Ratio	$\frac{\sigma_{min}}{\sigma_{max}}$	$\frac{\varepsilon_{min}}{\varepsilon_{max}}$

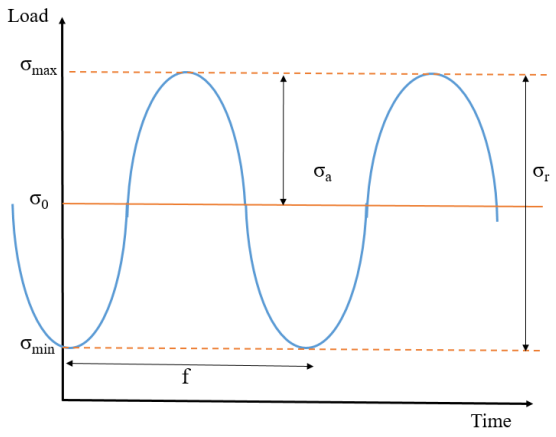

Figure 2-1: Schematic of sinusoidal loading cycle

Fatigue cracks can also be depicted by the physical loading orientation relatively to the crack front and crack faces, those different modes are shown in Figure 2-2 [30]:

- Mode I: Loads are perpendicular to crack plane, and crack faces are pulled away from crack plane, directing crack advance orthogonally to loads (opening mode).
- Mode II: Loads are parallel to crack plane, and crack faces are shearing collinearly to crack advance (in plane shear).
- Mode III: Loads are in plane with the crack plane, crack faces are sheared parallel to the crack front (anti-plane shear mode)

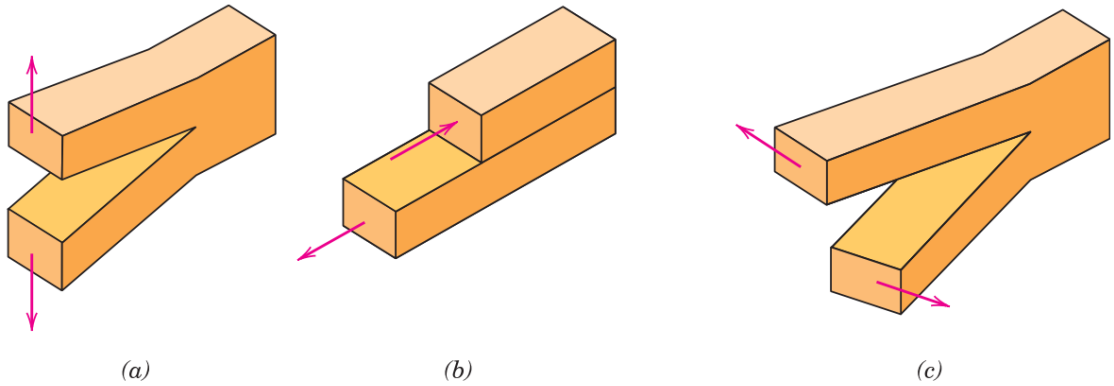

Figure 2-2: Schematic representation of different crack-opening modes, a) Mode I, b) Mode II, c) Mode III, from [29]

Cracks may start from the motion of dislocations at the atomic scale within the crystal structure, then dislocations combine to form a sub-structural defect at the microstructural level where permanent damage starts to nucleate, these subsequently grow and coalesce to form a macro-sized crack. Cracks can also initiate at existing microstructural defects such as pores, inclusions etc… that cause local stress concentrations that also initiate fatigue processes. The macro-size crack starts

to propagate stably, which eventually leads to material instability and grow into fast fracture. Cracks can be differentiated by their size and mode of growth behaviour. A brief description is given in Table 2-2 from [31], and more details on micro-mechanisms of crack initiation and propagation will be given in section 2.1.3.

Table 2-2 Definition and characteristic of fatigue cracks of different length from [31]

Abnormal crack-propagation behavior		K-determined crack-propagation behavior	
Microstructurally short cracks	**Mechanically short cracks**	**Physically short cracks**	**Long cracks**
• Strong influence of the microstructure • Mainly mode II crack propagation (stage Ia) and transition to mode I (stage Ib, see text) • Roughness-induced crack closure	• No pronounced crack-closure effects • Little influence of the microstructure • Mainly mode I crack propagation • Large plastic zone ahead of the crack tip (relative to the crack length)	• Little influence of the microstructure • Plasticity-induced crack closure not completely developed • Mainly mode I crack propagation • Negligibly small plastic zone ahead of the crack tip (relative to the crack length)	• Completely developed plasticity-induced crack closure (plastic wake) • Macroscopically long cracks (crack length of the order >0.5 mm)

2.1.2 Fatigue life approaches

The fatigue life is usually defined by the loading conditions experienced and the number of cycles to initiate a crack together with the number of cycles necessary to grow this crack to a certain critical size. The crack initiation size assumed varies depending on the prediction model employed [29]. Three strategies of fatigue life determination are commonly used:

• Total life approach: which comprises cycles for initiation and growth,

• Defect (or Damage) tolerant approach: which assumes that all real materials contain defects, hence primarily focuses on the influence of initial defects on subsequent crack propagation until final failure,

• Safe-life and fail-safe approach which is a combination of both.

However, only the two first approaches will be detailed further in this chapter, because safe-life and fail safe is essentially a combination considering both the first two approaches.

2.1.2.1 Total-life approach

The total life approach usually involves laboratory testing on relatively smooth surface specimens, at different stress or strain ranges. The number of stress or strain cycles needed to reach final

fatigue failure, are then presented in a curve named the Wöhler or S/N curve. In general, a specimen or component which has a life below 10^5 cycles is considered as being in the Low Cycle Fatigue regime (LCF), while a specimen or component where the life is longer than 10^5 cycles is considered as being in the High Cycle Fatigue regime (HCF). In LCF conditions, stresses are usually high enough to plastically deform specimens prior to failure, they are therefore often characterised in terms of strain range, and display predominantly a crack-propagation controlled life. While in HCF conditions, the specimens are elastically deformed, are usually characterised in stress range terms, and display predominantly a crack-initiation controlled life. Some materials reach a limit value below which specimen lives are considered quasi infinite (at very low stress level, usually in ferrous alloys) that is named the fatigue limit of the material [30]. Figure 2-3 shows the classic S-N curve where N is the number of fatigue cycles for a given value of stress range.

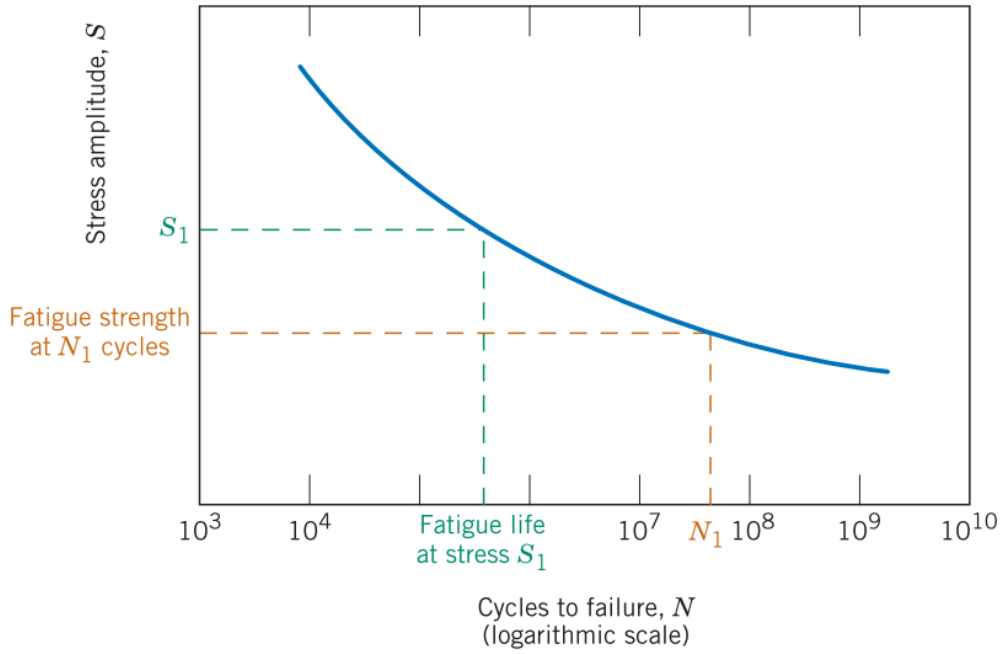

Figure 2-3: Schematic of Wöhler (or S/N) curve for metallic materials, from [30]

The Basquin equation is commonly used in the high cycle fatigue (HCF) regime, to establish the relation between fatigue stress amplitude σ_a, and fatigue life N_f using the fatigue strength coefficient σ'_f and the fatigue strength exponent *b*:

$$\sigma_a = \frac{\Delta\sigma}{2} = \sigma'_f (2N_f)^b \qquad (2\text{-}1)$$

In the LCF regime, the Coffin Manson equation is commonly used to link the plastic strain amplitude ε_a, to the fatigue life N_f using the ductility coefficient ε'_f and fatigue strain exponent *c*:

$$\varepsilon_a = \frac{\Delta\varepsilon_p}{2} = \varepsilon'_f (2N_f)^c \qquad (2\text{-}2)$$

Consequently the total strain amplitude $\frac{\Delta\varepsilon_{total}}{2}$ can be described as the sum of elastic and plastic strain amplitudes, giving the following equation:

$$\frac{\Delta\varepsilon_{total}}{2} = \frac{\Delta\varepsilon_e}{2} + \frac{\Delta\varepsilon_p}{2} \qquad (2\text{-}3)$$

When substituting the terms from the Manson-Coffin and the Basquin equations the total fatigue life can be characterised in terms of the elastic and plastic components of the total strain amplitude written as followed:

$$\frac{\Delta\varepsilon}{2} = \frac{\sigma'_f}{E}(2N_f)^b + \varepsilon'_f(2N_f)^c \qquad (2\text{-}4)$$

Where *E is* the Young's Modulus of the material. The total-life approach uses the S-N curve, as well as the Basquin (stress-life) equation and Coffin-Manson (strain-life) equation, in engineering design for selection of material for a component. However selection is then being made to mostly avoid fatigue crack initiation (rather than allowing for propagation explicitly). While most of the test data used are from smooth (defect free surfaces) specimens, in real life-applications the effect of defect levels and surface roughness, will affect the fatigue life of the component (considering also how temperature, corrosive environment, rough specimen surface, repetitive sliding or rolling contact affect initiation processes is also therefore necessary). For this reason, the total life approach is probably most useful for selecting materials where resistance to crack initiation is important, while it is unreliable in determining the resistance of a material to crack propagation or for use in direct structural integrity lifing. In applications where resistance to crack propagation is important, the damage-tolerant approach is adopted.

2.1.2.2 Damage-tolerant approach, using stress intensity factor K

The premise for the damage tolerant approach is that each mechanical component inherently contains imperfections, inner defects, microstructural flaws or inclusions, that sooner or later will form cracks which past a certain critical size will propagate. For engineering applications, the choice of a non-destructive detection technique (NDT), will limit the size of initial defect (a_0) detection due to the NDT resolution. The damage tolerant approach consists in crack propagation life prediction, based on empirical crack growth laws.

Amongst various fracture mechanics approaches developed to correlate fatigue crack growth with loading conditions, LEFM is therefore widely employed to calculate the stress field ahead of the crack tip. The present work will focus on the Mode I opening associated to the near crack tip stress field, and solely focus on the stress intensity factor K as a tool for crack propagation monitoring in a damage tolerant approach of the fatigue life of materials. As proposed by the basic hypothesis: the size of the specimen in which the small sharp crack (of length *2a*) is located, is an infinite

homogeneous, isotropic and elastic plate (LEFM), and the plastic zone ahead of the crack tip is very small in comparison with the flaw length hence small scale yielding (SSY) is assumed see Figure 2-4 [29].

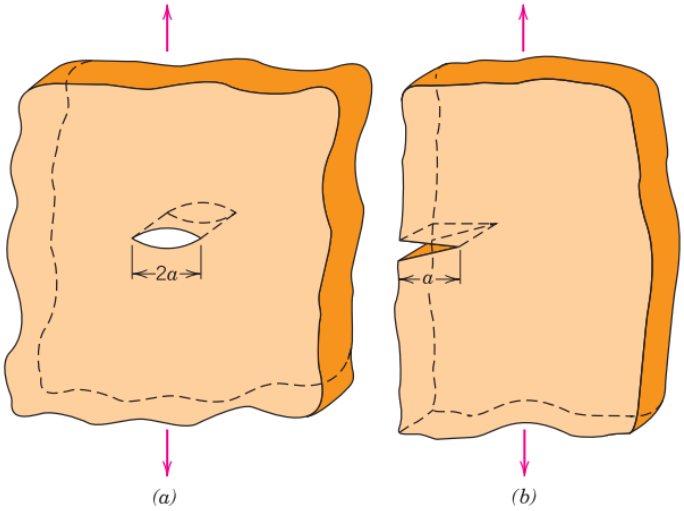

Figure 2-4: Schematic representation of a small sharp crack in a) a plate of infinite width and b) and semi-infinite plate with a small sharp crack on the edge [31]

Griffith has modelled a small sharp crack in infinite solid, where the advance depends on the energy balance between stress at the crack tip and cohesive energy in the material (strength), when the stress at the crack tip exceed the material strength the crack advances. These assumptions allow Griffith's energy balance theory:

$$\sigma_f = \sqrt{\frac{2E\gamma_s}{\pi a}} \qquad (2\text{-}5)$$

Where γ_s is the surface energy (or resistance to crack growth), σ_f is the fracture stress and a the crack length. Orowan's extension includes the elastic and plastic surface energy (that can be expressed with $\gamma_e + \gamma$) to Griffith's model as follows:

$$\frac{\sigma^2{}_f \pi a}{E} = 2\left(\gamma_e + \gamma_p\right) \qquad (2\text{-}6)$$

In order to measure the crack tip stress state, via the stress intensity factor, K, Linear Elastic Fracture Mechanics (LEFM) is usually coupled with the Small Strain Yielding (SSY) consideration, hence used to characterise the microstructure insensitive stage II crack propagation where the plastic zone ahead of the crack tip is considered to be very small compared to the crack size. In that case the radius of the plastic zone around the crack tip is considered to be small in comparison with the specimen dimensions and with the crack dimensions as well, hence elastic loading conditions prevail in the whole system and K is a good description of the crack tip stress state.

Traditionally, the initiation-based lifing approaches are made using the Mason-Coffin-Basquin equations, while propagation based lifing approaches are made using the Paris-Law equation. Due to their ease of application the Paris law is widely found in engineering applications. The Paris law's ability to predict crack propagation can additionally be complemented by incorporation of sub-structural phenomena to the model (i.e. geometrical or plasticity based theories [32]). The crack growth rate (da/dN) in LEFM-based model is considered to depend only on continuum parameters such as the far field stress range ($\Delta\sigma$), the crack length (a) and the load ratio (R).

The stress intensity factor (K) is a useful parameter in describing the stress state ahead of the crack tip and the driving force for crack propagation since it takes the contribution of crack size and applied stress into consideration and can be easily calculated by the specimen dimension and external loading conditions. In mode I opening the stress field at the crack tip can be described as followed (in polar coordinates (r,θ) close to the crack tip) [29]:

$$\begin{bmatrix}\sigma_{xx}\\ \sigma_{yy}\\ \sigma_{xy}\end{bmatrix} = \frac{K_I}{\sqrt{2\pi r}}\cos\left(\frac{\theta}{2}\right)\begin{bmatrix}1-\sin\left(\frac{\theta}{2}\right)\sin\left(\frac{3\theta}{2}\right)\\ 1+\sin\left(\frac{\theta}{2}\right)\sin\left(\frac{3\theta}{2}\right)\\ \sin\left(\frac{\theta}{2}\right)\sin\left(\frac{3\theta}{2}\right)\end{bmatrix} \qquad (2\text{-}7)$$

Here K_I represents the Mode I stress intensity factor, this term is defined by the applied stress σ and the flaw length a, as followed:

$$K = \sigma\sqrt{\pi a}\, f\left(\frac{a}{W}\right) \qquad (2\text{-}8)$$

Where f(a/W) represents the compliance function that expresses the component geometry and shape. K is used to describe the material's toughness, and the stress field at the crack tip; in mode I opening and in a perfect elastic condition, it can be considered that the K will be proportional to the nominal stress σ_n, in such condition K_{IC} can be written as follows, and can link back also to the strain energy approach of Griffith:

$$K_{IC} = \sigma_f\sqrt{\pi a} = \sqrt{2E\gamma} \qquad (2\text{-}9)$$

The concept of K has been adopted in fatigue theory to characterise crack growth behaviour, instead of using an applied stress range $\Delta\sigma$, the stress intensity factor range ΔK is used. By plotting the fatigue crack growth rate da/dN against ΔK in log-log co-ordinates, a sigmoidal curve can be obtained which can be divided into three distinct regions, as depicted in Figure 2-5 [29].

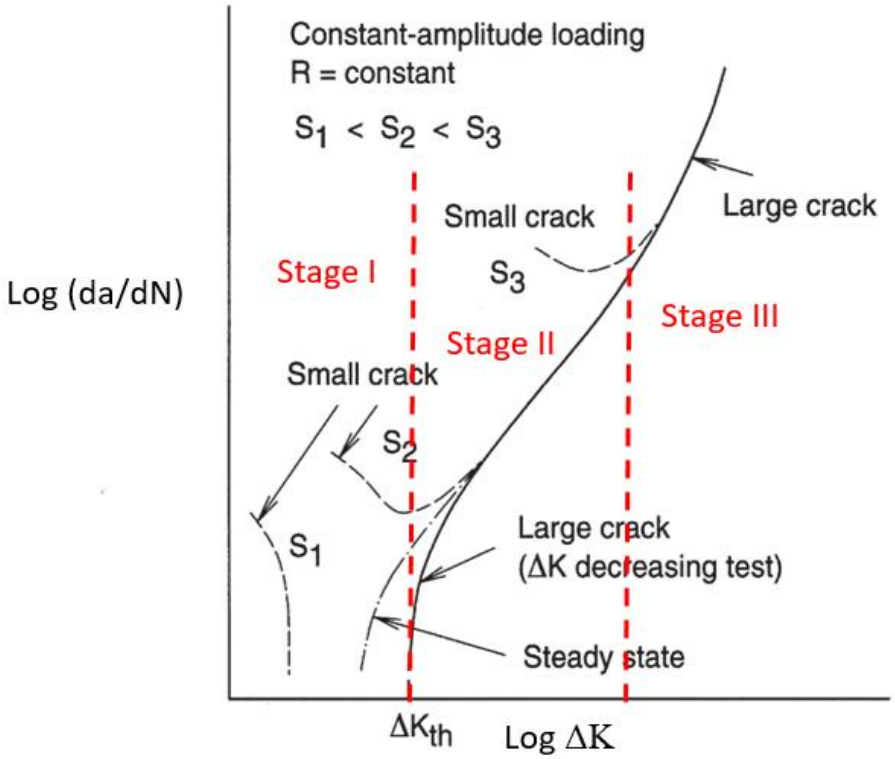

Figure 2-5: Fatigue crack growth representation for both short and long crack [31]

The lower part of the graph where small cracks nucleates is referred to as stage I fatigue growth and is very sensitive to the microstructure, whereas the central linear part of the plot is referred to as stage II crack growth and is microstructure-insensitive, where the Paris law applies, finally the third and fastest part of the curve is the final fatal fracture (or stage III)[33], [34]. The transition in fatigue from stage I, to stage II , mainly indicates that the plastic zone size ahead of the crack tip has reached a size that allows an averaging of the materials response above the microstructural characteristic dimensions (i.e. grain size). For this reason knowing the plastic zone size and average microstructure feature dimensions is useful to determine/understand the crack growth transition stage. Depending on the position of the crack front, i.e. the centre or the side of the specimen, either plane strain or plane stress conditions should be taken into account (see Figure 2-6 [35]). This is due to the effect the surrounding material has on the crack tip, the constraint is not the same within the core of the specimen and at the edges. Meaning that at the centre of the crack front (in the bulk/the core/the centre) of the specimen the strains following the out-of-plane axis (often referred to as z axis) are null, hence only the in-plane strains are calculated, due to the relative negligibility of this value within the thickness of a large specimen (from the Hooke's law formulation of strains) and a triaxial stress state exists. Whereas, plane stress often refers to the out-of-plane stress that is considered zero at the edges of the specimen (similarly to in a thin specimen where there is not enough bounding material to maintain the through-thickness stress).

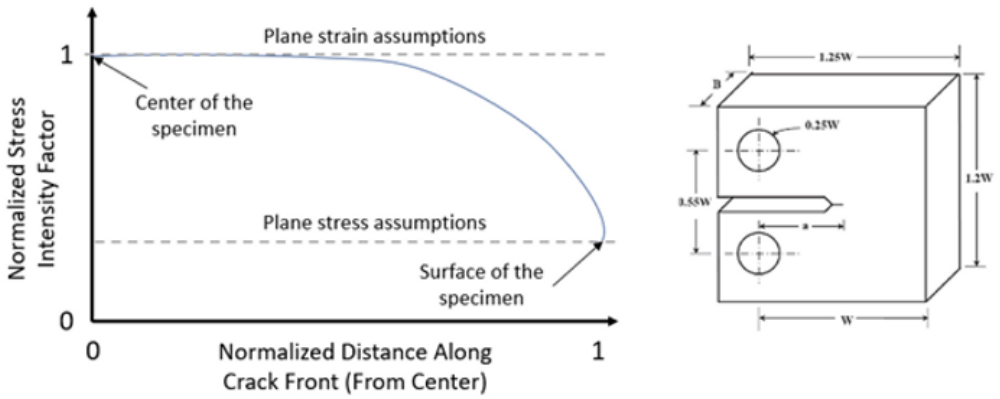

Figure 2-6: Schematic representation of the lateral view of the half-crack plane, in relation to the use of plane stress and plane strain assumptions [35].

The radius of the plasticity zone ahead of the crack tip can also be calculated by the Irwin equation, in plane strain conditions:

$$r_p = \frac{1}{3\pi}\left(\frac{K_I}{\sigma_0}\right)^2 \qquad (2\text{-}10)$$

And in plane stress conditions:

$$r_p = \frac{1}{\pi}\left(\frac{K_I}{\sigma_0}\right)^2 \qquad (2\text{-}11)$$

Where σ_0 is the yield strength (YS) of the material; and $\Delta K = K_{max} - K_{min}$ is the stress intensity factor range for the loading mode I, which is frequently used to compare crack growth behaviour. Assuming that two cracks of different size, loaded under different conditions, but having the same ΔK values, will have similar plastic zone size, this invokes the concept of similtude. The linear region of the *da/dN* against ΔK plot, central region also named stage II crack growth (also referred as crack growth in Paris regime), is commonly described by the Paris law:

$$\frac{da}{dN} = C\Delta K^m \qquad (2\text{-}12)$$

Where *C* and *m* are constants that describes material and environment and are specifically defined experimentally, albeit *m* is generally comprises between 2 and 4 for a ductile material. The Paris law is only applicable in constant load ratio cyclic tests. In the lower part of the graph (for low ΔK values) also called stage I crack growth, the Paris regime does not hold and the ΔK near zero or $da/dN \approx 10^{-10}\ m/cycles$, is referred to as the threshold value (ΔK_{th}). Commonly defined as the smallest driving force to attain a detectable crack growth rate [31].

So in summary: in damage tolerant fatigue analysis, K describes the local stress state at the crack tip, and can also be expressed in terms of: external loading conditions and specimen dimension. K describes the stress/strain conditions ahead of the crack tip, giving the crack driving force that correlates to the incremental crack growth per cycle. This can be directly translated to different types of crack (size or shape) under the same conditions, hence allowing a direct comparison with tests done under laboratory conditions to crack propagation within engineering components.

2.1.3 Micromechanisms of fatigue

2.1.3.1 Cyclic loading

Under cyclic loading materials can remain stable or undergo a softening or a hardening of their mechanical response, this is characterised by respectively an increase or a decrease of the material strength while being subjected to a constant cyclic stress or strain amplitude see Figure 2-7. This softening or hardening is due to the plasticity occurring in the material under cyclic loading.

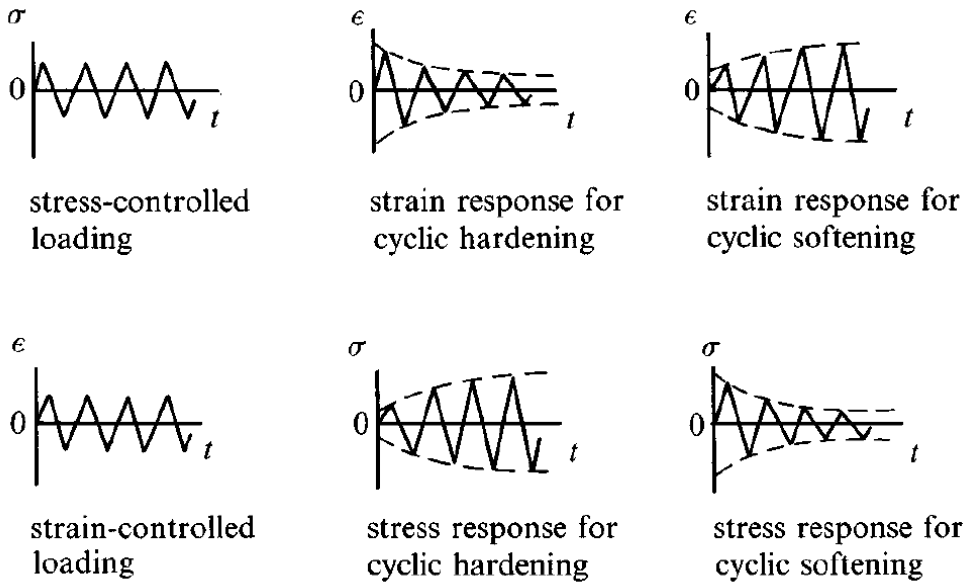

Figure 2-7: Hardening and softening mechanical response under cyclic fatigue loading (σ, ε and *t* standing for stress, strain and time respectively) from [29]

These mechanisms are linked to the dislocation rearrangements within the material structure during cycling, and usually reaches a saturation state. Damage accumulation induced by cyclic loading in the early stage of fatigue, can last up to 90% of the fatigue life in HCF before the nucleation of the first micro-crack leading to final catastrophic failure [29]. The monotonic stress-strain behaviour of ductile solids under uniaxial tension is generally represented by a constitutive law, such as the Ramberg-Osgood relationship. Ramberg-Osgood equation can also be used to describe a cyclic stress strain curve, when it is composed of the sum of two terms, ε_{as} the elastic strain amplitude and the plastic strain amplitude ε_{ap} [36]:

$$\varepsilon_{as} = \frac{\sigma_a}{E} \qquad (2\text{-}13)$$

$$\varepsilon_{ap} = (\frac{\sigma_a}{K'})^{\frac{1}{n'}} \qquad (2\text{-}14)$$

That gives the total strain amplitude ε_a, with n_f the cyclic strain hardening exponent and *K'* the cyclic strength coefficient:

$$\varepsilon_a = \frac{\sigma_a}{E} + \left(\frac{\sigma_a}{K\prime}\right)^{1/n\prime} \quad (2\text{-}15)$$

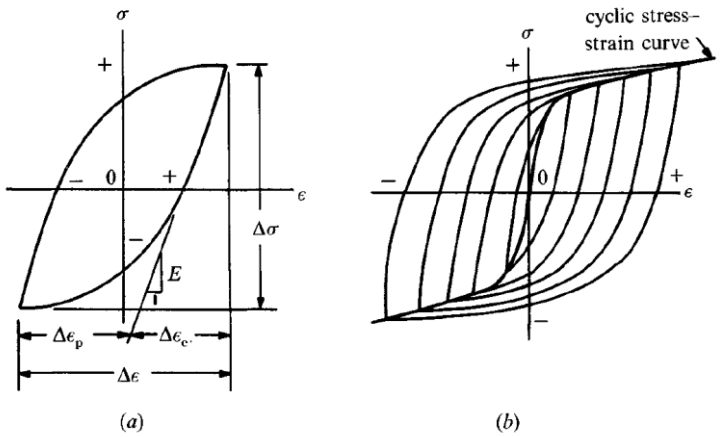

Figure 2-8: a) a cyclic stress-strain curve with parameters, b) stress-strain curve under cyclic loading by [29]

One cycle in cyclic loading can be represented by a hysteresis loop see Figure 2-8 a) and the stress-strain cyclic curve is presented Figure 2-8 b) [28]. A model of this hysteresis loop under cyclic stress-strain behaviour under uniaxial tension is commonly described by the Ramberg-Osgood equation using the amplitudes of stress and strain range:

$$\frac{\Delta\varepsilon}{2} = \frac{\Delta\sigma}{2E} + \left(\frac{\Delta\sigma}{2A}\right)^{1/n_f} \quad (2\text{-}16)$$

The expression of the strain amplitude related to the number of cycles to failure is expressed by the Manson-Coffin-Basquin equation, as described earlier [36]:

$$\varepsilon_{ac} = \frac{\sigma'_f}{E}(2N_f)^b + \varepsilon'_f(2N_f)^c \quad (2\text{-}17)$$

Where σ' is the coefficient of fatigue strength under tension compression, *b* is the fatigue strength exponent, ε'_f is the coefficient of fatigue plastic strain, *c* is the exponent of fatigue plastic strain, and N_f is the number of cycle to failure. This equation is also composed of the sum of the elastic and plastic strain amplitudes, such as:

The elastic strain amplitude:

$$\varepsilon_{as} = \frac{\sigma'_f}{E}(2N_f)^b \quad (2\text{-}18)$$

And the plastic strain amplitude:

$$\varepsilon_{ap} = \varepsilon'_f(2N_f)^c \quad (2\text{-}19)$$

2.1.3.2 Dislocation evolution of FCC crystal structure under cyclic loading

This work will focus around the FCC (face centred cubic) crystal structure, because both Inconel718 and 316L stainless steel matrix are mainly composed of the FCC crystal structure.

The FCC crystal structure primary slip systems are {111} slip planes and <110> slip directions and eventually at higher temperature, or after a certain density of dislocation accumulation, a secondary cross slip system can activate nominally: {100} and < 011 > [29].

Under cyclic loading of an FCC crystal structure, primarily dislocation piling occurs during the hardening (or softening) stage, under further loading the dislocation arrangement evolves from dislocation vein or wall structures, towards labyrinth or channel then cell structures. In other words, the dislocation-motion evolves from single plane edge motion to screw motion (where secondary slip or cross slip systems activate), inducing a temperature or strain-dependent evolution in dislocation motion, that creates different dislocation structures (from wall-shape to channel shape see Figure 2-9).

The formation of persistent slip bands (PSBs), are first confined to a single slip system (i.e. wall structure of dislocation during primary slip), then comes a transient state where the FCC material hardens or softens (depending on the alloy), and in some case both hardening then softening stages can be found. Afterwards FCC structures tend to plateau over a range of plastic shear strain amplitudes, then above a certain strain amplitude labyrinth and cell structure will appear and stabilize.

In their work on 316L austenitic stainless steel response to cyclic deformation under high strain amplitudes, Pham et al. [37] have shown the dislocation arrangement is different depending on the plastic strain amplitude of loading:

- under low plastic strain amplitude, 316L dislocation arrangement follow planar arrangement until failure.
- under intermediate plastic strain amplitude PSBs and veins coexist under vein arrangements until failure.
- under high plastic strain cyclic loading dislocations follow a cellular structure arrangement.

This dislocation cell arrangement is supporting consecutive hardening and softening stages in 316L material. At first a planar arrangement with an increase in dislocation density corresponds to the hardening stage of material properties under cyclic loading, then a softening stage corresponding to the veins of dislocation walls separated by dislocation free regions, and finally the steady state response of 316L material when it reaches a cell arrangement see Figure 2-9 [36].

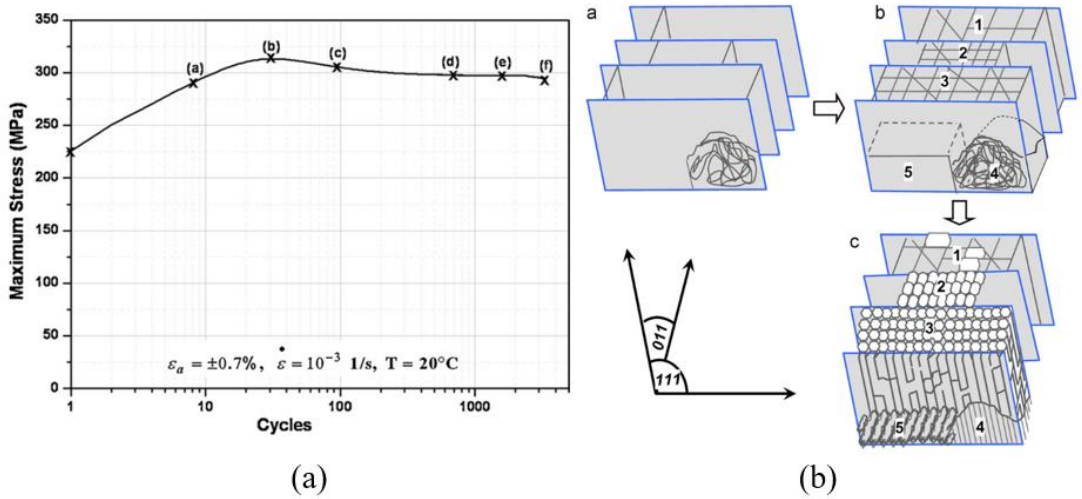

Figure 2-9: Austenitic 316L stainless steel behaviour, a) illustration of consecutive hardening and softening stages, b) schematic representation of dislocation arrangement into cell structure under cyclic loading from [37]

When dislocation structure evolves to the cell-shape, they tend to reach a saturation size (stress or deformation induce wavy slip). This wavy type of multiple slip system activation, is commonly found in Nickel based super alloys when temperature allows the secondary slip system to activate.

Low Stacking Fault Energy (SFE) due to the addition of certain elements (such as Aluminium for example) can inhibit the cross-slip (i.e. dislocation arrangements into the cell shape) and promote planar (i.e. primary) slip. Thermal history (i.e. cold work or annealing) can also influence PSB formation. A correspondence between saturation stress and deformation induced cell-size has been developed experimentally and expressed as follow:

$$\frac{\sigma_s - \sigma_0}{E} = B\frac{b}{\lambda_s} \qquad (2\text{-}20)$$

Where σ_s is the saturation stress, σ_0 is the back stress, *b* the magnitude of the Burger's vector, λ_s is the linear intercept cell size and *B* a material constant proportional to the SFE. This equation can be used in both monotonic and cyclic situations, for stress-induced steady-state cell size.

2.1.3.3 Fatigue crack initiation and stage I fatigue

Fatigue crack initiation, or nucleation stage, depends on the scale of observation. Starting from defects piling along a PSB, or a microscopic flaw accumulation at a GB or inclusion, causing a stress concentration artefact that leads to cracking. Different things can be the root-cause leading to crack nucleation:

- Roughness induced. Roughness on the surface causes stress concentration and can lead to crack nucleation. From a very smooth starting surface, roughness is usually induced by extrusion or intrusion of irreversible slip bands movement along shear planes due to cyclic

loading. Microstructure that promotes planar slip, along with low SFE are more subject to slip band crack initiation [38].

- Crack initiation along PSBs. PSBs are due to the accumulation of irreversible slip (dislocations) with the lattice, PSB and matrix interface is weakened leading to crack nucleation. These are often found at the root of intrusions or protrusions on the surface [39].
- Grains and twin boundaries, can lead to crack initiation. Stresses between grains due to orientation mismatch, or the presence of inclusions, of a brittle phase located between grains can all cause weakness at the GB area. If orientation of a large grain is at a favourable angle relatively to the tensile load axis, it can lead to long PSB formation, and thus lead to cracking [40].
- Porosities and inclusions can act as stress concentration areas. Porosities are commonly found in AM components and can be considered as pre-cracks because of their size and shape that correspond to the microstructural dimensions. Similarly particles and inclusions have an interface susceptible to debonding with the matrix. For instance mismatch in thermal expansion can lead to local strain at the interface, creating a weaker site or initiate slip, leading to crack nucleation [41] .
- Environment can lead to initiation sites by corrosion, oxidation, wear, hydrogen embrittlement. External environment conditions can enhance surface roughening or transport of chemically embrittling species along PSBs [42].
- Geometry can create a local stress concentration in mechanical components. This area can be reproduced experimentally by the investigation of notch effect on crack initiation [32].

Crack initiation is also sometimes called stage I fatigue, and refers to cracks of similar size to the surrounding microstructural dimensions. The corresponding plastic zone size has either equivalent or smaller dimension than the surrounding microstructural features (grain size, space between precipitates). Stage I cracks tend to initiate at the surface then propagate across a whole grain, preferentially with a 45 degree angle respectively to the loading axis, along a crystallographic plane (along PSB). Therefore coarser grains with optimal orientation, are preferential sites for short crack initiation. Stage I crack growth rate is usually fluctuating. Because stage I crack growth is predominantly limited to shear on preferential slip planes within grains, it leads to a zig-zag crack path with temporary arrests at grain boundaries (GB or any high angle boundaries). Additionally other microcracks can also lead to shielding effect, therefore creating a highly faceted appearance on the crack path on the specimen surface (see Figure 2-10). This is why this stage is stated as microstructurally dependent, due to the non-linear growth rate. LCF short crack growth, is preferentially studied by elastic-plastic fracture mechanics (EPFM) or statistical approaches.

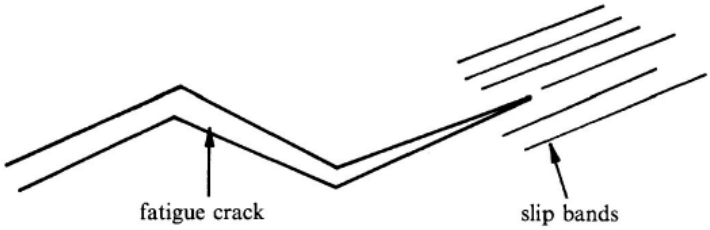

Figure 2-10: Schematic of stage I fatigue crack path along slip bands from [29]

- Microstructurally small cracks (MSC): have a non-uniform crack advance aligned to the interaction between crack tip and microstructure (grains boundaries precipitate etc...) and is due to the crack size scale which is comparable with the surrounding microstructure dimensions. (described as stage I in Figure 2-11 [43])
- Mechanically small cracks: when the near crack tip plastic zone size starts to grow bigger than the crack size and drive crack propagation, leading to growth on multiple slip systems (shown as stage I b in Figure 2-11 [43])
- Physically small cracks (PSC): cracks have reached a sufficient size to average the effect of surrounding microstructure, leading to more continuous growth, and more pronounced effect of crack closure mechanisms (roughness, plasticity...). It is also named the transition stage just before stage II crack growth starts.
- Chemically small crack: similar to PSC but environment is affecting crack growth inducing oxidation or closure.

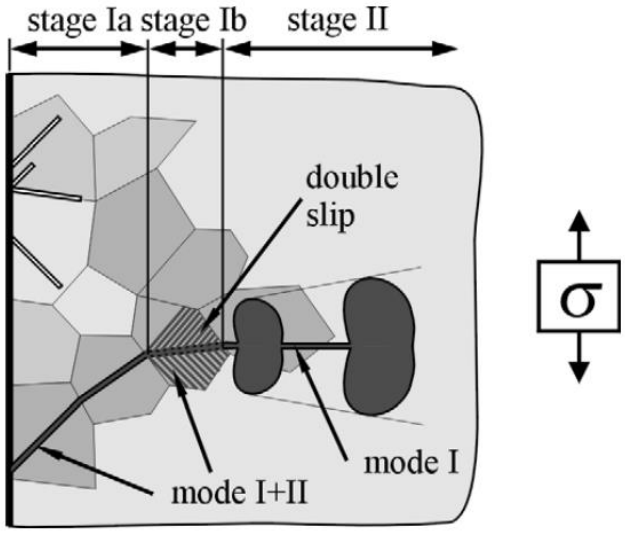

Figure 2-11: Stage I to Stage II fatigue crack transition from [43]

D. Kwon et al. [44] have enumerated different crack sizes corresponding to the different short crack types. The transition crack length from short to long crack growth regime in plane strain

conditions, can be defined by using the stress intensity factor at transition ΔK_T and the grain size d_g:

$$a_T = \frac{1}{A.\pi.Y^2}.(\frac{\sigma_y}{\Delta\sigma})^2 . m. d_g \qquad (2\text{-}21)$$

Where A is the coefficient in the cyclic plastic zone size in plane strain condition (i.e.≅ 0.03 − 0.04), $\Delta\sigma$ is the applied stress range, σ_y is the yield strength of the material, and Y is the shape factor in the stress intensity factor at transition such that:

$$\Delta K_T = \sqrt{\pi. a_T}.Y.\Delta\sigma \qquad (2\text{-}22)$$

Typical values for Y are 0.72 for a semi-circular crack and 1 for an embedded through crack.

Miller et al. [45] have defined MSC and PSC short crack growth equation, such as (see Figure 2-12):

- In MSC regime: $\frac{da}{dN} = A(\Delta\gamma)^{\alpha}(d-a)$ where Δγ is the shear strain range and A and α are material constants, d is the microstructural dimension in μm (most significant barrier spacing) and this equation is valid for the crack length a to be of size comprising between 0 and d.

- In PSC regime: $\frac{da}{dN} = B(\Delta\gamma)^{\beta}(a-C)$ where B and β are material constant and C representing the threshold condition (when $da/dN = 10^{-10} mm/cycles$). B and β are found by regression fitting of the experimental data points when a is superior to d (most significant barrier spacing microstructural dimension in μm).

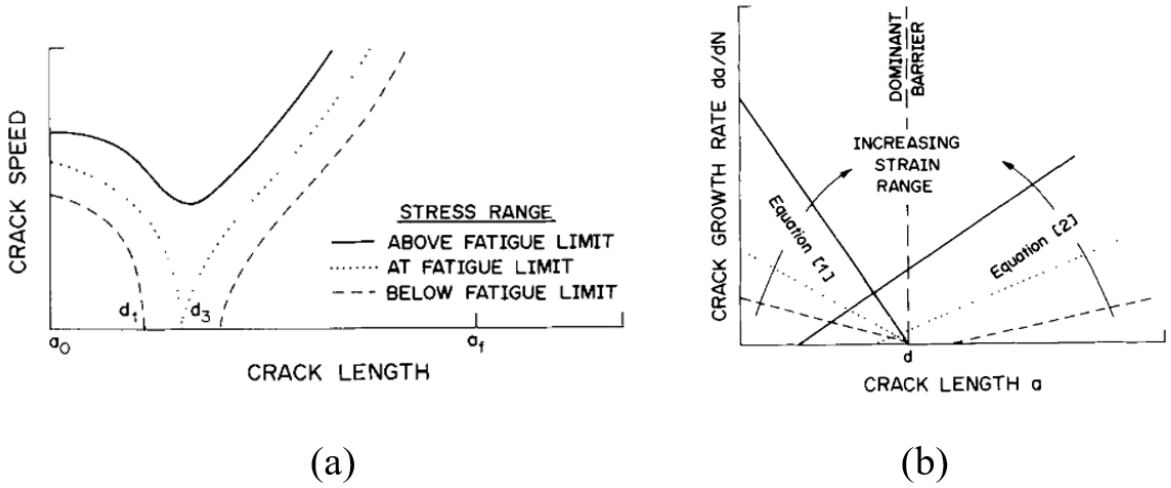

Figure 2-12: short crack behaviour a) growth behaviour above and below fatigue limit stress level, b) schematic of MSC and PSC crack growth from [45]

2.1.3.4 Fatigue crack propagation and stage II fatigue

In mode I loading under higher stress intensity factor range values, the crack will start to grow orthogonally to the loading axis. Then after a certain period of cyclic loading, the plastic zone size ahead of the crack tip will reach a critical size sufficient to encompass multiple grains and create dislocation movement over multiple slip systems, namely stage II fatigue crack growth may become observable by fatigue striations on the fatigue crack surfaces (see Figure 2-13) [30].

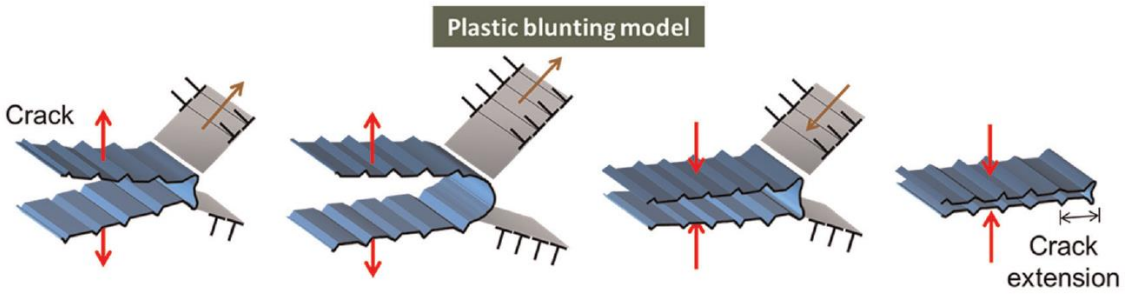

Figure 2-13: Schematic of the stage II crack propagation under cyclic loading, from [32]

Striations are characteristic of the crack advance in the Paris regime. The formation of a striation after each loading cycle is due to the activation of multiple slip systems oriented at 60^{o} from the crack plane. However, striations are not always observed in every material, but mainly in ductile alloys. Typically in the FCC crystal structure, alternating shear over intersecting slip planes causes planar crack advance. This is due to duplex slip, and can often be found in ductile materials. During stage II crack growth transgranular and intergranular or even a combination of both propagation modes, can be found on the fracture surface. Finally final fatal fracture is known as stage III crack growth, and it can be recognised by fast growth rate and high ΔK levels. A Stage III fracture surface tends to present cleavage or microvoid coalescence [29].

2.1.4 Fatigue in multi-layered structures

The propagation of long cracks through multi-layered specimen has been under investigation for many years before AM technologies were present, either for welded joints, or chemically deposed material layers, or by diffusion bonding, the effect of the interface transition on the crack propagation has been studied to have a better control over these structures and possibly improve their crack propagation resistance. Depending on the orientation of the interface relative to the crack front, it is said that the transition interface is positioned as a crack divider (CD) when the interface is parallel to the crack front, and as a crack arrester (CA) when the interface is orthogonal to the crack front. In this work only the CA orientation will be discussed.

The material's inhomogeneity ahead of the crack tip will influence the crack tip driving force, hence creating a gradient in properties. It was found that the two main forms of interface transition (in CA orientation), were the splitting (debonding) or the slipping [10]. It was found that when surfaces de-cohere the normal stress ahead of the crack tip can be drastically decreased (see Figure 2-14).

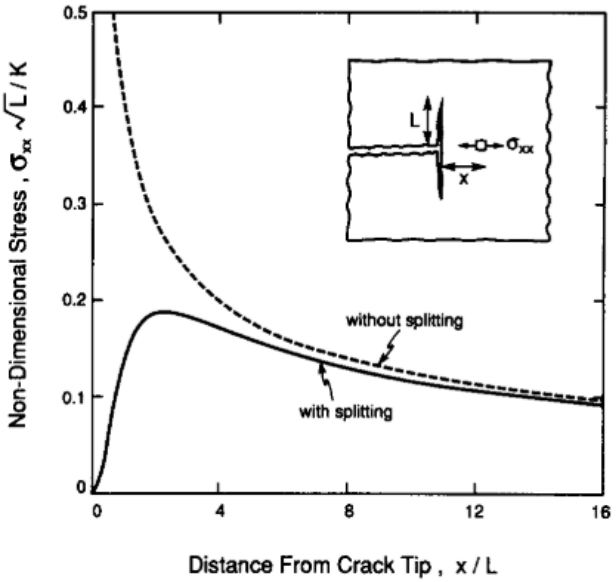

Figure 2-14: The in-plane stress ahead of the crack tip with and without a split at the interface, [10]

Additionally it was found that materials with thin layers and well-bonded interfaces have an initiation toughness exceeding that of the brittle constituent, then it was found that higher values of initiation toughness require either thicker layers or interfaces that exhibit extensive debonding and/or sliding. A more attractive approach is to introduce thin interface layers that allow extensive (but controlled) inelastic deformation, either by slip or debonding [10].

The mechanisms influencing the crack propagation by acceleration or deceleration were named anti-shielding (or amplification) and shielding respectively by Sugimura and Suresh et al. [46]. It was found by Kolednik et al. that a gradient in yield strength (YS) can have a positive effect on the mitigation of crack propagation [47]. And that in composite architectures the great difference in both elastic and plastic properties (being the elastic modulus and the yield strength respectively) of the compliant interlayer can cause a crack arrest without any delamination at the interface [48].

Models trying to implement the effect of a multi-layer structure in CA orientation to damage tolerant fatigue design are still very new and do not yet take into account the specific properties that the interface might have (local microstructure around the interface) [49], [50].

2.2 Materials and microstructure properties

2.2.1 Effect of L-PBF on metallic material microstructure

Laser Powder Bed Fusion technology (L-PBF) rely on a primary 3D CAD model, that is pre-sliced by tessellation language (.STL files), then successive layers of metallic powder are selectively fused by a focused laser source. The beam is oriented by mirrors and is concentrated at the surface of the powder layer. The part dimensions are limited by the dimension of the chamber, the process is conducted under protective atmosphere (usually an inert gas is used to fill the building chamber such as Argon), and the thickness of the layers are mechanically controlled by the level control on the vertical lowering of the plate and the deposition by roller of another layer of powder. The operation is repeated for as many successive layers of powder (see Figure 2-15 a) [5]. L-PBF technologies can manufacture components with an accuracy up to 25μm [3]. However L-PBF can also create defects such as: inner porosities that can be due to lack of fusion (these have an irregular shape), or from gas entrapped in the powder (these porosities have a spherical shape)[51], inclusions due to spatter particle [52], and rough surface finish [53], un-melted powder particles (or balling effect) can appear and is usually caused by insufficient energy input [54] (see Figure 2-15 b).

The L-PBF process, and AM of metallic material processes by extension, are characterised by a short interaction between the material and the heat source, and then by a thermal history of heating/cooling cycles where conduction and convection heat transfers are dominant, that can create within the component complex phase changes [55]. In addition, high cooling rates and thermal cyclic history will also affect the residual stress state within the component and/or can even cause cracking [56]. All these detrimental effects of L-PBF processes depend on the relation between material and process parameters which is the reason why many scientific studies are focusing around these topics [57] [58][59].

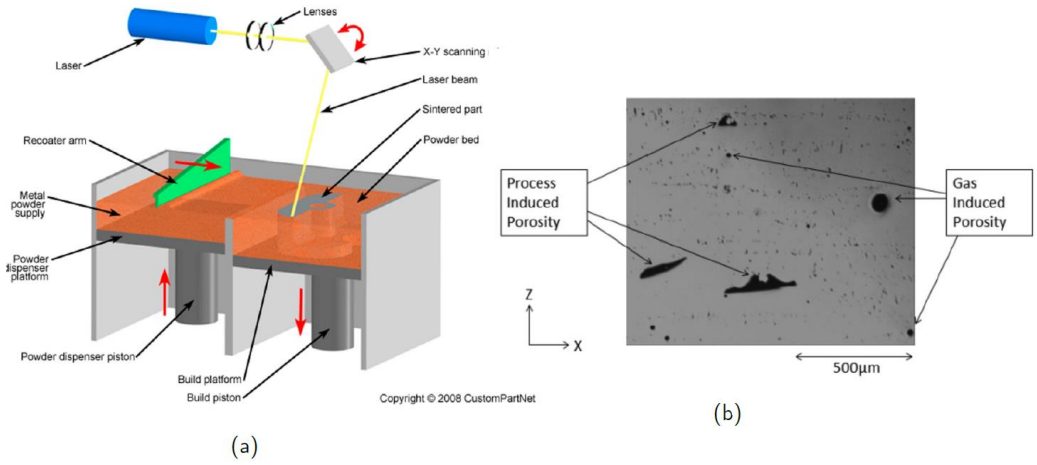

Figure 2-15: L-PBF process; a) schematic of L-PBF and b) Image of inner porosities types, from [60]

The powder roundness, flow ability, apparent density, size distribution and packing properties are playing an important role in the final quality of fused material [61]. The final part density can be improved from ~ 95 % up to more than 99 %, and final surface roughness can also be improved (see Figure 2-16). The use of smooth spherical powders, with a large size range distribution is therefore preferred. Re-used (or recycled) powders often show a certain decrease in quality during their life time, due to heat exposure and satellisation (i.e. agglutination of multiple powder particles creating a satellite), that can affect heat conduction and powder packing within the fused layer [62].
The microstructure commonly obtained from L-PBF is an elongated grained structure that follows the thermal gradient creating a directional solidification in the building chamber hence often causing directional anisotropic behaviour within the final manufactured part [6], [63]. Microstructure of materials processed by additive manufacturing (AM) usually presents fine cellular sub-grains, inside each individual larger grain of single crystal nature [64]. Study on intragranular segregation study in 316L made by L-PBF have classified the different scales of structure as [65]:

- The macro-level consisting of melt pools formed by the scanning trace of the energy source forming columnar grains in the range of 100 microns visible under EBSD,
- The micro-level being the intragranular cellular structure composed of fine elongated cells of same crystallographic orientation in the range of 0.5 to 1 micron,
- The nano-level, formed by nano oxides created during L-PBF process and spread randomly in the sample and are in the range of several tens of nanometers.

Different studies on grains and cellular sub-grain size, reveal a range of sizes that can vary from 10 to 100μm for large columnar grains, mainly influenced by the spot size and the process parameters employed, to a range of 0.5 to 5 μm for inner cells [66]. Strengthening mechanism by grain refinement is often characterised by the Hall-Petch relation, such as [67]:

$$\sigma_{YS} = \sigma_p + k_d . d^{1/2} \qquad (2\text{-}23)$$

Where σ_p is the lattice stress and k_d is the locking parameter value and d is the average grain size. Studies have been focusing on the relation between processing parameters often referred to as an energy density ratio (with P_{laser} the laser power in Watts, v_{scan} the speed of displacement of the laser h_{space} the spacing between each laser scan and t_{layer} the thickness of each powder layers displayed) and the defect content in produced parts [51][68]. This ratio is used to link the energy input by process parameters, to the final material needs, in order to obtain full density and melt in a stable manner [41]. Hence this ratio is commonly defined in a range, between a minima and a maxima values, where wetting and viscosity of liquids produce a stable meltpool allowing a three dimensional building, in order to obtain optimal densification of part (see Figure 2-16 from [68]).

$$E_{dv} = \frac{P_{laser}}{v_{scan} . h_{space} . t_{layer}} \qquad (2\text{-}24)$$

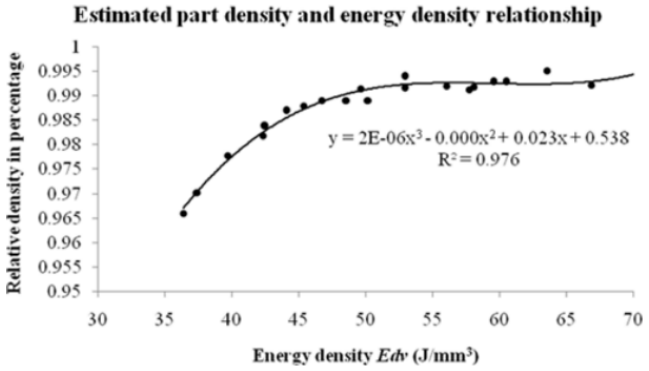

Figure 2-16: Polynomial part density and energy density relationship, from [68]

Other calculations have been proposed to characterise the interaction between laser source and the material [52], such as the laser energy transfer efficiency η_a:

$$\eta_a = \frac{E_{cal}}{P_t} \qquad (2\text{-}25)$$

With E_{cal} being the total energy absorbed by the work piece in Joules, P the laser power output and t the laser "on time". Additional attempts have been made to calculate the melting efficiency, by using the following calculations:

$$R_y = \frac{\eta_a PS}{\alpha^2 \Delta H_m} \qquad (2\text{-}26)$$

$$C_h = \frac{S^2 A}{\alpha^2} \qquad (2\text{-}27)$$

$$\eta_m = \frac{C_h}{R_y} = \frac{S.A.\Delta H_m}{\eta_a.P} \qquad (2\text{-}28)$$

Where η_a is the laser energy transfer efficiency defined in Equation 2-25, P is the laser power, S the travel speed, α is the thermal diffusivity at the liquidus temperature, ΔHm is the melting enthalpy, and A is the weld cross sectional area. While the ratio of C_h to R_y yields the melting efficiency [69].

The L-PBF process usually induces an increase in Yield Strength (YS) and in the Hardness (Hv) of material compared to the conventionally manufactured alloy [7]. This is partially due to refinement of the grains by Hall-Petch effect [67], and also due to the increase in dislocation density. The L-PBF process also induces a certain amount of residual stress within the component that can be reduced by adjusting the scanning strategy as was done by Lu et al. [70] in their study on the effect of island scanning strategy in Inconel 939. L-PBF tends to reduce materials ductility, however an increase in strength and a decrease in ductility can cause a reduction of the toughness of the material. Therefore in order to maintain a good balance between strength and ductility AM parts often require additional post thermal post treatment, such as annealing, to relieve the residual stresses in components. Hot Isostatic Pressing (HIP) has been investigated as a viable post treatment to close inner porosities from AM parts [71].

2.2.2 Effect of Heat Treatment on the L-PBF structures

As mentioned previously the AM processes induce an anisotropy of the mechanical properties within the components due to the orientation of the grain structure on solidification, following the direction of the thermal gradient. Additionally, commonly found defects such as porosities and inclusions can also be found aligned along the scanning tracks in a regular fashion [72]. The combination of such oriented microstructural characteristics can and will affect the overall structural integrity of the final part and its propensity for corrosion or crack initiation along its weaker features [73]. Having a more homogenous grain orientation would allow the specimen to display a predictable and continuous mechanical response throughout its geometry. Current research investigates various HT effect on AM specimens for many reasons such as: reducing the amount of residual stresses, supporting the formation of new strengthening phases and reducing the number of inner porosities within a component.

Techniques such as Hot Isostatic Pressing (HIP) have been investigated to support the closure of inner porosities. HIP can effectively be used if the compressive stress induced by the HIP pressure is greater than the yield strength of the material at the HIP temperature [74] [75] [76]. A combination of HIP treatment for 240 min at 1200 °C and 120 MPa was made onto IN718 alloy, by Kirka et. al, to support the closure of process induced porosities in addition to a standard HT which was reported to have successfully modified the microstructure's anisotropy from the columnar grain structure in AB specimens towards an equiaxed grain structure after the HT [77].

The annealing treatment is often used to allow the emergence of a supersaturated solution within the microstructure hence when applied to a very finely distributed cellular sub-structure, as it can be found within the columnar and elongated grains formed during the L-PBF process, it causes a relaxation of the dislocation network that surrounds the sub-cellular structure, hence causing an increase in the ductile response of the material. It is only on further ageing that strengthening can appear upon precipitation of the strengthening phases, that is the main finding of studies that have detailed the effect of each stage of a conventional HT separately on the microstructure of specimen made by L-PBF [78].

Post thermal treatment can also be used to relieve the structures from residual stresses after the AM process [79]. Some studies have also investigated the use of higher temperature homogenisation treatment to dissolve the carbides or reduce the amount of detrimental brittle phases within the microstructure such as laves phases [80]. But it was very well explained by Cheruvathur et al. that these types of processes involve added costs of production and may not be industrially acceptable. It was also found that while HT in the low-temperature regime may not yield a uniform microstructure due to slower diffusion kinetics, HT in the high-temperature regime tend to cause a coarsening of pre-existing carbides that may be unavoidable [81].

2.2.3 316L stainless steel alloy

2.2.3.1 316L SS conventionally manufactured

Austenitic stainless steels are known for their high Chromium content that provides a good corrosion resistance. Along with other elements Nickel is used in the 316L composition as an austenite stabilizer, and Molybdenum is used to resist pitting corrosion. However Molybdenum is also known to support formation of detrimental phases such as: *σ* ($(Fe,Ni)_x(Cr,Mo)_y$ intermetallic), and the Laves phases (such as Fe_2Mo, Fe_2Nb and Fe_2Ti which can also be found in austenitic stainless steels). Ferrite is a precursor for *σ* phase formation (see Figure 2-17), meaning that on increasing the temperature the ferrite phase will transform into σ phase. Chromium and Nickel equivalent calculations (see equation 2-30 and 2-31 below), are based on the Schaeffler diagram (not reported here) and rank 316L austenitic stainless steel in the range of 10% potential Ferrite formation on solidification [82].

$$Cr_{eq} = Cr + 1.37Mo + 1.5Si + 2Nb + 3Ti \qquad (2\text{-}29)$$

$$Ni_{eq} = Ni + 0.3Mn + 22C + 14.2N + Cu \qquad (2\text{-}30)$$

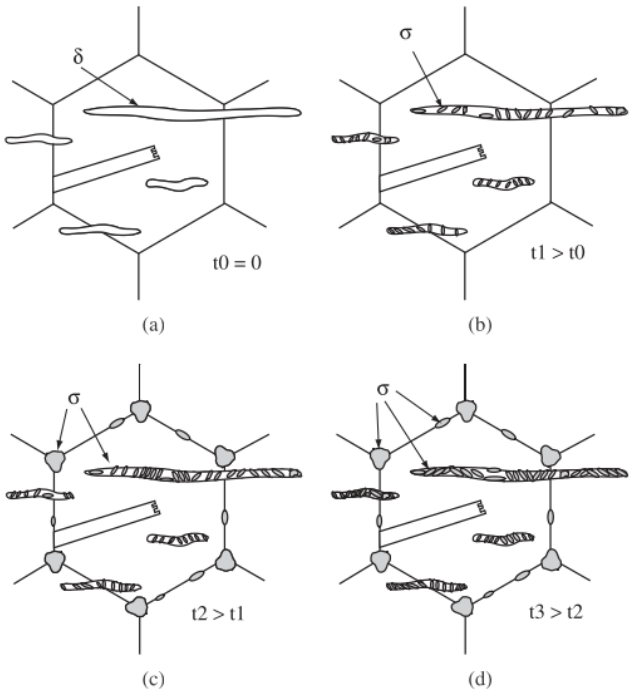

Figure 2-17: Schematic showing ferrite acting as sigma phase precursor from, a) from room temperature at t=0, then b) c) and d) show effect of a gradual temperature increase [82]

The *σ* phase is the only intermetallic phase among the three mentioned above that occurs in the binary Fe–Cr system. In the steels containing Mo and/or Ti, precipitation of Laves phase occurs below 850^oC. The presence of Nb significantly increases the highest temperature at which sigma

and Laves phase can form, increasing it to about 950^oC). According to Lai et al., below 700^oC the precipitation of sigma (σ) phase in an AISI 316L steel takes place after Laves phase precipitation is finished. The Laves phase of Fe_2Mo type was found in AISI 316 stainless steels with molybdenum contents between 2 and 3 wt% for long annealing times. The Laves phase nucleates predominantly on dislocations while the *σ* phase nucleates mainly on grain boundaries [83] (see Figure 2-17).

The ternary diagram of Cr-Fe-Ni elements is presented in Figure 2-18 showing that *σ* phase (intermetallic) can appear during ageing between 550 to 900^oC, with a composition $(Fe,Ni)_3(Cr,Mo)_2$ in 316LSS.

However *σ* phase has relatively slow kinetics (i.e. it requires long diffusion time to form, due to its composition that include a variety of elements, and its lattice arrangement has an important difference with the austenite lattice) and usually precipitates after carbides and nitrides. Sigma (σ) phase formation can be rapidly supported by ferrite phase (precursor phase) and on the contrary sigma phase formation can be delayed by increasing the annealing temperature. Similarly, with the presence of Mo the *χ* phase can form during ageing (see Figure 2-18 b)) between 550 to 900^oC, its precipitation precedes the *σ* phase and contains carbon, it tends to form at the grain boundaries (GB). Another IM phase that can be found in 316L stainless steel, is the $M_{23}C_6$ carbide (mostly composed of Chromium see Figure 2-19), that increase the lattice parameters, because the lattice parameter of the carbide is three time the size of the austenite it creates a characteristic diffraction pattern (lattice parameter: [1.0569-1.0676]nm). The temperature range of formation of this carbide can be found from 600 to 1100^oC, and preferentially occurs at a GB and/or at high angle boundaries which may occur within grains. The detrimental effect of this carbide precipitation is the depletion of Cr and Mo content in the vicinity, and increasing corrosion susceptibility of GB (see Figure 2-20 from [83]). The *η* carbide also known as M_6C, often found in austenitic stainless steel containing Molybdenum and Niobium, has an FCC diamond type lattice with dimension close to austenite, and it may appear from a transformation of $M_{23}C_6$ [84]. The intermetallic *σ* phase, *χ* phase, and Laves phase *η* are topologically close packed phases (TCP) that are characterised by large interatomic distances between layers of atoms.

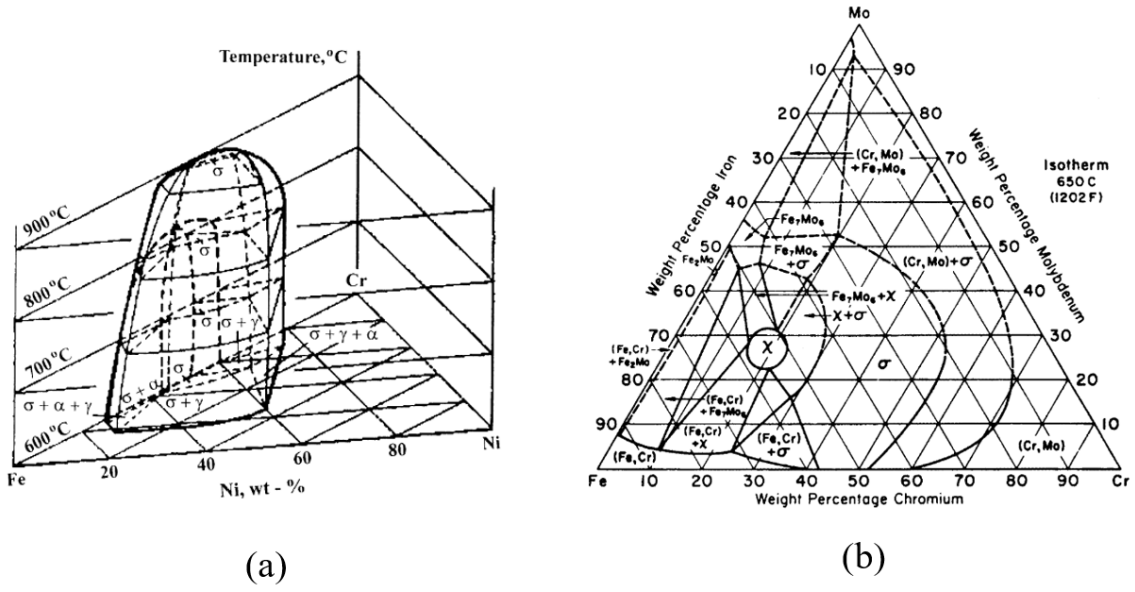

Figure 2-18: Austenitic stainless steel behaviour; a) 3D Schematic of Cr-Fe-Ni phase diagram, b) 2D diagram of Cr-Fe-Mo phase diagram, from [84]

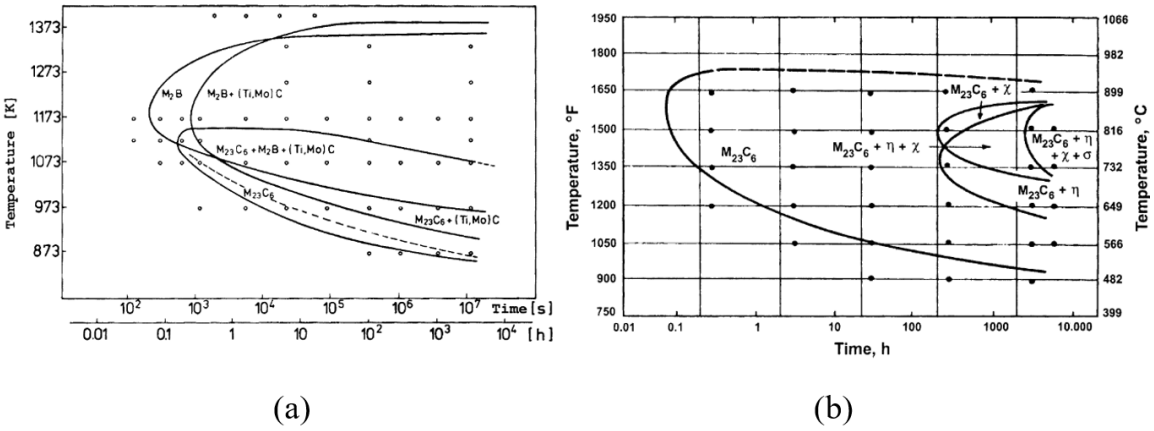

Figure 2-19: Time-Temperature precipitation diagram for Austenitic stainless steel [84]

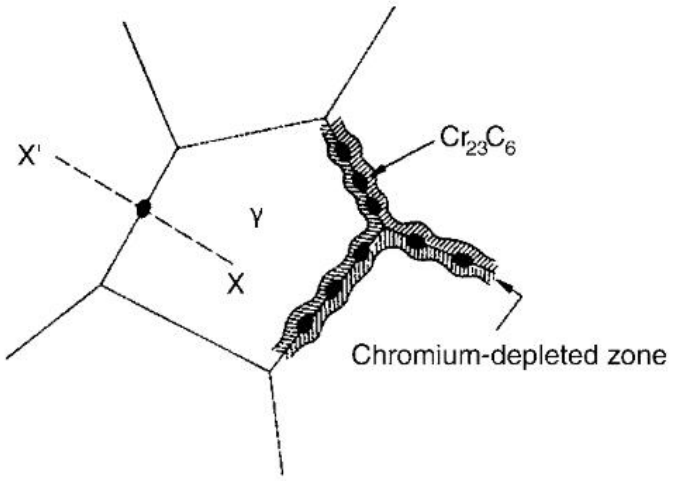

Figure 2-20: Schematic of Chromium carbide formation at the GB , [83]

2.2.3.2 316L SS manufactured by L-PBF

All the references discussed in this section are referring to AB material, no HT was made or has to be considered part of the following results. Peng et al. [68] in their study on the optimisation of the energy density parameter for 316L material, have defined a range between 35 and 70J/mm^3, which aims to reduce as much as possible inner porosities while keeping a high laser power and high scan speed. Whereas in their study Wang et al. [85] defined an optimal energy density ratio for 316L fabricated by L-PBF around 125J/mm^3, lower energy density uses were reported to cause insufficient densification and limited mechanical properties.

Saeidi et al. [86] describe elemental segregation occurring during rapid cooling at the cellular sub-structure external boundary leading to the segregation of heavier elements like Mo and Cr, and nano inclusions of Silicon Oxide at the cellular boundaries, this observation was later confirmed by Pace et al. and Wang et al. [64], [85]. The presence of nano inclusions has also been observed at the cellular boundaries, with Si and O elemental concentration as it is presented in Figure 2-21 [57]. The composition of L-PBF 316L is usually maintained as fully austenitic after the L-PBF process [65]. The residual stress state in 316L fabricated by L-PBF was studied by Wu et al. [56], and is related to the scanning strategy, where scanning island strategy shows different residual stress state, large islands show a reduced residual stress state, that can be reduced when continuous scanning strategy is used (3x3mm^2 islands present higher residual stress than 5x5mm^2, in 316L material).

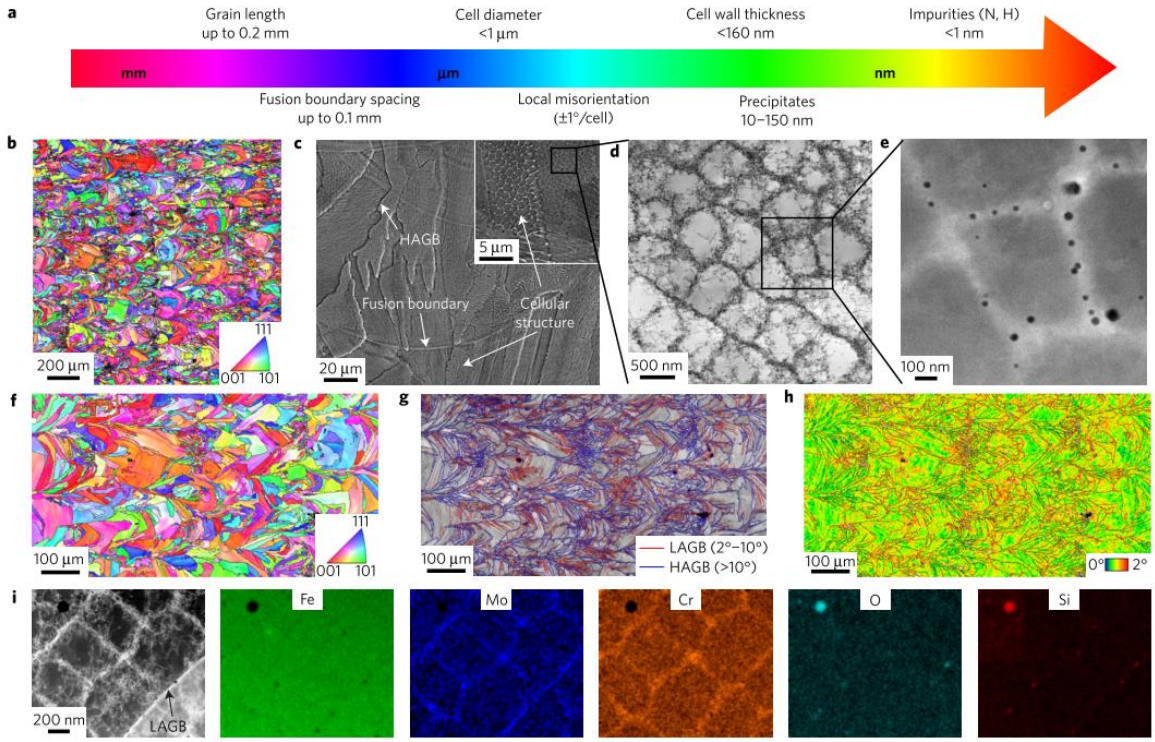

Figure 2-21: Elemental segregation and different level of structure present in L-PBF 316L, from [56]

The dislocation network around the sub cellular boundaries promotes slip and homogeneous deformation via shear, due to the already formed dislocation cells. This phenomenon called twinning induced plasticity of L-PBF 316L material, was described by Pham et al. [66] and tends to support shearing and plasticity between low angle boundaries, this deformation mechanism was also reported by Niendorf et al. [87]. The deformation mechanism in FCC crystal structure due to the formation of a network of dislocation cells was studied in conventionally manufactured 316L by Pham et al. [37], and was discussed earlier in the section 2.1.3.2.

2.2.3.3 Heat treatment of 316L SS

2.2.3.3.1 Heat treatment on conventionally manufactured 316L

It is stated in standard AMS 2759/4D [88] that annealing is the most common thermal post treatment for conventionally manufactured (wrought) 316L stainless steel, more specifically at 1066°C followed by air cooling or vacuum gas quenching.

2.2.3.3.2 Heat treatment on 316L manufactured by L-PBF

Due to the difference in the starting microstructure from wrought to L-PBF produced microstructure, the effect of heat treatment (HT) on the elements present within the microstructure will also differ. That is the reason why studies have emerged in the literature discussing the effect HT on the 316L microstructure produced by L-PBF. Study by Yin et al. [89] used direct ageing for 500°C to 800°C up to 400h to study the thermal stability of secondary phases in L-PBF 316L. It was found that due to the micro-segregation of heavier elements around the cellular sub-structure within grains and at high angle grain boundaries (HAGB) within 316L SS made by L-PBF, the precipitation of the σ (sigma) phase was facilitated at 800°C annealing temperature (within 30min) [89]see Figure 2-22.

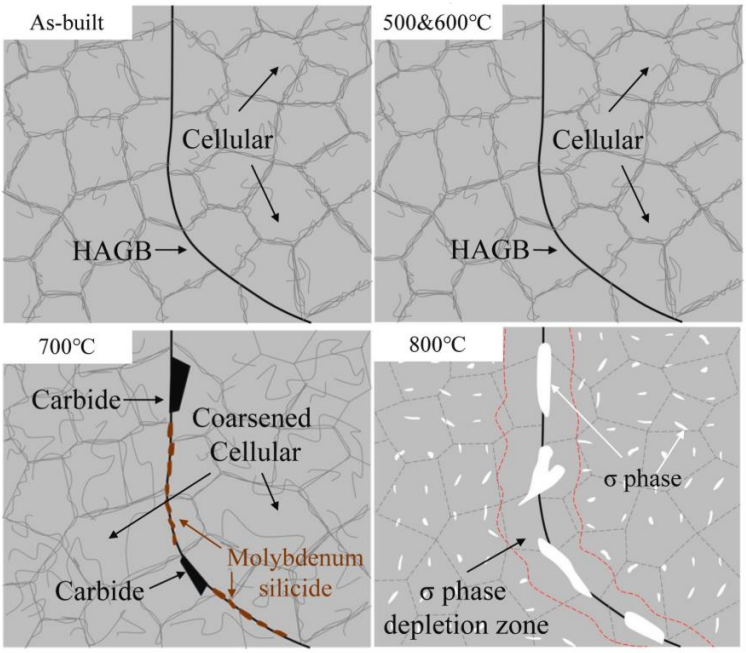

Figure 2-22: Schematic representation of 316L SS microstructure produced by L-PBF and exposed to annealing temperatures for 100h, from [89]

It was observed that past the 700°C annealing temperature, the sub-cellular structure starts to coarsen due to the reduction in dislocation density along the cellular walls. Additionally due to the recovery of the cellular structure after 100h of thermal ageing it also shows a decrease in Hardness [89]. Sistiaga et al. [90] studied three different types of HT (HT1: 600°C/2h+AC, HT2: 950°C/2h+AC and HT3: 1060°C/1h+WC). It was found that above 950°C HT the cell sub-structure was completely erased and while the YS and UTS of the HTed 316L show a decrease from the AB values, they were still above the requirements from standards (for conventionally manufactured 316L) and show an improvement in toughness (under Charpy tests) [90].

2.2.3.4 Mechanical properties of 316L manufactured by L-PBF

In this section the following results are reported for AB specimen, and the details of any HT used will be reported when appropriate. Similarly, all the results discussed in the present section are from tests made at room temperature (RT). Tensile properties of 316L L-PBF have been investigated and the general trend shows an increase in the yield strength (YS), despite the high content of inner porosities, compared to conventionally manufactured 316L SS [41]. The YS improvement was linked to the segregation network structure observed at the sub-cellular level, along with maintaining a ductile response [65]. In their study Tolosa et al. [91] investigated the general mechanical properties of 316L fabricated by L-PBF in different building orientations, and have found a minimal value of the yield strength to be around 525 MPa, which is superior to wrought 316L (YS ≈ 300 MPa), while maintaining an elongation around 30%. However it was found that anisotropic behaviour was

noticeable between the different specimen orientations (X, Y and Z with respect to the building orientation in the chamber). Specimens built in the X and Y orientation were showing higher yield strength values (around 650 MPa) compared to Z oriented specimen (530 MPa). Suryawanshi et al. [92] have observed a difference in tensile stress/strain response between specimens with different build directions. When the load was applied on the specimen parallel to the building orientation, the tensile response was superior to the specimen loaded orthogonally to the building orientation. YS was found to be 510 MPa for parallel loaded specimens, and to be 430 MPa for orthogonally loaded specimens. Similarly UTS = 621 MPa was measured for parallel loaded specimens, and UTS = 500 MPa was measured for orthogonally loaded specimens, and only 20% elongation for both orientations. L-PBF 316L specimens displayed 60% higher YS values in Gray et al.'s [93] study. Micro-hardness values for 316L produced by L-PBF can increase to 250-280 Hv in as-built (AB) condition [51]. While the yield strength can reach from 360 to 590 MPa depending on the optimisation of process parameters [85]. L-PBF 316L specimens have an elongation in the range of 30 to 45% up to almost 52% reported by Pham et al. [66] in their study on twinning induced plasticity in 316L samples fabricated by L-PBF, that can be qualified as ductile behaviour, similar results were also reported by Niendorf et al. [87].

This benchmarking is important for comparative purposes, with the results obtained in the present work, albeit from dissimilar processing parameters and defect populations, allowing relative assessments to previously published results, thus providing a potential basis for discussion and further explanation of the current findings.

2.2.3.5 Fatigue properties of 316L manufactured by L-PBF

In this section the following results are reported for AB specimen, and the details of any HT used will be reported when appropriate. Similarly, all the results discussed in the present section are from tests made at room temperature (RT). Total life approaches reveal that L-PBF 316L specimens could compete with conventionally manufactured 316L SS (see Figure 2-23) [8], [94]. Another high cycle fatigue study conducted by Zhang et al. [95] also revealed that porosity levels do not always have a detrimental impact on the fatigue performance of specimens (under HCF), but rather the fatigue resistance was found to follow a direct linear relationship with ductility in low cycle fatigue (LCF) regime and a direct linear relationship to strength in the high cycle fatigue (HCF) regime, which confers to L-PBF 316L its equivalent, if not superior, fatigue performance [96].

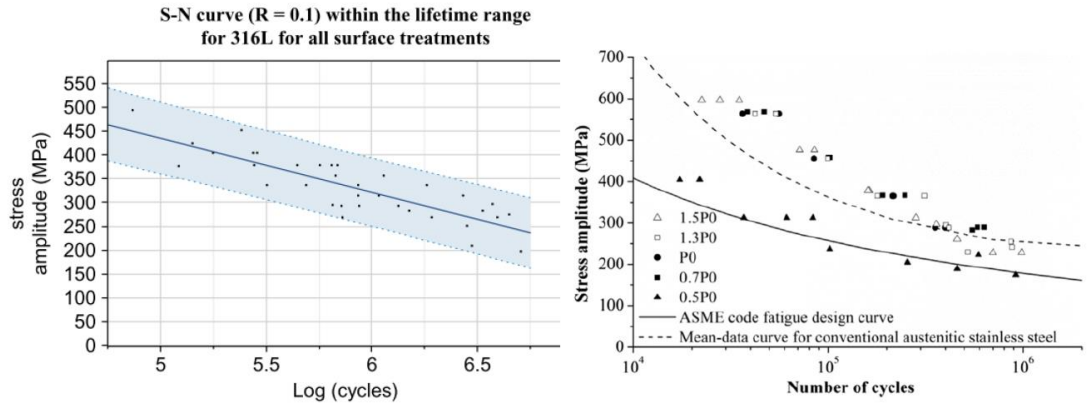

(a) (b)

Figure 2-23: Comparison between a) S/N curve for 316L L-PBF by [8] and b) S/N curve for 316L L-PBF, from [95]

Previous studies on L-PBF 316L have already presented its good fatigue performance, such as Riemer et al. [97] who reported a long-crack growth behaviour similar to conventionally processed 316L, and high ductility. No significant influence of process induced imperfections (such as internal porosities) was reported, with almost no effect of HIP (high isostatic pressing) post treatment on mechanical properties of L-PBF 316L. The elastic–plastic fracture toughness ($J_{0.2}$) values found by Ganesh et al. [98] using CT and SENB specimens were found to be in the range of 147–259 kJ/m2, which are similar values to those for the weld metal of similar austenitic stainless grade (AISI 316). Suryawanshi et al. [92] have also studied long crack growth in 316L fabricated by L-PBF, and have observed a very small difference in crack growth behaviour between the different building orientation of specimens, toughness values were found to be around 63 MPa√m (see Figure 2-24, from [92]), their specimen were HT by stress-relieving annealing treatment at 500 °C for 1 h, similar results have also been found by Yu et al. without any HT [99].

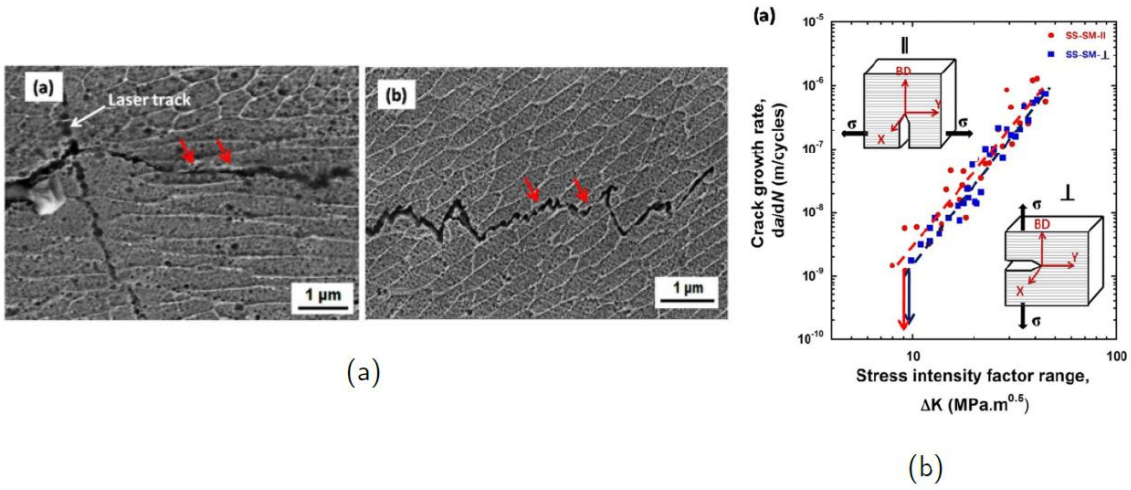

Figure 2-24: Difference in crack growth behaviour in L-PBF 316L, a) interaction with microstructure and b) crack growth rate vs stress intensity factor [92].

In the HCF regime the material's microstructure is subjected to cyclic plasticity which is characterised by hardening, and promotes mean stress insensitivity thus improving the fatigue resistance of the 316L SS L-PBF alloy [100]. However under HCF when 316L SS is annealed the high temperature HT leads to the formation of thermally-induced defects which become operative and cause fatigue crack initiation (annealing treatment was used at 982 °C and 1093 °C for 25 min then followed by a gas quench and a HIP treatment was used at 1190 °C and 145 MPa for hours by Zhang et al. to compare with AB specimens) [101] [102].

An interesting study by Cui et al. [103] revealed the effect of annealing HT on the cellular structure of 316L fabricated by L-PBF and its impact on the fatigue life of the specimen, showing that annealed specimens (at 900 and 1050 °C for 10 min, followed by a water quench) showed a decrease in the density of the cellular sub-structure, reducing by 23 times the fatigue life of the specimen due to the loss in twin plasticity, that offers the superior ductile behaviour of 316L fabricated by L-PBF in as-built (AB) condition. The sub-cells are formed during the L-PBF process due to the elemental segregation stabilized during rapid solidification and are surrounded by misorientations between the adjacent cells. The cellular sub-structure is retained during the entire plastic deformation, hence, can continuously interact with dislocations, and simultaneously promotes the formation of nanotwins, which provide a massive 3D network of obstacles to the dislocation motion. Partial dislocations are the major carrier for plastic deformation in 316L L-PBF alloy, and the formation of nanotwins is related to SFs, which requires high strains or stress concentrations (see Figure 2-25). This gives 316L material a great potential for being introduced in L-PBF design and to tailor the properties by varying AM process parameters hence creating energy absorbent structures, based on the dislocation deformation mechanisms.

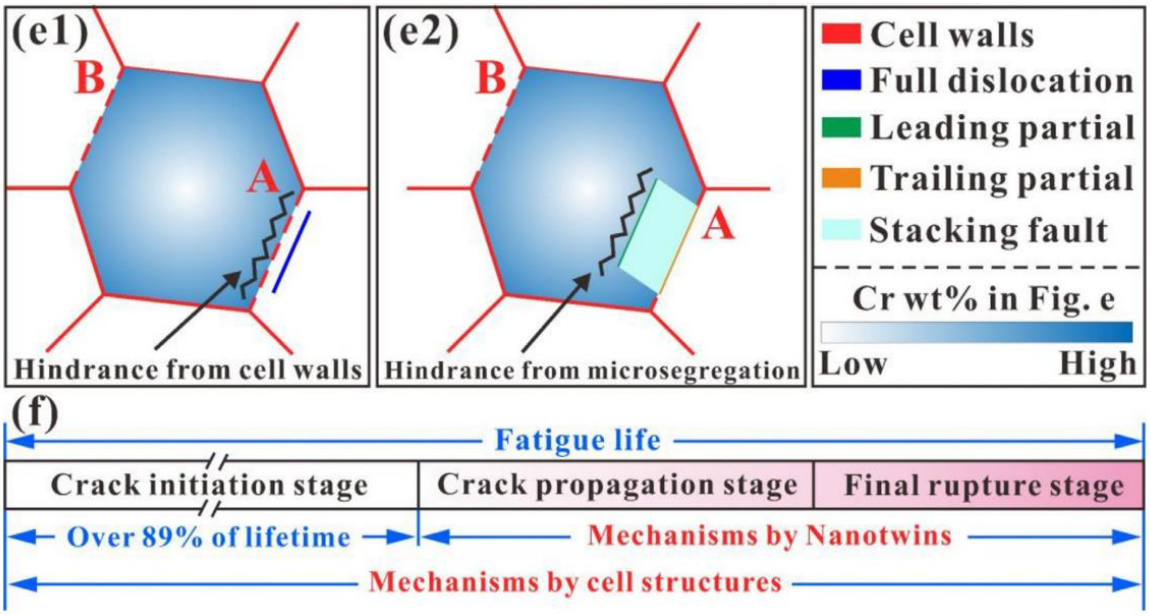

Figure 2-25: Schematic of the motion of dislocation in cellular structure of 316L L-PBF under fatigue deformation, hindered by both cell walls and compositional gradient and the deformation mechanisms over the entire fatigue life [103].

Cui et al. found that the dislocation mobility is impeded due to the increased density of twins (dynamic Hall–Petch effect) serving as effective barriers for the dislocation motion. Additionally, the twin–twin, twin–dislocation, and twin–cell structure interactions bring additional strengthening, reducing the tendency of cyclic softening response and prolonging fatigue lives [103].

A recent study on microstructure gradation within 316L specimens fabricated by L-PBF was establishing a processing strategy to obtain damage-tolerant parts. This could be achieved by structures featuring locally large grained and strongly textured areas, acting as crack stopping elements, while the outer areas are made up by smaller grains of higher strength (see Figure 2-6, from [104]). The differences in CGR can be related to different driving forces imposed by the thermal gradients and epitaxy within each specimen. The differences seem to be mainly related to different grain sizes. Additionally, the different grain morphologies (in the case of inter- crystalline crack growth) and different crystallographic orientations (for transcrystalline crack growth) are seen to affect the crack growth rate.

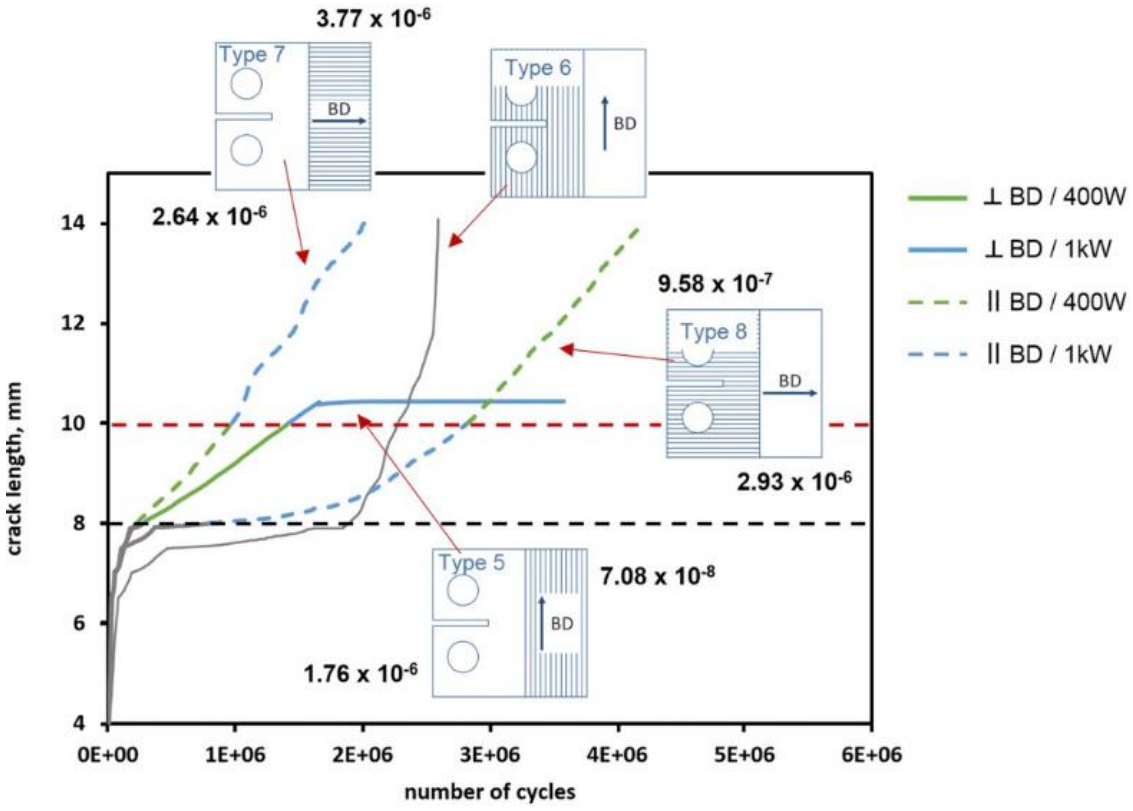

Figure 2-26 Crack length vs. number of cycles for 316L graded specimens. The numbers at the left and right sides to the specimen schematics reflect the CGR in mm/cycle^{-1} in each area of the specimen, i.e. the slope of the linear trendlines (not shown) corresponding to crack lengths from 8mm to 10mm and above 10 mm, respectively. In case of the specimen type 6, the CGR was not evaluated due to its peculiar behaviour, from [104]

2.2.4 Inconel 718 alloy

2.2.4.1 IN718 conventionally manufactured

Nickel-based super alloy IN718 is mostly employed for its ability to maintain strength at elevated temperature, and its ability to sustain high strength at room temperature along with its good corrosion resistance. Most of its very desirable properties are due to its specifically tailored microstructure, formed of multiple secondary phases formed via precipitation strengthening and age hardening in order to precipitate and grow the optimal proportion of phases within the microstructure. Inconel or Ni-based super alloys are especially attractive for aerospace applications and also in turbines, or petrochemical applications due to their good fatigue creep resistance and oxidation/corrosion resistance [105].

Phase formation and decomposition mechanisms are generally governed by diffusion processes, which are a strong function of concentration, time and temperature. Therefore, post-processing

treatments provide the driving force to diffuse atoms in a supersaturated solid solution in order to precipitate the thermodynamic stable phase in the optimal volume fraction [106]. Niobium is described as having a low diffusion compatibility with Nickel, causing the γ'' precipitation to have slow kinetics (slow to respond to treatment) and take a long time to occur hence is often qualified as sluggish.

Geometrically close packed (GCP) phases that mainly form in nickel based super alloy, usually have a coherent or semi-coherent structure with the matrix providing a strengthening effect such as: ordered FCC γ' $Ni_3(Al,Ti)$, the ordered BCT γ'' Ni_3Nb, $\eta - Ni_3Ti$ and δ-Ni_3Nb, at least at low temperature and low cycle fatigue, because at higher temperature and higher amplitude some intermetallics lose their strength and start to debond with the matrix creating weaker sites. Carbides, Laves and other detrimental intermetallic (IM) phases are usually found to precipitate at grain boundaries, and are detrimental to corrosion and fatigue performance of IN718.

The precipitation of coherent (and/or semi-coherent) γ' phase, within the γ (austenitic) matrix, causes a small degree of misfit in the lattice. This small mismatch locally lowers the mobility of dislocations and thereby results in a strengthening effect. During the deformation process, dislocations have to bypass the γ' phases by shear cutting (or Orowan looping or climb) mechanism depending on the size of the precipitates and also temperature.

The dislocations passing through the precipitates by a shear cutting mechanism is activated when following conditions are met: (1) the precipitates are coherent with the γ matrix and have the same slip plane with the matrix; (2) the size of precipitates is smaller than a critical size; and (3) the strength of precipitates is relatively low. It is well recognized that the anti-phase boundary (APB) is an unstable high-energy structure that will be formed when a *a/2*<110>{111} dislocation passes through γ' by this cutting mechanism and the required precipitate-cutting stress is expected to be proportional to the APB energy (γ *APB*) and inversely proportional to the Burgers vector *b* of the dislocation. In order to remove the APB, the dislocations must travel through the γ' precipitates in pairs, and such paired dislocations are termed a superdislocation which have been confirmed by transmission electron microscope (TEM) observation [107], [108].

2.2.4.2 IN718 manufactured by L-PBF

All the references discussed in this section are referring to AB material, no HT was made or has to be considered part of the following results. The solidification sequence of IN718 alloy, with respect to temperature, starts with $L \rightarrow \gamma$ reaction (1359°C) followed by the $L \rightarrow \gamma + M$-type carbide (NbC) eutectic reaction that occurs at 1289 °C. The liquid phase terminates at 1160°C, at which point Laves phase forms. The δ-phase precipitates were found to form based on a solid state reaction at 1145 ± 5°C. Which means that on rapid cooling after the L-PBF process the first phases to form are the

Carbides and Laves phase within the γ (gamma austenitic) matrix. A schematic of the solidification of IN718 in L-PBF process is presented in Figure 2-27 from [106].

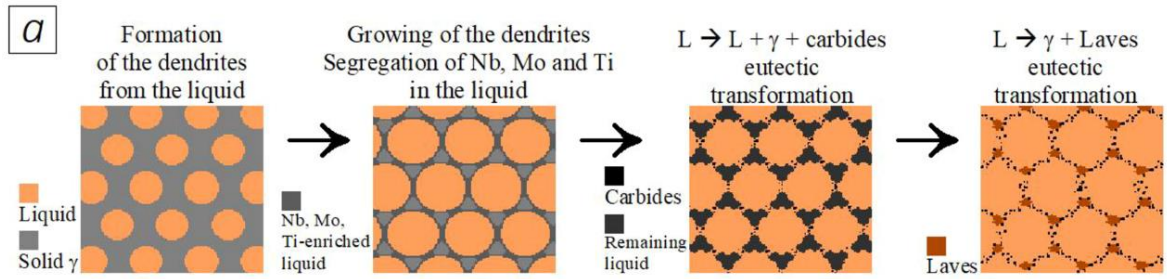

Figure 2-27: Schematic representation of rapid solidification happening in L-PBF of IN718, from [106]

The rapid solidification after the L-PBF process causes similar micro-structure as previously presented; the main orientation of grains tend to follow the thermal gradient and the equiaxed cellular sub-structure is usually formed within large grains by rapid solidification [106]. However the susceptibility of IN718 for hot cracking can also lead to the appearance of liquation cracking between grains (see Figure 2-28).

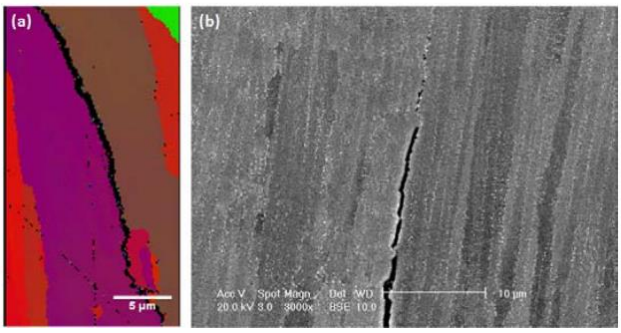

Figure 2-28: EBSD map of a liquation cracking within Ni-Based super alloy processed by L-PBF, from [71]

A network of dislocations is formed in intergranular sites and areas at the periphery of sub-cellular structure [109]. In the as-built sample, the *δ* (delta, needle-like) phase, the γ' (gamma prime, spherical) phase and the γ'' (gamma double-prime, disk-like) phase are very small and almost not visible, due to the rapid solidification happening in AM process. However because of the successive layer re-heating cycle, very small and diffuse precipitates (called nuclei) are present and dispersed within the cell cores. Similar observations were made in successive welding tracks, where Nb Mo and Si elements are pushed into the liquid phase during solidification (externally to the dendrites), and on the completion of solidification they remain in these sites where their concentration exceeds and tends to support the formation of intermetallic phases such as σ phase, δ phase, Laves phase or carbides [110].

Choi et al. [111] have found an optimised energy density ratio range of [60 − 150]J/mm^3, within which the level of inner process-induced defects and porosities is reduced. When high energy density is used to build an IN718 part, nuclei are not formed and the solidification process occurs in one of the six preferential growth directions of FCC structure, hence the dendrite competition for solidification growth will favour the main crystallisation orientation closest to the thermal gradient direction [112]. Columnar growth following the epitaxial orientation of thermal gradient <100>, gives rise to the formation of γ dendrites, that reconsolidate on multiple successive layers, forming dendrites that encompass multiple powder layers [113]. The FCC crystal structure has the favourable slip system {111} < 110 >. Since the L-PBF process produces microstructures which have a strong < 100 > fibre texture, hence based on an extrapolation of FCC single crystals: the elastic modulus can be calculated in any particular crystallographic direction by using the following equation [114]:

$$\frac{1}{E_{[hkl]}} = \frac{1}{E_{<100>}} - 3\left(\frac{1}{E_{<100>}} - \frac{1}{E_{<111>}}\right)(\alpha^2\beta^2 + \alpha^2\gamma^2 + \beta^2\gamma^2) \qquad (2\text{-}31)$$

Where *E* < 100 > and *E* < 111 > are the moduli in the < 100 > and < 111 > directions, respectively, and *α*, *β* and *γ* describe a unit vector *v* = [*α β γ*] within the crystallographic plane of interest with respect to [100], [010], and [001] directions.

Similarly to FCC single crystals, the Schmidt factor can be employed to describe the anisotropic behaviour with respect to the building angle. Therefore the yield stress can be expressed as follows [115]:

$$\sigma_{yield} \geq \frac{\tau_c}{\cos(\phi)\cos(\beta)} \qquad (2\text{-}32)$$

Where τ_c is the critical resolved shear stress in slip systems, ϕ is the angle between the axial load and the normal direction of the slip plane, and β is the angle between the axial load and the slip direction. The term $\cos(\phi)\cos(\beta)$is known as the Schmidt factor.

2.2.4.3 Heat treatment of IN718

2.2.4.3.1 Heat treatment on conventionally manufactured IN718

The conventional heat treatment sequence for Inconel 718 includes a high temperature solution treatment followed by rapid quenching in order to form a super saturated solution (i.e. dissolving the Nb in the matrix) and favours both fine and homogeneous γ' precipitation and also supports γ'' precipitation. This is followed by double ageing stages in the *γ/* γ' temperature range. The first age is to coarsen the γ', second age is for further finer γ' precipitation creating a bi modal γ' precipitate distribution [116] see Figure 2-29.

Two standard thermal treatment strategies for IN718 alloy are described as follows by the Aerospace Material Specification (i.e. AMS) [117], [118]:

- Solution heat treated at 980°C/ 1h with air or argon cooling; ageing treatment at 720°C for 8h then slow cooling in furnace for 2h to 620°C. Then, a second ageing at 620°C for 8h followed by air or argon cooling to room temperature.
- Homogenization heat treatment at 1065°C / 1h, then air or argon cooling; ageing treatment at 760°C for 10h then slow cooling in furnace for 2h to 650°C. Then second ageing at 650°C for 8h, followed by air or argon cooling to room temperature.

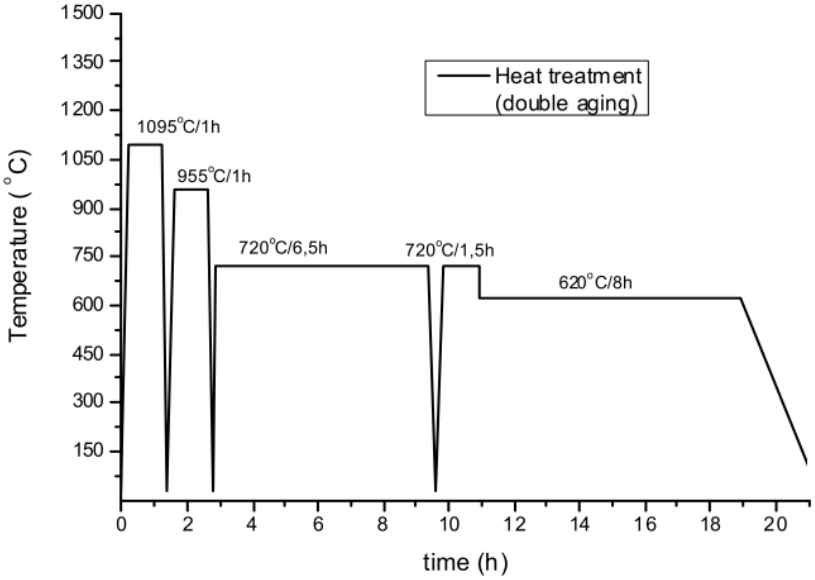

Figure 2-29: standard heat treatment strategy for IN718, from[116]

Both intergranular and transgranular precipitates are formed through the *γ* matrix, the time and temperature of ageing treatment will affect the size distribution of the secondary phases (or intermetallic) precipitates, γ' FCC Ni_3(Ti, Al) is responsible for high temperature strength of IN718, while γ'' BCT Ni_3(Nb, V) is responsible for providing IN718 strength at lower temperature.

Precipitation of γ' depends on the temperature range while γ'' depends more on the time for which the specimen is held at elevated temperature. In other words at long term exposure in the range of 700°C to 800°C for 100h γ' precipitation is observed, while γ'' is produced on ageing between 500-700°C and there is an increase in concentration with exposure to annealing up to 100h. Enhanced properties are associated with long term exposure at 575°C as a result of increased precipitation without excessive particle growth, while degraded properties result from long time ageing at 650°C [119]. Both γ'' and γ' particles precipitate between 550-660°C at long ageing times, and some authors state they precipitate between 700-900°C at short ageing times as long as the elemental ratio: (*Ti* + *Al*)*/Nb* = 0.66 *at*% is sufficient [120].

It is important to note that after 650°C and with long exposure, γ'' transforms to the stable *δ* phase, which results in loss of mechanical resistance, it is hence known that *δ* phase formation is a result of over-ageing. It is commonly stated that γ'' forms between 550°C to 900°C but is unstable above 650°C and can rapidly transform into *δ* phase that is more stable at this temperature. Hence care should be taken to avoid a shift toward the more stable *δ* phase precipitation during annealing at higher temperature [106].

2.2.4.3.2 Heat treatment of IN718 manufactured by L-PBF

The scientific community has investigated the effect of applying conventional thermal post treatments on Inconel produced by L-PBF. Most studies have investigated either the effect of each stage separately, or the effect of the complete thermal post treatment sequence. Below are detailed some findings of these studies to explain the effects of different thermal treatment sequences on the microstructure, and how these affect the microstructure and tensile properties of IN718 manufactured by L-PBF.

Tucho et al. [109] have investigated the impact of elevated annealing temperature on IN718 to dissolve Laves phases and micro segregated phases, the HT used was described as follow: 1100 °C for 1 h and 7 h, and 1250 °C, for 1 h and 7 h. Solution ageing treatment at a temperature above the solvus temperature of Niobium carbides has been applied to IN718 manufactured by L-PBF (temperature from 1100 to 1250 °C) with the idea to support the back diffusion of Niobium (Nb) into the γ matrix to support precipitation strengthening of γ' and γ''phases by Tucho and al. [109]. It was found that while some Nb had back diffused into the matrix, Niobium carbides were also observed to have coarsened (see Figure 2-30). Additionally it was found that after solution heat treatment at elevated temperature the grain structure was coarser and the sub-cellular dislocation network had decreased.

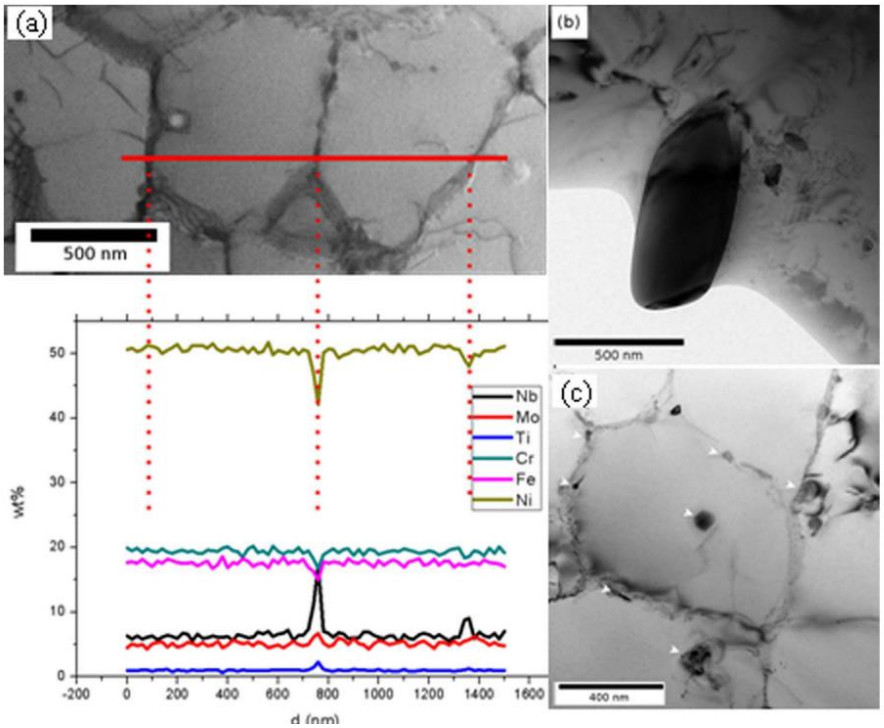

Figure 2-30: Microstructure on IN718 after a solution HT of 1100C for 1h: a) composition across sub-grains boundaries, b) a precipitate of NbC phase, c) small precipitates enriched in Nb, Al, Ti, O and C pointed by white arrows (from 20 to 150nm) from [109]

Messe et al. [121] investigated two sets of heat-treatments, first: annealing from 1120 °C to 1230 °C for 2 h followed by an aging treatment of 24 h at 840 °C, and the second was identical to the first one, but an initial stress relieving step of 24 h at 840 °C was included. Similar results were found by Messe et al. [121] and are exposed in Figure 2-31, the re-crystallisation happening at an elevated temperature treatment (>1200°C) causes grain coarsening (i.e. the stress relief HT results in larger grain size). This study shows that carbide formation (black dots indicated by red arrows in Figure 2-31) and Laves phases (white dots in Figure 2-31) are still happening at elevated temperature (not all Nb is back diffused into the matrix), instead carbides and Laves already present prior to thermal post treatment seem to either dissolve and disappear or grow coarser, most of the time along GB or at HAGB within grains. Other specimens were subjected to a stress relief HT for 24h, which caused the dissolution of $M_{23}C_6$ carbides (Cr-rich). The specimens that had received the stress relieve HT prior to undergoing the standard HT (solution treatment and two consecutive stage ageing) were dissolving carbides at higher temperature (1040-1090°C) and with greater effect, than as-built specimens (the $M_{23}C_6$ solvus temperature was found to be around 1050°C). However the MC-type carbide (Nb-Ti rich) solvus temperature was expected to occur at higher temperature. The MC-type carbides were then observed to have an increase in volume fraction after the standard HT.

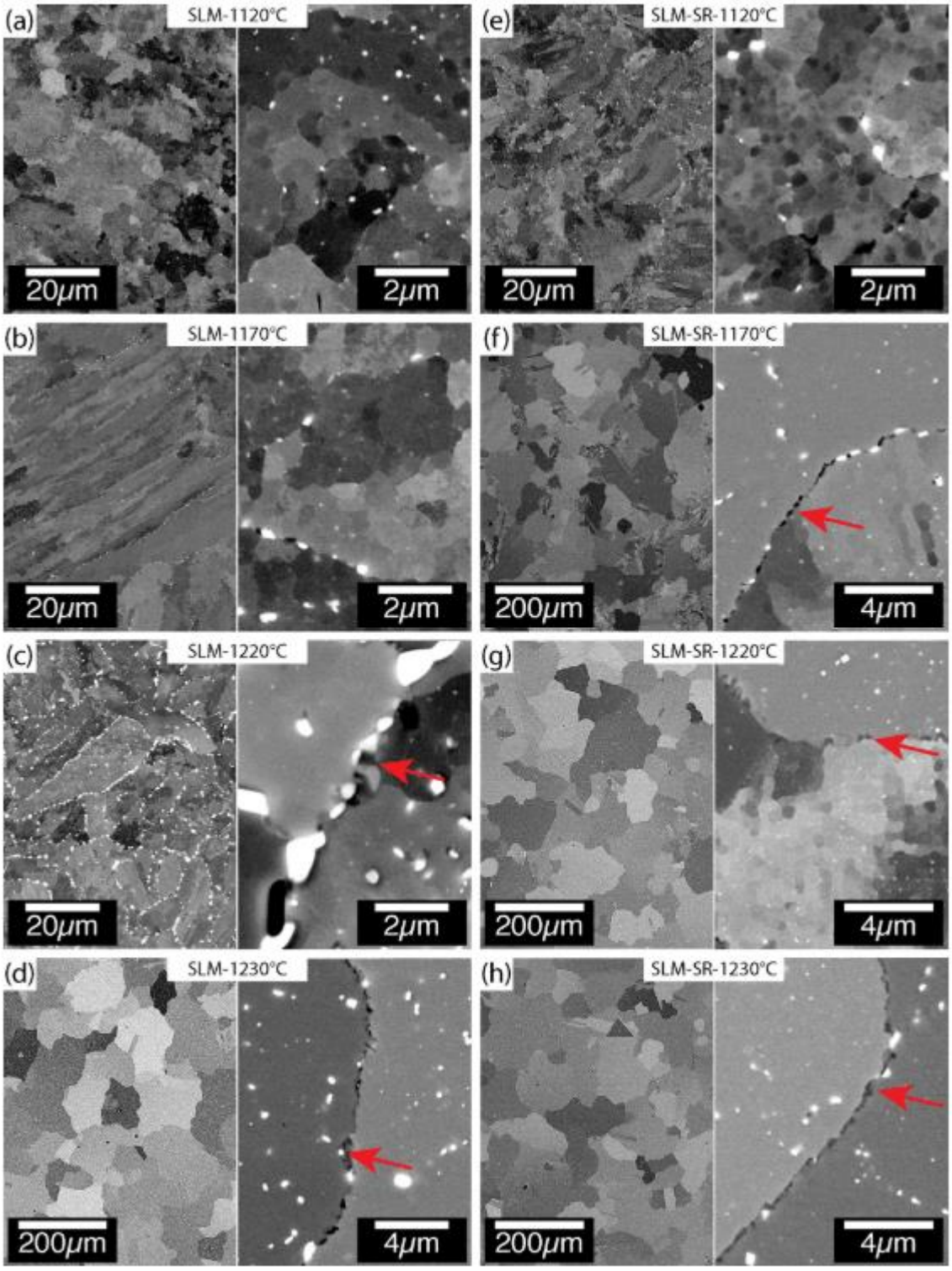

Figure 2-31: Carbide formation on homogenised specimen, with and without stress relief treatment (SR) prior to solution from [121]

These post thermal treatments using temperatures higher than suggested by standards for conventionally manufactured IN718, were also investigated for different purposes:

- Grain coarsening can erase the anisotropic behaviour of the part
- or increase the numer of twins within grains.

It was found that using a higher temperature of annealing (such as 1160°C at different exposure times from 1 to 8 hours, from [28]) resulted in forming an isotropic microstructure for all scan strategies considered, although it would also result in a loss in strength due to an increase in average grain size. It was found by Tucho et al. et al that solution HT over different lengths of time (the solid solution HT were carried out at 1100 °C for 1, 3, 6, 9, 16, or 24 h of hold time, one bypassed the annealing treatement and only undergo the ageaing treatment, but all the specimens followed the double ageaing treatment: 760 °C for 10 h, furnace cooled to 650 °C and held for another 10 h) could lead to the appearance of annealing twins (forming during recrystalisation)[122]. However, depending on the amount of recrystallization and grain growth, the hardness of solution treated samples decreased.

The standard temperature for solution HT of IN718 is usually 980°C (or 1065°C depending on the standard) and is then followed by a two stage ageing (as explained in section 2.2.4.3.1), it was found by the majority of the scientific community that the standard HT does support the precipitation of γ' and γ'' within the γ matrix (it is still less than expected from a conventionally manufactured Inconel due to the micro-segregation of elements on rapid solidification from L-PBF) and produces a more ductile response due to the grain coarsening and the decrease of dislocation density around the sub-cellular network [123]. The study of Li et al. [124] proposed a study of the effect of each part of the conventional HT sequence (from standard and exposed in Figure 2-32 a) separately (respectively the DA, HA and SA , were detailed as follow: DA for direct aging at 760°C for 10 h, furnace cooling (FC) to 650°C at the speed of 55 °C/h and holding for 8 h, followed by air cooling (AC) to room temperature, HA for homogenizing at 1065 °C for 1.5 h, followed by AC, and then the double aging treatment as described for DA, and finally SA for solutionizing at 980 °C for 1 h, AC, followed by double aging as described for DA, see Figure 2-32). It was found that the maximum volume fraction of γ'' was formed during the solution + consecutive ageing treatment, thus demonstrating that higher temperature of homogenisation is not necessary to support the γ'' phase formation. However more of the δ phases were dissolved after elevated temperature treatment. The Nb in the interdendritic region supports the formation of γ'' phase during ageing in the range 760°*C* and 650°*C*. As a result of heat treatment, γ'-Ni3(Al,Ti,Nb) and γ'' (BCT-Ni3Nb) phases dissolved in the matrix (Ni-Cr solid solution) and the needle-like δ-phase formed at the grain boundaries.

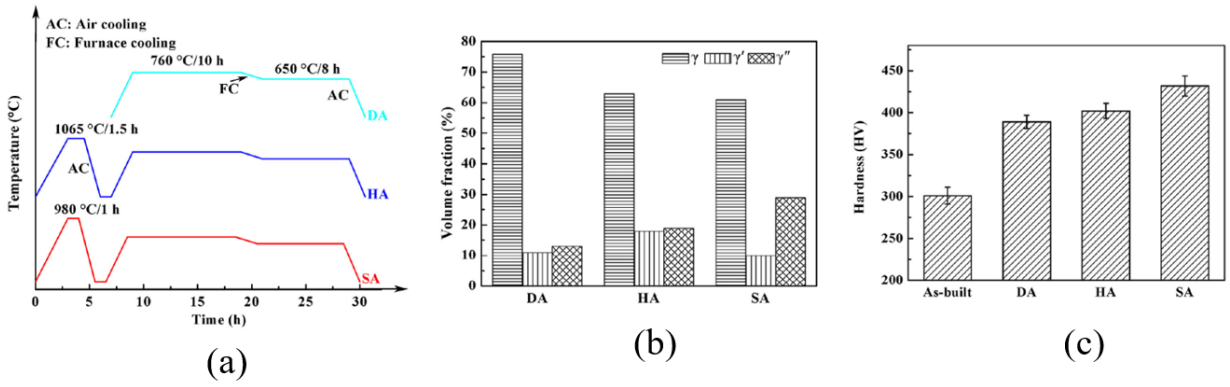

Figure 2-32: a) heat treatment profile (for DA, HA an SA) b) volume fraction of phase formation after different HT strategy, c) effect of each different HT sequence on the Hardness, from [124]

It was found that the γ' and γ'' precipitation starts within the dendrites. However higher temperature (such as homogenization or solution) support grain coarsening and recrystallization, while Laves phases are not yet fully dissolved and the *δ* phase is forming at the GB (see Figure 2-33) from [124].

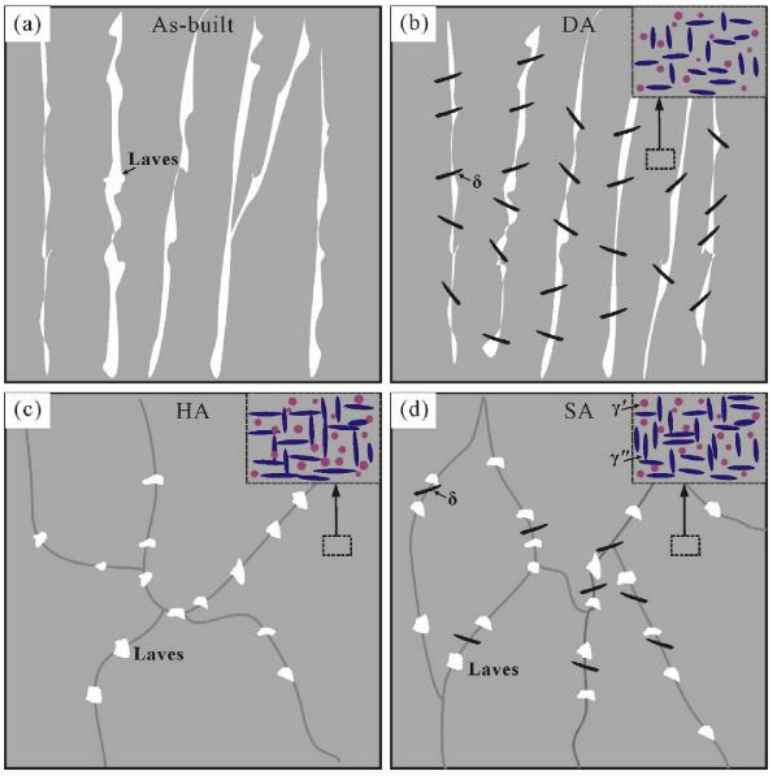

Figure 2-33: schematic representation of the phase formation depending on the HT sequence used (DA, HA, or SA) relatively to the columnar dendrites formed on rapid cooling from L-PBF, from [124]

Some scientific studies have investigated the use of HIP as a post thermal treatment and with additional benefit of closing inner porosities of IN718 manufactured by L-PBF, such as Medraj et al. [125] who investigated two post-treatments: homogenization (1100 °C, 1 h, furnace cooling) and hot isostatic pressing (HIP) (1160 °C, 100 MPa, 4 h, furnace cooling). Medraj et.al [125], in their study on the effect of HIP treatment, have observed an increase in the formation of *δ* phase and MC type carbides at the GB. No remarkable change in the *δ*-phase amount could be noticed after the homogenization followed by HIP-treatment processes. This is an indication that as long as *δ*-phase forms due to the homogenization heat treatment, it stays stable during the HIP treatment. However, both homogenization and HIP treatments have dissolved the γ''-phase to a certain degree. The homogenization treatment has been shown to reorient the columnar grains and provide the driving force for partial dissolution of γ'' in the matrix, and also precipitated grain boundary type *δ*-phase. Furthermore, both homogenization and HIP-treatments have promoted the nucleation and growth of MC-type carbides at grain boundaries (GB) as can be seen in Figure 2-34.

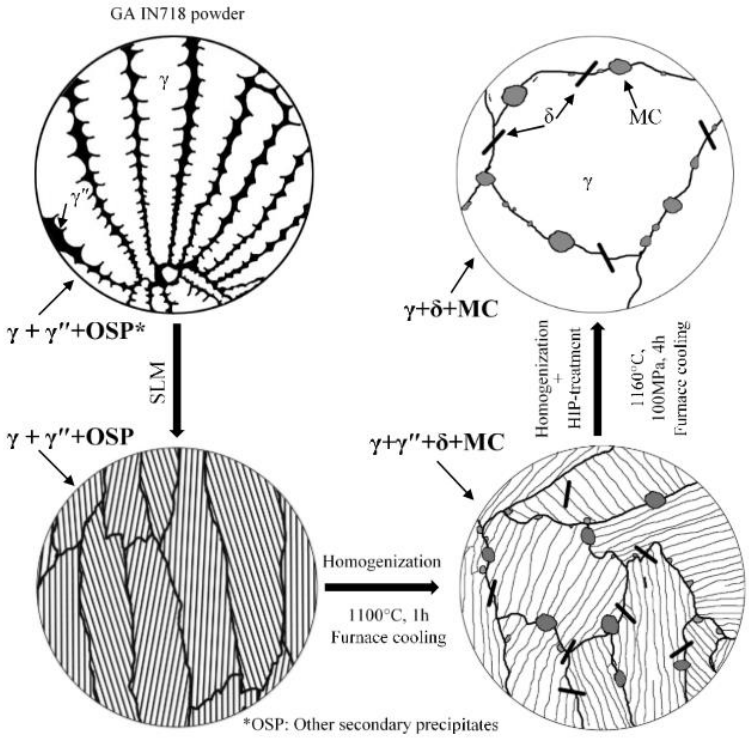

Figure 2-34: phase formation within IN718, after homogenisation treatment and HIP, from [125]

Studies have found that annealing at 850°*C* is not high enough either to dissolve Laves phases, nor to recrystallize the grain structure. However the temperature is high enough to support the *δ* needle-like phase precipitation[105]. The ratio of *δ* to γ'' precipitation is difficult to quantify due to the overlapping of diffraction peaks of these two phases that have the same composition (Ni_3Nb).

It is known that γ'' is unstable above 650°*C*, and that *δ* phase is not present in as-built specimens due to very rapid cooling.

2.2.4.4 Mechanical properties of IN718 manufactured by L-PBF

In this section the following results are reported for AB specimen, and the details of any HT used will be reported when appropriate. Similarly, all the results discussed in the present section are from tests made at room temperature (RT). The effect of L-PBF on the mechanical properties of IN718 have been studied and can be summarized as follows: the Yield Strength (YS) values obtained can range from around 1190MPa [126] to 590MPa [127], and YS within a range 830 − 907MPa was found by Chlebus at al.[128] . All specimens in the as-built state, tend to remain ductile and elongation usually falls within the range from 11 to 20 % [127]. Hardness values were constant throughout the literature and have been measured around 290Hv [109], [129], [130].

Ageing post treatment has been found to improve tensile properties such as UTS, YS, but reduce elongation at break of IN718, albeit HIP before ageing treatment has been found to improve elongation at break. In their work on nickel based super alloy made by L-PBF, Kanagarajah et al. [131] (have compared AB specimens to HT specimens following: a solution annealing for 4 h at 1160 °C followed by a single stage ageing for 16 h at 850 °C, tensile tests were then made at RT and at 750 °C) have found that as-built specimens were more ductile than cast material, and after post treatment an increase in strength was noticed, along with a decrease in ductility (see Figure 2-35).

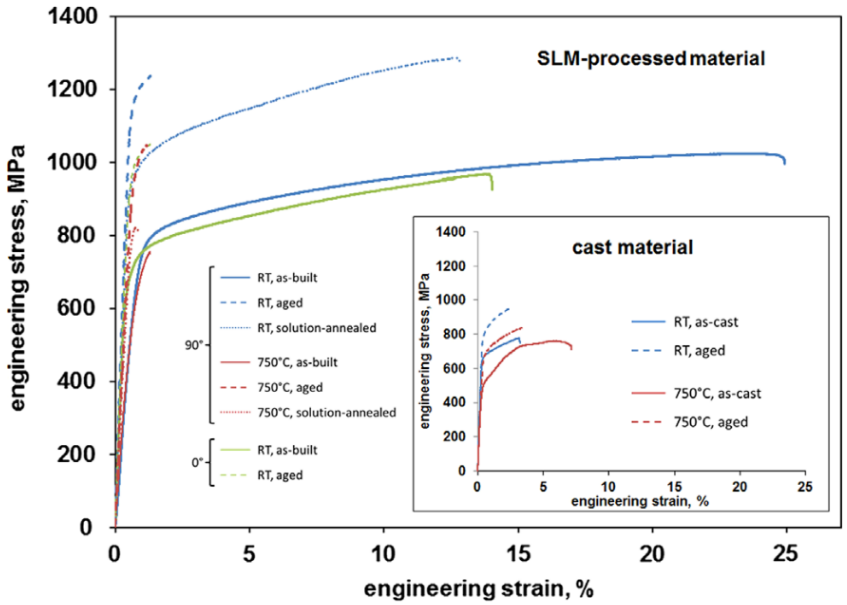

Figure 2-35: Monotonic stress-strain curve of Inconel 939 as cast and aged (at room temperature RT and at 750C) from[132]

Those results have been confirmed by Neumeier et al. [133], specimens were HT as follow: annealing treatment for 1h at temperatures ranging from 550 to 1050 °C followed by air cooling followed by a subsequent ageing of 8 h at 720 °C, furnace cooled to 621 °C and holding for 8 h followed by air cooling and then compared to samples left in the as-processed condition, they found similar results, and have also found YS of 1100MPa for aged specimen (see Figure 2-36).

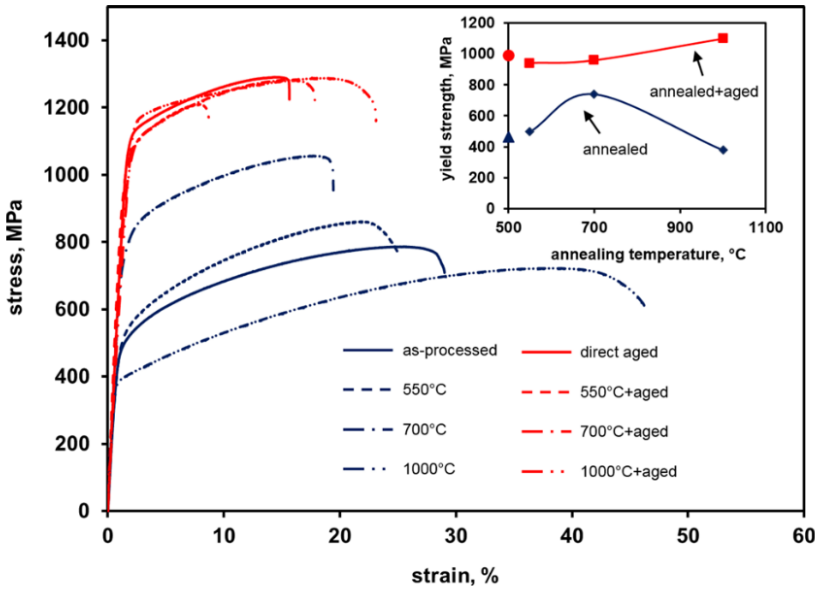

Figure 2-36: stress-strain curve of IN718 manufactured by L-PBF, after different HT, from[133]

Schneider et al. studied the effect of different stages of the standard post thermal treatment sequence separately. The specimen that only received the stress relief treatment showed a very ductile behaviour, and the lowest mechanical strength of all specimens. Specimens that were subjected to: only one stage ageing / two stage ageing / and solution treatment plus two stage ageing, were relatively ductile while maintaining a high YS (around 1200MPa) and high UTS (around 1300-1700MPa). However the specimen that had undergone the stress relieving treatment and HIP treatment only, were the ones that were showing the highest ductility with only a small reduction in YS values (around 1100-1200MPa) and good UTS (around 1300-1400MPa), that are characteristic of tough behaviour [114].

2.2.4.5 Fatigue properties of IN718 manufactured by L-PBF

In this section the following results are reported for AB specimen, and the details of any HT used will be reported when appropriate. Similarly, all the results discussed in the present section are from tests made at room temperature (RT). In order to obtain a tough material a good balance between strength and ductility is required. The influence of σ Laves phase was studied by Sui et al. [134] in L-PBF IN718 where a heat treated using direct aging in two stages (DA, 720 °C×8 h/ furnace cooling to 620 °C×8 h/air cooling) was applied in order to keep the laves phases present while

developing a consistent microstructure within the test specimens, and tests were conducted at 650°C. It was described that under high cycle fatigue at low stress amplitude the Laves phases were effectively hindering the crack propagation, by maintaining their morphology, hence forcing the crack to detour them and propagate through the austenite matrix [134]. While at higher stress amplitude in the HCF regime, the Laves phases were weakened and tend to break and debond with the matrix leading to microscopic hole formation at the interface, leading to degradation of fatigue life performance of L-PBF IN718 compared to wrought IN718. This mechanism is explained by the schematic representation of shearing of brittle Laves shown in Figure 2-37 [134].

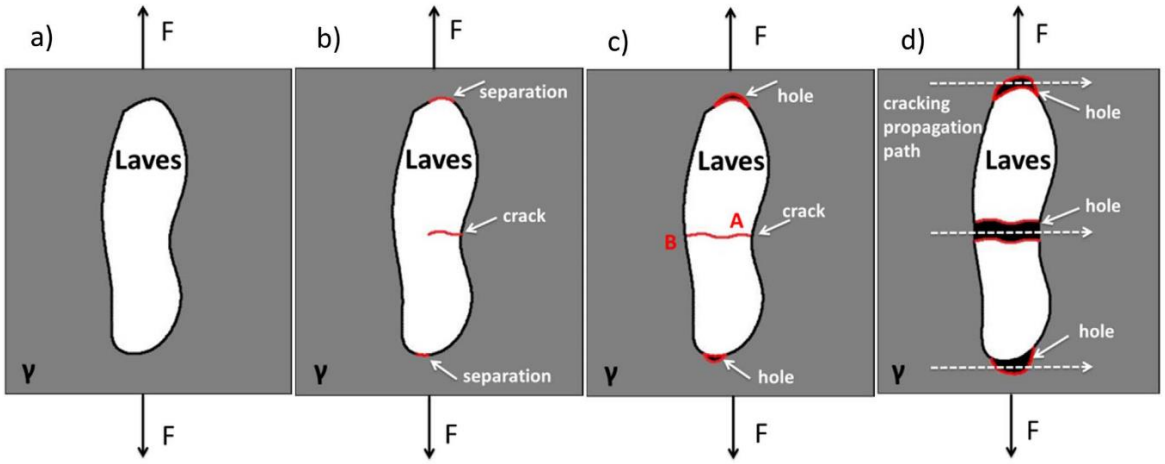

Figure 2-37: Schematic representation of the fragmentation of the Laves phase and the separation of the Laves phase and the surrounding austenitic matrix under fatigue, [134]

It was also described by Sui et al. that most initiation sites in L-PBF IN718 under HCF were observed to arise from crystallographic facets; facets that formed through transgranular cracking, and not arising from defects (such as inclusions or pores) as one might expect. Secondary cracks were also observed in the Paris regime, where it is known that secondary cracks consume a lot of energy leading to a reduction in crack propagation rate and improvement of high-cycle fatigue life.

Fatigue crack propagation within IN718 manufactured by L-PBF was described by Kunz et al. as based on planar cyclic slip ahead of the crack tip, mainly localized on slip planes, by damage accumulation on suitably oriented slip bands leading to micro-crack formation. The mechanism of the crack growth in the near-threshold region and in the Paris region is basically the same. The only difference is in the extent of the cyclically loaded volume, which increases with increasing ΔK and the size of the cyclic plastic zone. Higher ΔK levels induce larger micro-cracks. The crack paths were observed to be fully transgranular (from threshold to Paris regime regions), only changes toward ductile propagation at very high values of stress intensity factor range (final fast fracture, stage III). The plastic blunting model of crack growth was considered as appropriate for crack advance description at high crack growth rates [135]. The cycling leads to a gradual damage of suitably

oriented slip bands and formation. Stress intensity threshold was found at ΔK_{th} = 3MPa√m (see Figure 2-38).

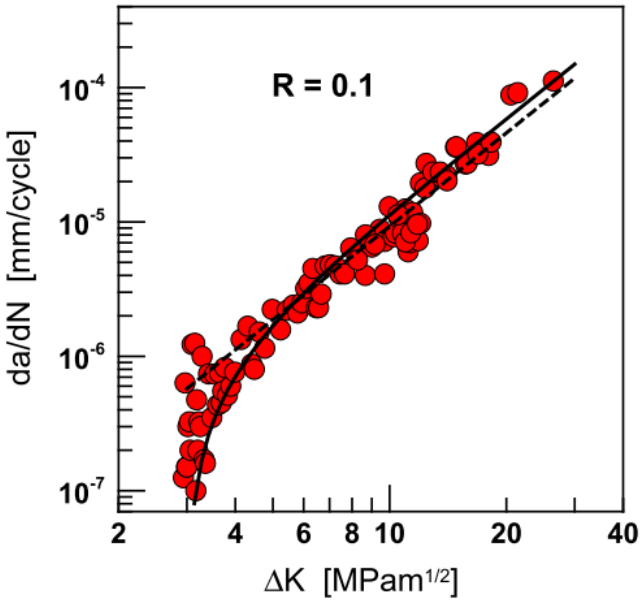

Figure 2-38: Fatigue crack growth rate versus stress intensity factor, in IN718 manufactured by L-PBF, from [135]

Kim et al. [136] also studied the fatigue crack propagation behaviour of IN718 manufactured by L-PBF in two directions respective to the building orientation of the specimen, and compared to a conventionally manufactured specimen at room temperature (i.e. 25°C) and the results are displayed below in Figure 2-39 . However in their study the specimen have undergo a heat treatment; all the specimens were solution annealed at 980 °C for 1 h, and subsequently double aged at 720 °C for 8 h and 620 °C for 8 h, respectively. It is noticeable that the ΔK_{th} values of L-PBF specimens were 5.6 and 6.4 MPa√m, which is approximately 60% lower than the conventionally manufactured (CM) specimens. Similarly, above the ΔK value of 30 MPa√m at 25 °C, the FCP rates of L-PBF and CM specimens became comparable with each other. It was also noted that the orientation effect on the FCP behavior of L-PBF Inconel 718 specimen was negligible over the entire ΔK regime studied.

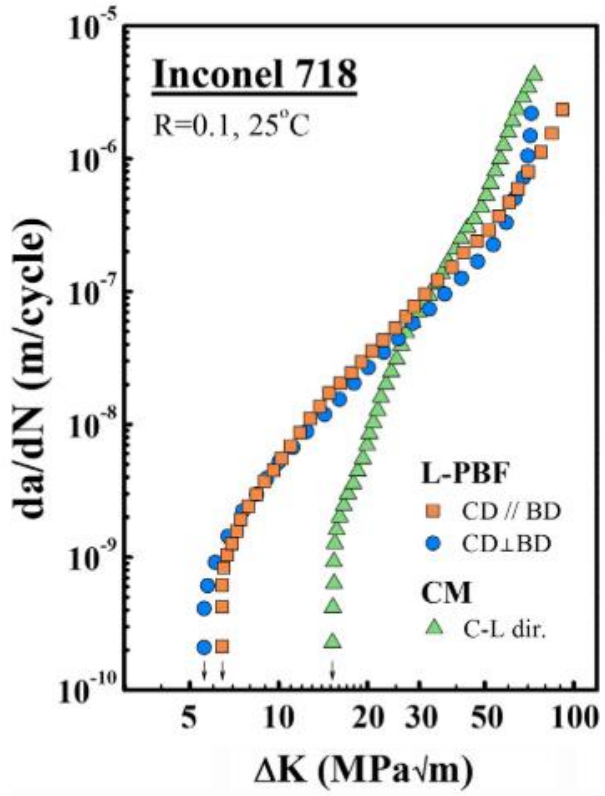

Figure 2-39: Fatigue crack propagation rate versus the stress intensity factor K, within IN718 both conventionally manufactured and manufactured by L-PBF, from[136]

2.3 Multi-material additive manufacturing (MMAM)

One of the unique capabilities of AM is that multi-material parts can be produced with material compositional and geometric complexity. This means throughout a single component, properties like hardness, corrosion resistance, and environmental adaptation can be defined in areas that require it the most. These new processes allow for exciting multifunctional parts to be built by MMAM [137][138]. While it could be of great advantage to tailor microstructure and properties in functional geometrical sites of a component, it is also a challenge with respect to materials and techniques, selection strategies for materials selection and process selection to optimise the design selection targeting the desired functional and technical requirement for the component to be fabricated (see Figure 2-40, [139]).

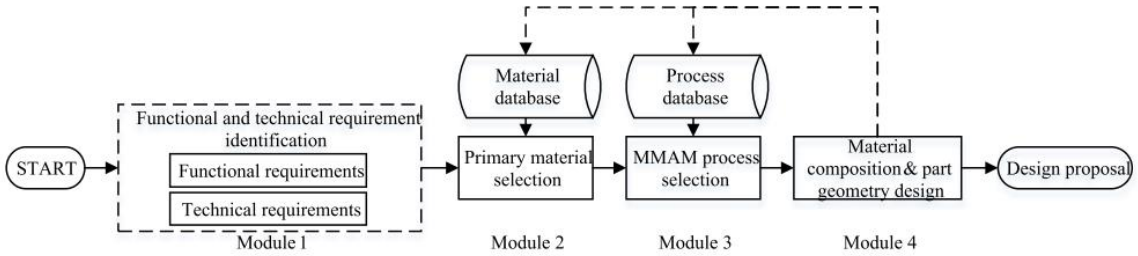

Figure 2-40: design for multi-material AM flow chart, from [139]

When combining dissimilar materials complexities can be encountered if the materials present have physical properties that are too dissimilar, which would play an important role in their ability to be mixed, such as thermal expansion, heat conduction and brittle phase formation. Therefore material combination is related not only to the final application, but is also limited by the materials "affinity", which should be compensated for (or accounted for) by a fabrication strategy [14]. In this respect some researchers have investigated the use of intermediate layers to allow good material bonding [140].

The powder delivery system used in Direct Laser Deposition (DLD) technology makes it easier for dissimilar material fabrication, by connecting two different powder feeders to the pneumatic delivery circuit, and allowing an homogeneous mixing through the system into the deposition nozzle, or by using Ball milling before processing [141] (see Figure 2-41).

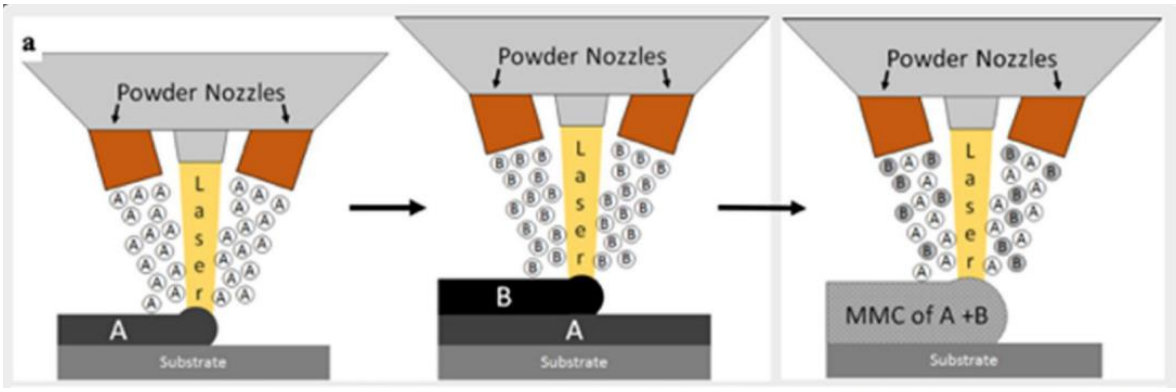

Figure 2-41: Multi-material powder delivery in Direct Metal Deposition technologies, from [137]

In powder-bed technologies the use of plural powder feeders can be coupled to a mixing powder hopper in order to produce gradient structures. To control the amount of powder within the mixing hoppers piezoelectric transducers are used before the classic layer deposition in L-PBF [20], [21]. Metal Matrix Composites (MMC) can also be manufactured by using Direct Laser Metal Deposition (DLMD) plural powder feeders, as demonstrated by Smurov et al. [142]. However, the latest development of technique leads to a Hybrid combination between AM and conventional manufacturing also allowing for customisable repairs such as shown in Figure 2-42.

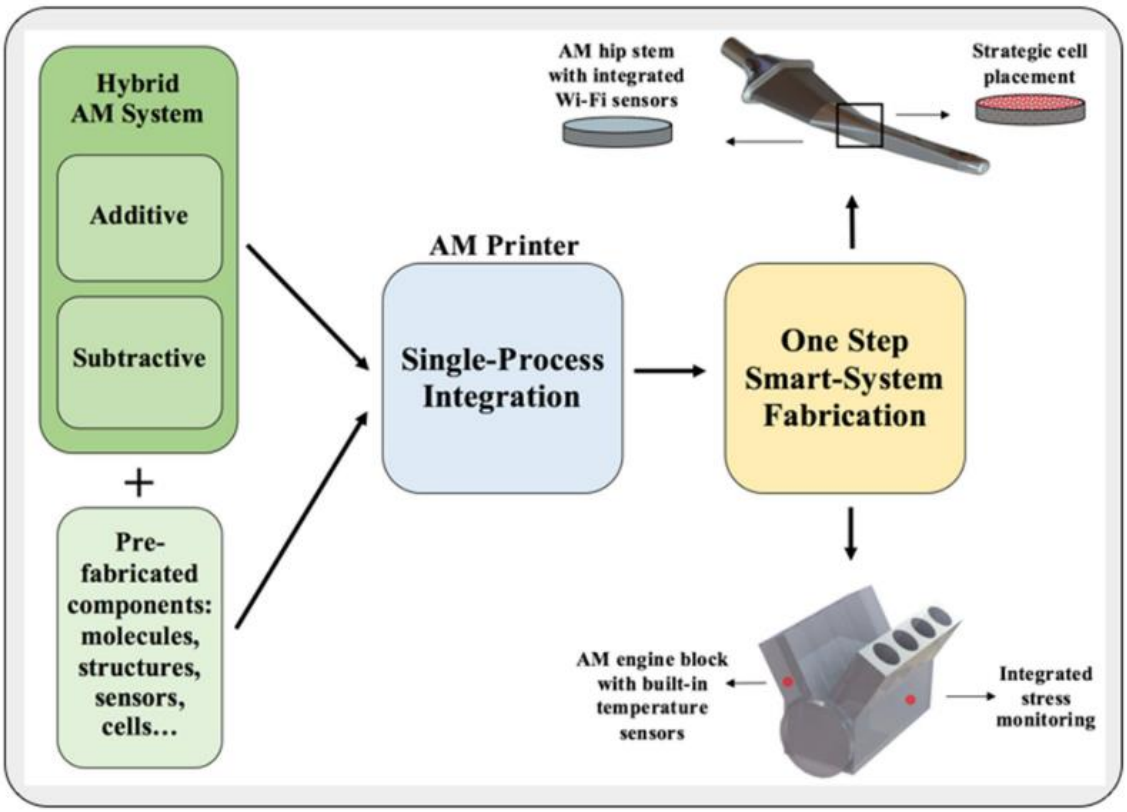

Figure 2-42: Emergence of Hybrid AM process [137]

2.3.1 316L/IN718 alloy combination by MMAM

Due to their wide range of application and their good compatibility it would be expected that 316L SS alloy and IN718 alloy would be good candidates for material combination using 3DMP techniques. However, due to the length of time needed to bring a new technology to the market MMAM machines were making their way progressively through prototypes, while 316L and IN718 alloy combinations were already under the investigation by the scientific community.

2.3.1.1 316L/IN718 combination effect on microstructure

The first paper to report a combination of 316L and IN718 by AM process, was in 2014 by Shah et al. [18] and using a DMD process to create a gradient transition between the two alloys. It was found that while Inconel was forming dendrites, the stainless steel was more prone to solidify as columnar grains, and that the secondary dendritic arm spacing (SDAS) was strongly dependent on the power and powder mass flow rate. Then, Hinojos et al. [143] studied the deposition of 316L powder fused by EBM onto an IN718 building plate, and reversibly the deposition of IN718 powder fused by EBM onto a 316L SS building plate. A result of their combination can be seen in Figure 2-43. It was found that areas in which there is a large concentration of refractory elements (such as Mo and Nb) and no enrichment in carbon, was symptomatic of the presence of topographically

close-packed (TCP) phases such as: Laves-(Fe, Ni, $Cr)_2$(Nb,Mo, Si) (hexagonal) or δ-Ni3Nb (orthorhombic). The presence of globular precipitates within the un-melted zone (UZ) and fused zone (FZ) were identified as IM phases the majority of which were found to be NbC or MoC and some Laves phase.

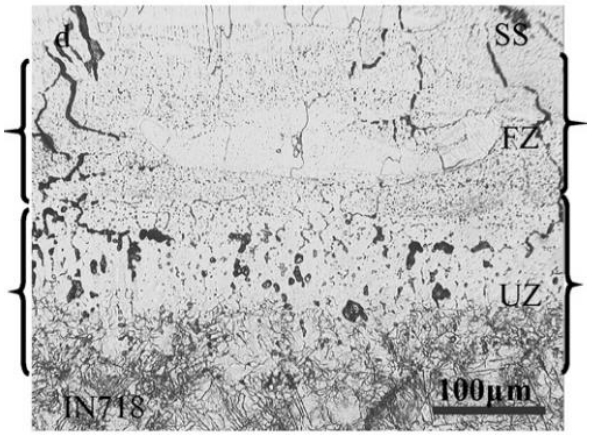

Figure 2-43: Micrograph showing 316L SS deposited on IN718 building plate, with brackets showing the UZ and FZ, from [143]

2.3.1.2 316L/IN718 alloy combination effect on fracture toughness

In this section the following results are reported for AB specimen, and the details of any HT used will be reported when appropriate. Similarly, all the results discussed in the present section are from tests made at room temperature (RT). The structural integrity of deposited graded material was evaluated by fracture toughness tests using Miniaturized Compact Tension (MCT) specimens and J-R curve concept was applied using unloading compliance method for a combination of 316L and IN718, published in 2021 by Melzer et al. [144], see Figure 2-44. Miniaturized Tensile Tests (MTT) were also performed and it was found that the tensile strength properties (YS and UTS) of the interfaces (regardless of sharp or gradual transition) were close to 316L steel, that is, the weaker of both investigated materials. Then it was found that despite the significant difference of the MTT results, the fracture toughness behaviour of sharp and gradual interfaces was comparable.

Two different interface orientations were investigated in crack arrester (CA) and crack divider (CD) here named YZS and ZYM respectively (see Figure 2-44). Significant differences in the YZS oriented crack growth mechanism across the interface were observed (see Figure 2-44).

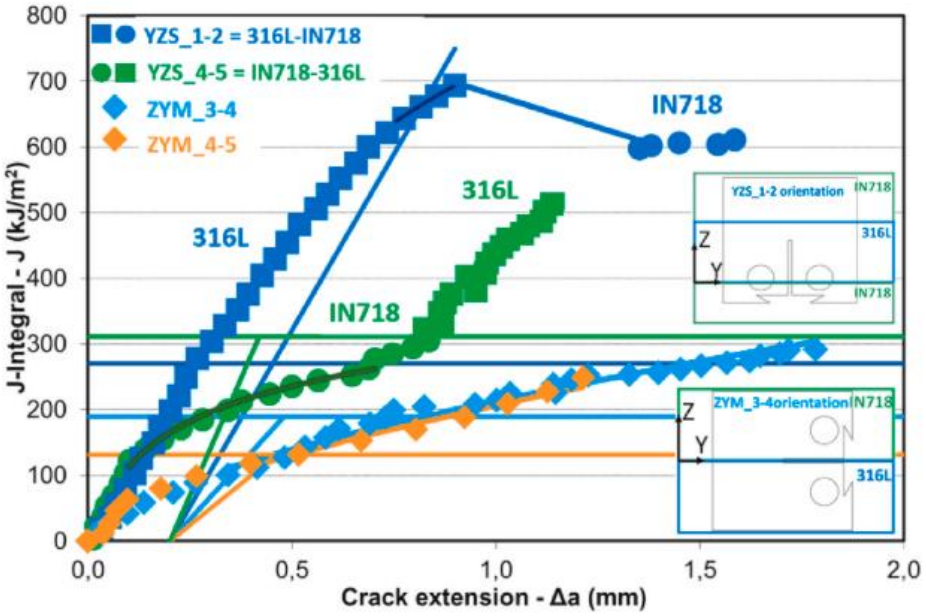

Figure 2-44: Fracture toughness test through 316L/IN718 CA interface, from [144]

The fracture toughness behaviour assessment across the interfaces demonstrated a significant increase of the fracture resistance for the gradual interface when the crack was growing from IN718 to 316L steel.

In the case of the sharp transition, when the crack was growing from 316L steel to IN718, a sudden stable crack extension was observed at the interface. i.e. represented by the dark blue J-R curve Figure 2-44. When the crack reached the sharp interface of 316L-IN718, a change in crack propagation occurred, a rapid decrease of the loading force and large crack length extension within a single step was observed. Subsequently, stable ductile crack extension continued in the single material layer of IN718 (blue circular points). This characteristic rapid change of fracture behaviour might be attributed to the rapid change of the material type. In the case of transition 316L to IN718, the energy input in the specimen that was needed for the crack propagation in 316L was too large for IN718 material. This value of approximately 650 kJ/m2 is twice of that for the IN718 at a corresponding ductile crack extension. Therefore, it results in energy consumption by a rapid crack growth, which is demonstrated by force drop with corresponding CMOD opening. A noticeable difference can be seen in the progress of the crack propagation from IN718 to 316L once past the gradual interface. The corresponding J-R curve is presented in green points in Figure 2-44. When the gradual interface is reached the fracture resistance increases gradually compared to sharp interface. The green points “turns” into green square and show the crack propagation in 316L. It can be concluded that when the crack propagates from the material of higher toughness to the material with lower fracture resistance, a failure of the material is more probable due to high stress intensity, which exceeds the fracture toughness of the less ductile material [144].

2.4 Summary

The mechanisms of fatigue crack initiation and propagation are related to the microstructure of the material, in order to have control over one we must first understand and optimise the later. In materials science, and especially in the additive manufacturing field, control over the microstructure is a new challenge. Often AM components require the use of post processing such as thermal treatment or mechanical finishing, in order to provide the mechanical properties that a specific component requires for their application.

MMAM technology offers great possibilities for new designs and material joining. It is a technology that holds the potential to considerably reduce the amount of assembly, the length cost and energy consumption (and material waste) of a production line, and hence can be a great tool for a more sustainable production. This technique also offers great advantages for complex part production and intricate design for new types of structures.

However, those major improvements require extensive study and characterisation, in order to fully control the resultant mechanical properties that can be then used in industrial systems, even more for key components that can be subject to highly challenging environment or service conditions.

The current state of scientific research around the topics of 3DMP, is mostly limited to single material components, and thus this current work has been conducted on a combination of 316L and IN718 alloys that are of high interest for a wide range of industrial applications.

The aim of the present work is therefore to provide an in depth understanding of the microstructure produced by MMAM, and propose an enhancement strategy by post treatment, aiming to improve both the mechanical properties and fatigue performance of this new type of multiple material combination.

This study should fulfil a gap in the scientific knowledge that strives to optimise the performances under cyclic fatigue of components made by MMAM technique, using microstructure control, the layered architecture and appropriate post processing, as the means to optimise the overall final performance of the component.

Chapter 3 Materials and Experimental Method

3.1 Introduction

In this chapter, a detailed description of the materials powders, processing and post processing methods will be laid out and explained, along with the details of the experimental procedures used for the metallographic, mechanical and fatigue analysis that were used throughout the rest of this study.

The choices in the experimental design and investigation strategy play a key role in the development of this work, thus this chapter will lay out the arguments leading to each experimental decision made. The choices made in materials combination and heat treatment will be thoroughly discussed. The limitations and necessary compromises that were made will be explained. Additionally an explanation of all the experimental techniques that were employed during this work will be detailed.

3.2 Materials

3.2.1 Materials choice for alloy combination

Before the start of any work, it is important to consider the industrial impact, or potential application, in current systems. The choice of 316L and IN718 alloys for this work on multi-materials combined by L-PBF, was made based on multiple reasons:

- Primarily due to the similarities between each alloy's crystal structure, both FCC crystal structure forming an austenitic matrix, with a = 3.591 Å dimension
- Thermal expansion coefficient (CTE), was a good match to produce specimen with minimal defects from the start: CTE (316L) = 16 (µm/m). $°C^{-1}$ and CTE(IN718) = 13 (µm/m). $°C^{-1}$ both thermal expansion coefficients are from RT to 200°C [143].
- Both alloys are widely used in industries such as aerospace, nuclear, or pharmaceutical industries [145].
- More specific application components can be identified such as: heat exchangers, turbo machinery, cooling pipes in nuclear power stations etc [3]

The specific need for cost effective part production and tailored complex part repair and/or replacement, in such demanding environments, is a very niche target, but one of key importance nonetheless.

3.2.2 Powder characterisation

As mentioned in the previous chapter the quality of the initial powder, its physical and chemical properties, and the potential contaminations from the environment can lead to effective success (or failure) to the rest of the work. Hence, a curated integration of the powder characterisation needs to be performed, and repeated for each variation of supplier, even if possible repeated between each new batch of material to ensure a consistency in the final results.

3.2.2.1 Powder morphology and size distribution

Both 316L and IN718 alloy powders were gas atomised by Sandvik Osprey producing spherical metallic powder particles in the size range of 20–50 μm. The powder used throughout this work will be referred to as “virgin powder” due to the batch of powder received as new at the start of this work. However, the un-used powder from the chamber was carefully swiped out and used again for the next build for all the specimens built for this work. However, the quality of the powder was considered to remain un-affected because the total number of build made from this batch of powder and in laboratory condition were inferior to ten. The powder size distribution and external morphology was measured using Malvern Mastersizer microscope (see Figure 3-1), according to ASTM B822 standard [146]. To perform particle size distribution analysis a specimen of powder is dispersed in a fluid (air or water) that is circulated through the path of a light beam. The powder particles scatter the light as they pass through the beam which is absorbed by photodetector and converted and treated by Fraunhoffer diffraction or Mie scattering then expressed in equivalent diameters.

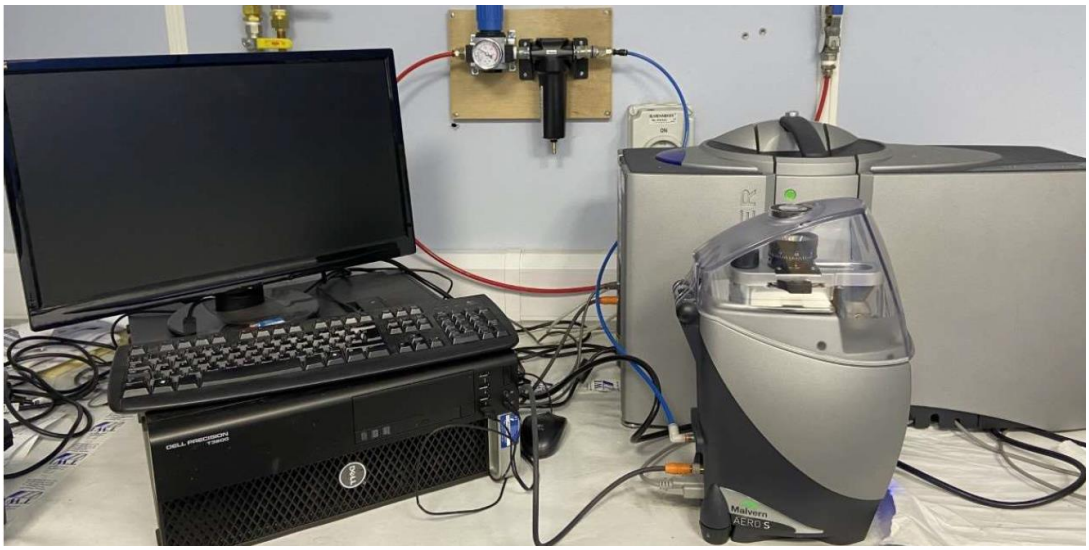

Figure 3-1 Mastersizer 3000 powder size distribution from Malvern

3.2.2.2 Powder flowability calculation

The powder flow rate is the speed at which a given amount of powder will naturally move by the action of gravity. The roundness or the overall shape of the powder will affect the interparticle friction and hence affecting their flow, which in the L-PBF process has an effect on the uniformity of the powder bed that is successively produced by rakes in the build chamber.

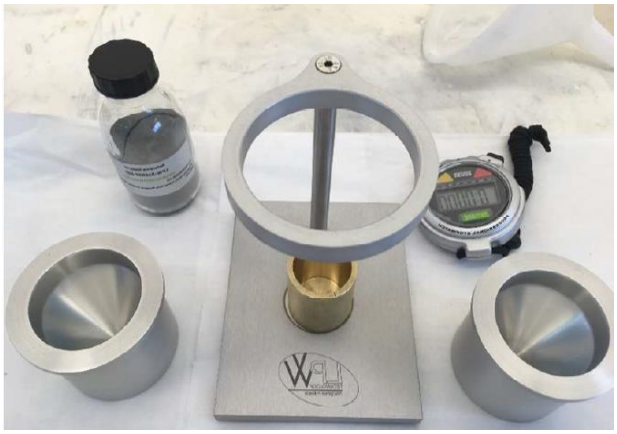

Figure 3-2 Powder flow kit with Hall (and Carney) funnels, funnel stand, density cup, stopwatch and calibration powder from LPW technologies, picture from [58]

The flowability was measured by the Hall Flowmeter funnel (see Figure 3-2), according to the ASTM B213 standards [147] . The following steps were made: 50 g of powder were measured, and placed in the Hall funnel with the orifice blocked, the powder was carefully handled in order to avoid any tapping or shaking that would produce packing and render the measurement null, then the orifice is opened at the same time that the stopwatch is started, and the final measure of the time taken by the powder to flow through the funnel is adjusted by the calibration factor (obtained by flowing the calibration powder) to get the final flow rate of the powder.

3.2.2.3 Powder density measurement

The use of powders as feed stock, has multiple effects in the L-PBF process, and around the calculations made to calibrate the process accurately. The density of the feed stock is important as it differs from the nominal density for bulk alloy (cast, wrought, ingots or bar…). Different density needs to be defined when using powders, as after some ‘tapping’ or shaking the level of packing of the powder will be affected, due to interstitial re-arrangement.

Figure 3-3 Tap density analysis instrument from Copley Scientific

The apparent density is measured according to ASTM B212 standard [148], following these steps: The Hall funnel is placed on the stand and an empty brass cup is weighed and placed below the funnel. Powder is loaded into the funnel and allowed to freely flow into the cup. The process continues until the cup starts to overflow, creating a pile on top of the cup. The powder is levelled flush with the top of the cup, using a spatula. The full cup is weighed and the apparent density can be calculated using the following equation:

$$D = \frac{M}{V} \qquad (3\text{-}1)$$

Where D= density in g/cm³, M= mass of powder in g, V = volume in cm³

The tap density is measured according to ASTM B527 standard [149] following these steps: An amount of powder is measured and placed into a graduated volumetric cylinder (using the apparent density measures explained above), the cylinder is placed in a tapping instrument (see Figure 3-3). Each 'tap' cycle consists in a free fall from a 3mm height, then the full tapping test cycle is set at 3000 repetitions. The final volume occupied by the powder is the measure of the tap density.

3.2.2.4 Chemical characterisation

Quality of the final part fabricated by L-PBF strongly depends on the elemental composition of the powder feedstock, this has been discussed in previous chapters (see section 2.2.1) how elements such as oxygen, nitrogen, sulphur etc can cause contamination and later down the line induce defects in the build. However, it is easier to detect heavier elements by methods such as EDX that are widely available, but for lighter elements such as hydrogen or oxygen it is advised to use more specific specialised techniques that are less commonly available.

The chemical composition of the powder was measured by external contractor AMG analytical (UK) by Inductively Coupled Plasma (ICP), and for lighter elements such as Carbon and Oxygen, contents were measured by thermal infrared and inert gas fusion respectively (LECO).

3.2.3 Results of Powder analysis

The physical properties of both alloy powders are displayed in Table 3-1. The 316L powder used in this study has more satellites and some agglomerations of powder are creating a larger mean diameter, but are also forming a more compact tap density by allowing interstitial powder stacking, which reduces the risk of creating porosities during the fabrication process. Figure 3-4 shows the difference between the distributions of both alloy powders' mean diameter size, by comparing the curves it can be seen that the IN718 powder has a narrow distribution curve in comparison with the 316L powder, which has a wider distribution. This is because the 316L powder had been used in different work prior to this study and has had a longer shelf life, while the IN718 powder was brand new at the beginning of this study. Recycling of the powder can be done several times before the powder physical and chemical properties become out of the tolerance range to produce a decent final product. However, each alloy has its own properties and specific weaknesses to specific contaminant and depending on the level of accuracy required in the final product, a regular analysis of the powder feedstock can be necessary [150].

Table 3-1: Physical powder properties

	316L	IN718
Powder diameter size	28.2±12 µm	22.5±7 µm
Tap density	5.4 g/cm³	6 g/cm³
Flow ability	15 ±0.3 g/s	11.6±0.1 g/s

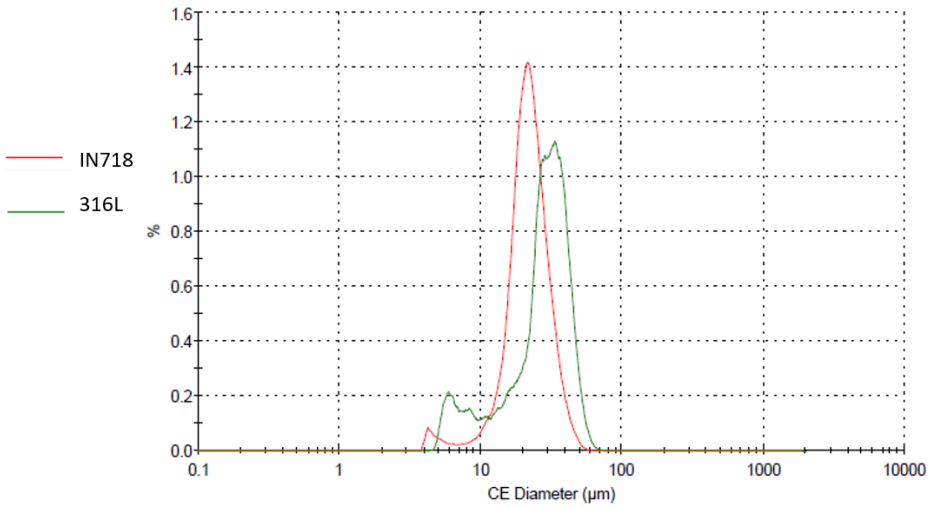

Figure 3-4: Powder mean diameter size distribution comparison between IN718 and 316L

The chemical composition of both powders is displayed in Table 3-2. The 316L powder shows a long list of minimal elemental additions however, these concentrations remain very low. Similarly, the main chemical composition of IN718 powder falls within the range of the standard alloy composition except for some minor elemental traces. However, it is important to note the presence of N in the composition of 316L. N solute atoms can lower the stacking fault energy of 316L SS and have an effect on deformation twinning, contributing to the high tensile ductility of L-PBF 316L [66].

Table 3-2: Chemical composition of IN718 and 316L powders used in this study, and comparison with standard material

Element (wt%)	316L Powder	IN718 Powder	Standard wrought 316L[151]	Standard wrought IN718[152]
Ni	12.29	52.46	10 - 14	50 - 55
Cr	17.34	18.71	16 - 18	17 - 21
Fe	64.95	19.57	Bal.	Bal.
Nb	0.04	4.8	-	4.75 - 5.5
Mo	2.49	2.93	2-3	2.8 - 3.3
Ti	<0.02	0.69	-	0.65 - 1.15
Al	<0.02	0.36	-	0.2 - 0.8
Cu	0.17	0.02	-	0.3 max
C	0.02	0.02	0.03	0.08 max
Co	0.08	0.09	-	1 max
Mn	1.49	0.04	2	0.35 max
Si	0.85	0.09	0.75	0.35 max
B	<0.02	<0.02	-	0.006 max
N	0.083	0.081	-	-

It can be concluded that the powder is suitable for processing because it fits the range of chemical concentrations. However, it should be noted that the level of Nitrogen (N) can have an effect on the ductility behaviour of 316L.

3.2.4 Specimen manufacturing

The L-PBF process was conducted using a HUAKE PM250 machine (from Chinese manufacturer, see Figure 3-5) under an argon gas protective atmosphere, using the parameters shown in Table 3-3.

Figure 3-5 HUAKE PM250 from Southampton University

The process parameters having the largest impact on density are the laser power, the exposure time and the layer thickness. As the laser power and exposure time are directly setting the amount of energy that is imparted to the powder, hence affecting the melting conditions. Layer thickness impacts the amount of material that needs to melt and the number of required layers to form a complete specimen, hence impacting the overall process time. The rotation of the scanning pattern between each layer is used to help relieve some of the residual stresses within the specimen build, due to the successive laser scan lines [70]. The island scanning strategy was chosen with a size of 5 mm, and the scanning direction of each layer was alternated through a 90◦ angle. The ratio of process parameters, also named as the energy density ratio (E_{dv}, see $E_{dv} = \frac{P}{h \times t \times v}\ [J/mm^3]$ (3-2)) is often used for process parameter optimisation:

$$E_{dv} = \frac{P}{h \times t \times v}\ [J/mm^3] \qquad (3\text{-}2)$$

Where *P* is the power, *h* the hatch spacing, *t* the thickness of the powder layer displayed and *v* the scanning speed [51]. The energy density ratio employed for both materials was E_{dv} = 140 J/mm^3, which is within the optimal range of process parameters for high densification of each material according to studies on process parameter optimisation [85], [153].

Table 3-3: L-PBF Process parameters used in this study for both 316L and IN718

Laser Power	Scanning speed	Hatch space	Layer thickness	Layer rotation

300W	900mm/s	0.08mm	0.03mm	90°

All specimens were built horizontally to the building plate, on multiple rows of “support structures” to ease the removal of the specimen from the plate, and when multiple-materials were made within the same build, 316L was always built at the bottom to accommodate a potential shrinkage on cooling. (Use of support structures is necessary to minimise part distortion after removal from the build plate as some residual stresses are released.)

Bend bar specimens for fatigue testing were manufactured with dimensions of 10x10x60 mm, with IN718 as the top layer and 316L as the bottom layer (10x5x60 mm dimensions for each layer, as shown in Figure 3-6). Six tensile rods of Ø10x60 mm dimensions were manufactured respectively for IN718 and 316L to test the tensile properties of each alloy separately.

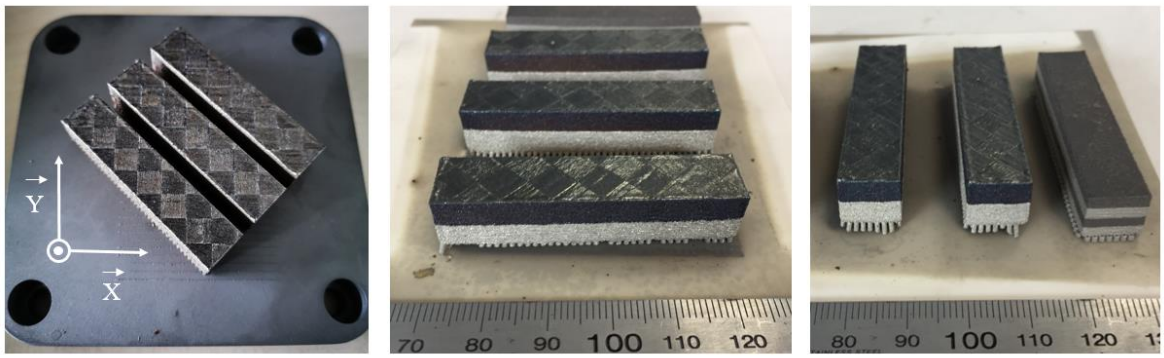

(a) (b) (c)

Figure 3-6: Bend bars a) on building plate, b) Bi-layer specimen lateral view, c) front view including 4-layers specimen

3.2.5 Heat Treatment choice for 316L/718 alloy combination

The choice to use a post process heat treatment was made on the evident basis that IN178 is a precipitation strengthening alloy that can only meet its standard mechanical properties by using a specific heat treatment. However the simultaneous presence of IN718 and 316L within the same component to be heat treated represented a challenge in the choice for the heat treatment strategy to employ. Hence in this chapter the choices made to design the heat treatment used in this work will be discussed.

316L is an austenitic stainless steel with high strength and high corrosion resistance due to its high chromium content and low carbon content. Usually its fully austenitic FCC structure provides 316L with good ductile behaviour but detrimental phases such as σ ($(Fe,Ni)_x(Cr,Mo)_y$) intermetallic, and the Laves phases such as Fe_2Mo, Fe_2Nb and Fe_2Ti can also be found [83]. σ phase forms between

600-1100°C[84]. AMS2759 [88] for 316L stainless steel recommend annealing at 1060°C followed by air or vacuum gas quench. AMS5662 [118] and AMS5383 [117] for IN718 recommend a first annealing stage followed by a double stage ageing treatment (720°C/8h FC to 620°/8h AC to RT). In this study, the annealing temperature was selected from the 316L standard annealing recommendation, because temperatures above 1032°C are considered elevated enough to promote the release of Nb in the IN718 matrix.

One stage of the ageing profile has been chosen, that reduces the temperature exposure to 8 hours instead of the 16 hours (recommended by standards above mentioned for IN718), hence the full precipitation strengthening from secondary phase γ' and γ'' won't be achieved because optimal coarsening and bi modal distributions of those secondary phases won't be fully reached. However the ageing time temperature was chosen, on the one hand to minimize the formation of detrimental phases such as: σ phase within 316L, and δ orthorhombic phase that is a derived for of γ'' Ni_3Nb , and on the other hand to support the γ' and γ'' precipitation in IN718. Sigma (σ) phase formation in 316L has a low kinetics of formation (i.e. it is sluggish) and requires an extended exposure within the temperature range 600-800°C [154]. Similarly for delta (δ) phase formation in IN718 with a high chromium content, both of which can potentially reduce the ductility and toughness. Exposure at 1000 °C can restore the ductility due to δ phase dissolution. A strength peak is usually achieved around 700°C due to γ'' formation and drastically drops in the temperature range [750-950]°C due to brittle δ intermetallic phase formation.

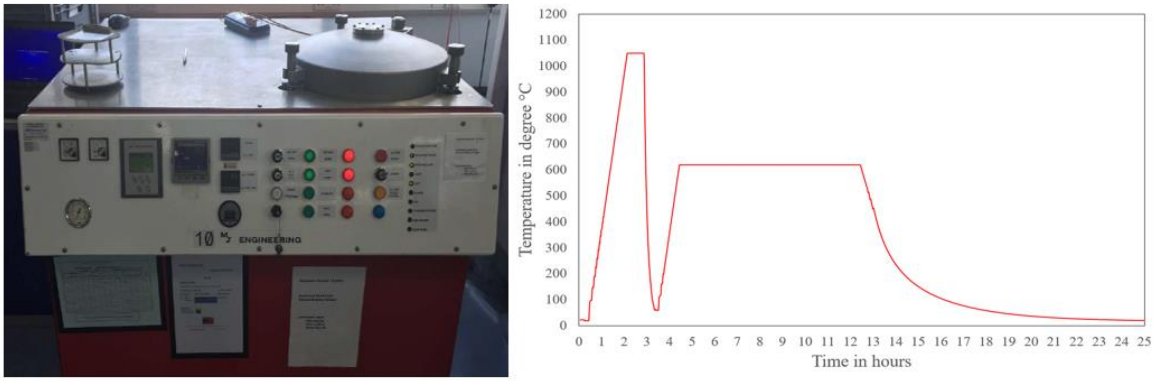

(a) (b)

Figure 3-7 (a) Photo of the vacuum furnace, b) and Heat treatment used on multi-material specimen

Heat treatment was performed as follows: annealing at 1050°C / 45 min, followed by argon gas quenching, then ageing at 620°C / 8 hours followed by air cooling, and performed in a vacuum brazing furnace from M&G Engineering using argon gas quenching after annealing (see Figure 3-7). The furnace can achieve vacuum of 10^{-6} MPa and maximum temperature of 1200°C. It is equipped with an argon fast cool facility to quickly bring the temperature of the specimens below detrimental

phase transformation temperatures (≈ 1050°C). The average cooling rate of the argon fast cool was in the range of ≈ 50°C/min. Temperature was controlled and monitored using Type K thermocouples.

The choice of heat treatment is detailed in the discussion section. However, AMS2759 standard for 316L stainless steel recommends annealing at 1060°C followed by air or vacuum gas quench [88]. AMS5662 and AMS5383 for IN718 recommend a first annealing stage (which temperature may vary depending on the final application) followed by a double stage ageing treatment (720°C/8h FC to 620°/8h AC to RT) [117], [118].

3.3 Microstructural analysis methods

3.3.1 Metallography

Metallographic preparation was used throughout this study on equipment such as shown in Figure 3-8. Bend bars were prepared prior to fatigue testing, all surfaces of the specimens were ground using 800, 1200 SiC grit paper and then polished using 6 µm, 3 µm, 1 µm diamond suspension to avoid any interaction between the external surface roughness, and the crack propagation during long crack fatigue tests.

Figure 3-8 Pictures of the turntables used during metallographic preparation. a) ATM Saphir 350 grinding machine, b) Buehler MetaServ 250 polishing wheel, c) ATM Saphir 560 automatic polisher, d) Buehler SimplyMet XPS1 mounting press. Pictures from [58]

For metallographic analysis, bend bars were cut by silicon carbide (SiC) cutting wheels, orthogonally to the longitudinal direction, then mounted in conductive Bakelite. Top surfaces of the specimens were mechanically ground using 800 and 1200 silicon carbide (SiC) grit papers before polishing using 6 µm, 3 µm , 1 µm and 0.25 µm cloth and non-oily lubricant with diamond particles to finish. The etching strategy was selected to affect both 316L and IN718 at the same time, and was performed with: H_2O : HCl : H_2O_2 solution in 4:2:1 proportions.

3.3.2 Light Microscopy

Figure 3-9 Optical microscopy station,

Porosity and microstructural observations were made using an Olympus BX-51 optical microscope (OM), using varying magnifying lenses from x5 to x100 (see Figure 3-9). Images were acquired with an Olympus stream essential software. ImageJ software was used to post-process multiple micrographs, and to quantify the porosity content of each specimen. For each specimen, six micrographs were taken in each plane orientation providing a total area of study of 54.6 mm^2 per plane orientation (i.e X-Y, Y-Z, and Z-X planes). Due to the limited accuracy of imaging and magnification using OM the lowest pore diameter range measured were included within 1 to 5 µm.

3.3.3 SEM/EDX/EBSD

In scanning electron microscopy (SEM), the surface of the specimen is impacted by a focused electron beam. The beam causes the emission of various types of particles and waves, emitted from different parts of a certain volume of material. Due to the energy electrons carry, they force the emittance of X-rays which can be detected using energy dispersive X-ray spectroscopy (EDX or EDS) giving information regarding the elemental composition of the material. Similarly, the electrons can be forced to diffract from the surface of the material giving information about the crystal structure using electron backscatter diffraction (EBSD) as demonstrated in Figure 3-10.

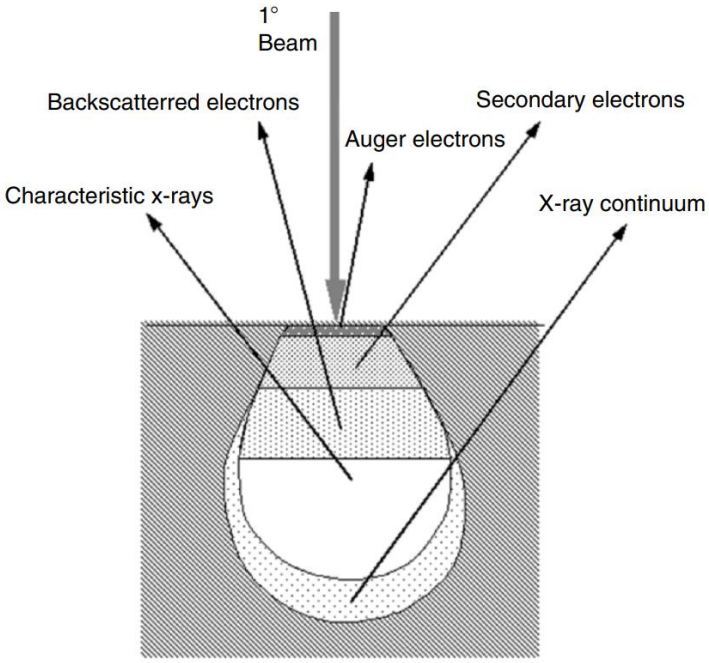

Figure 3-10: Schematic of electron beam interaction and material within the SEM, picture from [155]

Because electrons are particles thus have a mass and thus a kinetic energy, the microscopy needs to take place in a vacuum chamber to avoid interactions between the electron beam and air particles. Additionally, electrons carry a charge, necessitating grounding of a specimen to avoid electric charge build-up, which can deflect the electron beam. A conductive bakelite was used for the mounting of specimens, which is a conductive material and easily allows grounding.

Secondary electrons (SE) are electrons that have emitted off the surface of the specimen due to the primary electron beam. These can be detected using specialised detectors placed around the microscope (SE2) and within the electron beam gun (InLens). Secondary electrons give primarily topographic information of the surface being investigated.

Backscattered electrons (BSE) emit from within a teardrop shaped volume of the material. The energy of these electrons varies by the density of the illuminated material. Hence, the detection of this type of electrons reveals density differences of the surface.

Energy dispersive X-ray spectroscopy (EDX) involves detecting the wavelength and number of these X-rays and creating spectra for a given scanned location of the specimen. The spectra show the elemental composition of a given area. Because the X-rays are emitted from a volume, EDX is generally a qualitative analysis method. However, if the detector and SEM are accurately calibrated, EDX analysis can be semi-quantitative.

Electron backscatter diffraction (EBSD) is a technique that can be used to determine the crystal structure of an area of a metallographically prepared specimen creating an EBSD map. It is performed, by orienting the specimen at highly tilted angle (70°) towards a detector equipped with

a phosphor screen. The electron beam is focused on a specific point of the specimen and electrons are refracted towards the screen. When electrons hit the phosphor screen, they produce a diffraction pattern that is determined by the crystal structure and orientation of the point being illuminated. This diffraction pattern is called an electron backscatter pattern (EBSP) or Kikuchi pattern. The EBSP is acquired by a digital camera that is focused on the phosphor screen. The EBSP is then analysed by commercially available computer software to determine the crystal structure and orientation of the point being illuminated. By accumulating information for successive points, it is possible to create a map of the crystal structure of the specimen. EBSD maps can be used to determine information about the crystal structure of the investigated area. Firstly, EBSD maps can show the size and orientation of crystal grains. By statistical analysis it is possible to determine if the area is textured, i.e. a specific orientation is dominating over other orientations. In materials with a variety of crystal phases, an EBSD map can also show the distribution of these phases. Finally, EBSD maps can help to determine the misorientation of specific grains.

In this work the EBSD detector used was a Nordlys EBSD detector by Oxford Instruments. The software used to acquire the EBSD maps was AZtec also by Oxford Instruments. The postprocessing of the EBSD maps was performed using Channel 5 software by Oxford Instruments.

A Σigma and an EVO LS15 SEM, both manufactured by Zeiss (Oberkochen, GER), were used for scanning electron microscopy shown in Figure 3-11. Σigma SEM is equipped with a field emission gun allowing for higher resolution images to be acquired at higher magnification.

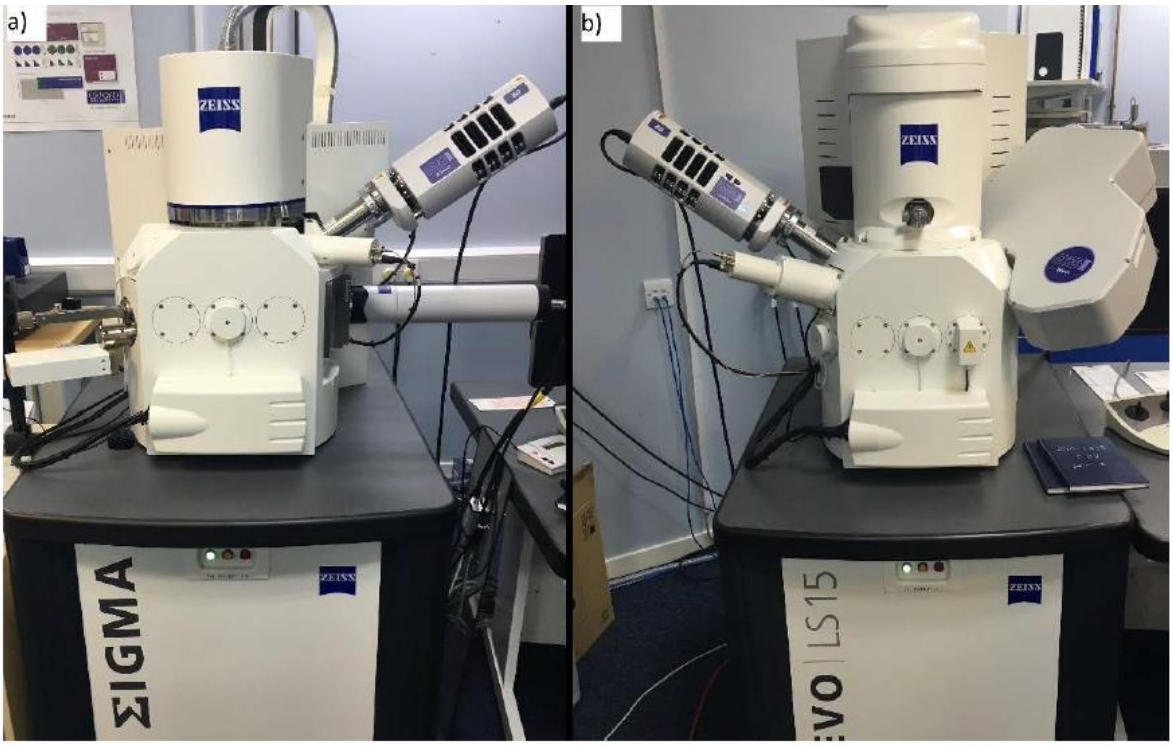

Figure 3-11: Scanning Electron Microscopes used for material characterisation manufactured by Zeiss, a) Σigma FE-SEM, b) EVO LS15 SEM, picture from [58]

Scanning electron microscope (SEM) and X-ray spectroscopy (EDS) analysis were conducted under 15–20 kV for SEI imaging, at a typical working distance between 8.5 and 10 mm. Backscatter electron (BSE) imaging and electron back scatter diffraction (EBSD) analysis were conducted using 20 kV and a 120 µm aperture, a step size of 0.57 µm and Channel5-HKL software. The observations were conducted along the build orientation of the specimen (z direction), then analysed by using Aztec software for grain size, shape and orientation.

3.3.4 Alicona

Figure 3-12 Alicona G4 infinite focus, from Southampton University

Macro-observation of specimen fracture surfaces was carried out using an Alicona G4 Infinite Focus, to allow roughness imaging for the fracture surfaces (see Figure 3-12). Alicona is a confocal microscopy technique that allows to take multiple pictures of a surface at different height levels (vertical scanning) and merge the areas that are within the plane of focus to each incremental step, then compile all the files in order to build a topographical map of the surface roughness.

3.3.5 X-ray Diffraction

X-ray diffraction (XRD) can be used to determine phase composition by capturing the spectrum of diffracted electrons that were projected by a focus beam on a surface, when the focused beam of electrons hits the surface it 'diffracts'. The diffraction comes from the electrons that have enough energy to dislodge inner shell electrons from the target material, hence emitting a characteristic X-ray in the process. These rays have a specific wavelength that is characteristic of a certain crystal structure (i.e. pure material or known phases). This phenomenon is known as elastic scattering; the electron is known as the scatter. In the majority of directions, these waves cancel each other out through destructive interference, however, they add constructively in a few specific directions, as determined by Bragg's law:

$$2d\sin\theta = n\lambda \qquad (3\text{-}3)$$

Where *d* is the spacing between diffracting planes, θ is the incident angle, *n* is an integer, and λ is the beam wavelength. However, this type of analysis has some limitations, such as for phases that have very similar d-spacing parameters such as for example γ and γ' phases in IN718. For this work a D8 Advance XRD machine by Bruker (Billerica, Massachusetts, USA) was used (see Figure 3-13). The machine is shown in Figure 3-13 below. The X-ray source was Copper, the 2θ angles were between 20° and 120° with a step size of 0.02° and 1 s/° scanning rate.

Figure 3-13 X-ray diffraction from TWI

3.4 Mechanical testing methods

Mechanical testing approaches are standardised methods of testing and data treatment allowing to define properties such as Hardness, Yield point, Tensile strength, Elongation. These tests were used in a systematic manner in order to obtain reliable and comparable results between the different alloys in both as-built (AB) and heat treated (HTed) conditions. These results were then used during the experimental fatigue test set up, in order to apply the corresponding load to the desired stress-strain response from the specimen, and correctly analyse the results obtained. These values were considered correct for the whole of the specimen, by considering the homogeneous nature of the specimens used in this research and for continuous properties purposes, even in multi-material specimens.

3.4.1 Microhardness

Vickers micro-hardness is a test where a diamond pyramidal indenter is applied to a surface for a certain amount of time under a certain load and measures of the final indent imprint is made via optical measurement. The indentation which is measured is then converted to a hardness value following the following equation:

$$\text{Hardness} = (\text{peak force})/(\text{contact area}) \qquad (3\text{-}4)$$

Test specimens must be highly polished to enable measuring the size of the impressions. Vickers micro-hardness (HV) tests were conducted in accordance with BS EN ISO 6507 [156]. Hardness was measured using 300gf with dwell time of 15 s. Measurements were made on cross sections of the specimens (10 mm of edge length), with 50 µm distance between each indentation.

3.4.2 Nano-Indentation

The Berkovich shaped indenter tip is the most common tip used for nanoindentation, a nanoindentation enables a very exact, depth-dependent measurement of plastic and elastic material properties such as the elastic indentation modulus. During the nanoindentation process, the indenter tip approaches the surface of the sample, after the sample is contacted, the force is linearly increased and the tip indents into the surface of the sample. A short dwell time occurs at the maximum force and then the sample is unloaded. At the initial point of unloading, the stiffness is measured. The load (P) is the force exerted on the sample, the displacement (h) is the distance the indenter travels into a material, and the area (A) is a measure of the interaction of the indenter in contact with the sample. The resulting load and displacement data along with the area from the

calibrated indenter tip allow for the determination of mechanical properties such as elastic modulus and hardness.

Figure 3-14: Nano indentation from University of Southampton

In this study, the interest in using nano-indentation as an analysis tool was to assess the elastic-plastic properties around the dissimilar material interface from the properties of each alloys (316L and IN718) that were tested under tension separately and in both AB and HTed conditions. The nano-indentation machine used during this study is presented in Figure 3-14. The nano-indentation measurements were taken across the interface to assess the hardness and modulus changes, 50 indent rows offset by 30 µm were made, with 5 indents per row spaced by 10 µm each, for a total length of measurement covering 1500 µm across the interface region (750 µm in the Inconel layer and 750 µm in the 316L layer). Measurements were done in depth control until 300 nm depth, indentation speed was set at 7mN/s.

3.4.3 Tensile test

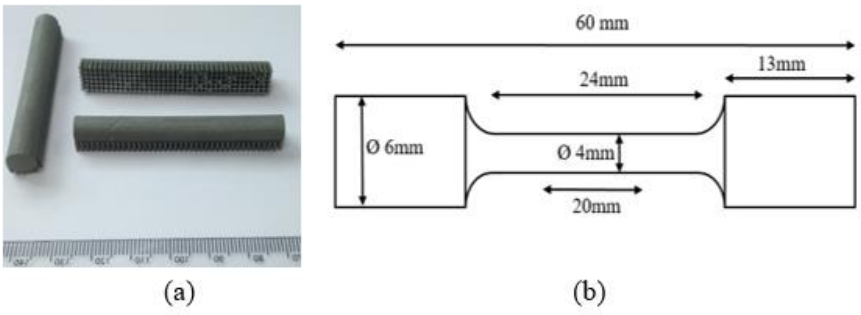

Figure 3-15 Tensile rods a) from L-PBF, b) schematic of tensile specimen after manufacturing

The tension specimens were cylindrical, machined down to 4mm diameter and 16 mm gauge length, as shown in Figure 3-15. Machining was performed to test the internal mechanical properties of the AM material without the influence of surface irregularities.

Tensile tests were carried out for each alloy separately at room temperature by an external contractor, Westmoreland mechanical testing (UK), in accordance with the ASTM E8 standard at room temperature [157]. Specimens were manufactured out of the AB tensile rods, horizontally built with respect to the building plate (i.e. the main rod axis is within the X-Y plane of the building plate). This choice was deliberately made in order to reproduce the grain directional growth within the tensile rods in regards to the tensile loading axis during the tensile tests, then within the bending bars, to have a more accurate description of the mechanisms a stake during the fatigue experiments. An extensometer was used for the first part of the test at a strain rate of 0.005 $.min^{-1}$, then past the yield point the cross head displacement was set at a strain rate of 0.05 $.min^{-1}$ for a faster displacement rate until final failure. All the tests were performed at room temperature.

3.5 Fatigue test methods

As explained in previous chapter, fatigue is a progressive evolution of permanent damage within a material, under fluctuating repetitive stresses (and/or strains), resulting in the appearance of a crack (or cracks) that may evolve into a final fracture. This is overall a long-term process that takes multiple cycles of tensile stress and plastic strain of the material to initiate and propagate any cracks.

Figure 3-16 Instron servohydraulic testing machine from Instron website

For the testing of metallic materials, the use of a servohydraulic testing machine (as seen in Figure 3-16) is usual, due to the amount of stress needed to trigger the mechanisms of fatigue in typical sample sizes and because well controlled loading cycles can be applied.

3.5.1 Long crack test

The objective of fatigue crack propagation testing is to determine the rates at which subcritical cracks grow under cyclic loading prior to reaching a size critical for fracture. Fatigue crack propagation testing is usually performed under constant-load-amplitude cycling of notched specimens that have been pre-cracked in fatigue. The crack length is measured and recorded in time (hence in number of cycles/s can be deduced via the frequency) and these data are analysed to establish the crack growth rate: da/ dN. The crack growth rate is then expressed as a function of the crack tip stress-intensity factor range, ΔK. The stress-intensity factor is calculated from expressions based on linear elastic stress analysis and is a function of crack size, load range, and specimen geometry. Fatigue crack growth data are typically presented in a log-log plot of da/dN versus ΔK [158]. Bend bar specimens for fatigue testing were manufactured with dimensions of 10x10x60 mm, with IN718 as the top layer and 316L as the bottom layer (10x5x60 mm dimensions for each layer) then polished down to 1µm finish (final dimensions are 10x10x60 mm $\pm$ 2mm) and a notch of 1.25mm depth located at the centre of the specimen (either in 316L or IN718 layer, never across both) see Figure 3-17.

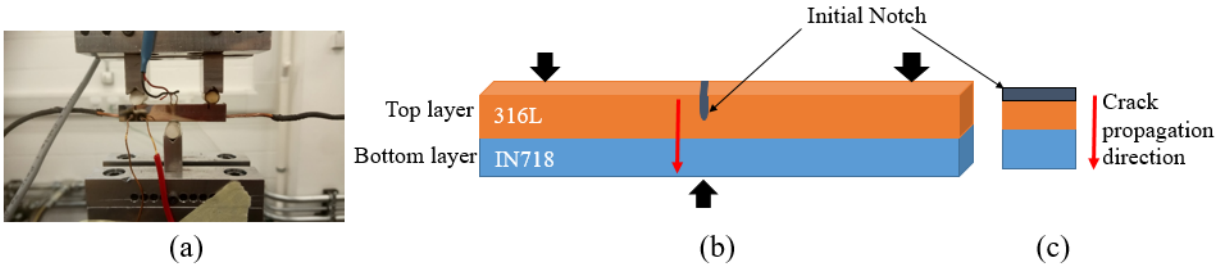

Figure 3-17 a) photo of long crack test bend bar set up experiment including the DCPD device, b) schematic of bi-layer specimen positioned in the 3 point bending test set up

In the present work, long crack tests were performed under three-point bending, on an Instron 8502 servohydraulic machine, with sinusoidal loading at R = 0.1, and frequency f = 10 Hz. All the tests were performed at room temperature. The bend bars were notched in the centre using wire cutting to produce single edge notched bend (SENB) samples as shown in Figure 3-17 b). The depth of the notch is 1.25 mm, corresponding to 1/4 of the depth of the layer (or 1/8 of the total depth of the bend bar). The pre-cracking was carried out by load shedding from an initial ΔK (of 15 MPa√m), then successively stepped down by 10% increments, after the crack grew through 4 monotonic plastic zone sizes at a given ΔK-level (down to a ΔK of 10.4 MPa√m for 316L and 12.6 MPa√m for IN718). Subsequent crack growth tests were conducted following the BS EN ISO 12108:2012 standard [159] under constant load, increasing ΔK-conditions. One test was performed under constant ΔK-conditions, by altering the loading condition as the crack advanced to keep ΔK within 10% of the original value, in order to determine the crack propagation rate base line within

each layer for a given crack tip stress intensity factor. Crack length was monitored by a direct current potential drop (DCPD) method. Two probes were welded on the top surface on each side of the initial notch (denoted as X values) and the other two probes (denoted as Y) were welded on the lateral side (away from the center) to measure the base line potential of the current flow in the specimen. The fatigue crack growth rates da/dN were then derived from the curve of the variation in the electrical potential with time, translated to an empirically determined crack length *a* versus *N* relationship, and *da/dN* determined by the secant method. A standard calibration using tin foil was carried out to ensure the correct V/Vo to *a/W* relationship for the DCPD device. This technique was employed because the resistivity of both alloys were considered similar in regards to the specimen dimensions: 7.400E-07 Ohm-m for 316L and 1.250E-06 Ohm-m for IN718, hence effects on the calculation of crack length were considered negligible, this was also checked by post-test crack length measurements.

3.5.2 Constant delta K test

Constant Δ K testing is used to discriminate each alloy's specific crack propagation behaviour for a given stress intensity factor. By applying the same stress intensity factor throughout the propagation of the crack any acceleration or deceleration will reveal how the local microstructure responds to a given value of stress, and hence how does it affect the crack propagation. This type of test is relevant in the framework of this multi-material study, because the interface between the two alloys has its own microstructure thus its own local mechanical properties that may differ from the bulk of each alloy, even more in the HTed condition, which will be discussed in Chapter 5. Most of the experimental set up is the same as for long crack test, with the exception that the load is manually modified after each crack propagation step. The crack propagation is monitored by the DCPD device and by using a pre-made calculation spread sheet using a reverse calculation loop to keep the same stress intensity factor (within 2%), after each increment of crack length the values of the amplitude and mean load are calculated, and hence can be manually entered into the testing machine (all the details for the calculations are visible in Appendix D and E). Again all the tests were performed at room temperature.

Chapter 4 Fatigue crack propagation in multiple-material layered 316L/IN718

4.1 Introduction

Multi-Materials Additive Manufacturing (MMAM) techniques allow the production of a new generation of components and the reduction of production cost, lead time, inventory and assembly [3], [11]. So far, multi-material parts have been predominantly made by using different types of joining techniques such as welding or brazing [160]. The joining of dissimilar materials inherently creates an interface, that can offer a gradient transition or a discrete interface, which locally affects the microstructure [161]. At the microstructural level, a number of defects can arise in the interface region during rapid solidification, such as intermetallic phase formation, distortions, porosities, residual stresses etc [143]. Whilst at the macroscopic level a gradient in mechanical properties is created, affecting the overall mechanical response of the component [47]. So far, Inconel 718 (IN718) and 316L austenitic stainless steel (316L) components produced as single-material AM have been extensively investigated [42], [91], [126], [128]. For instance, IN718 is widely used in aircraft turbines, jet engines and steam turbines for power plants, due to its strength and corrosion resistance that can be maintained at elevated service temperatures up to 700 ◦C. Whereas 316L is a well-known alloy, with good mechanical properties and excellent corrosion resistance, which can be found in infrastructure such as power plants, or pharmaceutical processing machinery. The combination of IN718 and 316L has been used in pressure tubes for nuclear fission reactors [91], [128], [162]. Both IN718 and 316L alloys possess a face centred cubic (FCC) crystal structure, and both alloys have similar coefficients of thermal expansion (CTE), of 13 µm/m.◦C for IN718 and of 16 µm/m.◦C for 316L, hence further supporting their ability to form a good cohesive interface, by reducing the residual strain caused by solidification shrinkage. In addition to the intrinsic properties of each alloy, layers of materials having different elastic and plastic properties create a gradient in mechanical properties that directly affects the crack driving force and therefore plays an important role in determining the fatigue and fracture behaviour of multilayer components. A gradient in mechanical properties can find a use in a variety of engineering applications for multi-phase materials [163]. Composites or graded structures have been designed to use this property gradient to benefit the component response [50]. Studies on the effect of a soft interlayer on crack propagation were conducted on aluminium and polymer layered systems, showing that the crack propagation was effectively shielded leading to crack arrest at the second interface (on transition from soft to hard material) [164]. However, the fatigue behaviour in components produced by AM techniques is relatively new due to the very specific microstructure and defects that can arise from

the manufacturing technique [60], [145]. Sub-surface porosities and inner defects are commonly found and can act as stress concentration sites, even more when the as-built (AB) surface roughness is not easily accessible and without the appropriate post treatment, these defects can dramatically affect the mechanical response under both static and cyclic loading [165]. However due to its ductile behaviour L-PBF 316L in both AB and heat treated (HTed) condition has been shown to maintain, under both HCF and LCF, good fatigue performance [97]. On the other hand the fatigue behaviour of IN718 has been shown to be affected mainly by the presence of hard and brittle secondary phases, also known as Laves phases, that can also act as sub-surface stress concentration sites [134]. The rapid cooling induced by AM affects the phase formation, grain structure, and the mechanical response of alloys fabricated in this way [41], [85]. IN718 is a precipitation strengthened alloy that commonly requires thermal post-treatment to obtain the optimal precipitation of secondary strengthening phases. However, IN718 produced by L-PBF is known to develop localised micro-segregation of heavier elements such as Nb and Mo surrounding sub-cells and grain boundaries with high density dislocations [109], [110]. Additionally in the AB state IN718 does not undergo the appropriate precipitation of the main strengthening phases such as gamma prime (γ') and gamma double prime (γ''), the alloy has not been exposed to the appropriate thermal post treatment, hence has not achieved its optimal strength. The cyclic properties of IN718 produced by L-PBF have been demonstrated by the literature to be strongly affected by heat treatments, while in the AB state the motion of dislocations through the sub-micron cell structure is still possible due to their unstable nature, allowing a hardening/softening response under cyclic loading [78]. 316L produced by L-PBF in its AB state possesses high strength and good ductility [65], [166]. The behaviour of 316L produced by L-PBF in AB state under cyclic loading has been shown to allow high levels of plastic deformation due to a micro-mechanism of twinning between dislocations [37], [97]. High cycle fatigue (HCF) and long crack propagation behaviour of L-PBF 316L have been studied by other researchers, showing that the ductile response of 316L leads to good fatigue performance in the AB state [92], [167] . In this study, L-PBF multi-material layered 316L/IN718 specimens are investigated in their AB state to study the effect of the microstructure on mechanical properties and fatigue performance and to understand the underlying controlling mechanisms of crack propagation in MMAM layered structures.

4.2 Results

4.2.1 Microstructural analysis

4.2.1.1 Etched Micrograph analysis

Figure 4-1 shows the L-PBF IN718/316L layered structure in the AB specimen microstructure viewed on the YZ plane. IN718 has solidified directionally forming columnar dendritic grains with a cellular sub-structure across multiple layers, while the cellular sub-structure observed in 316L was affected by the meltpool shape. These would abruptly change in growth direction from one melt track to the next (Figure 4-2 a) [168]. Sub-cells grow from the external boundary of the melt pool towards the centre, aligning with the heat flux direction [169]. Sub-cells are observed within the range of 0.5 to 1 µm in diameter for both 316L and IN718, which is consistent with values from the literature for similar material [65].

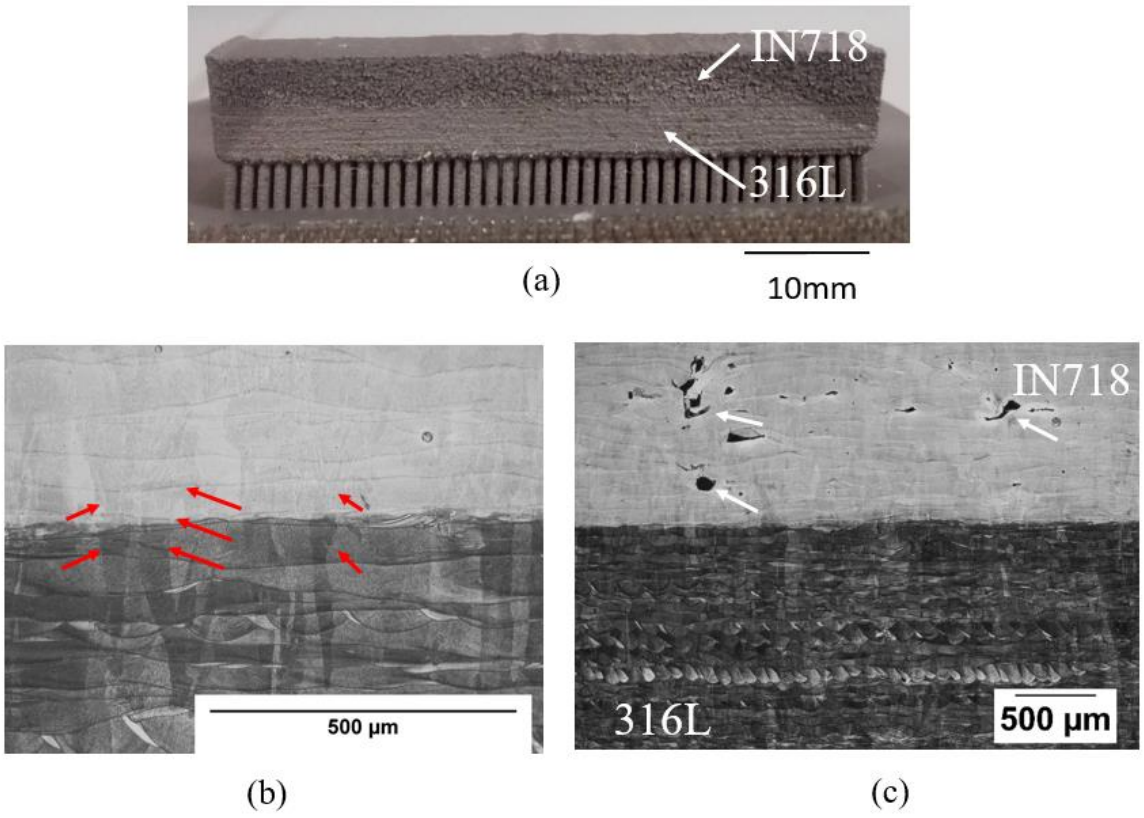

Figure 4-1: a) Image of bend bar specimen building orientation on base plate, b) Polished and etched cross section of the interface, with red arrows pointing at co-axial cellular formation encompassing multiple layers at the interface, c) lack of fusion pores (indicated by white arrows) are seen in IN718 on the cross section of the bi-layer specimen.

The AB microstructure reveals the presence of processing defects: some lack of fusion pores were observed in the IN718 layer (indicated by white arrows in Figure 4-1 c), while small cracks due to liquation cracking are observed at the dissimilar materials interface (indicated by red arrows in Figure 4-2 b). Liquation cracking can be found in rapidly solidified alloys with high alloying contents, which widen the solidification temperature range. Liquation cracking occurs in the remaining partially melted zones, surrounding the primary solidified grains and usually forming cracks along grains or sub-grain boundaries [154], [170].

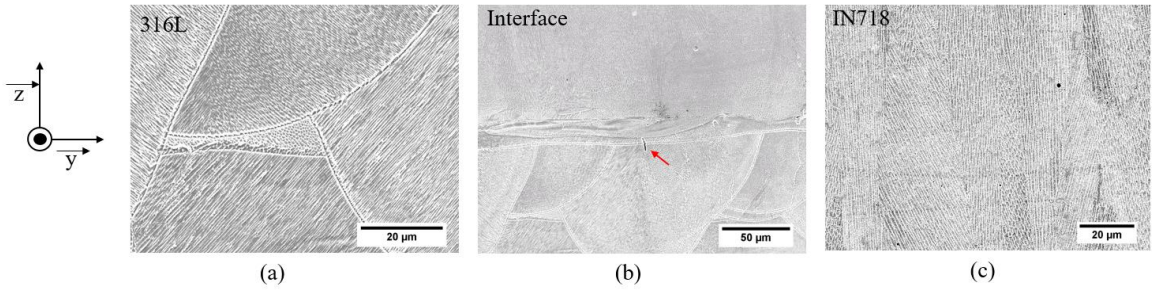

Figure 4-2: SEM view of polished and etched specimen, a) 316L layer, b) at the interface, with red arrow pointing to small crack likely due to liquation, c) IN718 layer

4.2.1.2 Grain structure analysis by EBSD

Figure 4-3 shows a grain orientation map across the bi-material interface. The columnar texture in the 〈001〉 direction is visible in both materials, which is expected for a face centred cubic (FCC) crystal structure when the building orientation (following the z-axis) is aligned with a favourable grain growth for the crystal structure. Because both 316L and IN718 alloy matrices are FCC, some grains show coherent growth across the interface. No major defects were observed at the interface, except for the sporadic liquation cracking.

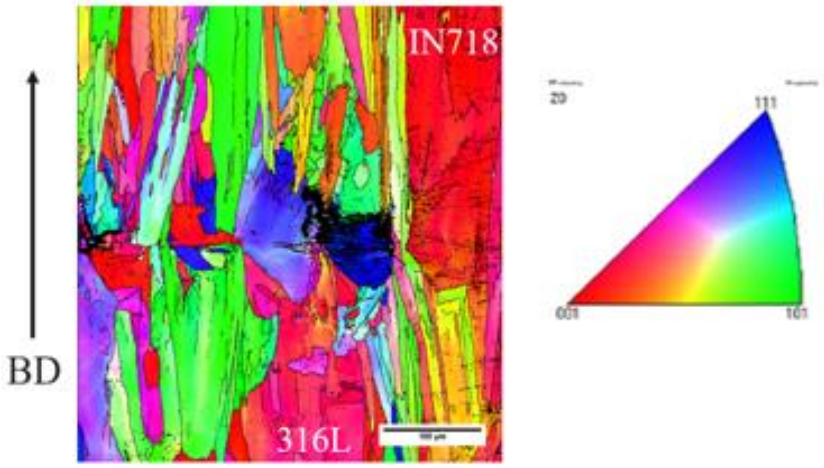

Figure 4-3: EBSD grain orientation map of the interface with IN718 at the top and 316L at the bottom

Figure 4-4 shows the percentage distribution of grains by size range and the associated aspect ratio in both IN718 and 316L layers. It shows that smaller grains (≤5µm) tend to be rounder than large grains (30–40 µm diameter). This is due to the directional solidification of larger columnar grains oriented in the thermal gradient direction (following the build orientation along the z-axis direction). Over 50% of the total grains are below 5 µm diameter for both alloys, and the smaller grains are formed around the columnar grains due to partial remelting and adjacent meltpool overlap. It can also be observed that IN718 grains have a high aspect ratio that correspond to the SEM observation of the strong columnar texture in the 〈001〉 building orientation, while the 316L grains possess a rounder shape due to the meltpool solidification they appear to have experienced.

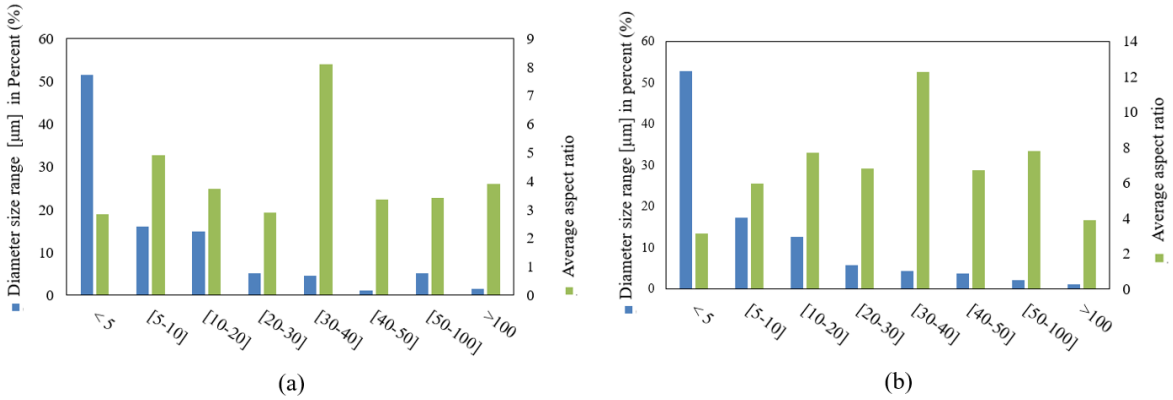

Figure 4-4: Grains size range percentage and aspect ratio: a) within the 316L layer, b) within IN718 layer

4.2.1.3 X-ray Diffraction results

Figure 4-5 shows XRD curves for both 316L and IN718 material in the as-built condition. The X axis represents the angle of reflection of X-rays and the Y axis is the intensity of reflection in arbitrary units. In the present case both 316L peaks and IN718 peaks are seen mainly for the austenitic matrix, which was to be expected due to the AB condition of both alloys (no heat treatment has been done in order for IN718 to precipitate any strengthening secondary phases). All the curves plotted in the figure show peaks for the same 2θ angles which are mainly caused by the matrix γ phase: Fe for 316L and Ni for IN718, this generally happens because secondary phases, present in IN718, reflect X-rays at similar Bragg angles as the primary γ phase due to similar crystal patterns [171]. Additionally, due to the presence of residual stresses inside the material, diffraction of the γ phase can occur within a few tenths of a degree of the 'ideal' angle leading to wider peaks.

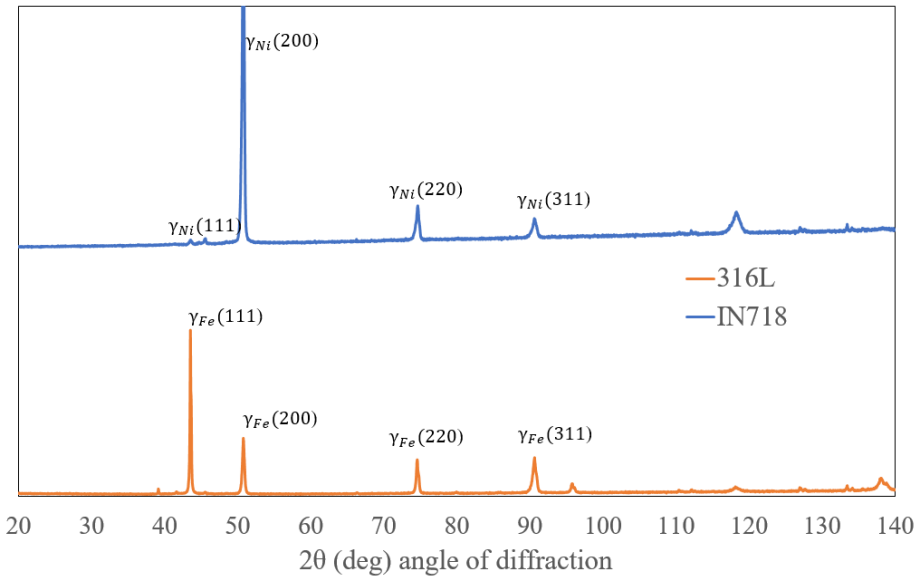

Figure 4-5: X-ray diffraction of 316L and In718 in AB condition

4.2.2 Mechanical properties

4.2.2.1 Micro-hardness

Vickers micro hardness was measured on the cross section of the bilayer specimen, 10 measurements were made at each depth and the standard deviations are plotted along with the average value for each point as shown in Figure 4-6. It can be seen that an average of 237 Hv and 290 Hv is obtained for the 316L and the IN718 layers respectively, both values are consistent with studies on similar materials processed by L-PBF in AB state [22], [129].

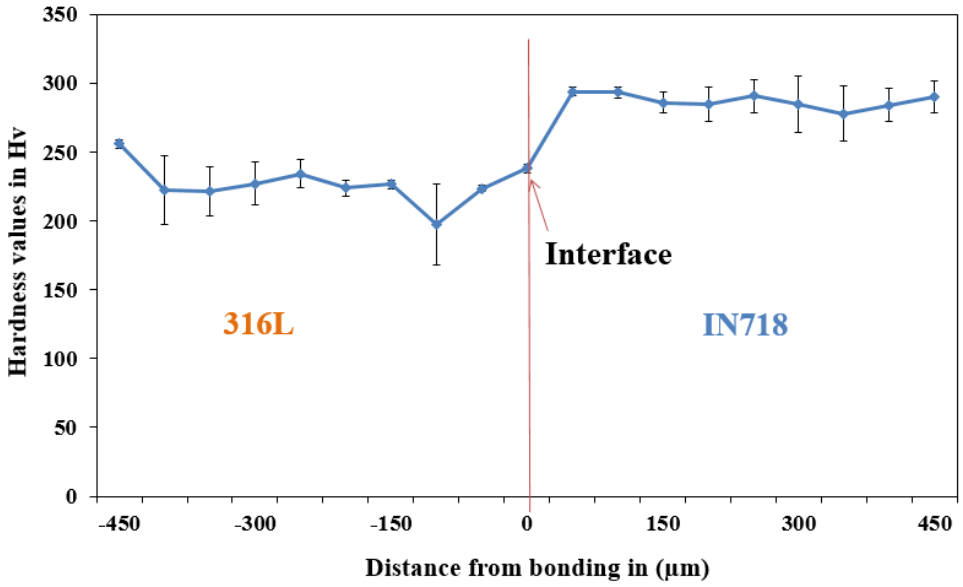

Figure 4-6: Vickers micro-hardness measured on the cross section of the specimen

4.2.2.2 Nano-Indentation

Nano indentation was used to perform a more detailed analysis of the nano-hardness and reduced modulus variation across the interface. A map was created by averaging all the data points, and the results are displayed in Figure 4-7. The hardness transition at the interface shows an average value of 250Hv by micro-hardness measurement, while nano-indentation mapping shows a clear transition between each layer without showing any local loss of properties. The reduced modulus presents a more continuous transition from IN718 to 316L because the elastic properties of both materials is more dependent on the close-packed nature of the FCC crystal structure and similar bonding strengths for the transition metal alloys. The overall reduced modulus is 156 ± 58 GPa for 316L and 164 ± 15 GPa for IN718, these are somewhat less in comparison to the values typically reported in the literature, ie ~ 200GPa [172].

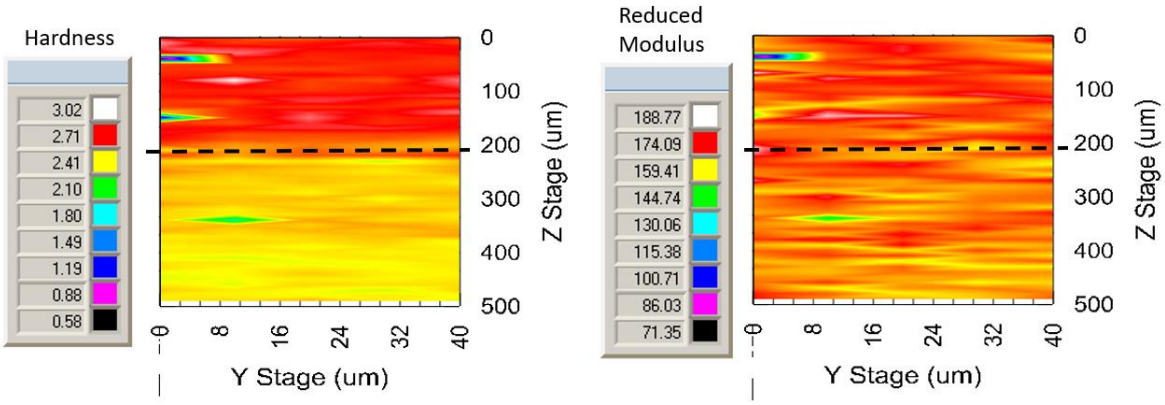

Figure 4-7: Scaled maps of nano indentation measurements at the interface between 316L (lower layer) and IN718 (upper layer) with interface marked at the dotted line, a) Nano-hardness, b) Reduced modulus

4.2.2.3 Tensile tests

The tensile properties of each alloy were tested separately by static tension testing, each tests were repeated 3 times (i.e. 3 specimen were used per test and the values display in the Figure 4-8 are the average result and the standard deviation) and the results are displayed in Table 4-1.

Table 4-1: Mechanical properties of each material from tensile tests, microhardness and nanohardness* tests

	Reduced modulus (GPa)*	Yield strength (MPa)	Ultimate tensile strength (MPa)	Hardness (GPa)*	Strain to failure (%)
316L	156 ± 2	588 ± 2	709 ± 3	2.1 ±0.04	33.9±2.4
IN718	165 ± 2	677 ± 11	784 ± 55	2.7 ±0.3	6.4±2.7

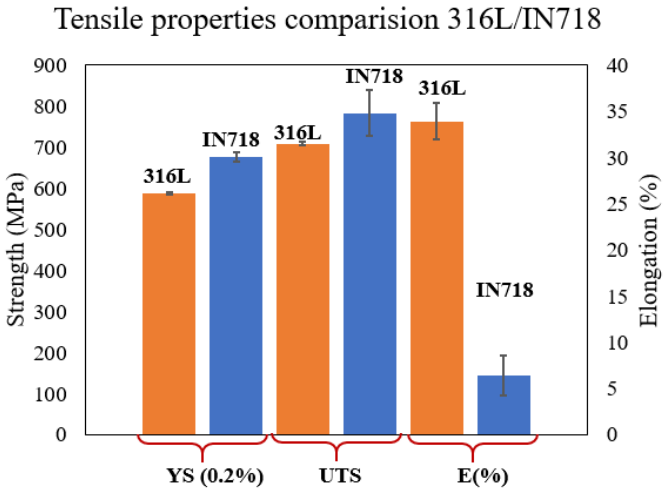

Figure 4-8: Comparison of 316L and IN718 static tensile properties

As shown in Table 4-1, the elastic properties of both alloys are more or less similar, which was expected considering that both alloys share the same FCC crystal structure. However, the yield strength (YS) and the ultimate tensile strength (UTS) show some difference. Compared to wrought 316L, the properties of L-PBF 316L are higher. YS of 300 MPa and UTS of 590 MPa are typical in wrought 316L alloy [151]. Whereas AB-IN718 does not provide the static tensile properties seen in conventionally manufactured (cast and wrought) IN718, to obtain this usually requires further thermal post treatment, at room temperature a YS of 1030 MPa and UTS of 1240 MPa are typically seen in IN718 alloy [117], [152]. Additionally, the overall ductility achieved in both alloys shows a significant difference, as displayed in the engineering stress–strain curves in Figure 4-9.

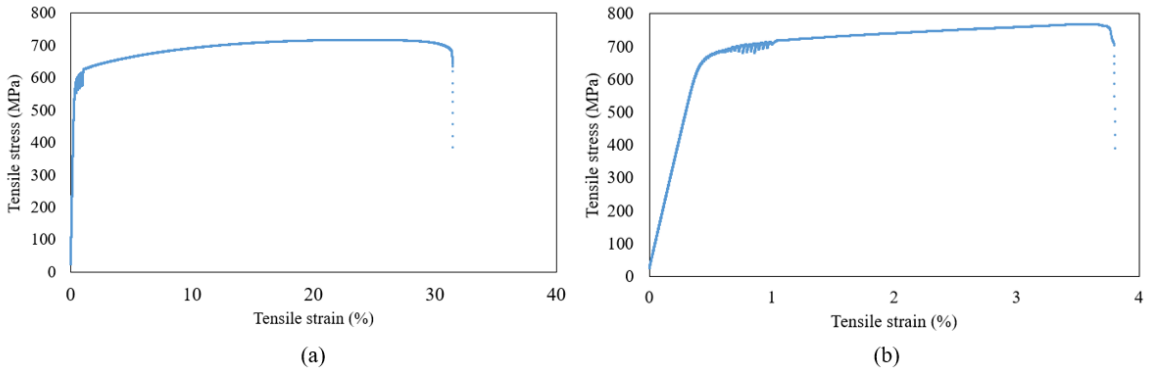

Figure 4-9: Stress strain curves obtained under displacement control loading for a) 316L material and b) IN718

The % elongation of the 316L alloy fabricated by L-PBF in AB condition is remarkable, and this mechanical response has been reported extensively elsewhere in the scientific literature [166]. However, the elongation of IN718 seems to be lower than the values found in the literature that is typically in the range of 11–33% elongation [114]. Under severe plastic deformation when the necking of the specimen takes place, the triaxial stress state activates more shearing and allows twinning induced plasticity to occur within the crystal structure, causing the remarkable elongation and ductility of L-PBF 316L in the AB condition [37], [66], [166]. The plastic response under deformation is relevant in contributing to the fatigue crack propagation response in multi-layer specimens.

4.2.3 Fatigue tests

4.2.3.1 Long crack test in bi-layer specimen

Long crack fatigue propagation tests were performed in order to assess the crack propagation response of layered 316L/IN718 MMAM specimens. The crack growth configuration presented here is named the Crack Arrester (CA) configuration as the direction of the crack propagation is growing orthogonally through layers, in opposition to a Crack Divider (CD) configuration where a crack propagates through multiple layers at once [172].

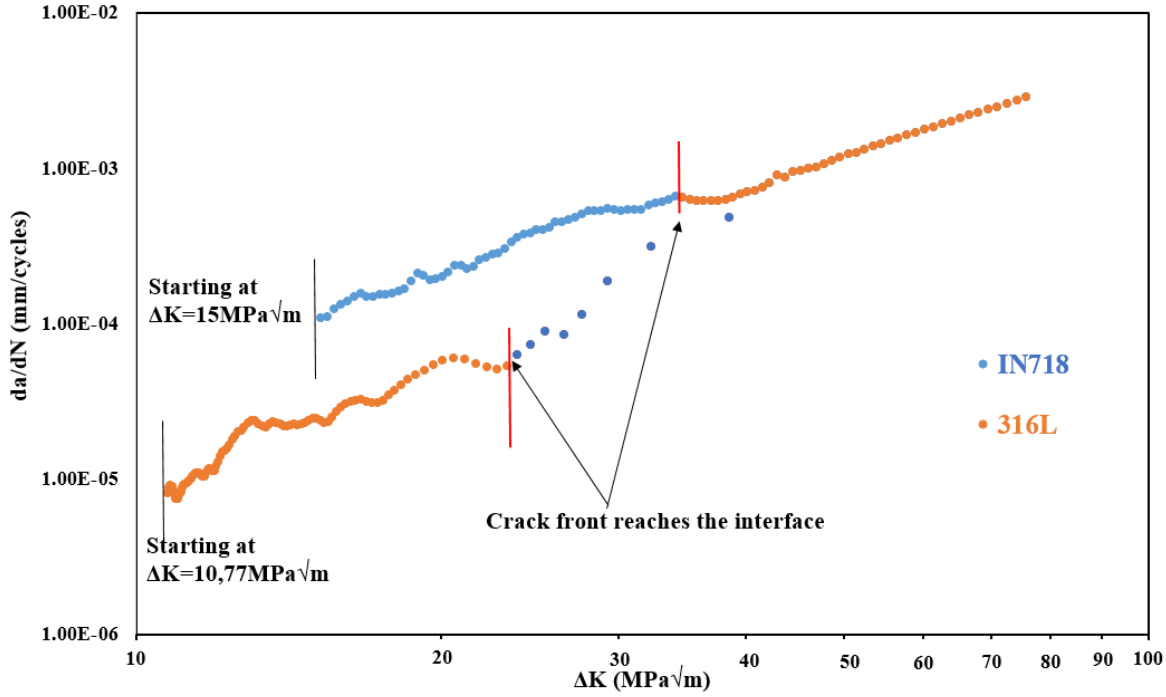

Figure 4-10: Crack growth rate (da/dN) versus the stress intensity factor range ΔK, propagation through bilayer specimen

The crack growth rate is a function of the local crack tip stress intensity factor range ΔK, and is displayed in Figure 4-10 for the two fatigue tests performed on the bi-layered specimens. For the first test specimen with the initiating notch located within the 316L layer, the crack propagates within the 316L layer (plotted in orange), and then crosses the interface and further grows toward the IN718 layer (plotted in blue), thus transitioning from soft-to-hard layer. For the second test specimen with a notch in the IN718 layer, the crack firstly initiates within the IN718 layer and propagates through the interface in a transition from hard-to-soft layer. The second test specimen that started crack growth within the IN718 layer (top curve) displays a Paris law growth curve linearly fitted to log da/dN versus log ΔK data within the range of ΔK = 27 - 70$MPa\sqrt{m}$ that can be described by the following equation:

$$da/dN = 7 \times 10^{-7}.\Delta K^{1.9} \qquad (4\text{-}1)$$

This description seems consistent with the results published for similar crack growth data for IN718 fabricated by L-PBF in AB condition found by Kunz et al. which indicates a Paris law relationship of: $da/dN = 4.54 \times 10^{-8}.\ \Delta K^{2.3}$ for da/dN higher than $1 \times 10^{-6} mm/cycles$ [135]. It appears that the softer 316L layer has not further increased the crack growth rate noticeably, although that could simply be due to the fact that crack growth rates were very high anyway at this point in the test. When crack propagation gradually crosses a transition from a material with lower strength or stiffness (a softer layer, in this case 316L) towards a material with higher strength (a stronger layer in this case IN718), the gradient in mechanical properties induced by the dissimilar materials transition can

directly affect the crack tip driving force. Theoretically the shielding effect occurs when the stronger layer just ahead of the crack tip experiences less deformation (than the softer/more compliant layer) for the same applied load, it is commonly considered that the stronger layer "carries the load", and hence decreases the local driving force at the crack tip (embedded within the softer layer). Conversely when the transition occurs from a harder material towards a softer one the crack tip stress field undergoes an anti-shielding effect (more deformation occurs ahead of the crack tip), hence causing an acceleration in crack propagation rate. The bigger the difference between the materials properties, the more visible the effect of shielding and/or anti-shielding should be [47]. However, multiple phenomenon can simultaneously affect the crack propagation rate and it was observed that in the first crack growth test the crack that initiated from the 316L layer displayed a more scattered early growth rate behaviour and has reached a high enough ΔK that rapid failure ensued shortly after the crack crossed the interface. The increased crack growth scatter and local decreases in growth rate within the 316L layer are linked to the solidification of the microstructure in 316L that is more affected by the meltpool shape. The presence of grain boundaries and high angle boundaries surrounding the meltpools, are expected to form locally weaker zones with defects and enhanced localised deformation, hence causing preferential tortuous crack propagation. Such crack growth rate scatter was not observed in the 316L layer at higher values of stress intensity factor when the crack growth was initiated within the IN718 layer.

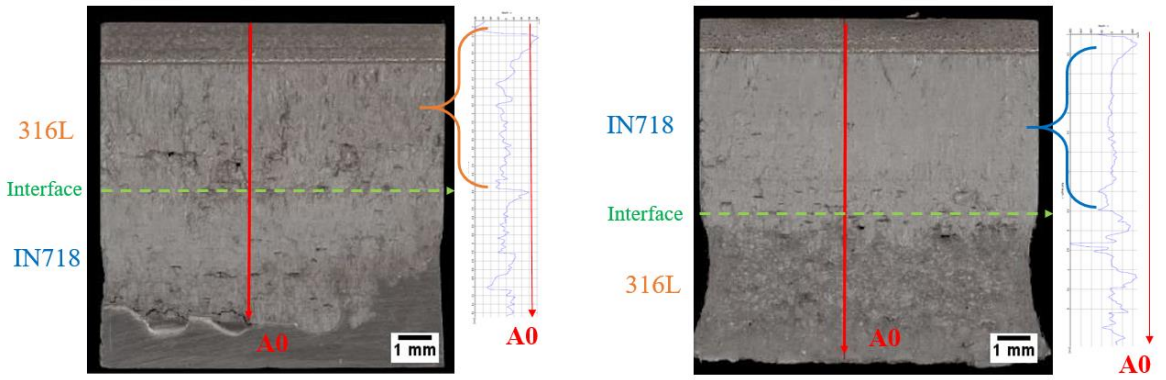

Figure 4-11: Alicona view of each fracture surface and roughness profile (named A0 on the right side of each surface) along with a downward pointing red arrow to display the crack propagation direction, a) crack initiated from 316L layer, b) crack initiated from IN718 layer

The overall difference in roughness of the fracture surfaces are compared in Figure 4-11. The crack propagation under increasing ΔK conditions through the bi-layer specimen has showed that no significant effect of the dissimilar material interface such as shielding and anti-shielding was observable. However, at lower stress intensity factor values it was considered that the variation in grain structure and orientation may have a great impact on crack tortuosity and hence on

propagation rate. This is further proven in the fractography analysis in section 4.2.4). It was observed that within the IN718 material the large elongated columnar grain structure, where the longest axis was parallel to the direction of the crack advance, causes an apparently continuous growth rate. While the grain structure of the 316L material that was affected by the meltpool shape has caused more local crack slowing and tortuosity in the crack propagation at lower stress intensity levels as can be seen in the comparison of the overall fracture surfaces in Figure 4-11. The effect of residual stresses on the crack propagation were considered to be minimal as the bending SENB specimens were cut from the supports from the building plate and polished down to 1 µm on each face prior to testing. When the part is removed from the base plate, the stress state in the part is changed; due to the relaxation, due to a combined effect of the relaxation stress corresponding to the shrinkage of the part, and of the relaxation stress corresponding to the bending deformation, as it was quantified by Kurth et al. in their study up to -300MPa for a part built of 50 layers up directly on a base plate in 316L [173]. Additionally, both 316L and IN718 FCC structure have shown good coherence between grains at the interface (see Figure 4-3) and have similar coefficient of thermal expansion hence limiting the amount of residual strain during solidification of the interface [174].

4.2.3.2 Constant delta K test

In order to study this effect more fully, a crack propagation test was performed at constant ΔK through a bi-layer SENB specimen. In this test, the crack was initiated from the IN718 layer, and subjected to manual modification of the applied stress in order to keep the stress intensity at the crack tip constant (within ±10%) throughout the crack extension. The initial notch depth was a = 1.3 mm, then pre-cracking was performed by load shedding. The load was stepped down to a crack tip stress intensity factor of ΔK_{app} = 10.6 MPa√m, then was kept constant (within ±10%) for the rest of the experiment by adjusting the load iteratively, following the crack advance monitored by DCPD device. The starting crack depth including the pre-crack was a_i = 1.99 mm, and the test was conducted at R = 0.1 and a frequency of 10 Hz. The crack growth rate (da/dN) versus the crack depth is displayed in Figure 4-12.

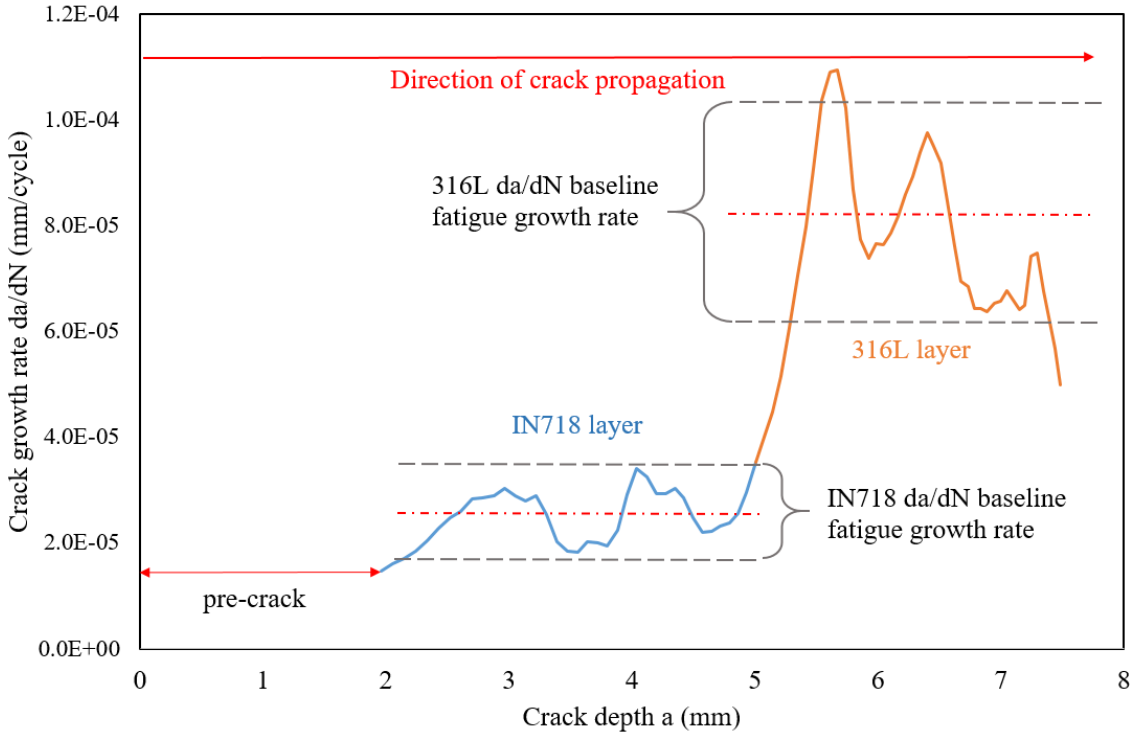

Figure 4-12: Crack growth rate versus crack tip depth, at ΔK=10.6MPa√m ±10%

Figure 4-12 shows that the crack growth rate is about $2.45\times 10^{-5} \pm 4.9\times 10^{-6}$ mm/cycle within the IN718 layer then increased to $7.53\times 10^{-5} \pm 1.6\times 10^{-5}$ mm/cycle within the 316L layer. An increase by a factor of three was noticed immediately after the interface transition, around 5 to 5.5 mm depth. A clear anti-shielding effect of the transition from harder IN718 into the softer 316L layer is visible here, it should be noted that no interface delamination was observed in the post-mortem fractography. In order to incrementally extend the crack, the deformation and stresses at the crack tip need to overcome the local potential energy within a certain radius representative of the plastic zone size ahead of the crack tip. Hence the definition of the necessary crack driving force for an incremental extension of the step size of the same radius. A given load will determine the radius of the pseudo-plastic zone ahead of the crack tip, for a given specimen geometry and material yield strength [31]. However, during the crack propagation through dissimilar material the yield stress follows a gradient that will cause changes in the local stress field, hence in the necessary potential energy to overcome for crack propagation. Local variation in the yield stress directly affects the near crack tip driving force. When the yield stress increases (in a transition gradient from soft to hard) the crack tip driving force is decreased, hence causing a crack propagation deceleration also known as a shielding effect [47]. However, it is important to mention that due to the nature of the microstructure made by L-PBF (meltpool shape, cellular sub-structure…) and the potential presence of defects around the interface (cracks potentially due to liquation, or presence of secondary phases such as Laves…) the crack tip driving force can also be affected by other types of factors simultaneously affecting the fluctuations in propagation rate.

4.2.3.3 Long crack test in 4-layer specimen

Another fatigue crack growth experiment was conducted on a 4-layer specimen in AB condition under constant load range (increasing ΔK conditions). The crack propagation rates with increasing ΔK through the thickness of SENB specimen was recorded by DCPD again. Figure 4-13 shows that the notch is located in the IN718 top layer, a first pre-crack was obtained by load shedding until a depth of a = 2.16 mm and a starting ΔK of 12.3 MPa√m. The results of the crack propagation test through the multi-layer specimen is displayed in Figure 4-13. The crack was initiated in the IN718 layer, then propagated through the first interface IN718/316L (hard to soft) transition indicated by the first red line on graph. After that, the crack propagated through the 316L layer before reaching the second interface 316L/IN718 (from soft to hard), indicated by a red line on the graph. It can be seen that in the middle of the 316L layer, the crack propagation decreases and then reaches a plateau in growth rate, despite the increase in ΔK meaning that the crack is effectively slowed as it approaches the harder material and the crack tip experiences a positive yield stress gradient. Similarly, at lower range of values of ΔK (around 12 to 20 MPa√m) the crack propagation rate displays a considerable amount of scatter, due to a combination of the effect of grain misorientation in the 316L layer and of the shielding effect from the second interface transition with a decrease in driving force energy, usually linked to the plastic zone of material ahead of the crack tip being reduced, hence effectively decreasing the crack growth rate in the second half (lower part) of the 316L layer.

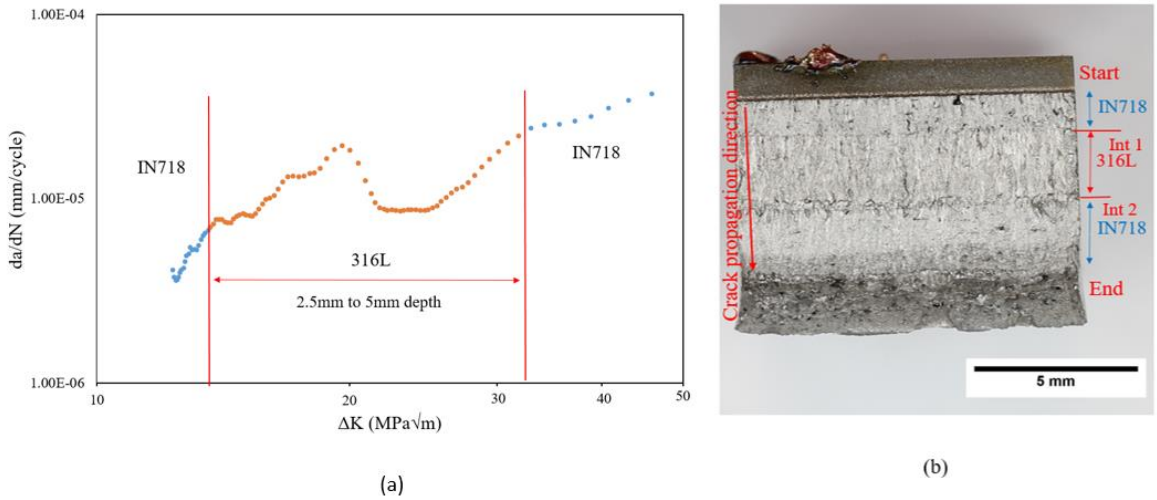

Figure 4-13: Crack propagation through multi-layer specimen, a) crack growth rate versus crack tip stress intensity factor, b) top view of final fracture surface.

Layered architectures of dissimilar materials have been investigated as a means to mitigate the crack propagation, by locally lowering the crack tip driving force using the shielding effect of a soft

to hard interface transition. Such structures have shown beneficial effects [46], which also depends on the thickness and location of the interlayer [50].

4.2.4 Fractography Analysis

4.2.4.1 Fractography analysis of Bi-layer specimen

Fractography analysis were performed on the crack surfaces of the specimen post mortem, and all the pictures show a downward propagation of the crack. Within the first bi-layer specimen the crack propagation was initiated from the notch located in the 316L (softer) layer is displayed in Figure 4-14. The fracture surface in the 316L layer left behind by the downward propagation of the crack front, displays rough features. The observations show that tortuous intergranular crack path propagation has occurred along the meltpool boundaries. The measurement of striations width was made by calculating the average value over 5 measurements made from the center of a striation to the center of the next. At the lower part of the 316L layer (just before the interface), striations of the size ~1.6 µm can be seen, which are characteristic of crack propagation rates in the Paris regime. The crack propagation rate had reached 1 µm/ cycle at an already advanced propagation stage around a stress intensity factor range of 22–25 MPa√m. Up to this point the tortuous intergranular crack path was more prevalent than Stage II crack growth evidenced by striation marks. This could then explain the scatter in the crack propagation rate at lower stress intensity factors in the early stages in the crack propagation. The importance of grain misorientation in crack propagation in AB L-PBF 316L material has also been observed by Riemer et al.[97] in their study on crack growth within 316L CT specimen. Melt pool boundaries and grain boundaries have lower bonding strength because they are preferential sites for segregation of defects, intermetallics or carbide formation. Hence, the melt pool boundaries and grain boundaries, which are also visible as high angle boundaries in the EBSD map, can be regarded as the weaker regions of the material [65].

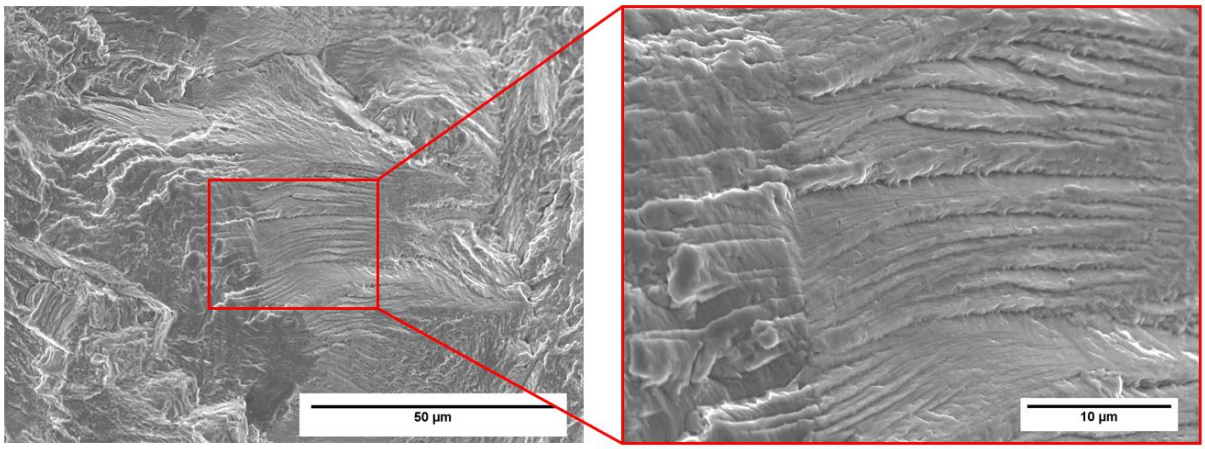

Figure 4-14: SEM image of 316L initiating layer, a) fracture surface around 23MPa√m, b) magnified view of striations.

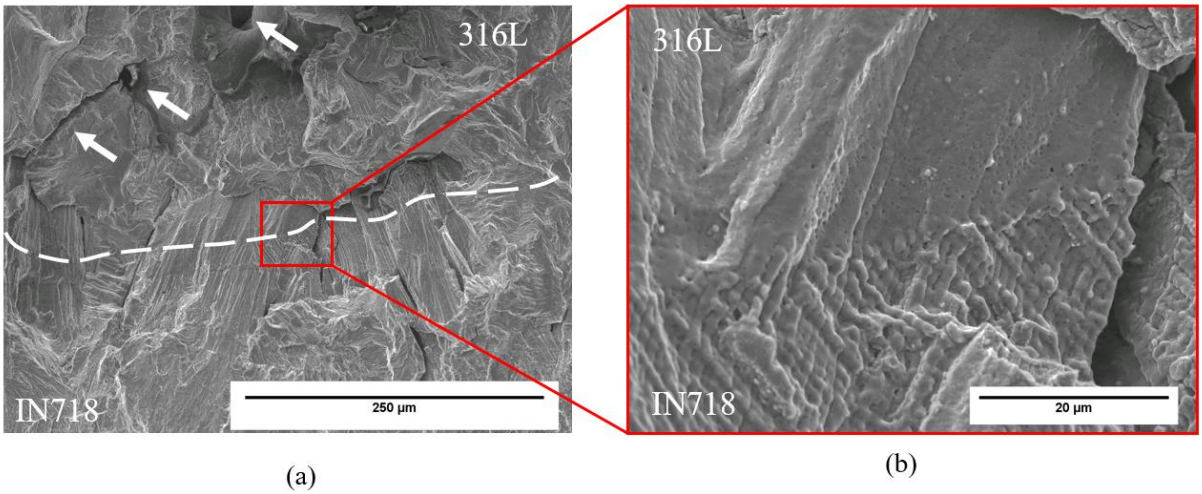

Figure 4-15: SEM fractography of the interface between the upper 316L layer and the IN718 bottom layer a) with white arrows pointing at secondary crack linking inner porosities and a white dotted line marking the interface and b) a magnified view of the interface area.

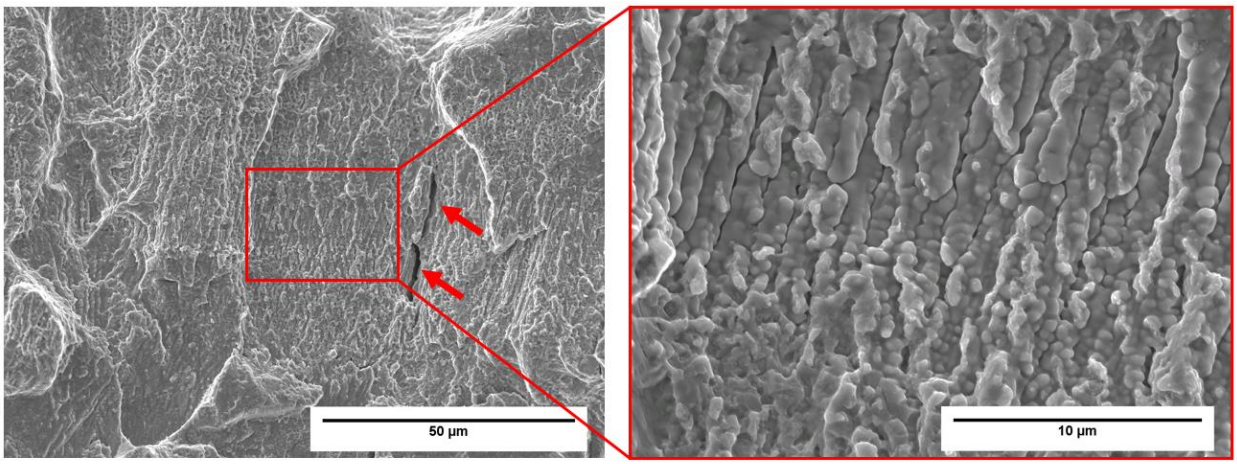

Figure 4-16: SEM fractography of crack propagation in the IN718 bottom layer, a) red arrows pointing to interdendritic cracks likely to be liquation cracks, and b) a magnified view.

Figure 4-15 a) shows small porosities (indicated by white arrows) and what resembles liquation cracking around the interface, supporting local secondary crack joining in the 316L. As display in Figure 4-15 a) secondary cracks were observed within the 316L layer around 1 mm before the interface transition but were not quantified as they were scarce and only related to already present defects (such as inner porosities). Figure 4-15 b) shows an enlarged view of the transition in the microstructure at the interface. It can be seen that IN718 and 316L SS do not display similar microstructural features, due to the difference in grain solidification. Dendritic solidification appears in the IN718 layer and the fracture surface shows clearly dendritic decohesive crack propagation in the IN718 layer as can be seen in Figure 4-16. Some cracks that resemble liquation cracking are visible in between the columnar dendrites (indicated by red arrows), which seem not to have affected the crack propagation process much. Alicona imaging has been used to quantify the roughness difference of the fracture surface of each specimen and the results are displayed in Figure 4-11. It can be seen that 316L as the upper layer (shown in Figure 4-11(a)) displays a rougher profile than IN718 as the upper layer (shown in Figure 4-11(b)) within equivalent stress intensity factor ranges (ΔK was typically 12–20 MPa$\sqrt{m}$ within the upper layer). In the specimen where the crack started from the IN718 layer, a very flat and smooth surface was observed, mainly transgranular with no specific features. This is consistent with the obvious columnar dendrite microstructure of IN718 shown in Figure 4-16 and the very smooth crack growth rate displayed in Figure 4-10. Because of the directional solidification of columnar dendrites and the associated crack path, the crack front has not deviated and propagation behaviour was not shielded by crack path tortuosity [97]. This fractography analysis reveals the impact of the grain structure on the crack propagation, and how the lower alignment of the 316L grains has impacted the crack tortuosity, while the elongated and favourably aligned columnar grains of the IN718 layer tend to have

facilitated the crack propagation path through the microstructure. Therefore, the impact of the dissimilar plastic properties transitioning at the interface, was less apparent than the impact of the as-built grain structure. It can be argued that in the AB state the grain solidification and orientation has more effect on the crack propagation than the intrinsic mechanical properties difference between the dissimilar alloys IN718 and 316L. This could be explained further because, in the AB state, the IN718 does not display its full strength difference, as no thermal treatment was applied in order to allow the growth of its main strengthening secondary phase (γ‘ and γ’’). In addition the ductile behaviour of 316L fabricated by L-PBF in its AB state provides a high degree of toughness, which explains how 316L in the AB state can compete quite favourably with AB IN718 under cyclic testing. Hence the main discriminating factor between both alloys in the as-built case would be the structure of grain solidification (equiaxed for 316L and columnar for IN718) and the orientation of such grain structures with respect to the stress direction and direction of crack advance.

4.2.4.2 Fractography analysis of 4-layer specimen

Fractography analysis were performed on the crack surfaces of the specimen post mortem, and all the pictures show a downward propagation of the crack. The fracture surface of the 4-layer specimen has shown clearer mechanisms of crack shielding and anti-shielding in 316L/IN718 AB specimen. Due to the cellular nature of the grain structure in material fabricated by L-PBF, the local elemental segregation causes a fine network of weaker areas within grains. In the first IN718 layer (shown in Figure 4-17), where the crack growth was initiated, this cellular sub structure was encompassed by the crack propagation. Very fine striation spacing of < 1 µm can be discriminated which is corresponding to the low initial crack propagation rate at a stress intensity factor range around < 15 MPa√m. The spherical features observed within the IN718 layer are likely to be secondary phases such as carbides and Laves phases, found in IN718 due to the non-equilibrium solidification where two consecutive eutectic transformations create a divorced eutectic reaction and isolated precipitates of carbides and Laves phases form within the liquid phase around the γ matrix dendrites which are coarsening [106], [109]. The fracture surface remained overall flat and featureless showing a transgranular propagation with fine fatigue striations observed. This transgranular fatigue fracture surface is consistent with long crack test observations carried out on IN718 in the AB condition in the near threshold regime (with ΔK around 15 MPa√m, which corresponds to what was observed in previous section) from the literature [135].

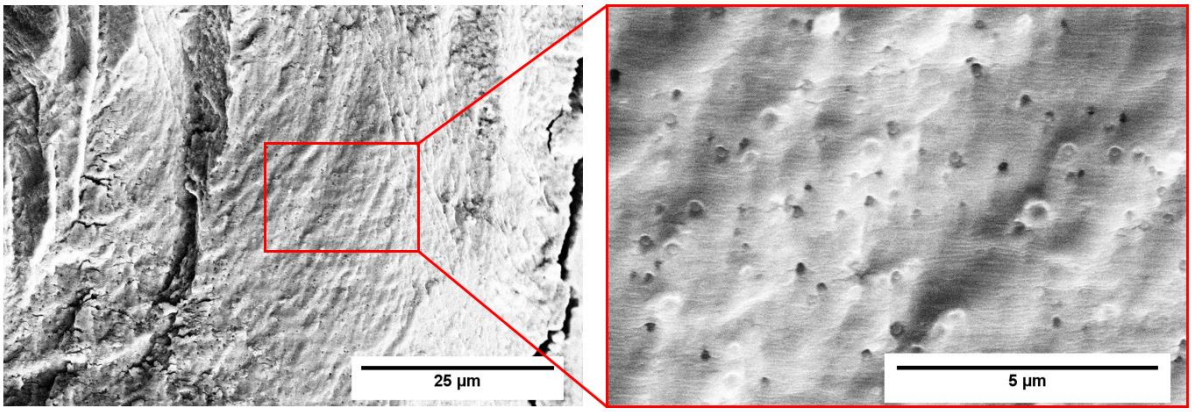

Figure 4-17: SEM image of IN718 initiating layer, a) fracture surface around 12 MPa√m, b) magnified view of striations and transgranular propagation.

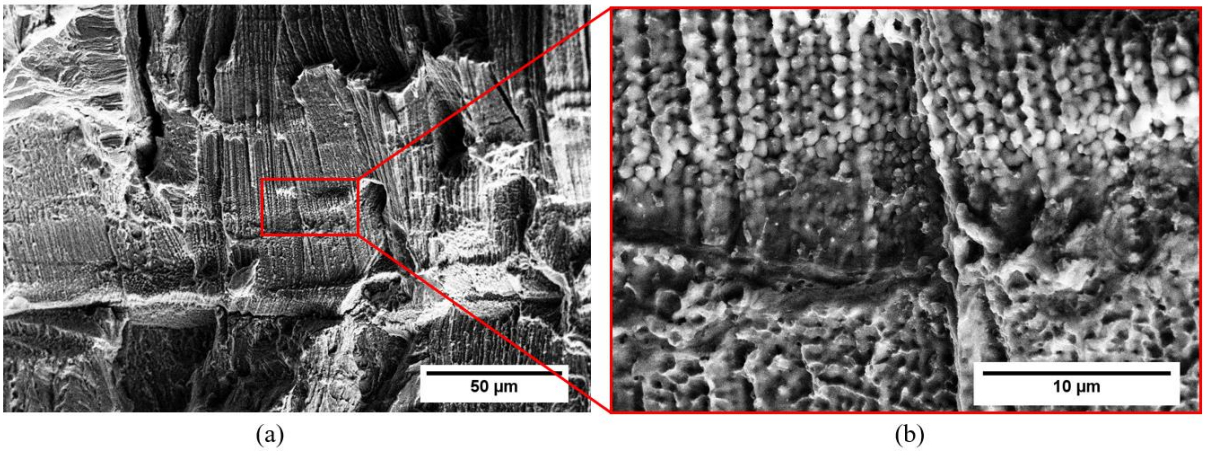

Figure 4-18: SEM image of a) the first interface, b) magnified view of dendritic decohesion.

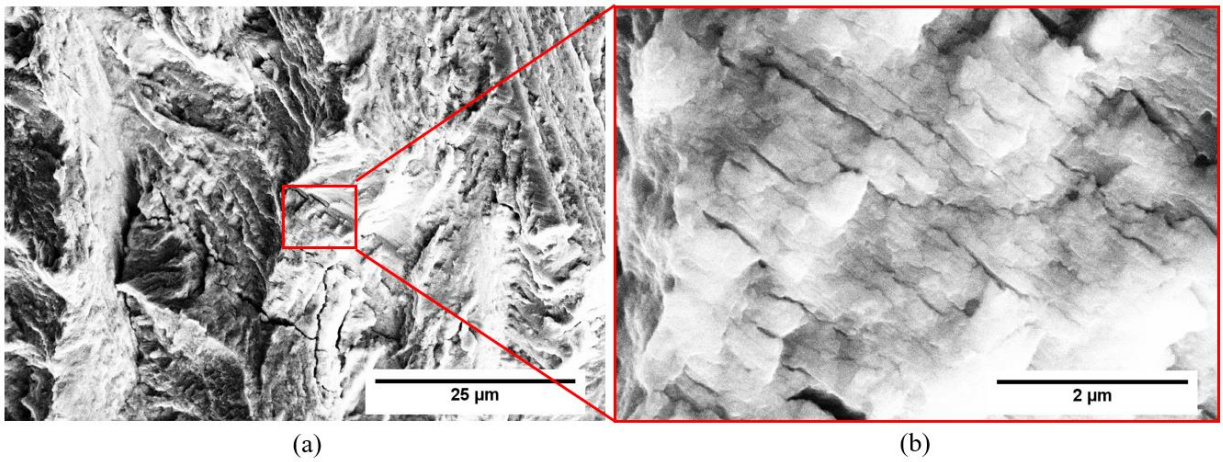

Figure 4-19: SEM image of 316L interlayer layer, a) fracture surface around 14 MPa√m, b) magnified view of secondary cracks.

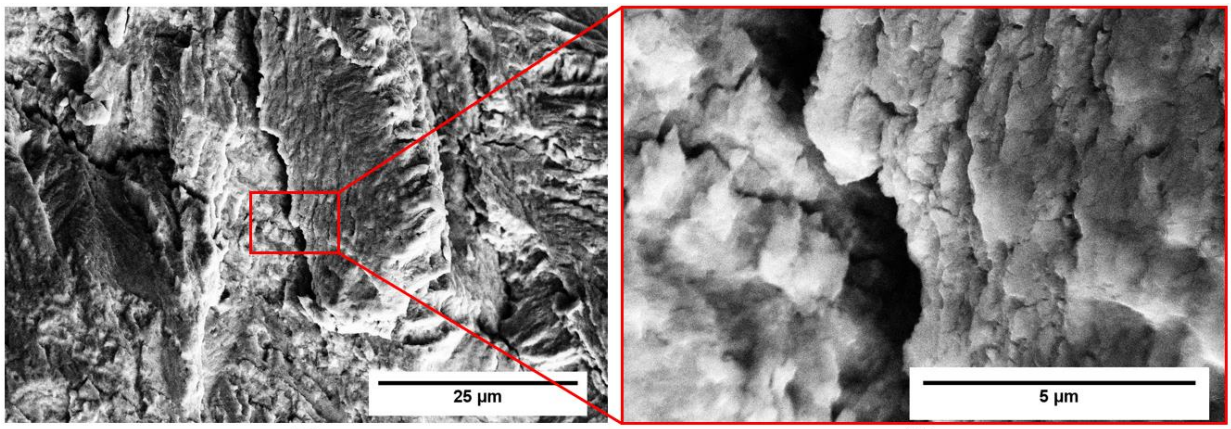

(a) (b)

Figure 4-20: SEM image of 316L interlayer layer, a) fracture surface around 26 MPa√m, b) magnified view of secondary cracks.

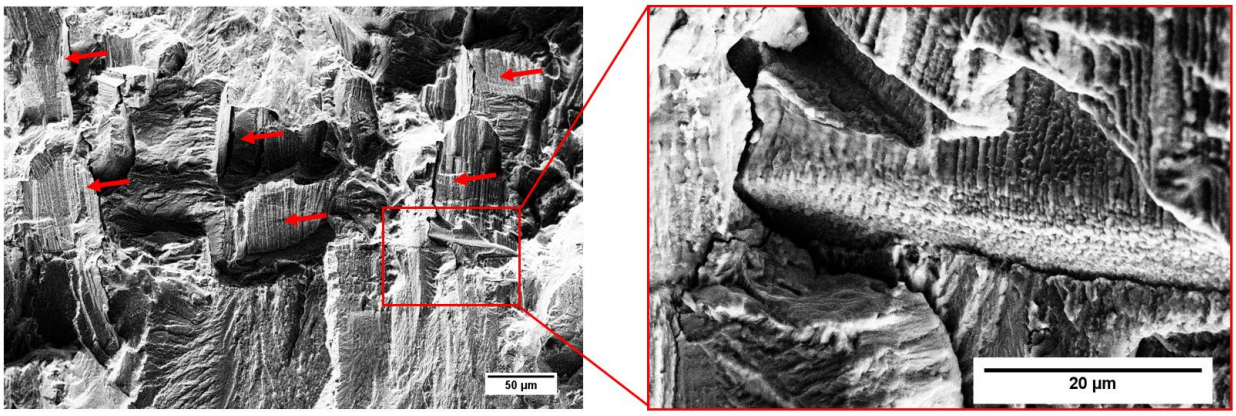

(a) (b)

Figure 4-21: SEM image of a) the second interface with red arrows pointing at cracks likely to be liquation cracks, b) magnified view of dendritic decohesion.

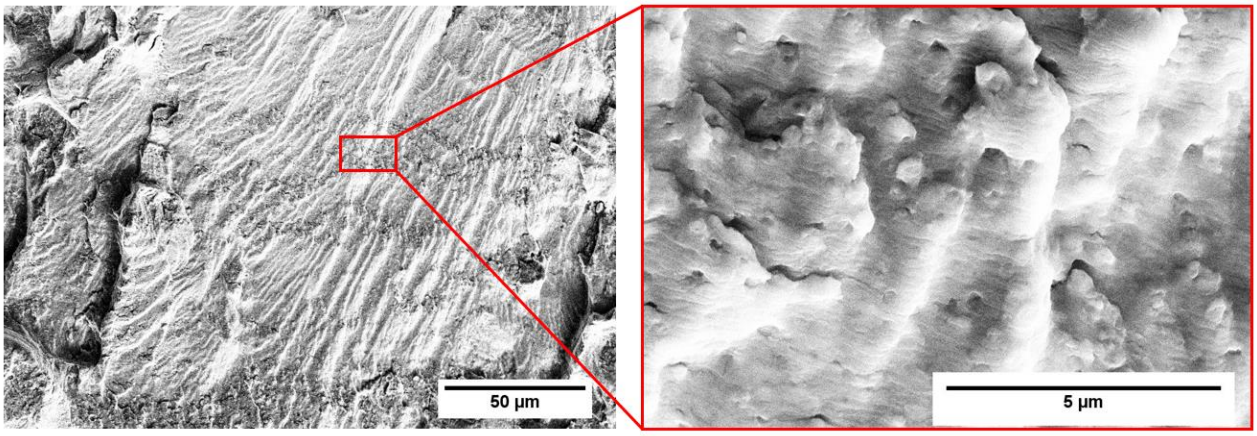

(a) (b)

Figure 4-22: SEM image of IN718 final layer, a) fracture surface around 45 MPa√m, b) magnified view of striations, secondary cracks and transgranular propagation.

In Figure 4-18 the first interface shows a clear interdendritic decohesion fatigue mechanism that is considered to be due to the stronger effect of partitioning around the interface. Within the dendrite the gradual solidification causes the core of the dendrite to first solidify as γ matrix, then an eutectic layer of γ/γ', and an outer layer of the last solidified elements segregate such as Nb which is one of the most sluggish to react with Nickel, or carbides. At the interface the elemental concentration of Iron is inferred from the local partitioning of Niobium, that has an even lower solubility in Iron than in Nickel, hence supporting a stronger partitioning effect in this area [175]. Figure 4-19 and Figure 4-20 are both SEM views of fatigue propagation in the 316L interlayer. Figure 4-19 shows the fracture surface for ΔK of 14 MPa√m and for a growth rate da/dN of 8.10^{-6} mm/cycle while Figure 4-20 shows the fracture surface for ΔK of 26 MPa√m, and a growth rate around 1.10^{-5} mm/cycle. While both areas of the fracture surface show an overall rougher macro-texture, the presence of secondary cracks around the cellular sub-structure was observed. The density and degree of widening of these secondary cracks was not quantified. But it was observed that the secondary cracks are more widely opened at the bottom of the layer, just before the second interface transition (which occurs at higher ΔK levels around 30 MPa√m). Due to the difference in yield strength and ductility levels between 316L and IN718 it is expected to see a shielding effect of the crack propagation around (just before) the second interface, but simultaneous effect of the grain-misorientation (surface roughness) and secondary cracks formation were also reported to affect the crack propagation rate. A stabilisation in the crack propagation rate was measured around 0.5 mm before the second interface, and the fractography revealed the presence of multiple secondary cracks that show significant opening throughout the 316L microstructure in this area. The release of energy via the local opening and widening of the secondary cracks surrounding the cellular sub-structure within the 316L layer is causing additional shielding effects in this area. In Figure 4-21 interdendritic decohesion was observed (indicated by red arrows in Figure 4-21 a) at the second interface, and a similar transgranular crack propagation was captured in the bottom IN718 layer, see Figure 4-22. Some secondary cracks appear as well in this layer due to the increase in stress intensity factor range, from 30 to 60 MPa√m that is represented by the final fast growth of the crack propagation, up to 5.10^{-5} mm/cycle on the graph shown in Figure 4-13, which in that area is approaching final monotonic failure of the specimen.

4.3 Summary

The present work shows the clear effect of the microstructure, and varying mechanical properties of 316L and IN718 alloys built by MMAM in their AB state, on the fatigue behaviour of layered specimens. The main results are summarised as follows:

• Solidification of 316L and IN718 was observed to create very different grain structures, a columnar grain growth was observed in IN718 and a rounder grain structure affected by the meltpool in the 316L region.

• The mechanical properties of 316L and IN718 in AB state show similar elastic response, while showing a more pronounced difference in plastic properties, most importantly in the % elongation under plastic deformation (and a more modest difference in yield strengths).

• The crack propagation rate was measured through bi-layer specimens under increasing ΔK conditions and it was observed that the grain structure and orientation most strongly affect the crack propagation rate, particularly at lower ΔK levels.

• A transgranular crack growth mode was observed through the IN718 layer compared to a mix of transgranular and intergranular more tortuous crack paths taken within the 316L layer

• A clear inter-dendritic decohesion was observed at the dissimilar material interface showing a stronger effect of elemental partitioning at the interface, weakening the interdendritic areas

• The crack propagation through the 4-layer specimen has showed a shielding effect of the crack propagation just before the transition from the soft 316L layer to the hard IN718 layer

• The shielding of the crack propagation process was linked to the apparent release of energy by the opening and widening of secondary cracks within the 316L interlayer.

Chapter 5 Effect of heat treatment on fatigue crack growth in IN718/316L multiple-materials layered structures fabricated by laser powder bed fusion

5.1 Introduction

Components under demanding service environments are often required to withstand cyclic loading, such as: pressure tubes for nuclear power station, turbo jet engines, aerospace or pharmaceutical industrial production lines, amongst many others [2] [3]. They normally operate under elevated temperature condition and/or highly corrosive environments, and the presence of defects in the material induced by the loading or environmental conditions, can lead to crack initiation, thus it is crucial to mitigate the subsequent crack propagation to avoid a catastrophic failure of the component [162]. Such complex technical requirements can now be met more efficiently by producing multi-material components that allow the tailoring of material to the properties required at a certain geometrical location within the design of a component [160]. Additionally, Multiple-Material Additive Manufacturing (MMAM) technology allows a reduction in the production time, cost, waste and assembly [11]. However, multi-materials components are fairly new in the field of additive manufacturing. The laser powder bed fusion (L-PBF) technology more specifically has been under scientific interest over the last 20 years [5][60]. The joining of dissimilar material structures has been investigated for both discrete [22] or graded architectures [16]. The structural integrity of such components produced by L-PBF technology is thus an important issue [145].

Inconel 718 (IN718) is a precipitation strengthened nickel-based alloy, used extensively due to its ability to maintain good strength under elevated temperature of service and its corrosion resistance [176]. Extensive scientific studies have been carried out on IN718 fabricated by L-PBF, mainly focusing on the mechanical response of the as-built (AB) microstructure [71][172], and on the effect of the standard heat treatment for IN718 on the mechanical response [124][123]. It was reported that IN718 produced by L-PBF tends to form a cellular sub-structure within columnar grains, due to the micro-segregation of heavier elements such as Nb and Mo at external areas surrounding sub-cells [110]. Meltpool boundaries, grain boundaries and external sub-cellular areas were reported to show a network of high density dislocations [109]. Due to this elemental micro-segregation in the as-built (AB) state, researchers have tried to apply the conventional heat treatment strategy, which is normally used for wrought or cast IN718, on additively manufactured specimens of IN718. However it has led to the formation of fine Laves phases and carbides agglomerated in those pre-segregated areas, surrounding the sub cellular structure and at grain boundaries [124]. Higher

solutioning temperatures have also been applied, in order to dissolve carbides in the matrix, but major grain coarsening was observed, fewer and coarser carbides were still present at grain boundaries [121]. Some studies then were carried out on the fatigue life of IN718 L-PBF [134], but very few were made on the process of fatigue crack propagation in L-PBF IN718 material [135].

316L stainless steel (SS) is an austenitic stainless steel with high strength and high corrosion resistance due to its high chromium content and low carbon content. Its austenitic FCC crystal structure provides good ductile behaviour, but some detrimental phases can form such as σ ($(Fe,Ni)_x(Cr,Mo)_y$ intermetallic [83]. The σ phase forms in the range of 550-900°C. However, it has relatively slow kinetics, while the $M_{23}C_6$ carbides can also be found in 316L SS forming between 600-1100°C [84]. 316L SS produced by L-PBF in its as-build (AB) state possesses high strength and good ductility [166][65]. High cycle fatigue and long crack behaviour of 316L produced by L-PBF have been studied, which shows that the ductile properties of 316L SS also supports its good fatigue performance in the AB state [92][86] .

The use of multiple-layers of materials having different elastic and plastic properties creates a gradient in tensile strength that directly affects the crack tip driving force, and therefore can play an important role in the mitigation of fatigue crack propagation behaviour [47]. Studies on the effect of a soft interlayer on crack propagation delays were conducted on aluminium and polymer systems, showing that depending on the soft interlayer thickness, the crack propagation was effectively shielded leading to crack arrest at the second interface (transition from soft to hard material) [164]. Recently the work of Melzer et al. started to investigate the mechanical behaviour of 316L and IN718 manufactured by direct energy deposition (DED), while most of their study was on the tensile response with respect to the build orientation of their specimen, two compact tension (CT) fatigue tests were also set up with a similar orientation in terms of the crack propagation direction and the interface transition (oriented as a crack arrester (CA) i.e. the dissimilar material interface being orthogonal to the crack propagation direction)[144].

In this study, heat treatment has been performed on 316L/IN718 multiple-materials layered specimens produced by L-PBF, in order to investigate the effect of the heat treatment on the microstructure, mechanical properties and fatigue performances of these structures.

5.2 Results

5.2.1 Microstructural analysis

5.2.1.1 Etched micrographs analysis

Figure 5-1 shows two micrographs obtained using backscattered electron imaging on a polished and etched specimen showing the interface region of a heat treated (HTed) bi-layer (IN718/316L) specimen compared with the interface of a specimen in the as-built condition. An inter-diffusion zone of ~140µm width was measured, in which some cracking that are likely to be ductility dip cracking was observed (indicated by the red arrow).

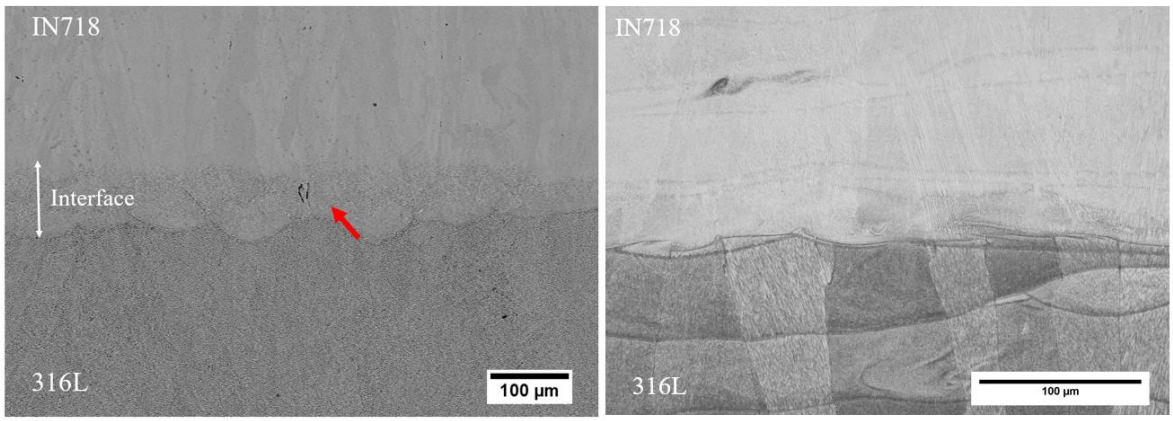

Figure 5-1: BSE micrograph of the interface in a) of heat treated (HTed) specimen with red arrow point to cracks likely to be DDC, and b) as-built (AB) specimen.

The HTed microstructure of the IN718/316L specimen (shown in Figure 5-2) reveals the difference in the microstructure at several locations. Figure 5-2 a) shows a view within the 316L region where the sub-cellular structure has almost been fully erased, in comparison with the AB cellular structure seen in Figure 5-1 b), although some secondary particles are visible (<1 µm diameter, see Figure 5-2 a). The microstructure within the IN718 layer (Figure 5-2 d) is showing a dissolution of the sub-cellular structure, fine homogeneous precipitation can be observed within the grains (very fine, <0.5 µm, see Figure 5-2 d), and coarser intermetallics are visible along meltpool boundaries (~1 µm diameter). A spherical gas entrapped pore is also visible in Figure 5-2 c). The magnified view in from Figure 5-2 b) shows an increase in the number and size of intermetallic phases within the inter-diffusion zone. These intermetallic white particles are expected to be Laves phases and were observed both within the local substructure in finer size (<1 µm dimeter) and in larger size on the inner surfaces of the DDC (~1 µm dimeter). However no needle-like precipitates were observed,

which suggests that the formation of δ phase (detrimental brittle phase) seems to have been successfully avoided, as a result of the choice made in the heat treatment strategy.

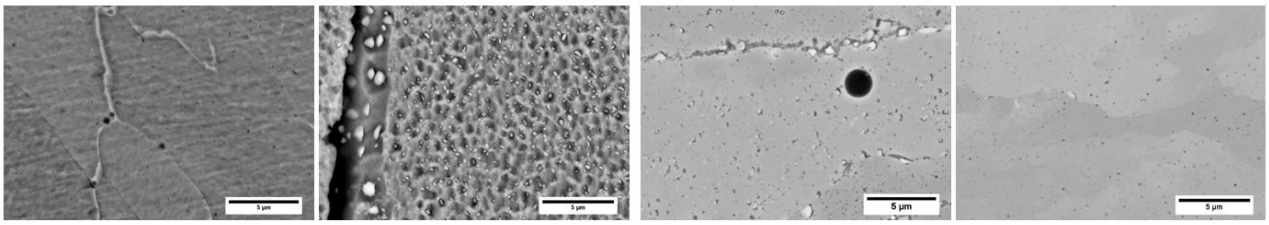

Figure 5-2: BSE imaging of the interface of Heat Treated (HTed) specimen; a) within 316L layer, b) within the inter-diffusion zone at the interface, c) on the outskirt of the interdiffusion zone, and c) within the IN718 layer.

5.2.1.2 EDX analysis of the microstructure

Figure 5-3 shows an EDX map of the magnified Figure 5-2 (c), which is a view of the outskirts of the interdiffusion zone on the IN718 layer side. It can be seen that iron, chromium and nickel elements are homogeneously distributed across the view forming the main γ matrix, but niobium and molybdenum are heavily segregated at the meltpool boundary forming secondary phases most likely to be Laves phase. Because both IN718 and 316L alloys have a low concentration in carbon, hence topologically close-packed (TCP) phases, such as Laves phases (hexagonal $(Fe, Ni, Cr)_2(Nb,Mo,Si)$ phases) is more likely to happen in areas where refractory elements (Nb and Mo) are heavily partitioned [143]. Aluminium and titanium seem to have segregated on the inner surface of the gas entrapped pore, most likely forming an oxide. Some fine particles are also visible, which are evenly distributed within the grain and seem to contain Niobium and Molybdenum that would be consistent with a fine distribution of γ' and γ''.

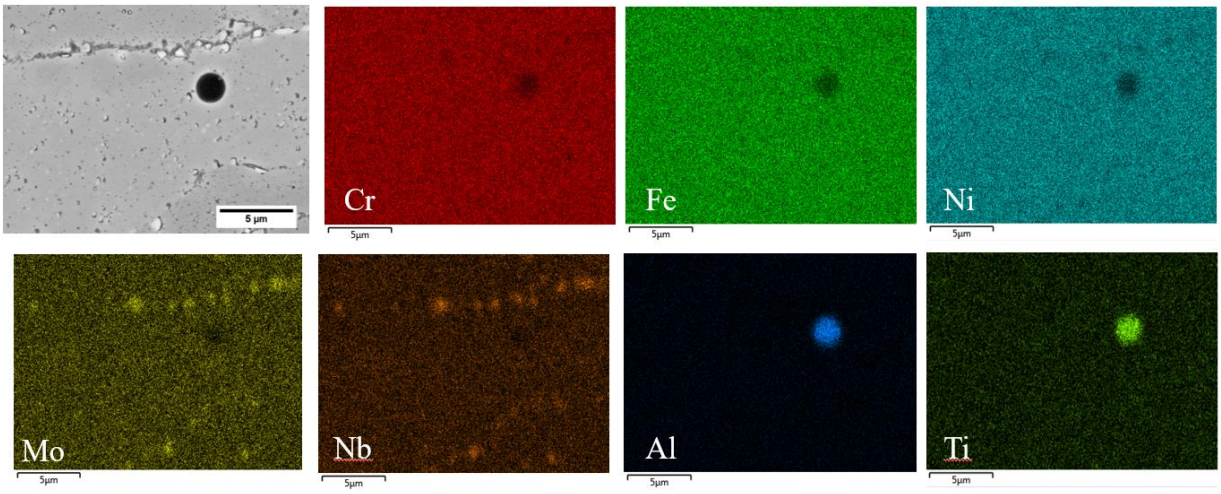

Figure 5-3: EDX map of the BSE image from Fig. 39 (c).

Figure 5-4 shows a comparison of the elemental concentration distribution across the interface region, between the specimen in AB state (Figure 5-4 a) and in HTed state (Figure 5-4 b) by EDS linescan analysis. The elemental interdiffusion zone is clearly apparent in the HTed specimen, where iron and nickel elements display a steady slope over a band of ~140µm width (this distance represents 4 to 5 layers of the specimen build). The Fe and Ni elemental concentration curve across the HTed specimen interface shows a gradual slope interrupted by a "dip" around the 600 µm mark (see Figure 5-4), which is characteristic of the local presence of an intermetallic phase formation. It is not uncommon for Ni-based alloys to form intermetallics as a part of their strengthening mechanism, however by using the average composition detected by an EDS line scan across an interface, this allows the determination of a zone of stability in elemental concentrations, that is different from each alloy's nominal composition [177].

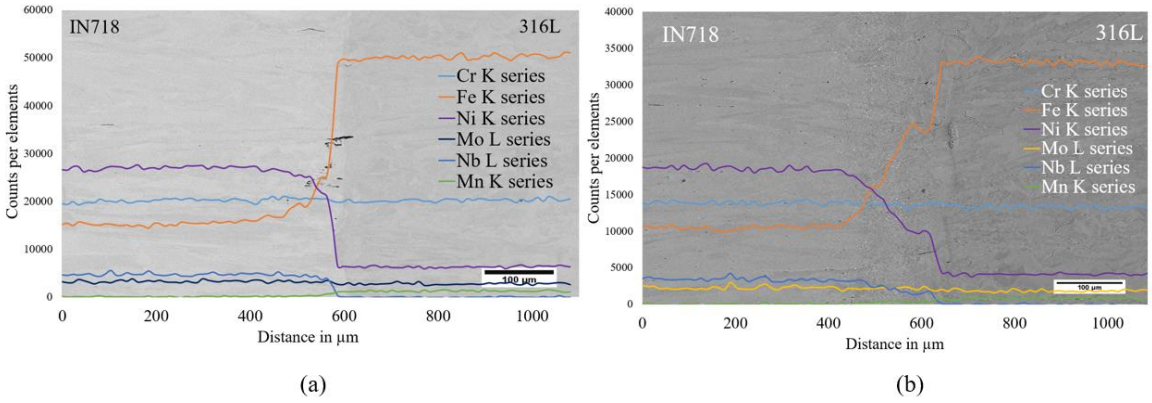

Figure 5-4: EDX linescan analysis of the interface region in a) AB specimen, b) HTed specimens.

5.2.1.3 BSE imaging of the interface region

The presence of Laves phases is further supported by the BSE view of this area displayed in Figure 5-5, where a large number of secondary phases can be observed throughout the microstructure, in finer precipitates within the sub-cellular grains structure and in coarser form at grain boundaries and within the ductility dip cracking (DDC) sites.

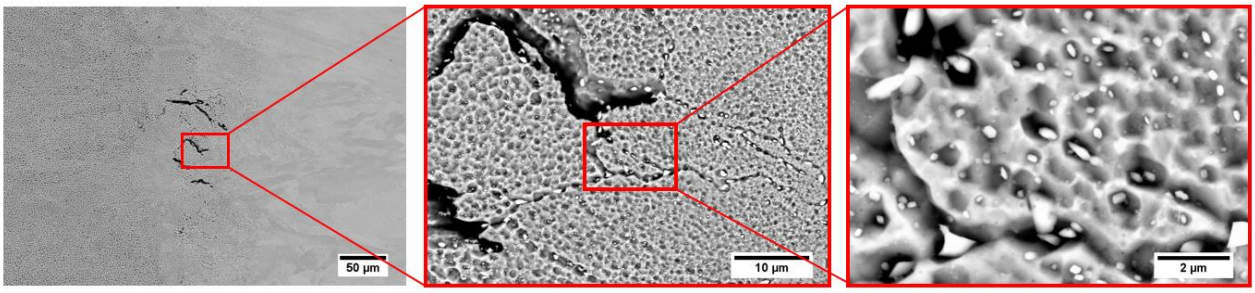

Figure 5-5: BSE of ductility dip cracking (DDC) and secondary phases formation in the interdiffusion zone at the interface of HTed specimen.

5.2.1.4 Grain structure analysis by EBSD

Modification of the grain structure was observed via EBSD and a comparison of the grain orientation map around the interface area is displayed in Figure 5-6. The comparison between the grain size distribution and the grain aspect ratio over the 316L and IN718 region is displayed in Figure 5-7. It can been seen from Figure 5-6 that after HT, the number of very small grains (<5 µm) decreases and the number of medium size grains (5 to 30 µm) increases. It can also be observed at the interface in the HTed specimen. Figure 5-7 b) the appearance of smaller grains at the interface. It is believed that the exposure to elevated temperatures during the annealing treatment (45 min at 1050°C), has led to some solid-state recrystallization and possible grain growth.

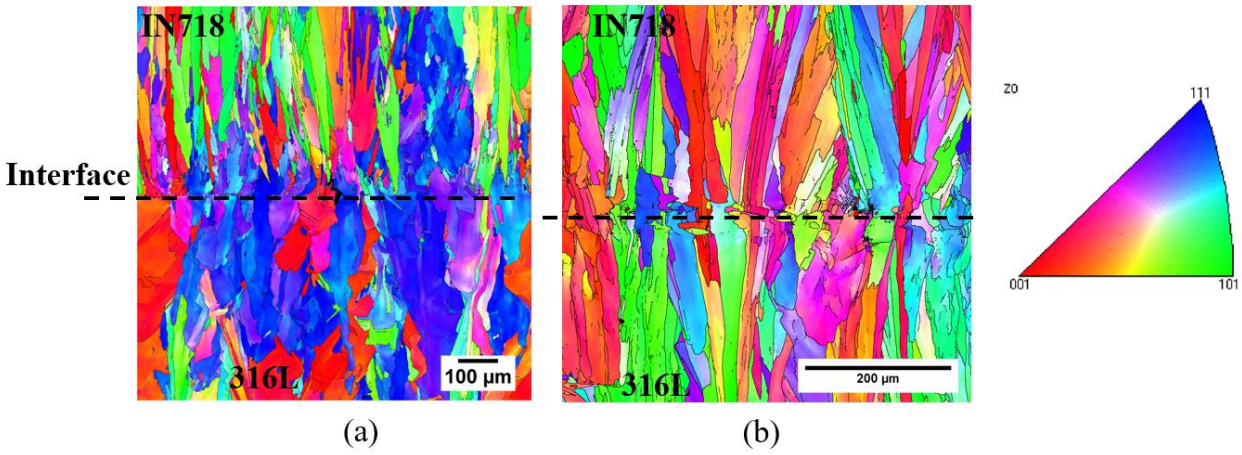

Figure 5-6: EBSD grain orientation map at the interface in a) AB and b) HTed specimens.

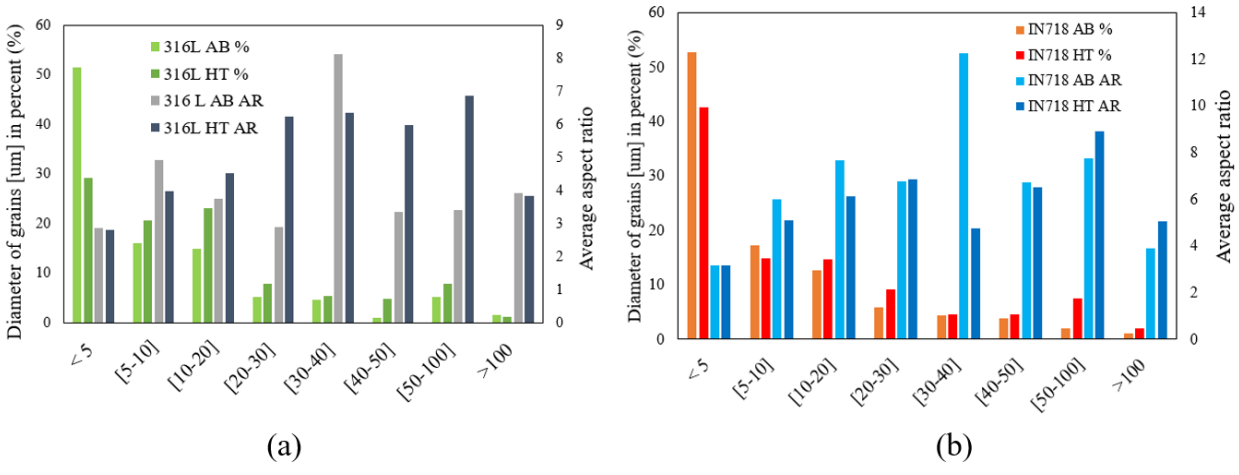

Figure 5-7: Grain size range distribution and aspect ratio of as-built (AB) and Heat treated (HT) state for a) 316L layer, b) IN718 layer.

The evolution in the grains size range and aspect ratio before and after heat treatment reveals a degree of grain boundary motion. The overall reduction in grains aspect ratio reveals a tendency to form rounder grains. This observation is consistent with the previous observation of the HTed

microstructure, where the sub-cellular structure seems to have been at least partially erased by thermally activated recovery of the dislocation network during the annealing, hence causing a release in strain energy from the cellular sub grain structure, which is consistent with similar studies [50].

5.2.1.5 X-ray Diffraction results

Figure 5-8 shows the difference in X-ray diffraction for IN718 before and after the HT. Split peaks (where a diffraction peak gets divided into two) can be seen for the material after the HT treatments for angles of 50°, 76° and 90°. Peak splitting in the HT condition can be attributed to the presence of the δ phase which reflects X-rays at different Bragg's angles to γ and γ''. Additionally, the peaks in the AB condition are slightly wider than in the HT condition. A probable cause of peak splitting in the HT condition is the relaxation of residual stresses which means that the γ phase would reflect in a very narrow band of angles to the γ'' phase. Normalized XRD patterns show intense peaks of the γ phase, the probable γ' phase, and the Laves phase, while the δ phase for AM specimens remained under the detectable range [178].

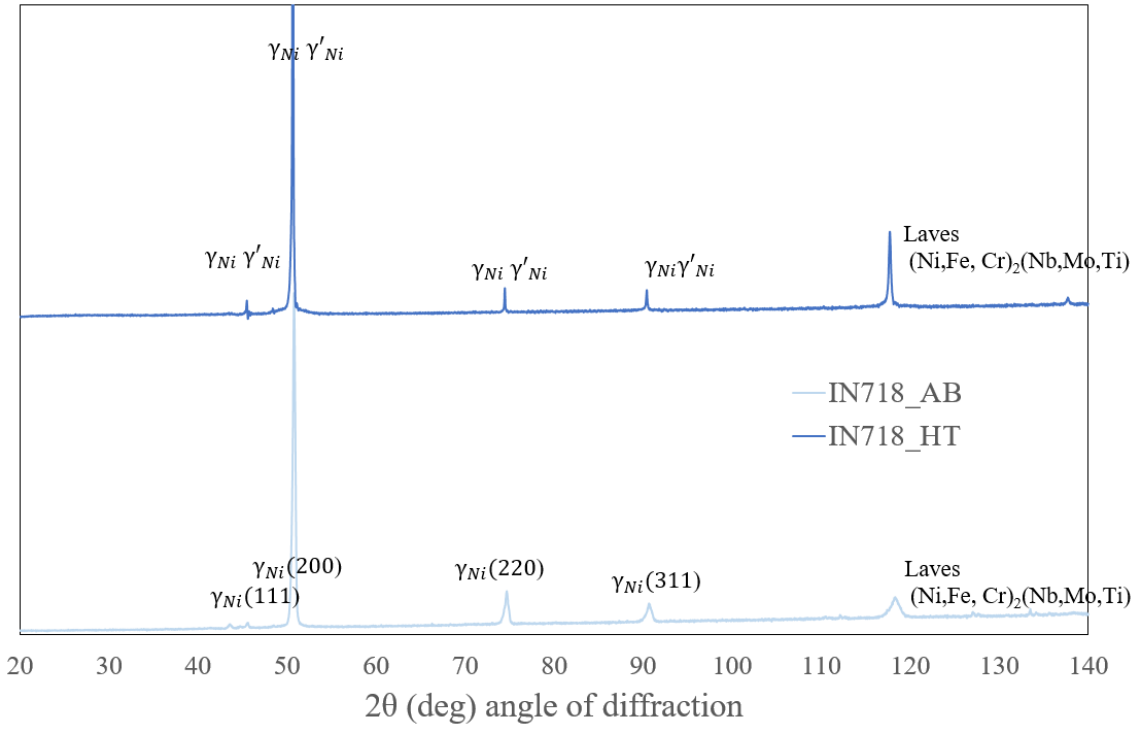

Figure 5-8: X-ray Diffraction of IN718 before and after HT

5.2.2 Mechanical properties analysis

5.2.2.1 Micro-hardness

A series of 10 micro-hardness measures per depth were performed across the interface of bi-layer specimen in both AB and HTed state, and the average data points along with the corresponding standard deviations are plotted in Figure 5-9.

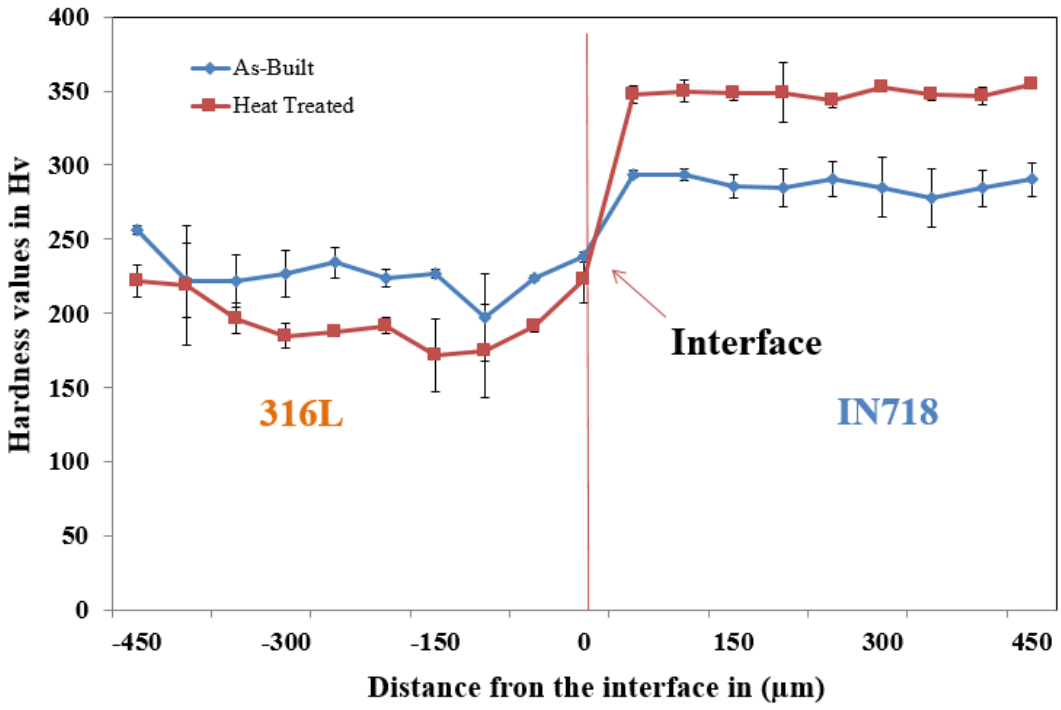

Figure 5-9: Vickers Micro-Hardness values of AB and HT specimens, measured across the interface.

Vickers hardness for the IN718 layer has increased by about 100Hv and the hardness of the 316L layer has dropped by about 50Hv after heat treatment. These measures can be explained by a thermally induced recovery from dislocations network in AB state, that was surrounding the sub-cellular structure, and hence reducing the hardness in the 316L layer. On the other hand, the IN718 layer has precipitated hard secondary phases, such as the strengthening γ' and γ'' phases, along with the brittle Laves phases increasing its overall hardness.

5.2.2.2 Tensile test analysis

The results of the tensile tests are displayed in Figure 5-10 for a clearer comparison of the effect of the thermal treatment on the mechanical behaviour of each alloy. Each test was repeated 3

times (i.e. 3 specimens were used per test) all the tests were made at room temperature and the results displayed in Figure 5-10 are the average value and standard deviations from these tests.

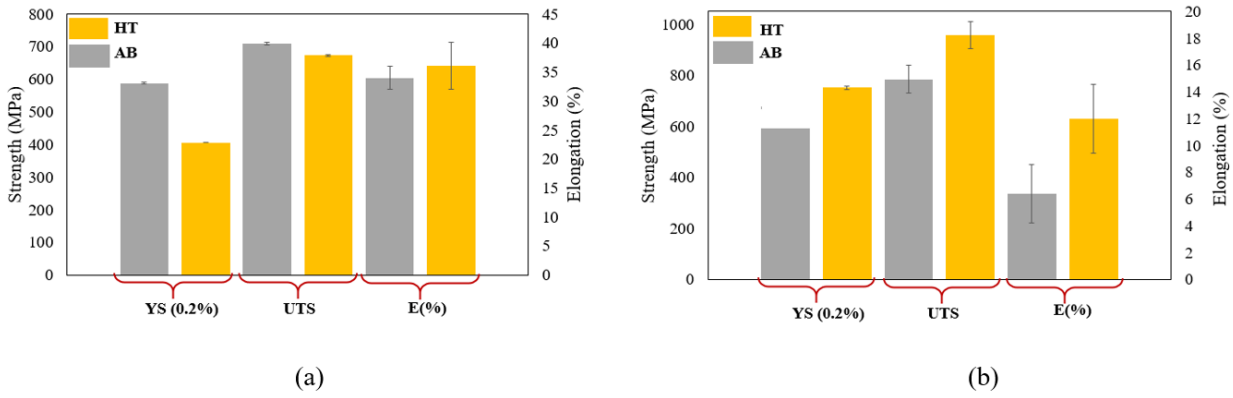

Figure 5-10: Tensile properties of a) 316L before and after HT b) IN718 before and after HT.

It can be seen that the heat treatment has a positive impact on the IN718, with an increase of 11% in YS (0.2%) from its AB condition, and a more obvious increase of 22% and 50% in UTS and in Elongation respectively. However, the results for the 316L demonstrated a loss of 31% in YS, a decrease of 5.2% in UTS and a slight increase of 5.8% in Elongation. The increase in Elongation for both alloys is expected to be the result of the thermally induced recovery of the sub-cellular dislocation network. Tensile response of IN718 after HT is close to values expected from ASTM standard for this Nickel based alloy produced by additive manufacturing [179] but remain lower than values found in the literature for conventionally HTed IN718 produced by L-PBF [114]. Meanwhile the tensile response of 316L after HT has suffered a decrease that is expected to be due to both the recovery of the dislocation network surrounding the cellular sub-structure and the decrease in the amount of twins present within the grain structure, as similar results have been reported on by Yin et al. [89] and Sistiaga et al. [90] However, these values remain superior to those expected from conventionally manufactured 316L ($YS \approx 220 - 270$ MPa fom [91]).

5.2.3 Fatigue crack propagation

5.2.3.1 Long crack test in bi-layer specimen

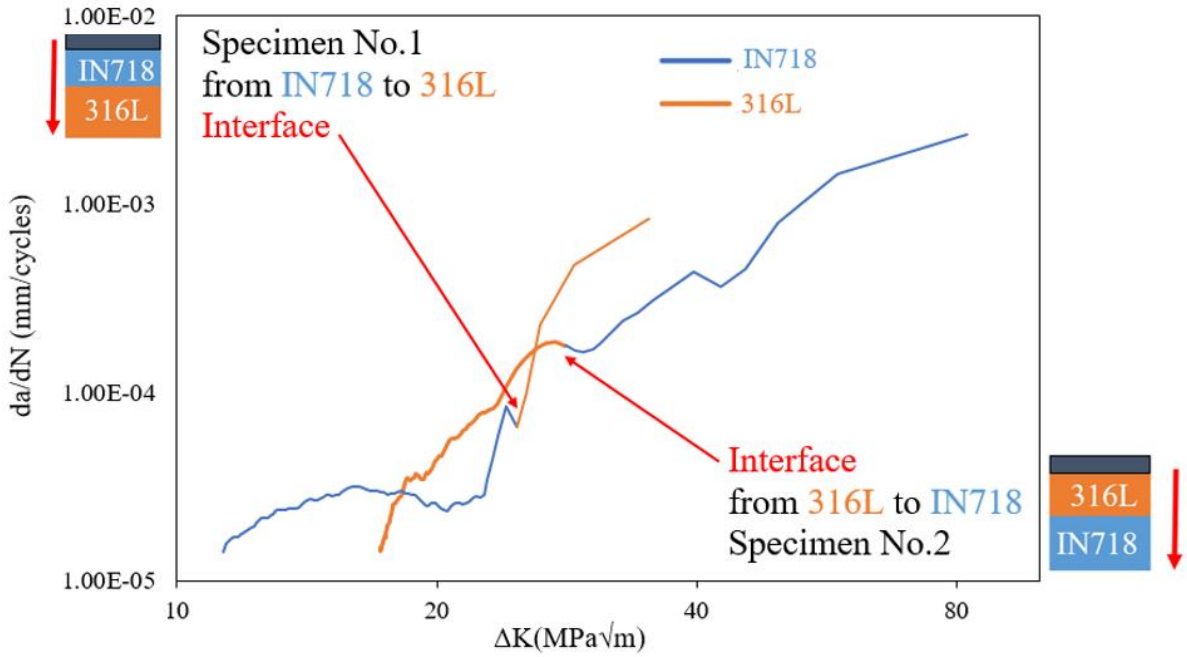

Figure 5-11: Long crack test, increasing ΔK propagation test in HTed specimen: Bilayer propagation from 316L to IN718 (specimen No.2) and from IN718 to 316L (specimen No.1)

For specimen No.1 with the notch in IN718, crack propagation started at a ΔK of 11.3 MPa√m and displayed a slow propagation rate within the top IN718 layer, until the crack tip gets close to the interface where a rapid increase in propagation rate is observed leading to a rapid final failure within the 316L bottom layer (see Figure 5-11). The crack growth rate started to increase around a ΔK of 23 MPa√m (which corresponds to a crack depth of 4.7 mm), and then reached the interface at a ΔK of 25 MPa√m (the interface is located at the mid-section of the specimen *i.e.* 5 mm depth). Figure 5-12 a) shows the corresponding roughness map of the final fracture surface, for specimen No.1 observed by Alicona. A clear distinction can be seen between the IN718 top layer which displays a rather flat surface, and the 316L bottom layer which displays rough features characteristic of a ductile fast failure. However no clear delamination was observed at the interface region.

The crack propagation within specimen No.2 (see Figure 5-11) started at a ΔK of 13.6 MPa√m, which is well above the threshold value and has caused a rapid growth rate within the 316L top layer. The interface was reached at a ΔK of 29 MPa√m, and transitioned into the IN718 bottom layer. The effect of shielding on the propagation rate was not recorded as a drop in the growth rate. However

a decrease in propagation rate slope can be observed. In addition, Figure 5-12 b) shows a roughness map of the final fracture surface of specimen No.2. A very rough fracture surface can be observed within the 316L top layer, even showing a larger granular artefact clearly detached within the 316L region before the interface. While within the IN718 bottom layer of the specimen, the surface remains smooth and propagation shows a homogeneously flat surface, even with higher values of stress intensity factor.

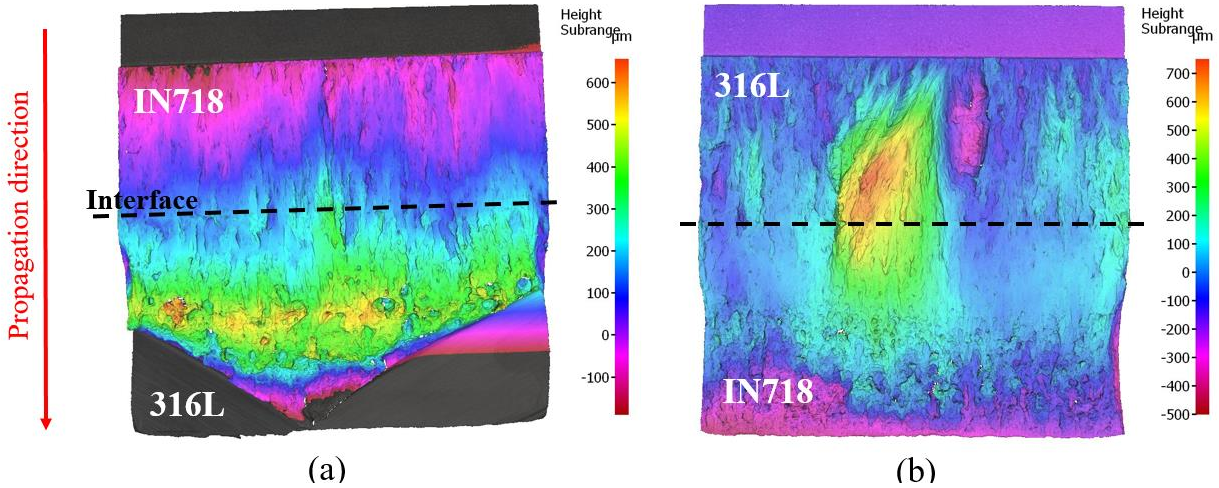

Figure 5-12: Roughness map of fracture surfaces, long crack test with increasing ΔK in HTed bi layer specimen, a) specimen N°1, b) specimen N°2.

The crack propagation measured in both bi-layer specimens are within the Paris regime and fast final failure regime. No delamination was observed at the interface for both specimens. The value of the stress intensity factor recorded for both specimens at the interface transition are above 20 MPa√m. It could be hypothesized that if the crack tip had reached the dissimilar material interface at lower values of ΔK (closer to the threshold values) the micro-structural effect on crack propagation would have complemented the macro effect of geometrical material strengthening and have produced more significant effects.

5.2.3.2 Long crack test in 4-layer specimen

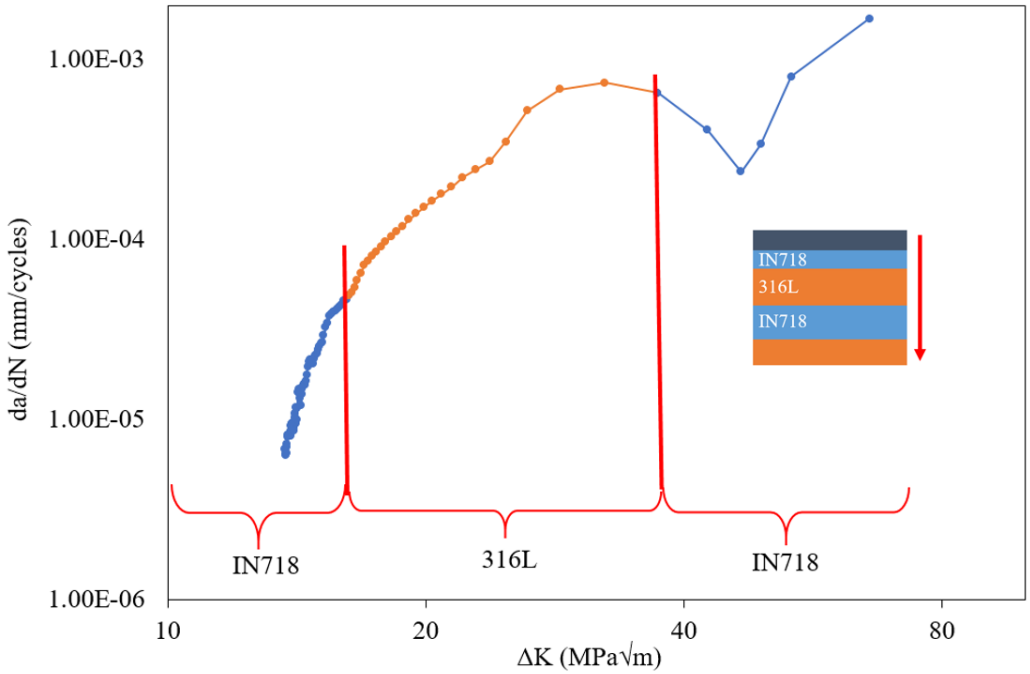

Figure 5-13: Long crack test with increasing ΔK through 4-layers specimen No.3 in HTed condition.

A long crack propagation test was performed on a HTed 4-layer specimen No.3 and the results are presented in Figure 5-13. The test started at a ΔK of 13.6 MPa√m. The first interface is crossed at a ΔK of 16.2 MPa√m, and the second interface is crossed at a ΔK of 37.3 MPa√m. Comparing with the bi-layer specimen No.1, the anti-shielding transition (going from hard to soft) caused a smaller amount of acceleration in crack propagation, this is expected to be due to the lower value of stress intensity factor during the interface transition. On the other hand, the shielding effect was affected by a larger stress intensity factor in comparison to the bilayer specimen No.2. Figure 5-14 shows the roughness map of the 4-layer specimen, and it can be seen that the 316L "interlayer" does not display any rough features previously observed in the bi-layer specimen, and below the second interface (mid-section of the specimen) the IN718 "bottom" layer displays a rough feature on the left side of surface which could have affected the final crack propagation.

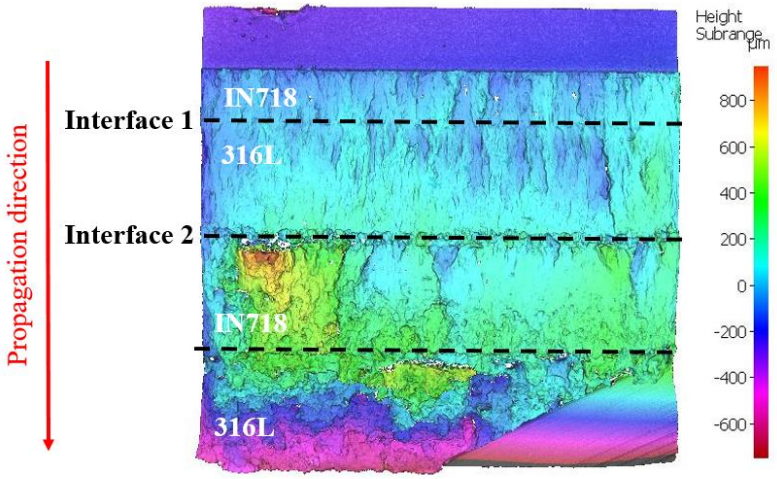

Figure 5-14: Alicona view of final fracture surface of 4-layer HTed specimen.

5.2.4 Fractography analysis

5.2.4.1 Fractography analysis of bi-layer specimen

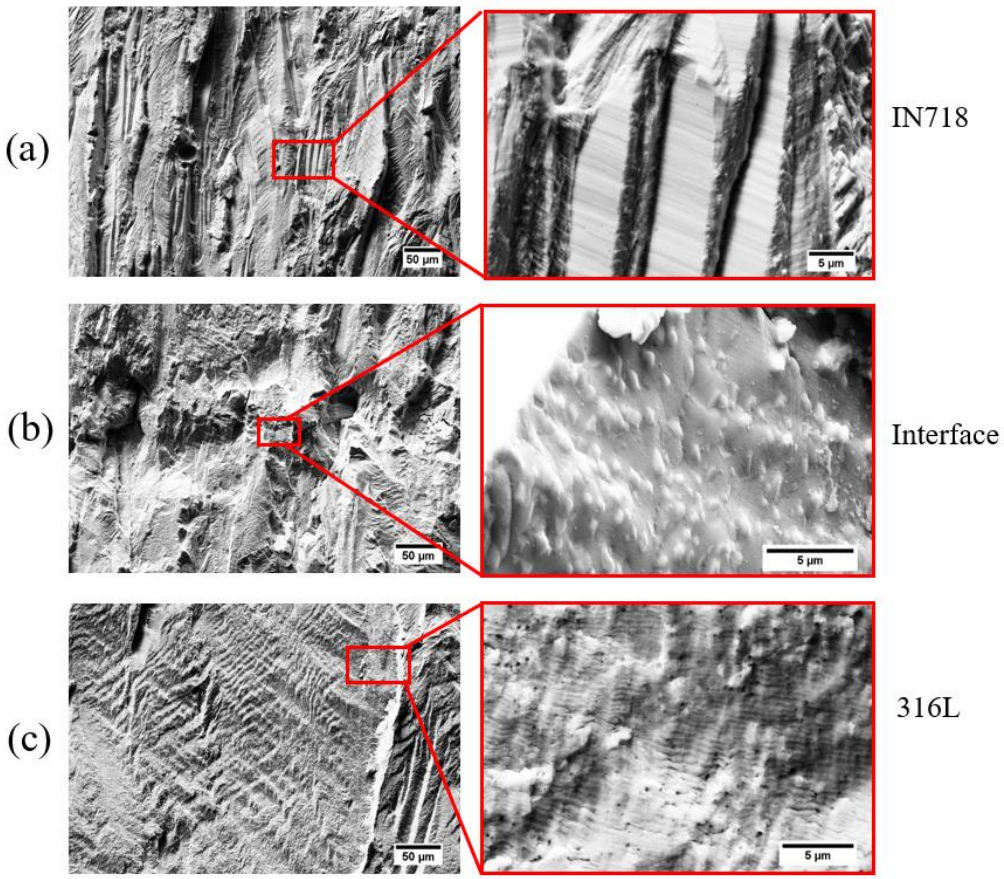

Figure 5-15: SEM view of specimen N°1 fracture surface, magnified view of a) IN718 top layer, b) Interface, and c) 316L bottom layer.

Fractography analysis were performed on the crack surfaces of the specimen post mortem, and all the pictures show a downward propagation of the crack. Figure 5-15 shows SEM images of the final fracture surface of specimen No.1. It can be seen within the top IN718 layer there are flat elongated areas adjacent to step-like regions, no secondary cracks were observed. At the interface region secondary phases can be observed, which is consistent with previous observation of the HTed microstructure (see Figure 5-1), but no decohesion around the intermetallic phases were observed. In the 316L bottom layer of specimen No.1, wavy type of features and striations were measured around ~ 0.4 µm at 5.715 mm depth which corresponds to the propagation rate displayed in Figure 5-11 for a ΔK of 30 MPa√m.

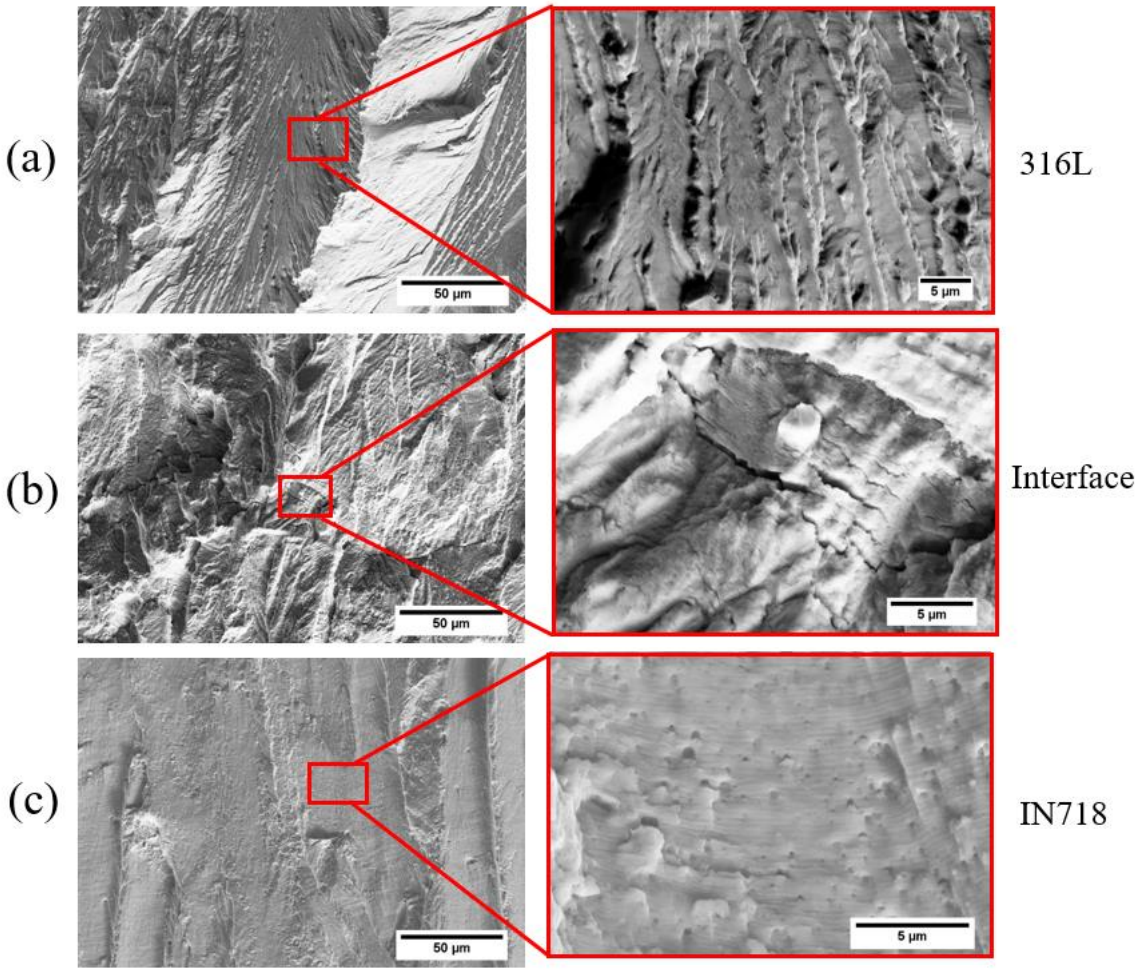

Figure 5-16: SEM view of specimen No.2 fracture surface, magnified view of a) 316L top layer, b) Interface, and c) IN718 bottom layer.

Figure 5-16 shows SEM images of the final fracture surface of No.2 specimen. The 316L top layer displays rough macroscopic features on the surface, and shows slip lines locally oriented under magnified view. Many secondary cracks were observed around the interface area within the 316L layer but these were not quantified, along with secondary phases, but still no decohesion was observed. Magnified view of the IN718 bottom layer shows long flat transgranular crack

propagation and striations are about ~ 0.21 µm at 5.7 mm depth which is consistent with the propagation rate displayed in Figure 5-11 for a ΔK of 35MPa√m.

5.2.5 Fractography analysis of 4-layer specimen

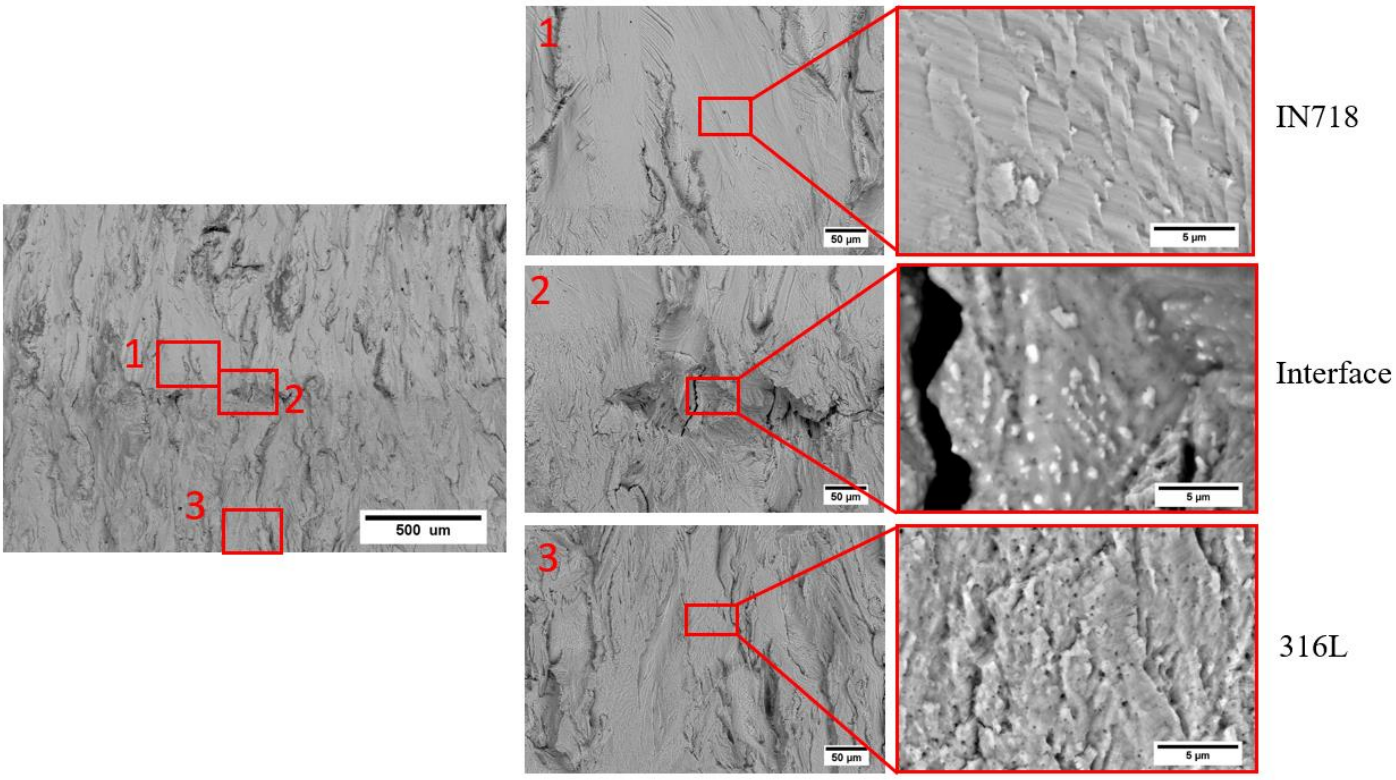

Figure 5-17: SEM view of the 4-layer (No.3) final fracture surface around the first interface

Fractography analysis were performed on the crack surfaces of the specimen post mortem, and all the pictures show a downward propagation of the crack. Under SEM observation, the final fracture surface of the 4-layer specimen No.3 is divided into 2 areas, the first interface (detailed in Figure 5-17) and the second interface (Figure 5-18).

The first half of the 4-layer specimen's fracture surface around the first interface (transition from IN718 to 316L) can be seen in Figure 5-17. The top IN718 layer undergoes a crack propagation at low ΔK (from 13 to 16 MPa√m) in the Paris regime, which displays a flat transgranular surface and small secondary phases (< 1 µm) can be seen under higher magnification. Magnified view of the first interface shows the presence of likely ductility dip cracking (DDC) surrounded by coarser secondary phases (~ 1 µm), and secondary cracks have been observed along the meltpool boundaries but the presence of these secondary cracks was relatively scarce. The 316L "interlayer" can be observed in both Figure 5-17 magnified view 3 (at the top of the layer around ΔK ~ 18 MPa√m) and in Figure 5-18 magnified view 1 (at the bottom of the layer for ΔK ~ 30 MPa√m). Small secondary cracks were observed along with small black particles (< 0.5 µm) that are expected to be

carbides. While the presence of secondary crack was noted to increase in density and widening from the top to the bottom of the interlayer these were not quantified.

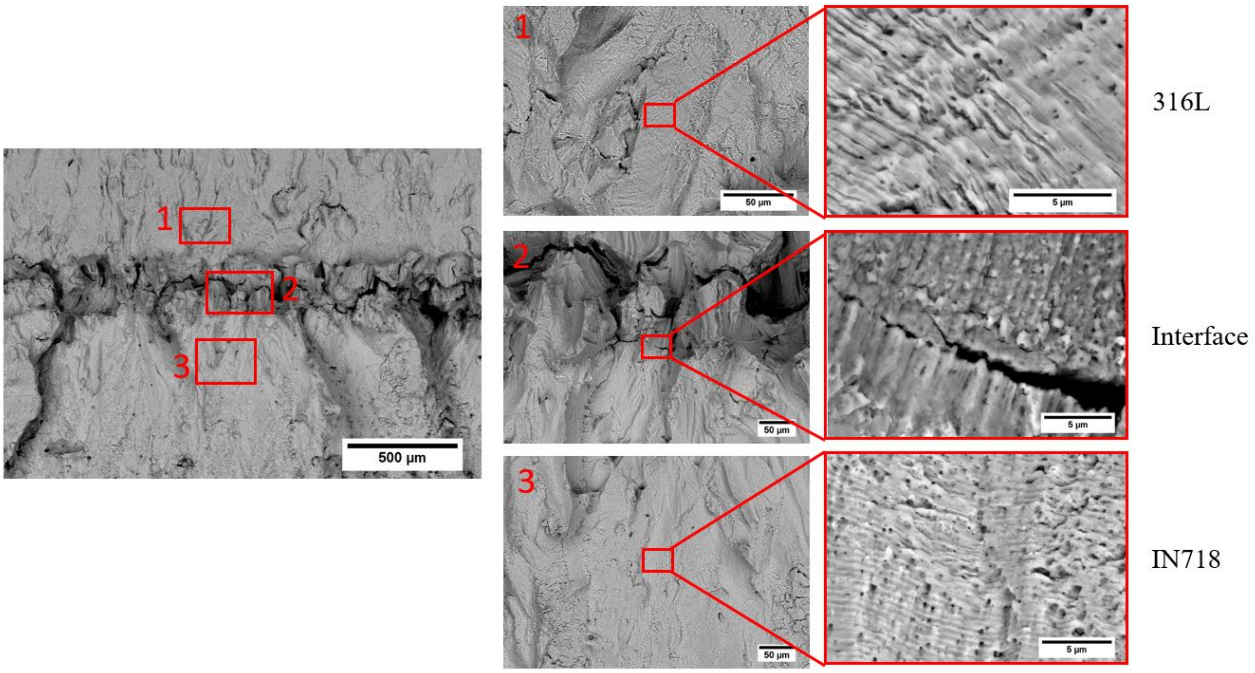

Figure 5-18: SEM view of the 4-layer (No.3) final fracture surface around the second interface.

The second half of the SEM images of the 4-layer final fracture surface are displayed in Figure 5-18. The crack propagation moves from the 316L layer through the second interface located at the mid-section of the bend specimen (5 mm depth) corresponding to a ΔK of 37 MPa√m, toward the IN718 layer, which are detailed in magnified images 1, 2 and 3 respectively. It can be seen that some delamination has occurred at the 2nd interface. However this has not caused a significant deviation of a crack path. This can be explained by a good cohesion between 316L and IN718 displayed in both AB and HTed condition, due to both alloys having FCC crystal matrix structure, and the similitude of coefficient of thermal expansion (13 µm/m.°C for IN718, and 16µm/m.°C for 316L) [180] [143]. The final fracture surface of the 4-layer specimen displays the presence of many secondary cracks within the weaker interdiffusion area leading to a delamination. The delamination is expected to be a result of the release in stress accumulation locally to the “shielding interface”. This observation is further supported with the EDS map analysis carried out around the delaminated area of the fracture surface (see Figure 5-19). It can be seen that the delamination did not exactly happen on the interface, but within the 316L layer, supporting the hypothesis of a release in strain by opening of secondary cracks at the weaker region, the multiplication and widening of these secondary cracks is supposed to coalesce hence forming at a larger scale this delamination-like crack opening at the interface.

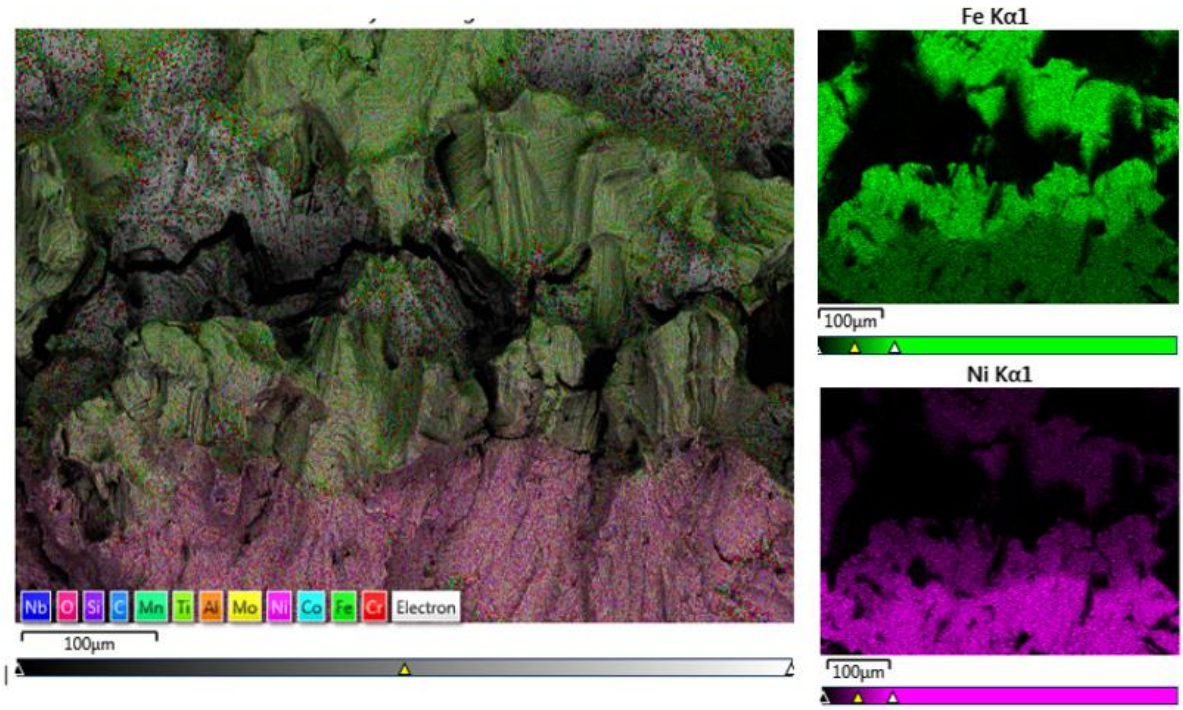

Figure 5-19: EDX map of the 4-layer specimen (No.3) fracture surface at the second interface

5.3 Summary

The present work has demonstrated that 316L/IN718 multi-material specimens manufactured by L-PBF could be heat-treated to improve the fatigue behaviour of these complex structures. The effect of the HT on the microstructure was observed under SEM and EDX. The effect of the HT on the tensile properties was measured on each alloy separately. Then, two bi-layer specimens (No.1 and No.2) and one 4-layer specimen (No.3) were tested under 3 point bending fatigue loading to compare the crack propagation resistance through multiple arrangements of dissimilar material interfaces. It was demonstrated that both micro and macro structural features will interact with the crack propagation, and should be accounted for during the design of such components, in order to optimize the resistance to crack propagation. The main results of the present work can be summarized as follows:

- The effect of HT (980°C/45min/AQ + ageing 620°C/8h/AC) on IN718 has shown an improvement of its tensile strength and elongation by 22% and 50% respectively.
- The effect of HT on 316L has shown to decrease its tensile strength by 5.2% due to a recovery from the cellular network. However, the ductility shows an increase of 5.8%.
- The HT effect of multi-layer IN718/316L specimen was observed to cause the appearance of cracks that are likely to be DDC at the interface along with the formation of Laves phases.
- The effect of the interface transition on the crack propagation was observed to have a minor effect on the mitigation of crack propagation in comparison to changes in the intrinsic material strength, for stress intensity factor ranges above 20 MPa√m.
- Improved crack propagation resistance was observed for IN718, showing a transgranular mode of propagation on the final fracture surface.
- The shielding effect was mostly observed via secondary crack opening within the weaker material, which causes delamination-like horizontal crack opening within the softer layer at the interface region at high values of ΔK (32MPa√m).

Chapter 6 Discussion

6.1 Introduction

This chapter will discuss the previously presented results and aims at putting them into perspective with the current state of the art in the multi-materials AM research field.
Researchers working with MMAM technologies are currently facing challenges such as the ability for dissimilar materials to coherently bond [181]. Compared with conventional manufacturing techniques, MMAM provides a more reliable method to manufacture geometrically complex multi-material components and reduce the manufacturing cost. However to achieve a porosity and crack-free interface with strong bonding is a critical challenge [182]. Hence one topic of interest has emerged to understand the phenomena of brittle intermetallic phase formation, defects and lack of fusion formation, and element segregation at the interface of dissimilar materials produced by MMAM [183]. Another challenge facing multi-material structures is the effect post thermal treatment will have on the combined material's properties [184]. Then, once the microstructural aspect of a multi-material specimen has been studied, before and after heat treatment (HT), the effect of dissimilar layers on the fatigue crack propagation behaviour opens the discussion about the design of damage tolerant structures, which can be more easily produced by MMAM.

6.2 Discussion

6.2.1 Effect of AB microstructure and layered architecture on crack propagation

Layered specimens of 316L/IN718 were produced by L-PBF process and the microstructure obtained with both materials using the same set of parameters produced high quality specimens with good interfacial properties. While the grain structure and orientation varied slightly from the IN718 columnar grains to the rounder grains shaped by the melt pool for 316L, the defects were scarce in each layer and few cracks likely due to liquation were observed at the interface and no interdiffusion was observed between layers.

The main matrix of both alloys was identified as mainly austenitic which is consistent with their ductile behaviour, while the hardness and strength were maintained by the network of dislocation that surrounds the sub-cellular structure obtained from as-built (AB) microstructure which is characteristic of metals produced by L-PBF.

Regarding the effect of AB microstructure on the FCP in layered specimen; it is important to recap the results from Chapter 4 section 4.2.3, which showed that the elastic properties were measured

as continuous throughout the interface, only showing a difference in yield stress and ductility. This indicates the stress intensity assumption of similitude to hold, as long as the elastic properties remain continuous throughout the specimen [47]. Theoretically an increase in strain energy is expected with regards to the distance of the crack tip from the interface, when the crack advances from a soft (σ_{y1}) to hard layer (σ_{y2}) (σ_y having a negative gradient). Using this rule of thumb the decrease of the crack tip driving force could reach up to 33% where $\sigma_{y2} = 2 * \sigma_{y1}$. The radius of the plastic zone (Eq. 6-1) ahead of the crack tip for plane strain condition (in the centre of the specimen) can be calculated as follows [46]:

$$r_{pl} = (1/6\pi) \times (K_{max}/\sigma_y)^2 \propto (K/\sigma_y)^2 \qquad (6\text{-}1)$$

Thus theoretically at a constant ΔK value of 10.6 MPa√m, the plastic zone ahead of the crack tip is about 0.32 mm within the 316L region and about 0.24 mm within the IN718 layer. If the interlayer thickness is larger than the radius of the plastic zone dimension, it will effectively affect the crack propagation. In this case (i.e. the 4-layer specimen where each layer's thickness is 5mm) the thickness of the 316L interlayer is three times larger than the radius of the plastic zone size, hence if the magnitude of the effect of shielding can be entirely calculated by the yield stress difference the crack driving force should be shielded when the plastic zone radius ahead of the crack tip is reaching the dissimilar materials interface (at the second interface, see Figure 4-13). Hence, the anti-shielding effect measured in these specimens (see Figure 4-12) was greater than expected and has showed a three fold increase in the crack propagation rate at a distance relatively close to the expected plastic zone size, right after the dissimilar material interface (falling back to a lower level once the crack tip has progressed beyond the interface transitioning between the materials). Which shows that multiple factors are at play, and the shielding/anti-shielding effect due to the gradient in properties are only one of the factors affecting the crack propagation rate at the interface.

Due to the difference in yield strength and ductility levels between 316L and IN718 it is expected to see a shielding effect of the crack propagation around (just before) the second interface. A stabilisation in the crack propagation rate was measured around 0.5 mm before the second interface, and the fractography (see Figure 4-20 in section 4.2.4) revealed the presence of multiple secondary cracks that show significant opening throughout the 316L microstructure in this area. The release of energy via the local opening and widening of the secondary cracks surrounding the cellular sub-structure within the 316L layer is causing additional shielding effects in this area, and is expected to participate in the decrease of the crack growth rate in this area.

6.2.2 Effect of HT on the microstructure

In Chapter 5, an annealing temperature of 1050°C/45min followed by a rapid cooling then a single stage ageing of 620°C/8h, has been specifically tailored with the intent to allow both strengthening of the IN718 alloy and limiting the appearance of the detrimental σ-phase within the 316L alloy. The annealing temperature was chosen to reach the temperature range above the δ-phase solvus temperature, which has been reported to be the most beneficial temperature range for annealing L-PBF IN718 [106]. The needle like δ-phase was reported to be prone to appear when annealing at 980°C [105]. Fast cooling was chosen to support the nucleation of γ', which is coherent with the γ matrix hence allowing a high nucleation rate. The ageing stage promotes the growth kinetics of the γ' and γ'' nuclei.

The standard HT for wrought IN718 usually requires a two stage ageing to reach the optimal number and size distribution of strengthening phases [117]. However, the ageing treatment was limited to only a single stage in the present work, in order to limit the time of exposure of the 316L alloy at elevated temperature, and also limit the formation of the σ-phase, which is brittle and detrimental to the fatigue performance of the alloy [82]. Hence the choice of the heat treatment was made to offer a trade-off between the strengthening of IN718 and the embrittlement of 316L.

According to the model of Brody-Flemings the solute redistribution is primarily controlled by k, the coefficient of equilibrium distribution (or partitioning coefficient) and on the diffusivity in solid (Ds) of each elements within the matrix [175]. Within a Nickel-based matrix, elements such as Fe, Cr and Co have a $k \approx 1$ meaning they will be found within the solidified core of the columnar dendrites, while elements such as Al and Ti will find themselves segregated around the dendrites, and further out elements such as Nb and Mo will remain in the liquid phase and solidify on the outskirt of the columnar dendrites causing a pre-existing concentration gradient of elements around the dendrites in the AB microstructure.

The heat treatment has had a different effect on the dissimilar material interface than on the rest of the microstructure. Elements with similar atomic radii tend to exhibit good solubility, typically the solubility of iron in nickel (at 1000°C) is 17 times superior to the solubility of niobium in iron, and 3 times superior to the solubility of molybdenum in iron (at the same temperature), meaning that during the annealing treatment, certain elements such as iron have diffused across the interface creating an interdiffusion zone between the Fe-based matrix and Ni-based matrix (see Figure 5-4) [175]. The solid state diffusion of Fe further affects the secondary phase formation in the interdiffusion zone during the thermal post treatment as the concentration in Fe exerts a strong influence by affecting the segregation potential of Nb, namely a variation of k_{Nb} as a function of nominal Fe content: i.e. decrease in k value of Nb correlates with the increase in concentration of

Fe. There is also a difference in various alloying elements' solubility between the mostly FCC Fe structure (316L layer) and the mostly FCC Ni structure (in IN718 layer). For comparison, differences in solid solubility of solute atoms are quoted as: in FCC Fe austenite can only dissolve 3wt% Mo, while FCC Ni austenite can dissolve 28wt% Mo, similarly Nb has 1.5wt% solubility in Fe and 18wt% solubility in Ni [175]. Therefore the increase in Fe concentration in the interdiffusion zone leads to a further partitioning of pre-segregated elements such as Nb and Mo, causing a preferential area for intermetallic precipitation (see Figure 5-5).

The precipitation of these intermetallic phases within the interdiffusion zone were likely to induce the opening of ductility dip cracks (DDC), which is a solid state grain boundary embrittlement phenomenon, that occurs within a specific temperature range from 0.6 to 0.8 times the solidus temperature (Ts ~[756−1100]°C) where secondary phase precipitation and carbide formation at the grain boundaries, can prevent grain boundary gliding and may further cause the formation of voids and small cracks along grain boundaries [170]. The appearance of these cracks likely due to DDC are supposed to take place during the annealing stage of the heat treatment, whereas as-built specimens showed the presence of rounder and smaller cracks likely to be due to liquation (also referred to as "hot" cracking and occurring at a higher temperature than DDC, see previous work [180]) [69].

6.2.3 Relation between the HTed microstructure and the crack propagation

The propagation of cracks within IN718 was mainly observed to be transgranular, thus the propagation resistance is mostly due to the intrinsic strength of the material. This is in agreement with a recent study made by Kim et al. [136] that specifically described the ductile cleavage mode of intragranular propagation in HTed L-PBF IN718, at medium to high values of ΔK. Their study also reported a featureless feather-like final fracture surface and the appearance of secondary cracks (at similar ΔK level). The strengthening effect of the HT of the IN718 alloy resulted in an increase in both strength and ductility creating a more damage tolerant response to fatigue crack propagation. Whereas the opposite can be seen in 316L alloy after the HT. The effect of the HT on the fatigue crack propagation can be compared for similar values of stress intensity factor range (ΔK), to previous research made on crack propagation in similar specimens in AB condition [180]. Under the Paris regime in stage II of crack propagation within a stress intensity factor range (ΔK) between 20 to 30 MPa√m, the coefficient *C* and exponent *m* from the material tested, in the case of HTed 316L, the material can be described with a *C* coefficient of 5.10^{-11} and exponent $m \approx 4.6$ (values from specimen N°2, see Figure 5-11), which is considerably superior to the same material in AB condition ($C \approx 1.10^{-11}$ and $m \approx 5.1$ from [180]) over the same ΔK range (between 20 to 30 MPa√m) giving a coefficient $C \approx 4.10^{-10}$ and exponent $m \approx 4.3$. Such rapid crack growth rates (>10^{-5} m/cycles)

are usually associated with nearing the fracture toughness of the material, in this region the stress levels are high enough so that the crack extension is mainly due to the static modes of failure. However, because the static fracture modes are sensitive to microstructure and stress state, the growth rates are sensitive to the microstructure, the load ratio and the specimen thickness. The fracture surface roughness of 316L shows a ductile rapid crack propagation (see Figure 5-12) while IN718 only shows an increase in the roughness of the fracture surface profile after the 2nd interface transition (by delamination in sample N°3 see Figure 5-14) which is coherent with the very fast crack growth rate at this stage. The effect of HT on the fatigue crack propagation seems to have maintained a ductile mode of propagation even at elevated propagation rates for both materials, while decreasing the fracture toughness of 316L in favour of improving the fracture toughness of IN718, which is coherent with the tensile test results from both alloys in AB and HT condition (see Figure 5-10).

No detrimental interactions between the Laves phases and the matrix were observed around the interface area (see Figure 5-15 b), and the delamination observed in the 4-layer specimen was mostly observed around the meltpools (see Figure 5-18) due to the secondary crack opening mechanism rather than a consequence of the decohesion between the Laves and the matrix. However, it should be noted that the presence of the Laves phases at the interface inherently causes a depletion in strengthening alloying elements that creates a weaker zone [143], which is more prone to secondary crack opening.

6.2.4 Effect of the multi-layered architecture (in HT condition) on the crack propagation

The work presented in Chapter 5 shows that the effect of interface transition on mitigation of crack propagation rate is not obvious, when comparing each alloy's respective crack propagation resistance, for a stress intensity factor above 20 MPa√m (see Figure 5-11). This is because above a certain value of stress intensity factor range, the crack propagation is in stage II rather than the quasi-stage I crystallographic regime (corresponding to lower values of ΔK closer to threshold). At this faster crack propagation stage, the classic Campbell-Laird plastic blunting crack propagation process is expected in polycrystalline alloys [185]. In addition the crack-tip process zone itself will be larger and so less affected by the localised change in materials properties at the interface. Riemer et al. [97] found in their study that L-PBF 316L post heat treatment showed better performance in the near threshold regime. Zhang et al. [101] explained that the reduction in 316L yield strength after heat treatment is more important than any loss in fatigue strength due to the increase in ductility allowing more damage prior to fracture.

In Chapter 5 the effect of shielding was mainly observed via the opening and widening of secondary cracks within the weaker layer (316L layer) just before the interface transition, and was supposed to be the root cause for the interlayer opening (see Figure 5-18) effectively reducing the crack propagation rate (see Figure 5-13) by multiple secondary cracks opening and joining causing a "delamination" of the second interface.

This gradient in yield strength caused a shielding of the crack propagation, affecting the plastic zone ahead of the crack tip, the thickness of the soft layer should be of the order of a few plastic zone sizes. Therefore, the use of a soft "interlayer" to mitigate crack propagation should be thought of in terms of a "fuse-layer", which should be as thin as possible, in order to reduce the acceleration of propagation within the soft layer itself. Figure 6-1 summarizes the idea of the soft interlayer used as a "fuse-layer" to delay the crack propagation. The values ' d_1, d_2, and d_3 represents the different layers thickness, which in the present work are all the same (2.5mm, see Figure 6-1 a) the I_t represents the interdiffusion zone surrounding the interface after HT (in the present work ~140µm), r_p represents the radius of the plastic zone size ahead of the crack tip (which in plane strain condition can be estimated as $r_p \propto (\frac{K}{\sigma_y})^2$) and a_i represents the initial notch or defect size while a_n represents the crack length after n cycles. The optimal interlayer thickness should be greater than the plastic zone radius in order for it to be effective at shielding the crack tip driving force when crack propagation reaches the second interface, and greater than the interlayer diffusion spread to avoid the microstructure at the interface becoming the dominant microstructure, and finally reduce the distance of the "fuse-layer" from the surface to reduce the stress intensity factor range ΔK value when propagating through the second interface and more effectively shield the crack propagation as shown in Figure 6-1 b) [50][46].

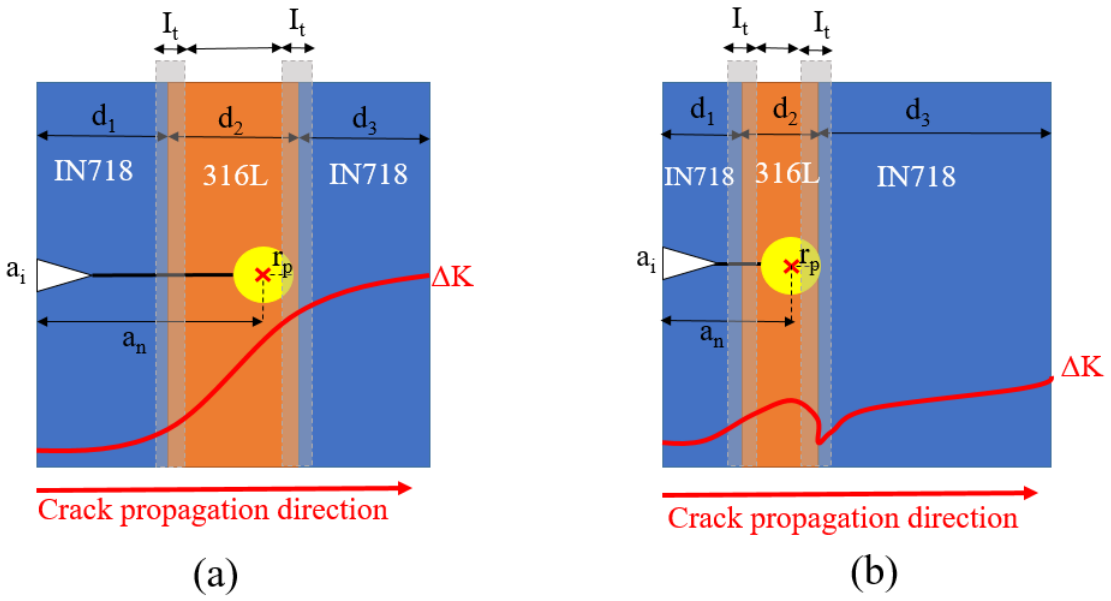

Figure 6-1: Schematic representation of crack propagation through a) multi-layer specimen with same layer thickness (as proposed in our 4-layer crack growth test), and b) "fuse-layer" concept using thinner soft interlayer to delay the FCP

Additionally, the regime of crack propagation plays an important role in the effect any shielding will have when crossing the interface. At lower ΔK values, closer to threshold (below 20 MPa√m), the regime of propagation is still quasi Stage I crystallographic and is expected to be more affected by a change in the material strength. Otherwise in the Paris regime and fast final failure regime, the plastic blunting ahead of the crack tip encounters a weak interface where Laves formation have locally depleted the area of the strengthening alloying elements, and is more prone to secondary crack opening and even possible delamination.

6.2.5 Comparison of the fatigue crack propagation between AB and HT bi-layered specimens

Figure 6-2 a) shows the crack propagation rate versus the stress intensity factor through bi-layers specimen, initiating within the 316L layer and growing into the IN718, comparing the AB and HTed specimens. It can be seen that the HTed specimen showed an overall lower propagation rate but no major effect of crack shielding was observed in either specimens. While Figure 6-2 b) shows the same comparison (between AB and HTed) but this time both of the specimens are oriented in the anti-shielding configuration (i.e. the crack initiates with the stronger layer of IN718 and grows into the softer 316L layer). The anti-shielding effect on the HTed specimen created a very visible acceleration of the growth rate at the interface, but overall the IN718 HTed layer of the specimen was still showing a slow propagation rate.

It can be seen that the phenomena of anti-shielding is more visible than the shielding, but this can be explained by the elevated values of the stress intensity factor at these stages (above 20MPa√m). While both HTed specimens have generally maintained a better resistance to crack propagation, compared to the AB specimens, the crack mitigation effect expected from the crack shielding interface transition was not as obvious as the anti-shielding observed. Moreover the antishielding phenomenon was exacerbated in the HTed specimen due to the loss in tensile strength of the 316L after the HT (see results from section 5.2.2) and from the wide interdiffusion zone at the interface where Laves and ductility dip cracking were observed (see previous section 6.2.2).

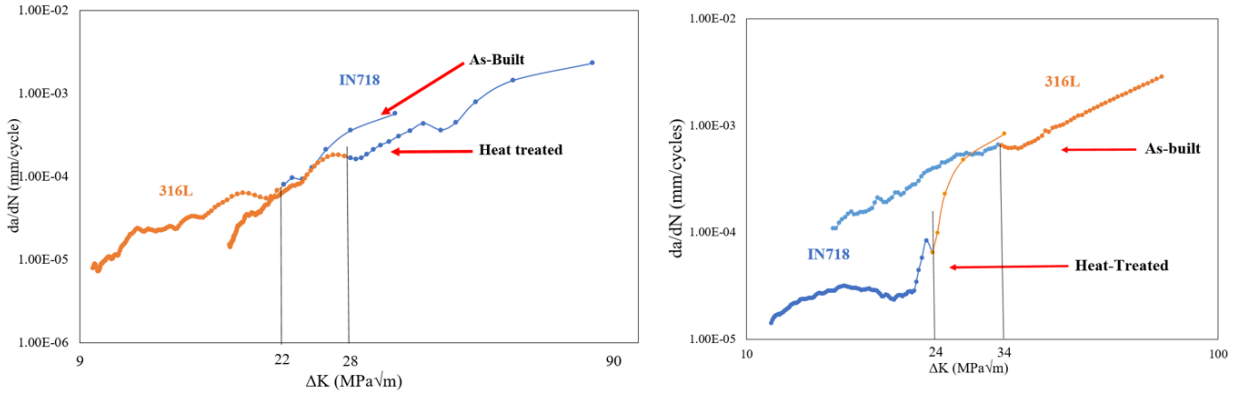

Figure 6-2: Comparison between the fatigue crack growth rate as a function of stress intensity factor, a) comparing the transition from 316L to IN718 (shielding bi-layer configuration), b) from IN718 to 316L (anti-shielding configuration), between AB and HT specimen conditions.

Due to the limited number of specimens for long crack testing and the need to perform a load-shedding pre-crack at the bottom of the notch before starting the actual crack growth test, the initial stress intensity factor is different for each specimen, and those which have initiated their growth above 10 MPa√m have rapidly increased and reached 20 MPa√m before propagating through the interface, hence placing the interface transition into the fast propagation stage. Thus the conditions for observation of the shielding and anti-shielding phenomenon would have been better at lower stress intensity factor ranges where the crack propagation was more microstructurally dependent (stage I).

However it can still be argued that the intrinsic properties of each alloy have affected the crack propagation. This is very visible when comparing the difference between IN718 in AB condition and IN718 in HTed condition, a clear change in propagation rate shows that the HT has positively affected the toughness of the IN718 layer. The opposite is also visible, the very fast propagation rate through the 316L HTed layer in the anti-shielding configuration shows both that the 316L loss

of tensile strength has affected its behaviour under cyclic fatigue, but also that the location of the 316L layer has affected the fatal failure of the specimen (i.e. a sensitive configuration as a combination of anti-shielding configuration, and placement just behind the weak interdiffusion zone of the interface).

It can be seen that the intrinsic properties of each alloy were affected by the HT (positively for the IN718 but negatively for the 316L) and that the extrinsic effect of the interface transition would be beneficial at lower values of stress intensity factor range (in early stages of crack propagation at lower ΔK). The intrinsic and extrinsic properties of multi-material components need to be assessed carefully during the design stage, and when two dissimilar alloys' elasto-plastic behaviour will be affected by a HT, the thickness of each layer and disposition of each interface should be considered carefully [186].

6.2.6 Comparison of the fatigue crack propagation mitigation between 4-layer specimen in AB and HTed condition

Figure 6-3 a) shows the crack propagation rate versus the crack tip depth comparing the AB and HTed 4-layers specimens, and Figure 6-3 b) is the same comparison (AB and HTed) but this time the diagram shows the crack growth rate versus the stress intensity factor range ΔK. It can be seen that the HTed specimen had an overall weaker resistance to crack propagation compared to the AB specimen and this is due to the fact that the main part of the crack propagation happened within the 316L layer. As previously detailed, the 316L alloy has suffered a loss in strength after the HT leading to a decrease in its toughness. The 4-layer specimen allows the crack to propagate through two interfaces: the first (IN718 to 316L) being in the anti-shielding disposition, and the second (316L to IN718) being in the shielding disposition. It can be seen that the first interface was at 13 and 16 MPa$\sqrt{m}$ for the AB and HTed specimen respectively, and due to this lower level of stress intensity factor range the anti-shielding effect was not as pronounced as observed in previous section (see Figure 6-2 b). On the other hand, the shielding effect of the second interface transition was visible in both specimens at elevated values of the stress intensity factor range ΔK.

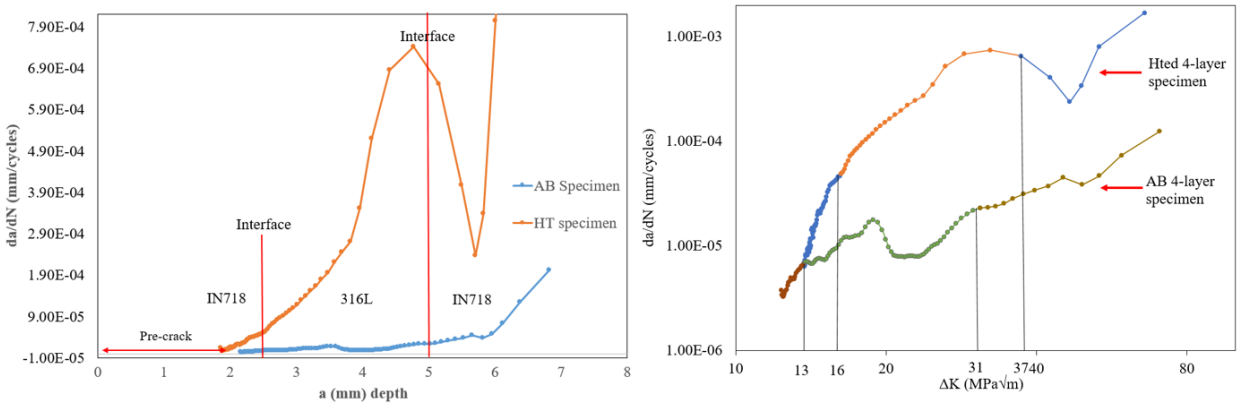

Figure 6-3: Comparison between the fatigue crack propagation through 4 layers specimen in AB and HTed condition, a) crack growth rate versus crack front depth, b) crack growth rate versus stress intensity factor.

As discussed in a previous section (see section 5.2.5), the shielding at the second interface of the HTed specimen was adjacently supported by a delamination at the weaker zone of the interface (where interdiffusion was locally supporting secondary phase formation), while the AB specimen has shown the effect of shielding by locally opening secondary cracks (micro-crack toughening) within the softer layer a few plastic zone sizes ahead of reaching the interface transition. These two types of reactions were mainly dependent on the behaviour of the 316L material (in different conditions, AB and HTed). Additionally the magnitude of the effect of the secondary cracks opening has not been fully investigated and the secondary cracks density and widening could be assessed more thoroughly and compared to the magnitude of the stress intensity factor, or to the distance from the interface (oriented in shielding transition) in order to investigate what causes these secondary cracks opening and understand their impact on the crack propagation rate, and their impact on potential delamination.

The 4-layer specimens could be compared with multi-layer specimens where a ductile interlayer is imbedded into a stronger material in order to improve its damage tolerance [164]. However these types of damage-tolerant designs usually tend to tailor the thickness of the interlayer to mitigate the crack propagation [187], [188]. The extrinsic mechanism of shielding at the second interface is the inelastic zones surrounding the crack wake that can lead to a decrease in the propagation rate. Shielding has affected each specimen differently, in the AB specimen the ductile behaviour of the 316L layer has allowed for secondary cracks to open, while in the HTed specimen the weaker area was the interdiffusion zone which has responded by opening a delamination at the interface to overcome the stress accumulation ahead of the crack tip before the interface. Another study has also reported the appearance of secondary cracks within grains in AB 316L made by L-PBF under creep testing [189], or crack branching was observed in Titanium alloy made by L-PBF and HTed

then tested under constant amplitude fatigue crack growth test [190], but because secondary cracks are a complex phenomenon [191] very few studies have investigated their causes and their effect of fatigue crack propagation in -PBF specimens.

6.3 Summary

It should be understood that the crack growth is a simultaneous effect of both intrinsic microstructural damage mechanisms, which promote crack extension ahead of the tip, and extrinsic mechanisms (crack-tip shielding), which act primarily behind the tip to retard crack growth, differing only by their relative importance [192]. In metallic materials, intrinsic damage mechanisms typically involve dislocation pile-ups in the highly stressed region ahead of the tip, leading to classical failure by cleavage, intergranular cracking or microvoid coalescence; comparable mechanisms under cyclic loads involve the repetitive blunting and resharpening of the crack tip. Extrinsic shielding mechanisms, conversely, result from the creation of 'zone shielding' by microcrack toughening, or by in situ dilatant phase transformations or 'contact shielding'.

This discussion was aimed at effectively putting into perspective the results presented in Chapter 4 and Chapter 5, in order to gain a better understanding of the competing mechanisms at stake in the approach to damage tolerant design using MMAM layered specimens.

It can be concluded as follows:

- IN718 and 316L alloys have good compatibility allowing to produce test specimens of good quality with a strong bonding at their interface.
- In the AB state both alloys demonstrate a reasonable strength and ductile behaviour, and a sufficient discrepancy in plastic properties to allow for structural toughening mechanisms such as secondary crack opening and shielding to happen.
- Both alloys were very differently affected by the HT, an overall improvement of strength and ductility has been observed in the IN718 alloy, while an overall loss in strength and ductility was measured for the 316L alloy.
- It should also be noted that after the HT an interdiffusion zone was formed at the interface, locally creating a weaker zone were secondary phase formation was promoted.
- The effect of the HT on the crack propagation has been divided in two sub categories: the intrinsic effect (which was overall improved for IN718 and decreased for 316L) and the extrinsic effect of the interface transition (shielding and anti-shielding were expected to be more effective for low values of the stress intensity factor range $\Delta K < 20$ MPa$\sqrt{m}$)

It was finally stated that the intrinsic and extrinsic properties should be first be taken into consideration during the design phase, in order to truly tailor the materials and the geometry to achieve damage tolerant designs.

Chapter 7 Summary and conclusions

Virgin powder of 316L stainless steel and Inconel 718 were used to fabricate multi-material specimens using Laser powder bed fusion (L-PBF). Every specimen was built horizontally on supports. The specimens were built always starting with 316L as the bottom layer in order to allow the more ductile alloy of the two to absorb some potential residual stresses linked to shrinkage of the material on cooling after L-PBF process. Both alloys mainly formed austenite on rapid cooling (in the AB condition), which is a Face Centred Cubic (FCC) type of crystal structure; FCC(Fe) and FCC(Ni) have close crystal parameters, as well as similar coefficients of thermal expansion, allowing a good bonding between each alloy. The parameters were selected on prior experience to allow a good densification and limit the number of inner defects such as lack-of-fusion's porosities. The L-PBF process produced materials with a fine cellular microstructure that is composed of elongated sub-cells oriented in the direction of the heat flow, while the grains' orientation and shape may vary depending on the meltpool size orientation, rescanning strategy or dendrite growth ability. While 316L grains were more influenced by the meltpool shape, IN718 grains were more elongated, forming dendrites often encompassing multiple layers in the built specimen. This phenomenon cannot be due to the fabrication strategy, as both alloys were fabricated using the same set of parameters, nor because of the thermal inertia that starts to build up within the chamber after a certain time, simply because the process was stopped and cooled down in between the fabrication of each alloy (within the multi-material specimens), in order to empty the hoppers and replace the alloy powders, hence restarting the process with a thermal neutrality when changing the material.

The gradient of elemental concentration within the microstructure in both as-built and heat treated conditions, are very important to define, as the local concentration or depletions of certain elements can cause a number of changes in the overall mechanical response of the system. At the sub-cellular level the gradient in elemental composition is caused by the very rapid cooling. The elements will not have an extensive time in the liquid state to move very far and elemental re-arrangement is mostly due to solid state diffusivity and segregation by affinity and ranking from first solidifying to last, forming the very fine and dense network of elongated cells, surrounded by dislocations. Most of the heavier elements such as Niobium and Molybdenum remain in the last elements to solidify and end up at the external boundaries of the sub-cells or grains, other elements such as small interstitial Carbon of Silicon can find themselves entrapped as well and end up either at grain boundaries or surrounding entrapped gas pores and form a local oxide or carbide. The subcells are also surrounded by a network of dislocations that is due to the very rapid solidification and again the elemental concentration gradient due to this solidification. This overall results in a homogeneous FCC austenite formation where the obtained tensile strength rely on the hardening

effect of the dislocation network, and the good elongation properties is due to the ability of these dislocation networks to re-arrange under strain.

Mostly the 316L has a very good mechanical response due to plasticity induced twinning and is able to exhibit good strength and good ductility in the as-built state post L-PBF process. However IN718 in the as-built condition has a mostly austenitic matrix and does not exhibit the same amount of tensile strength as expected from a conventionally manufactured and conventionally heat treated Inconel alloy. While the ductility is maintained in AB-IN718, the tensile strength level is barely superior to the Fe-FCC austenitic strength from the 316L layer.

The mitigation of crack propagation, when propagation through a multi-layer specimen happens, firstly occurs because of the orientation of the dissimilar material's interface in a crack arrester (CA) (i.e. perpendicular) direction to the propagation. If the difference in material strength causes the plastic zone ahead of the crack tip to be shielded by causing a gradient in strength this also causes the plastic wake ahead of the crack tip to blunt, and the crack to, if not stop completely at least, slow the crack propagation.

Hence in the AB condition the difference in crack propagation was mainly observed to be a result of the grain orientation within each layer rather than due to the difference of tensile strength between each alloy. Tortuosity caused by a greater grain misorientation in the 316L layer has been observed to mitigate the crack propagation at lower level of stress intensity factor range (ΔK). While the propagation in IN718 was facilitated by the alignment between the elongated grain orientation and the crack propagation direction. However due to good homogeneity within each alloy layer and a good bonding at the interface every crack propagation test showed no delamination nor any deviation from straight crack propagation.

Multi-layered specimens in the CA orientation produced interesting results in terms of the mitigation of crack propagation in the AB condition. By improving the tensile strength of the IN718 alloy (via HT) a more significant effect on the crack propagation mitigation via shielding effects due to the enhanced dissimilar material transition was expected. However applying any heat treatment to a multi-material specimen is a trade-off between the properties desired for one alloy and the ones obtained in the other while undergoing a common heat treatment.

The choice of heat treatment therefore was made to allow the back diffusion of some elements with lower solid state diffusion kinetics such as Niobium (which is found in the strengthening phase γ''), or Aluminium and Titanium which are usually pushed on the external side of the dendrite leaving the core of the dendrite to be purely austenitic γ matrix, within the IN718 layer. Meanwhile the trade off was to limit the formation of the orthorhombic δ phase (within IN718) which appears

after a long exposure at temperature above 700°C, and limiting the formation of the σ brittle phase in 316L which appears after exposure between 500 to 700°C. The use of annealing, both allowed the nucleation of γ/γ' in IN718 and also the release of some residual stresses due to the thermally activated recovery of the dislocation network surrounding the sub-cellular structure.

The mechanical response of 316L and IN718 was altered by HT, leading to a loss in tensile strength by 33% and increase in tensile strength by 12.5% respectively. However in the multi-material specimen the appearance of an interdiffusion zone was also observed, and locally a diffusion of Fe caused a partitioning of elements that were originally micro-segregated and further caused the precipitation of brittle Laves phases, causing cracking likely due to a ductility dip in this region.

The effect on crack propagation through multi-layers oriented in the CA configuration, within heat treated specimens, has shown that while IN718 displayed a tougher response to fatigue loading, 316L conversely displayed a weaker response to crack propagation. The effect of the interface shielding transition was also limited for values of the stress intensity factor range above 20MPa√m. The local microstructure of the interface in the HTed specimen was observed to cause delamination for higher values of stress intensity factor range (ΔK).

It was concluded that to optimise the effect of both IN718 strengthening and multi-layer CA shielding effect, the interface transition between soft to hard material (in the shielding disposition) should be designed to be located close to the initial stage of the crack propagation (ideally before the stress intensity factor range ΔK reaches 20MPa√m).

Chapter 8 Directions for future work

8.1 Interest of MMAM research field

8.1.1 Life cycle assessment of MMAM components for industrial application

The use of multiple material AM technology is fairly recent and could hold the potential for significant reduction in production time, assembly, and overall cost in energy, time and material waste for the production of highly complex components. However due to the level of complexity and the specific design necessary to produce these types of components, only a few key applications are currently envisaged. But the future is also a new place, where each component will need to be optimised from its fabrication, its in-service use, up to its end-of-life, in order to limit the impact of the production on the environment and on the population. That is why a pre-study of the commercial and sustainability environment is necessary in order to assess the viability of such products in the market and ensure the best choice is made for both the industrial need that will produce said product, but also the component itself to reduce its impact in service on the environment. This study will also raise the question of the end-of-life of such products and how multi-material components can find a place in a circular economy. The questions over material and energy use are a wider topic that need to be integrated into engineering design and new technologies such as AM and MMAM can lead to new interesting opportunities that are currently needed more than ever before.

8.1.2 Different material combination and assessment of feasibility

The combination of 316L and IN718 by MMAM was made feasible mainly because of the good match between their crystalline structures. However investigation around different types of alloy combinations, or MMCs and composites, could also widen the perspectives on the potential feasibility and potential applications that such a technique can offer. In considering a more environmentally sustainable life style, the design of our infrastructures and our industries need to be optimised from the production line to the end-of life. MMAM technique (as well as AM technologies at large) can be used in the design of a new life cycle of products and commercial components. This can start by differentiating the potential feasibility and limitations such techniques can offer, along with a detailed calculation of the effect on the environment (using all relevant indicators) the material combination by AM applied to specific case studies, can offer (or not) for improvements on the management of resources.

8.2 Multi-layer effects on fatigue crack propagation

8.2.1 Experimental strategy of distinct layers versus gradient limitations and optimisation

The mitigation of fatigue crack propagation by using multi-material AM technique, is a topic of interest. By exploring different alloy combinations, gradients in tensile properties can also be explored and potentially improved using the appropriately tailored post-treatment. The combination of 316L and IN718 for example could be investigated further by choosing different layering architectures, a finer “fuse” layer using the softer alloy (316L in this case) as a protective shield against the crack propagation. However because of the inter-diffusion gradient caused by the heat treatment, locally supporting the precipitation of brittle phases such as Laves, the design of a finer interlayer should account for the spread of the inter-diffusion region during the heat treatment in order to find the appropriate interlayer thickness for the mitigation of crack propagation.

As a comparison, multi-material specimens produced by AM can also be fabricated by a gradual combination of powders (more often found in direct deposition technique) such a mix between alloy powders can lead to larger “grey areas” in term of mechanical performances, and could be investigated for improving the bonding technique, or potential limitations in precipitation strengthening ability by a thermal post treatment, which may result in effective structural changes for fatigue resistant design in the future.

Further quantitative investigation can be made in order to discriminate between the effects of secondary cracks opening for each material and the shielding effect at a given stress intensity factor level. Maybe by reproducing constant ΔK test on multi-layered specimen and using method such as 3D-tomography to quantify the appearance of secondary cracks versus the crack depth (in regards to the distance to a shielding interface transition) at a given ΔK.

8.2.2 Modelling of fatigue and/or microstructural precipitation

Finally, combining experimental results with a numerical model is getting a step closer to automated and integrated production systems. Prediction models of the potential phases formation within multi-material specimens before and after heat treatment could help predict the local mechanical properties and differentiate the weaker and stronger areas present within a multi-material component. However it is important to note that the numerical modelling of the microstructural formation in AM processes is only at its earliest stages, and is currently split between two fields: the geometrical grain shape formation based on the heat flux and solidification time, and the energy model of phase formation based on the local partitioning of elements and the

interdependency of time temperature and spatial location of certain elemental concentrations to predict the phase formation during the cooling and reheating cycles of AM process. Due to the relative novelty of AM processes, where the nature and intensity of the heat sources can vary (from electron to laser the volume of material affected and the speed of displacement as well as the depth of penetration of the heat vary considerably) and nature of the feed stock materials is also variable (powder density, flowability, chemical composition, will vary and affect the final component), it is difficult to get accurate results solely based on numerical modelling.

Similarly a numerical model of a multi-layered specimen, including each separated alloy's tensile properties and some allocated boundary conditions for the interface could help predict the mitigation of crack propagation within such a layered architecture design, and could potentially be adapted to more complex compositional gradients, if the experimental testing can provide sufficient data to cover the whole range of properties that may vary within the transition zone.

Appendix A Figures from Chapter 1 Introduction

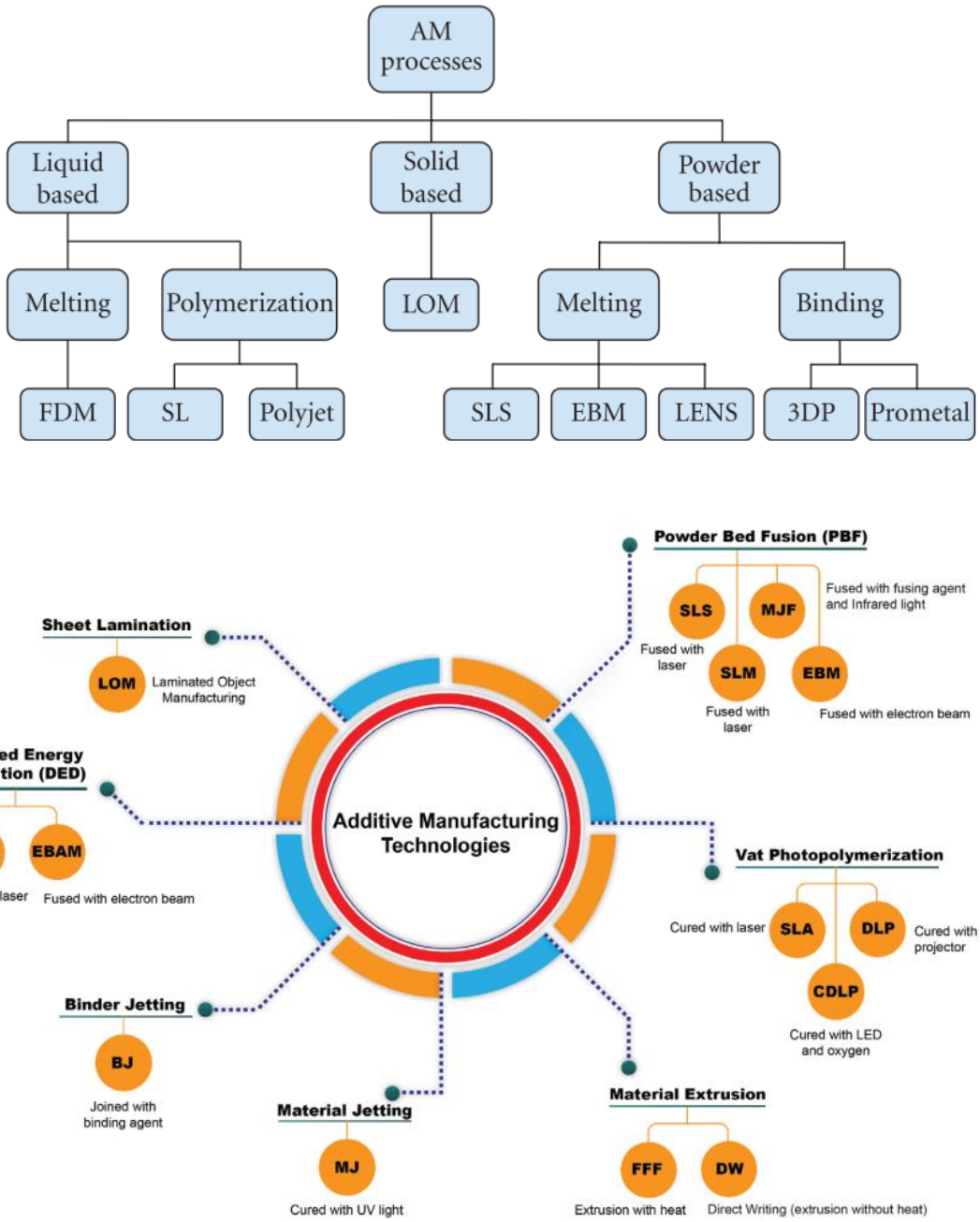

Figure 8-1: Categories of AM processes, from [2]

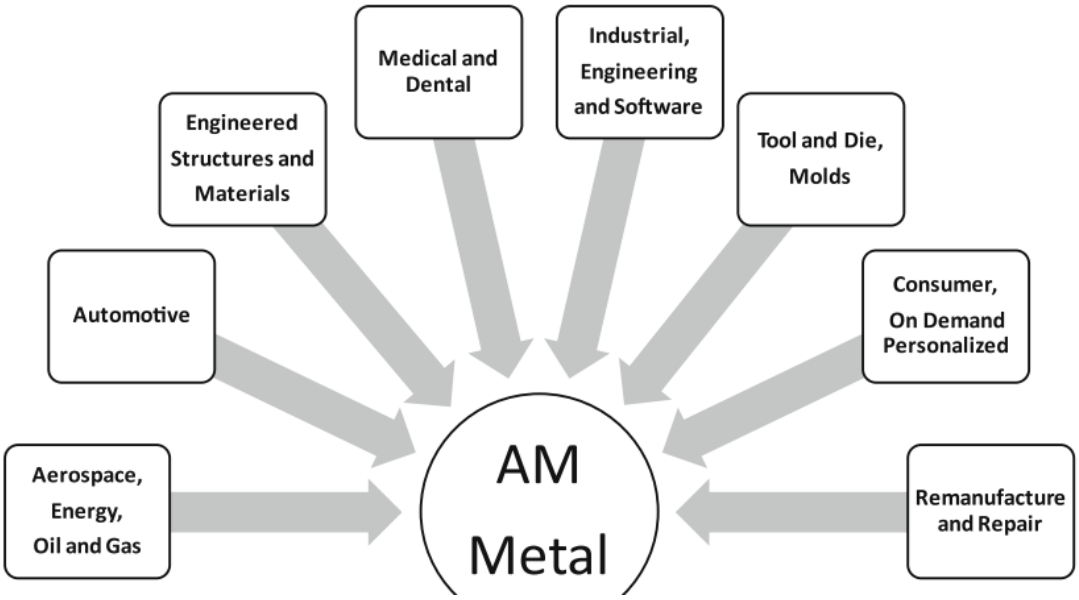

Figure 8-2: 3DMP applications from [4]

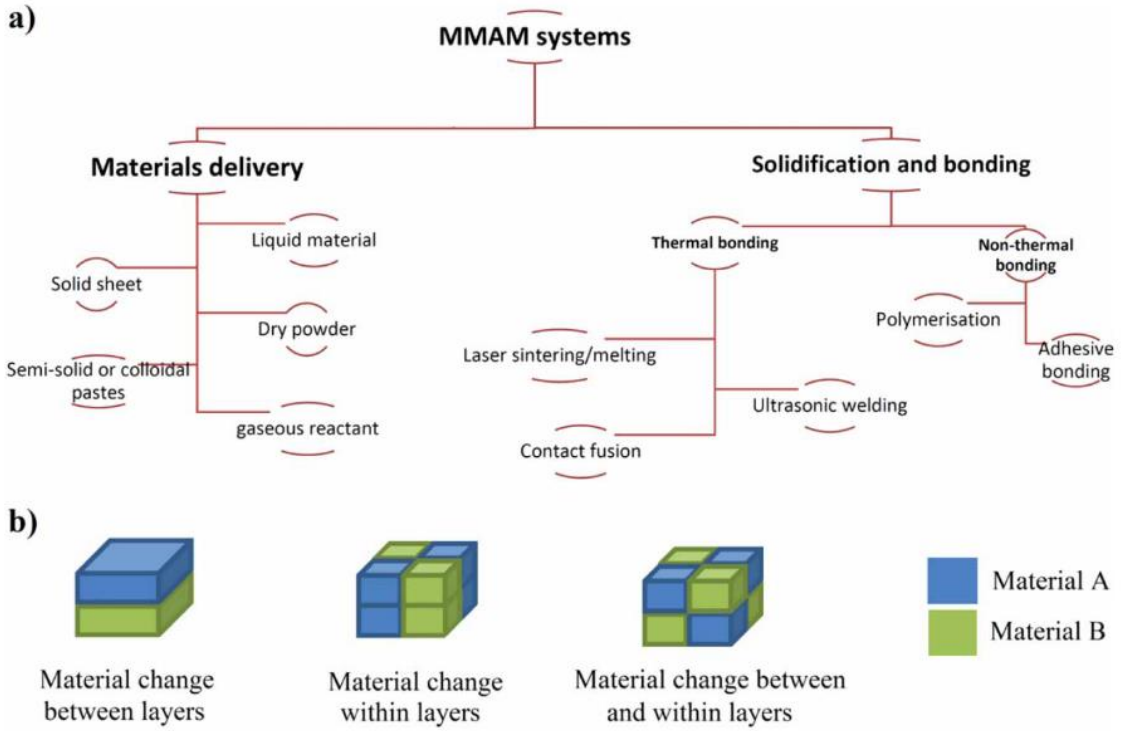

Figure 8-3: a) MMAM main sub-systems, b) different type of material combination, from[11]

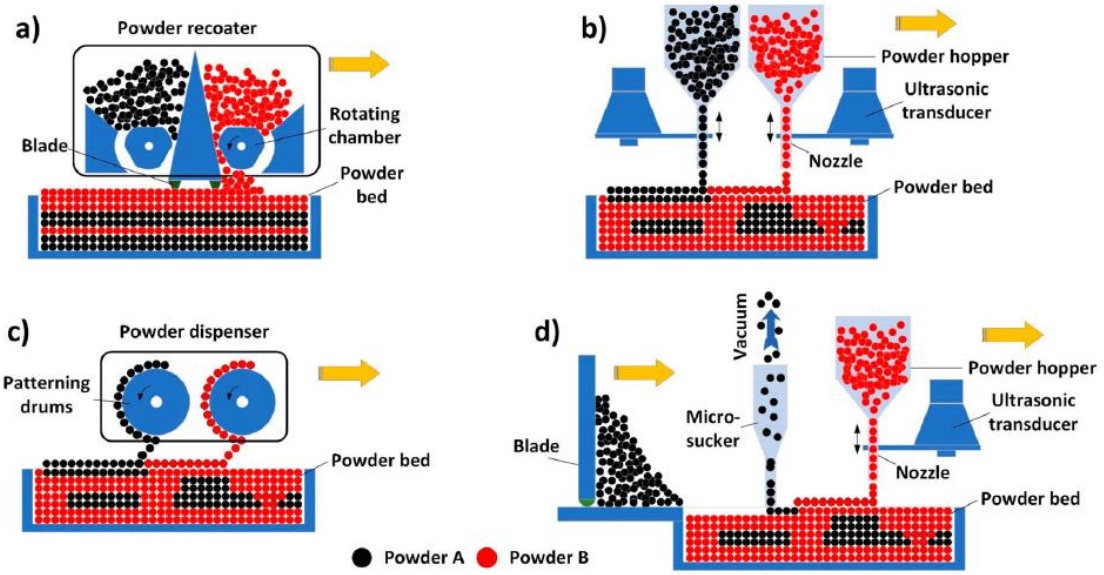

Different Multi-material dispensenry technologies : Schematics of a) blade-based dual powder recoater, b) ultrasonic-based dual powder dispenser, c) electrophotographicbased dual powders dispenser, and d) 'blade + ultrasonic' hybrid powder spreading system for multi-material L-PBF from [183]

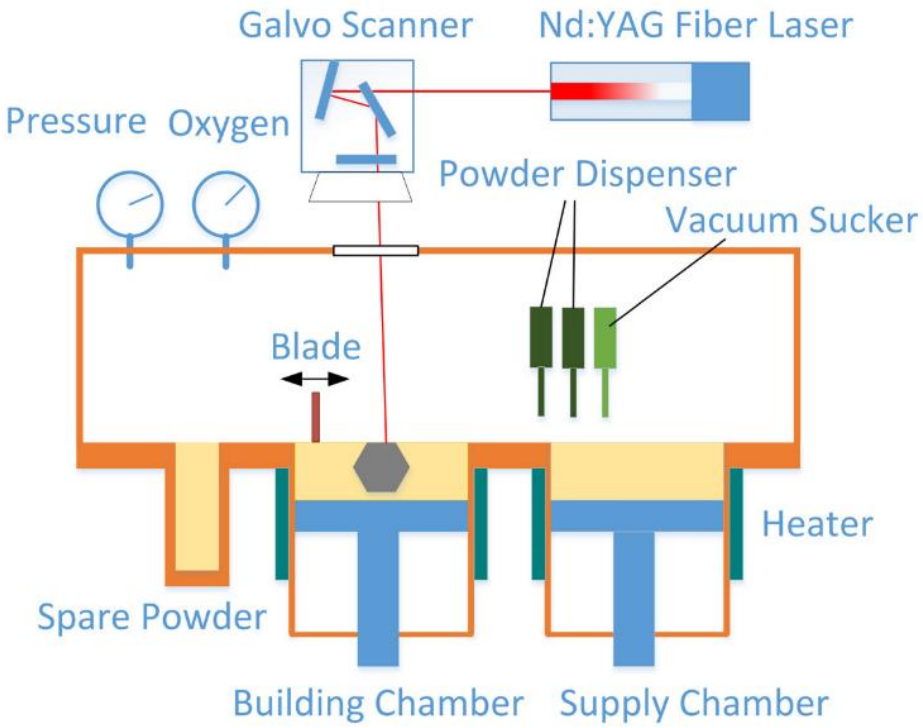

Figure 8-4 : ,from[22]

Appendix B Table of comparison of MMAM technologies [11]

Category	Techniques	Advantages	Disadvantages	Bonding Interface	Materials resolution	Capability of multiple materials printing	Material solidification and bonding in layer
Photopolymer Vat	Scanning SL	High dimensional accuracy, offering transparent materials, living cells can be incorporated	Only photopolymers, time consuming materials changing, material contamination and waste in process	Between and within layers	Low	Good	Point by point
	DMD[2]-based SL	Same as scanning SL	Same as scanning SL	Between and within layers	Low	Good	Whole layer once
Material extrusion	Material extrusion with melting	Fast, no toxic materials, good material properties	Low dimensional accuracy, delamination, weak bonding between dissimilar polymers	Between and within layers	Medium	Good	Line by line
	Material extrusion without melting	Easy and cheap mechanism, no trapped materials, low material waste, fair fabrication speed, living cells can be incorporated	Relatively low dimensional accuracy and mechanical strength	Between and within layers	Medium	Good	Line by line
Powder bed fusion	SLS	Wide range of materials, great material properties, high materials strength	Thermal stress, degradation, accuracy limited by the particle size of materials, material contamination when changing to other materials, require atmosphere control for metals	Between layers	Low	Fair	Point by point
Directed energy deposition	LENS DMD[1] LC	Wide range of materials, great material properties	Low dimensional accuracy, thermal stress, require atmosphere control, require machining process for finishing the part	Between and within layers	High	Fair	Point by point
Sheet lamination	LOM	Fast process, accuracy in Z-axis is lower than SL and SLS	Shrinkage, great amount of scrap, delamination, require changeover when changing other materials, require pyrolysis process	Between layers	Low	Fair	Plane
	UC	High dimensional accuracy, Fast process, Low temperature effects	Wastage of material in the machining process, delamination, only metals, require changeover when changing other materials	Between layers	Low	Good	Plane
Material jetting	Inkjet Printing	Fast process, wide range of materials, materials mixing on droplet scale	Limited to jettable materials, clogging problem, low viscosity prevents build-up in 3D	Between and within layers	High	Very Good	Point by point
	PJT	Fast process, wide range of materials, materials mixing in droplet scale	Limited to jettable photopolymers, clogging problem	Between and within layers	High	Excellent	Multi-Point
Binder jetting	3DP	Low temperature process, fast process	High porosity, low surface quality, accuracy limited by the particle size of materials, difficult to remove trapped materials	Between and within layers	Medium	Poor	Point by point
Hybrid & DW	LCVD	high-resolution process, metals and semiconductors	Low-deposition rate, toxic/explosive gas might be involved	Between and within layers	Medium	Poor	Point by point
	Aerosol Jet Printing	High resolution, wide range of materials, ability of writing in 3D space, ideal for deposition of biological inks, noncontact, easy material handling	Solvent involved, Shield gas may blow off powders when integrated with powder bed systems	Between and within layers	High	Good	Line by line
	SDM	Wide range of materials	Require machining process during fabrication, feature size is limited by cutting tool	Between and within layers	Low	Fair	Line by line
	DPP + binder printing or laser sintering	Wide range of materials, possible complex materials and geometry control	Limited to good flowability powders, overflow problem, low compaction density of discharged powders	Between and within layers	High	Good	Point by point

Appendix C K Evaluation based on Scott and Thorpe's review

Schematic of semi-elliptical crack is shown in [193]. At the bottom ($\theta = \pi/2$) of the notch, crack tip intensity factor:

$$K_I = M_{f(\frac{\pi}{2})}[1 - 1.36(\frac{a}{t})(\frac{a}{t})^{0.1}]\frac{\sigma_b}{E(K)}\sqrt{\pi a}$$

While the front face magnification factor:

$$M_{f(\frac{\pi}{2})} = 1.13 - 0.07(\frac{a}{c})^{0.5}$$

While

$$E(K) = [1 + 1.47(a/c)^{0.5}$$

Is the elliptic integral of the second kind; and the finite area for the bending case ir:

$$B_w = 1 + \frac{F\left(\frac{a}{c}\right)G\left(\frac{c}{w}\right)H(\frac{a}{t})}{(0.2745)^2}$$

$$F\left(\frac{a}{c}\right) = 0.38 - 0.141\left(\frac{a}{c}\right) - 0.366(\frac{a}{c})^2 + 0.569(\frac{a}{c})^3 - o.246(\frac{a}{c})^4$$

$$G\left(\frac{c}{w}\right) = -0.0239 + 1.43a\left(\frac{c}{w}\right) - 2.984(\frac{c}{w})^2 + 7.822(\frac{c}{w})^3$$

$$H\left(\frac{a}{t}\right) = -0.0113 + 0.323\left(\frac{a}{t}\right) + 0.749(\frac{a}{t})^2 - 0.535(\frac{a}{t})^3$$

F(a/c) G(c/w) and H(a/t) are polynomial functions based on standard laboratory specimen size. At the surface θ=0 stress intensity factor:

$$K_I = (\frac{1+\gamma}{3+\gamma})\sigma_b\sqrt{\pi c}$$

For steel Poisson's ratio γ=0.3, therefore:

$$K_I = 0.394\sigma_b\sqrt{\pi c}$$

With interpolation in a/t:

$$K_I = [[M_{f(0)}\left(1 - 0.3\frac{a}{t}\right)\left(1 - \left(\frac{a}{t}\right)^{12}\right)] + \left[0.394.E(k).\left(\frac{a}{t}\right)^{12}.\sqrt{c/a}\right]\frac{\sigma_b}{E(k)}\sqrt{\pi a}$$

Where;

$$M_{f(0)} = [1.21 - 0.1\frac{a}{c} + 0.1(\frac{a}{c})^4]\sqrt{a/c}$$

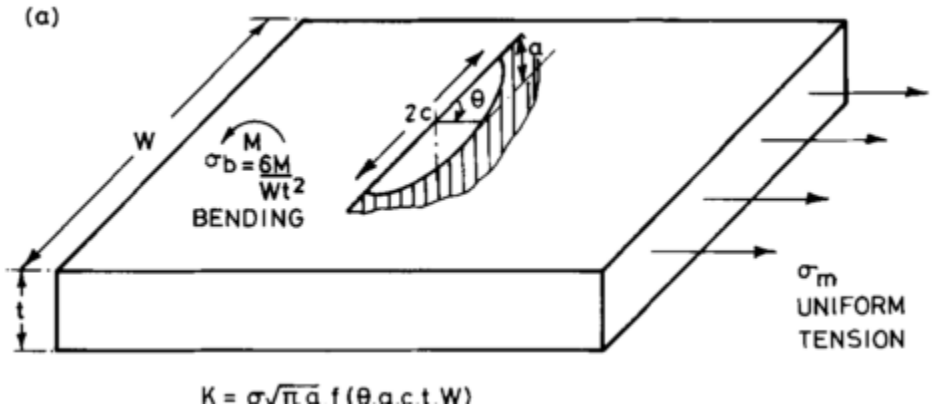

Figure 8-5: Schematic of a semi-elliptical crack from Scott and Thorpe 1981

Appendix D Calculation from standard BS EN ISO 12108 2012

Pre-cracking at the root of notched bend bars is the first step to establish sharp crack tip. Considering the material tested (316L) the lowest K_{max} value was set around 10MPa√m based on study. Reading of X value on DCPD device gives the potential difference across the cracked area, and Y is the reference value (of potential difference), to correct possible measures drift as followed:

$$\frac{X_{initial}}{Y_{initial}}$$

$$\frac{X_{n-1}}{Y_{n-1}} - requiredchange = \frac{X_n}{Y_n} = requireddreading$$

Each change in ratio value of 0.01, signifies that the crack has advanced and the stress intensity factor associated to the crack tip has increased, in order to keep the stress intensity factor value stable values of loading (P_{mean} and P_{ample}) need to be changed. Therefore by iterative step, of interrupted testing ΔK values will be slowly decreased in a fluctuation range 2%.

When the crack advance as reached 6 times the plastic zone size, the ΔK has to be decreased of 9%. (See plastic zone size calculation in section [159].

P_{mean} and P_{ample} are iteratively re-calculated and set up into testing machine. For that the following procedure is employed:

Crack length is calculated from voltage reading as followed:

$$\frac{a_{initial}}{W} = \alpha_{initial}$$

Then $\alpha_{initial}$ value and X_0 voltage reading are matched as followed:

$$\alpha_{initial} = \frac{AX_{initial}^3}{X_0} + \frac{BX_{inital}^2}{X_0} + \frac{CX_{initial}}{X_0} + D$$

In the above polynomial equation the A, B, C and D values were previously calculated from a calibration study on tin foil (these are baseline values for metallic components testing and local DCPD device used). From this polynomial equation, suitable X_0 value is fund, and will be used for crack length calculation from X readings. Potential variation and drift due to local temperature shift is corrected by using:

$$\frac{V}{V_0} = \frac{XY_{initial}}{YX_0}$$

Then these corrected reading ratio values is used in crack length calculation as follow:

$$\alpha = A(\frac{V}{V_0})^3 + B(\frac{V}{V_0})^2 + C\left(\frac{V}{V_0}\right) + D$$

Thereafter the compliance for SENB test specimen is calculated as follow:

$$Y = \frac{6\alpha^{1/2}}{(1+2\alpha)(1-\alpha)^{3/2}}[1.99 - \alpha(1-\alpha)(2.15 - 3.93\alpha + 2.7\alpha^2)]$$

With using the compliance a certain load to produce the desired ΔK value can be calculated, as follow:

$$\Delta P = \frac{\Delta K_{rep} B W^{0.5}}{Y \times 10^{1.5}}$$

In dead from this values of P_{max}, P_{min}, P_{ampl}, and P_{mean} can easily be calculated as followed:

$$P_{max} = \frac{\Delta P}{1-R}$$

$$P_{min} = RP_{max}$$

$$P_{ample} = \frac{P_{max} - P_{min}}{2}$$

$$P_{mean} = \frac{P_{max} + P_{min}}{2}$$

Then values are implemented into testing, iteratively avoiding an increase in ΔK value above when pre-crack advance. When pre-crack as reached the length of 6 plastic zone size, ΔK value is decrease of 6%:

$$6r_p = \frac{2000}{\pi}(\frac{\Delta K_{req}}{1-R})^2$$

ΔK is decreased that way until reach the steady value were no longer crack growth is recorded also called the threshold value, it the threshold value is not reached after an average of 4 decrease of 10%ΔK the crack growth experiment will be started anyway (in order to keep a sufficient amount material thickness to record growth).

Remark: It is important that the pre-crack is straight, and symmetrical in order not to corrupt crack length growth recording.

Finally the recording of crack growth is made with keeping P_{mean} and P_{ample} constant and record the crack growth rate.

Appendix E Recorded Crack growth

Once the crack growth values were recorded ΔK values need to be calculated. First X_0 value is calculated from the polynomial equation using X reading:

$$\alpha_{init} = \frac{AX_{initial}^3}{X_0} + \frac{BX_{inital}^2}{X_0} + \frac{CX_{initial}}{X_0} + D$$

This value of α is the corrected by the actual values of crack length at the end of pre-cracking test, and at the end of the final failure:

$$\alpha_r = \frac{\alpha_1 - \alpha_i}{\alpha_f - \alpha_1}$$

$$\alpha_1 + \alpha_r(\alpha_f - \alpha_1) = \alpha_{cal}$$

$$\alpha_1 \times W = \alpha_{cal}$$

Now the corrected value α is determined known as $\alpha_{cal}$the compliance can be found in similar manner than previously presented (but using the calibrated value):

$$Y = \frac{6\alpha_{cal}^{1/2}}{(1+2\alpha_{cal})(1-\alpha_{cal})^{3/2}}[1.99 - \alpha_{cal}(1-\alpha_{cal})(2.15 - 3.93\alpha_{cal} + 2.7\alpha_{cal}^2)]$$

Finally the ΔK value can be calculated by using similar equation the presented previously:

$$\Delta K = \frac{\Delta P \times Y \times 10^{1.5}}{BW^{0.5}}$$

In a natural manner the growth rate is calculated as followed:

$$\frac{da}{dN} = \frac{N_{i+1} - N_i}{a_{i+1} - a_i}$$

Thereafter the log da/dN by log ΔK can be plotted after smoothing whereby the gradient gives the values of coefficient C and exponent m of the Paris law equation:

$$\frac{da}{dN} = C\Delta K^m$$

$$\log\left(\frac{da}{dN}\right) = mlog\Delta K + \log C$$

References

[1] ISO/ASTM, “Additive manufacturing — General principles — Fundamentals and vocabulary,” *52900*, 2021.

[2] K. V. Wong and A. Hernandez, “A Review of Additive Manufacturing,” *ISRN Mech. Eng.*, vol. 2012, pp. 1–10, 2012.

[3] A. Busachi, J. Erkoyuncu, P. Colegrove, F. Martina, C. Watts, and R. Drake, “A review of Additive Manufacturing technology and Cost Estimation techniques for the defence sector,” *CIRP J. Manuf. Sci. Technol.*, vol. 19, pp. 117–128, 2017.

[4] J. O. Milewski, *Springer Series in Materials Science 258 Additive Manufacturing of Metals*. .

[5] J. J. Lewandowski and M. Seifi, “Metal Additive Manufacturing: A Review of Mechanical Properties,” *Annu. Rev. Mater. Res.*, vol. 46, no. 1, pp. 151–186, 2016.

[6] M. Ni, C. Chen, X. Wang, P. Wang, R. Li, and X. Zhang, “Anisotropic tensile behavior of in situ precipitation strengthened Inconel 718 fabricated by additive manufacturing,” *Mater. Sci. Eng. A*, vol. 701, no. June, pp. 344–351, 2017.

[7] D. Herzog, V. Seyda, E. Wycisk, and C. Emmelmann, “Acta Materialia Additive manufacturing of metals,” *Acta Mater.*, vol. 117, pp. 371–392, 2016.

[8] A. B. Spierings, T. L. Starr, and K. Wegener, “Fatigue performance of additive manufactured metallic parts,” *Rapid Prototyp. J.*, vol. 19, no. 2, pp. 88–94, 2013.

[9] M. Gorelik, “Additive manufacturing in the context of structural integrity,” *Int. J. Fatigue*, vol. 94, pp. 168–177, 2017.

[10] M. C. S. M.Y.He, F.E. Heredia, D.J. Wissuchek, “The mechanics of crack growth in layered materials,” *Acta Metall. Mater.*, vol. 41, no. 4, pp. 1223–1228, 1993.

[11] M. Vaezi, S. Chianrabutra, B. Mellor, and S. Yang, “Multiple material additive manufacturing - Part 1: A review: This review paper covers a decade of research on multiple material additive manufacturing technologies which can produce complex geometry parts with different materials,” *Virtual Phys. Prototyp.*, vol. 8, no. 1, pp. 19–50, 2013.

[12] M. Rafiee, R. D. Farahani, and D. Therriault, “Multi-Material 3D and 4D Printing : A Survey,” vol. 1902307, pp. 1–26, 2020.

[13] V. E. Beal, P. Erasenthiran, C. H. Ahrens, and P. Dickens, “Evaluating the use of functionally

graded materials inserts produced by selective laser melting on the injection moulding of plastics parts," *Proc. Inst. Mech. Eng. Part B J. Eng. Manuf.*, vol. 221, no. 6, pp. 945–954, 2007.

[14] K. Salonitis, J. Pandremenos, J. Paralikas, and G. Chryssolouris, "Multifunctional materials: Engineering applications and processing challenges," *Int. J. Adv. Manuf. Technol.*, vol. 49, no. 5–8, pp. 803–826, 2010.

[15] B. E. Carroll *et al.*, "Functionally graded material of 304L stainless steel and inconel 625 fabricated by directed energy deposition: Characterization and thermodynamic modeling," *Acta Mater.*, vol. 108, pp. 46–54, 2016.

[16] G. Udupa, S. S. Rao, and K. V. Gangadharan, "Functionally Graded Composite Materials: An Overview," *Procedia Mater. Sci.*, vol. 5, pp. 1291–1299, 2014.

[17] M. Horn *et al.*, "Multi-Material Additive Manufacturing – Recycling of binary Metal Powder Mixtures by Screening," *Procedia CIRP*, vol. 93, pp. 50–55, 2019.

[18] K. Shah, I. ul Haq, A. Khan, S. A. Shah, M. Khan, and A. J. Pinkerton, "Parametric study of development of Inconel-steel functionally graded materials by laser direct metal deposition," *Mater. Des.*, vol. 54, pp. 531–538, 2014.

[19] S. Chianrabutra, B. G. Mellor, and S. Yang, "A Dry Powder Material Delivery Device for Multiple Material Additive Manufacturing," *Proc. Solid Free. Fabr. Symp.*, pp. 36–48, 2014.

[20] J. Santosa, D. Jing, and S. Das, "Experimental and numerical study on the flow of fine powders from small-scale hoppers applied to SLS multi-material deposition–part I," *SFF Symp.*, pp. 620–627, 2002.

[21] P. Kumar, J. K. Santosa, E. Beck, and S. Das, "Direct-write deposition of fine powders through miniature hopper-nozzles for multi-material solid freeform fabrication," *Rapid Prototyp. J.*, vol. 10, no. 1, pp. 14–23, 2004.

[22] C. Wei, L. Li, X. Zhang, and Y. H. Chueh, "3D printing of multiple metallic materials via modified selective laser melting," *CIRP Ann.*, vol. 67, no. 1, pp. 245–248, 2018.

[23] Y. Chivel, "New approach to multi-material processing in selective laser melting," *Phys. Procedia*, vol. 83, pp. 891–898, 2016.

[24] K. Laappo, B. Jackson, and D. Wood, "Discrete multiple material selective laser sintering (M2SLS): experimental study of part processing," *Solid Free. Fabr. Symp.*, vol. 6, pp. 109–

119, 2003.

[25] O. M. Al-Jamal, S. Hinduja, and L. Li, “Characteristics of the bond in Cu-H13 tool steel parts fabricated using SLM,” *CIRP Ann. - Manuf. Technol.*, vol. 57, no. 1, pp. 239–242, 2008.

[26] S. L. Sing, L. P. Lam, D. Q. Zhang, Z. H. Liu, and C. K. Chua, “Interfacial characterization of SLM parts in multi-material processing: Intermetallic phase formation between AlSi10Mg and C18400 copper alloy,” *Mater. Charact.*, vol. 107, pp. 220–227, 2015.

[27] A. G. Demir and B. Previtali, “Multi-material selective laser melting of Fe/Al-12Si components,” *Manuf. Lett.*, vol. 11, pp. 8–11, 2017.

[28] D. J. Newell *et al.*, “Mitigation of scan strategy e ff ects and material anisotropy through supersolvus annealing in LPBF IN718 ☆,” *Mater. Sci. Eng. A*, vol. 764, no. April, p. 138230, 2019.

[29] S. Suresh, “Fatigue of Materials,” in *Fatigue of Materials*, Cambridge University Press, Ed. Cambridge University Press, 1998.

[30] W. D. Callister and J. Wiley, *Materials Science and Engineering, an introduction*. 2007.

[31] U. Krupp, *Fatigue Crack Propagation in Metals and Alloys*. Wiley-VCH, 2007.

[32] P. Chowdhury and H. Sehitoglu, “Mechanisms of fatigue crack growth – a critical digest of theoretical developments,” pp. 1–23, 2016.

[33] J. C. Newman, I. S. Raju, J. Lewis, and G. Sines, “Stress intensity factor equations for cracks in three-dimensional finite bodies,” *Fracture Mechanics*, vol. 1, no. January 1983. pp. 238–269, 1983.

[34] J. C. N. Jr, “Fatigue-life prediction methodology using small-crack theory,” vol. 21, pp. 109–119, 1999.

[35] “https://www.fidelisfea.com/post/plane-stress-vs-plane-strain-what-are-they-and-which-should-you-choose.”

[36] T. L. Ewa MARCISZ, Adam Neslony, “Concept of fatigue for determining characteriatics of materials with strengthening,” *Mater. Sci. Forum*, vol. 726, pp. 43–48, 2012.

[37] M. S. Pham, C. Solenthaler, K. G. F. Janssens, and S. R. Holdsworth, “Dislocation structure evolution and its effects on cyclic deformation response of AISI 316L stainless steel,” *Mater. Sci. Eng. A*, vol. 528, no. 7–8, pp. 3261–3269, 2011.

[38] J. Vogt and P. Villechaise, “Study of crack initiation in low-cycle fatigue of an austenitic stainless steel,” vol. 072, 2011.

[39] R. Strubbia, S. Hereñú, A. Giertler, I. Alvarez-Armas, and U. Krupp, “Experimental characterization of short crack nucleation and growth during cycling in lean duplex stainless steels,” *Int. J. Fatigue*, vol. 65, pp. 58–63, 2014.

[40] W. Wang, T. Liu, X. Cao, Y. Lu, and T. Shoji, “In-situ observation on twin boundary evolution and crack initiation behavior during tensile test on 316L austenitic stainless steel,” *Mater. Charact.*, vol. 132, no. August, pp. 169–174, 2017.

[41] H. D. Carlton, A. Haboub, G. F. Gallegos, D. Y. Parkinson, and A. A. Macdowell, “Damage evolution and failure mechanisms in additively manufactured stainless steel,” *Mater. Sci. Eng. A*, vol. 651, pp. 406–414, 2016.

[42] S. Mohd Yusuf, M. Nie, Y. Chen, S. Yang, and N. Gao, “Microstructure and corrosion performance of 316L stainless steel fabricated by Selective Laser Melting and processed through high-pressure torsion,” *J. Alloys Compd.*, vol. 763, pp. 360–375, 2018.

[43] B. Künkler, O. Düber, P. Köster, U. Krupp, C. P. Fritzen, and H. J. Christ, “Modelling of short crack propagation - Transition from stage I to stage II,” *Eng. Fract. Mech.*, vol. 75, no. 3–4, pp. 715–725, 2008.

[44] D. Kwon, H. Lahodny, and A. Brückner-Foit, “Limitations of growth regimes for cracks initiated in smooth fatigue specimens,” *Theor. Appl. Fract. Mech.*, vol. 16, no. 1, pp. 63–71, 1991.

[45] K. J. Miller, “the Behaviour of Short Fatigue Cracks a N D Part 11-a General Summary,” vol. 10, no. 2, pp. 93–113, 1987.

[46] Y. Sugimura and S. S. Lim, P G, C.F. Shih, “Fracture normal to a bimaterial interface : effect of plasticity on crack-tip shielding and amplification,” *Acta Metall. Mater.*, vol. 43, no. 3, pp. 1157–1169, 1995.

[47] O. Kolednik, “The yield stress gradient effect in inhomogeneous materials,” *Int. J. solids Struct. 37*, vol. 37, pp. 781–808, 2000.

[48] J. Zechner and O. Kolednik, “Fracture resistance of aluminum multilayer composites,” *Eng. Fract. Mech.*, vol. 110, pp. 489–500, 2013.

[49] A. Burke-veliz, S. Syngellakis, and P. A. S. Reed, “Assessment of three-dimensional crack

growth in ductile layered material systems," *Eng. Fract. Mech.*, vol. 88, pp. 15–27, 2012.

[50] S. Lu, R. Cook, Y. Zhang, and P. Reed, "Effect on overall fatigue performance of varying thickness of an intermetallic sublayer within a soft multilayer coating," *Int. J. Fatigue*, vol. 146, no. November 2020, p. 106155, 2021.

[51] S. M. Yusuf and N. Gao, "Influence of energy density on metallurgy and properties in metal additive manufacturing," *Mater. Sci. Technol.*, vol. 33, no. 11, pp. 1269–1289, 2017.

[52] Y. Liu, Y. Yang, S. Mai, D. Wang, and C. Song, "Investigation into spatter behavior during selective laser melting of AISI 316L stainless steel powder," *Mater. Des.*, vol. 87, pp. 797–806, 2015.

[53] A. Townsend, N. Senin, L. Blunt, R. K. Leach, and J. S. Taylor, "Surface texture metrology for metal additive manufacturing: a review," *Precis. Eng.*, vol. 46, pp. 34–47, 2016.

[54] S. K. Everton, M. Hirsch, P. I. Stavroulakis, R. K. Leach, and A. T. Clare, "Review of in-situ process monitoring and in-situ metrology for metal additive manufacturing," *Mater. Des.*, vol. 95, pp. 431–445, 2016.

[55] M. . Griffith *et al.*, "Understanding thermal behavior in the LENS process," *Mater. Des.*, vol. 20, no. 2–3, pp. 107–113, 1999.

[56] A. S. Wu, D. W. Brown, M. Kumar, G. F. Gallegos, and W. E. King, "An Experimental Investigation into Additive Manufacturing-Induced Residual Stresses in 316L Stainless Steel," *Metall. Mater. Trans. A Phys. Metall. Mater. Sci.*, vol. 45, no. 13, pp. 6260–6270, 2014.

[57] X. Wu, "A review of laser fabrication of metallic engineering components and of materials," *Mater. Sci. Technol.*, vol. 23, no. 6, pp. 631–640, 2007.

[58] K. Georgilas, "Multiscale experimental and computational techniques for optimising selective laser melting additive manufacturing process parameters," 2020.

[59] Q. Saby *et al.*, "Laser Powder Bed Fusion printability of cobalt-free steel powders for manufacturing injection molds," vol. 44, no. March, 2021.

[60] W. J. Sames, F. A. List, S. Pannala, R. R. Dehoff, and S. S. Babu, "The metallurgy and processing science of metal additive manufacturing," *Int. Mater. Rev.*, vol. 61, no. 5, pp. 315–360, 2016.

[61] R. H. Bochuan Liu, Ricky Wildman, Christopher Tuck, Ian Ashcroft, "Investigation the effect of particles size distribution on processing parameters optimisation in selective laser melting

process," *Addit. Manuf. Res. Group, Loughbrgh. Univ.*, no. mm, pp. 227–238.

[62] D. Powell, A. E. W. Rennie, L. Geekie, and N. Burns, "Understanding powder degradation in metal additive manufacturing to allow the upcycling of recycled powders," *J. Clean. Prod.*, vol. 268, p. 122077, 2020.

[63] L. N. Carter, C. Martin, P. J. Withers, and M. M. Attallah, "The influence of the laser scan strategy on grain structure and cracking behaviour in SLM powder-bed fabricated nickel superalloy," *J. Alloys Compd.*, vol. 615, pp. 338–347, 2014.

[64] M. L. Pace *et al.*, "3D additive manufactured 316L components microstructural features and changes induced by working life cycles," *Appl. Surf. Sci.*, vol. 418, pp. 437–445, 2017.

[65] Y. Zhong, L. Liu, S. Wikman, D. Cui, and Z. Shen, "Intragranular cellular segregation network structure strengthening 316L stainless steel prepared by selective laser melting," *J. Nucl. Mater.*, vol. 470, pp. 170–178, 2016.

[66] M. S. Pham, B. Dovgyy, and P. A. Hooper, "Twinning induced plasticity in austenitic stainless steel 316L made by additive manufacturing," *Mater. Sci. Eng. A*, vol. 704, no. April, pp. 102–111, 2017.

[67] N. Hansen, "Hall – Petch relation and boundary strengthening," vol. 51, pp. 801–806, 2004.

[68] T. Peng and C. Chen, "Influence of energy density on energy demand and porosity of 316L stainless steel fabricated by selective laser melting," *Int. J. Precis. Eng. Manuf. Technol.*, vol. 5, no. 1, pp. 55–62, 2018.

[69] R. R. Unocic and J. N. DuPont, "Process Efficiency Measurements in the Laser Engineered Net Shaping Process," *Metall. Mater. Trans. B Process Metall. Mater. Process. Sci.*, vol. 35, no. 1, pp. 143–152, 2004.

[70] Y. Lu *et al.*, "Study on the microstructure, mechanical property and residual stress of SLM Inconel-718 alloy manufactured by differing island scanning strategy," *Opt. Laser Technol.*, vol. 75, pp. 197–206, 2015.

[71] L. N. Carter, M. M. Attallah, and R. C. Reed, "Laser powder bed fabrication of nickel-base superalloys: influence of parameters; characterisation, quantification and mitigation of cracking," *Superalloys 2012*, pp. 577–586, 2012.

[72] M. D. Sangid *et al.*, "Role of heat treatment and build orientation in the microstructure sensitive deformation characteristics of IN718 produced via SLM additive manufacturing,"

Addit. Manuf., vol. 22, no. January, pp. 479–496, 2018.

[73] Y. Kuo, S. Horikawa, and K. Kakehi, "Scripta Materialia Effects of build direction and heat treatment on creep properties of Ni-base superalloy built up by additive manufacturing," *SMM*, vol. 129, pp. 74–78, 2017.

[74] J. Benzing, N. Hrabe, T. Quinn, R. White, R. Rentz, and M. Ahlfors, "Hot isostatic pressing (HIP) to achieve isotropic microstructure and retain as-built strength in an additive manufacturing titanium alloy," *Mater. Lett.*, vol. 257, p. 126690, 2019.

[75] A. Kaletsch, S. Qin, S. Herzog, and C. Broeckmann, "Influence of high initial porosity introduced by laser powder bed fusion on the fatigue strength of Inconel 718 after post-processing with hot isostatic pressing," *Addit. Manuf.*, vol. 47, no. August, p. 102331, 2021.

[76] A. Rezaei *et al.*, "Materials Science & Engineering A Contribution of hot isostatic pressing on densification , microstructure evolution , and mechanical anisotropy of additively manufactured IN718 Ni-based superalloy," *Mater. Sci. Eng. A*, vol. 823, no. July, p. 141721, 2021.

[77] M. M. Kirka, D. A. Greeley, C. Hawkins, and R. R. Dehoff, "Effect of anisotropy and texture on the low cycle fatigue behavior of Inconel 718 processed via electron beam melting q," *Int. J. Fatigue*, vol. 105, pp. 235–243, 2017.

[78] M. E. Aydinöz, F. Brenne, M. Schaper, C. Schaak, W. Tillmann, and J. Nellesen, "Materials Science & Engineering A On the microstructural and mechanical properties of post-treated additively manufactured Inconel 718 superalloy under quasi-static and cyclic loading," *Mater. Sci. Eng. A*, vol. 669, pp. 246–258, 2016.

[79] Ó. Teixeira, F. J. G. Silva, and P. Ferreira, "Quality and Residual Stresses of the Ti – 6Al – 4V Parts Produced by Additive Manufacturing," *Metals (Basel).*, no. Figure 1, 2020.

[80] X. Chen, J. Li, X. Cheng, H. Wang, and Z. Huang, "Materials Science & Engineering A E ff ect of heat treatment on microstructure , mechanical and corrosion properties of austenitic stainless steel 316L using arc additive manufacturing," *Mater. Sci. Eng. A*, vol. 715, no. July 2017, pp. 307–314, 2018.

[81] S. Cheruvathur, E. A. Lass, and C. E. Campbell, "Additive Manufacturing of 17-4 PH Stainless Steel : Post-processing Heat Treatment to Achieve Uniform Reproducible Microstructure," *Miner. Met. Mater. Soc.*, vol. 68, no. 3, pp. 930–942, 2016.

[82] R. Lesley, C. Herrera, D. Maribel, P. Rangel, and A. Fernando, "A Short Review on Wrought

Austenitic Stainless Steels at High Temperatures : Processing , Microstructure , Properties and Performance," vol. 10, no. 4, pp. 453–460, 2007.

[83] Stainless Steels for Design Engineers, "Austenitic Stainless Steels," *ASM Int.*, 2008.

[84] A. F. Padilha, "Decomposition of Austenite in Austenitic Stainless Steels," no. January, 2002.

[85] D. Wang, C. Song, Y. Yang, and Y. Bai, "Investigation of crystal growth mechanism during selective laser melting and mechanical property characterization of 316L stainless steel parts," *Mater. Des.*, vol. 100, pp. 291–299, 2016.

[86] K. Saeidi, X. Gao, Y. Zhong, and Z. J. Shen, "Hardened austenite steel with columnar sub-grain structure formed by laser melting," *Mater. Sci. Eng. A*, vol. 625, pp. 221–229, 2015.

[87] T. Niendorf and F. Brenne, "Steel showing twinning-induced plasticity processed by selective laser melting - An additively manufactured high performance material," *Mater. Charact.*, vol. 85, pp. 57–63, 2013.

[88] AMS2759/4D, "Heat Treatment Austenitic Corrosion-Resistant Steel Parts," *SAE Int.*, 2019.

[89] H. Yin, M. Song, P. Deng, L. Li, B. C. Prorok, and X. Lou, "Thermal stability and microstructural evolution of additively manufactured 316L stainless steel by laser powder bed fusion at 500 – 800 ℃," *Addit. Manuf.*, vol. 41, no. September 2020, pp. 20–22, 2021.

[90] M. L. M. Sistiaga, S. Nardone, C. Hautfenne, and J. Van Humbeeck, "Effect of Heat Treatment Of 316L Stainless Steel Produced by Selective Laser Melting (SLM)," *Proc. 26th Annu. Int. Solid Free. Fabr. Symp. – An Addit. Manuf. Conf.*, pp. 558–565, 2016.

[91] I. Tolosa, F. Garciandía, F. Zubiri, F. Zapirain, and A. Esnaola, "Study of mechanical properties of AISI 316 stainless steel processed by 'selective laser melting', following different manufacturing strategies," *Int. J. Adv. Manuf. Technol.*, vol. 51, no. 5–8, pp. 639–647, 2010.

[92] J. Suryawanshi, K. G. Prashanth, and U. Ramamurty, "Mechanical behavior of selective laser melted 316L stainless steel," *Mater. Sci. Eng. A*, vol. 696, no. April, pp. 113–121, 2017.

[93] G. T. Gray *et al.*, "Structure/property (constitutive and spallation response) of additively manufactured 316L stainless steel," *Acta Mater.*, vol. 138, pp. 140–149, 2017.

[94] S. Leuders, T. Lieneke, S. Lammers, T. Tröster, and T. Niendorf, "On the fatigue properties of metals manufactured by selective laser melting - The role of ductility," *J. Mater. Res.*, vol. 29, no. 17, pp. 1911–1919, 2014.

[95] M. Zhang *et al.*, “Fatigue and fracture behaviour of laser powder bed fusion stainless steel 316L: Influence of processing parameters,” *Mater. Sci. Eng. A*, vol. 703, no. April, pp. 251–261, 2017.

[96] E. Hietikko, M. Hoffren, and M. Kesonen, “The Fatigue of Additive Manufacturing Metal Parts,” vol. 2, no. 6, pp. 219–224, 2015.

[97] A. Riemer, S. Leuders, M. Thöne, H. A. Richard, T. Tröster, and T. Niendorf, “On the fatigue crack growth behavior in 316L stainless steel manufactured by selective laser melting,” *Eng. Fract. Mech.*, vol. 120, pp. 15–25, 2014.

[98] P. Ganesh *et al.*, “Fatigue Crack Propagation and Fracture Toughness of Laser Rapid Manufactured Structures of AISI 316L Stainless Steel,” *Metallogr. Microstruct. Anal.*, vol. 3, no. 1, pp. 36–45, 2014.

[99] C. Yu *et al.*, “Effect of Build Direction on Fatigue Performance of L - PBF 316L Stainless Steel,” *Acta Metall. Sin. (English Lett.*, vol. 33, no. 4, pp. 539–550, 2020.

[100] M. Zhang, C. Sun, X. Zhang, J. Wei, D. Hardacre, and H. Li, “High cycle fatigue and ratcheting interaction of laser powder bed fusion stainless steel 316L : Fracture behaviour and stress-based modelling,” *Int. J. Fatigue*, vol. 121, no. December 2018, pp. 252–264, 2019.

[101] M. Zhang *et al.*, “Effect of heat treatment on fatigue crack initiation of laser powder bed fusion stainless steel 316L,” vol. 22006, pp. 1–6, 2018.

[102] B. Voloskov, S. Evlashin, S. Dagesyan, and S. Abaimov, “Very High Cycle Fatigue Behavior of Additively,” *Materials (Basel).*, pp. 1–11, 2020.

[103] L. Cui *et al.*, “Journal of Materials Science & Technology Superior low cycle fatigue property from cell structures in additively manufactured 316L stainless steel,” *J. Mater. Sci. Technol.*, vol. 111, pp. 268–278, 2022.

[104] F. Brenne and T. Niendorf, “Materials Science & Engineering A Damage tolerant design by microstructural gradation – Influence of processing parameters and build orientation on crack growth within additively processed 316L,” *Mater. Sci. Eng. A*, vol. 764, no. June, p. 138186, 2019.

[105] V. A. Popovich, E. V. Borisov, A. A. Popovich, V. S. Sufiiarov, D. V. Masaylo, and L. Alzina, “Functionally graded Inconel 718 processed by additive manufacturing: Crystallographic texture, anisotropy of microstructure and mechanical properties,” *Mater. Des.*, vol. 114, pp. 441–449, 2017.

[106] M. Calandri *et al.*, “Solution Treatment Study of Inconel 718 Produced by SLM Additive Technique in View of the Oxidation Resistance,” *Adv. Eng. Mater.*, vol. 1800351, pp. 1–16, 2018.

[107] B. Reppich, “Some new aspects concerning particle hardening mechanisms in γ’ precipitating Ni-base alloys—I. Theoretical concept,” *Acta Metall.*, vol. 30, no. 1, pp. 87–94, 1982.

[108] B. Reppich, “Some new aspects concerning particle hardening mechanisms in γ’ precipitating nickel-base alloys—II. Experiments,” *Acta Metall.*, vol. 30, no. 1, pp. 95–104, 1982.

[109] W. M. Tucho, P. Cuvillier, A. Sjolyst-kverneland, and V. Hansen, “Materials Science & Engineering A Microstructure and hardness studies of Inconel 718 manufactured by selective laser melting before and after solution heat treatment,” *Mater. Sci. Eng. A*, vol. 689, no. February, pp. 220–232, 2017.

[110] P. Petrzak, K. Kowalski, and M. Blicharski, “Analysis of Phase Transformations in Inconel 625 Alloy during Annealing,” *Acta Phys. Pol. A*, vol. 130, no. 4, 2016.

[111] J. Choi, G. Shin, S. Yang, D. Yang, and J. Lee, “Densi fi cation and microstructural investigation of Inconel 718 parts fabricated by selective laser melting,” *Powder Technol.*, vol. 310, pp. 60–66, 2017.

[112] M. Cloots, P. J. Uggowitzer, and K. Wegener, “Investigations on the microstructure and crack formation of IN738LC samples processed by selective laser melting using Gaussian and doughnut pro fi les,” *JMADE*, vol. 89, pp. 770–784, 2016.

[113] N. J. Harrison and K. Mumtaz, “ScienceDirect Reduction of micro-cracking in nickel superalloys processed by Selective Laser Melting : A fundamental alloy design approach,” *Acta Mater.*, vol. 94, pp. 59–68, 2015.

[114] J. Schneider, B. Lund, and M. Fullen, “Effect of heat treatment variations on the mechanical properties of Inconel 718 selective laser melted specimens,” *Addit. Manuf.*, vol. 21, no. March, pp. 248–254, 2018.

[115] E. W. Hovig, A. S. Azar, F. Grytten, K. Sørby, and E. Andreassen, “Determination of Anisotropic Mechanical Properties for Materials Processed by Laser Powder Bed Fusion,” *Adv. Mater. Sci. Eng.*, vol. 2018, 2018.

[116] F. R. Caliari *et al.*, “Study of the Secondary Phases in Inconel 718 Aged Superalloy Using Thermodynamics Modeling,” *Key Eng. Mater.*, vol. 553, pp. 23–28, 2013.

[117] AMS5383, “Nickel Alloy, Corrosion and Heat-Resistant, Investment Casting, 52.5Ni-19Cr-3.0Mo-5.1Cb(Nb)-0.9Ti-0.6Al-18Fe, Vacuum Melted Homogenization and Solution Heat Treated,” *SAE Int.*

[118] AMS5662, “NickelAlloy, Corrosion and Heat Resistant, Bars, Forging, and Ring 52.5Ni19Cr3.0Mo5.1Cb0.9Ti0.5Al18Fe, Consumable Electrode or Vacuum Induction Melted 1775F Solution Heat Treated, Precipitation Hardenable,” *SAE Int.*

[119] J. W. Brooks and P. J. Bridges, “Metallurgical Stability of Inconel Alloy 718,” pp. 33–42, 1988.

[120] A. Thomas, M. El-wahabi, J. M. Cabrera, and J. M. Prado, “High temperature deformation of Inconel 718,” *Mater. Process. Technol.*, vol. 177, pp. 469–472, 2006.

[121] O. M. D. M. Messé, R. Muñoz-moreno, T. Illston, S. Baker, and H. J. Stone, “Metastable carbides and their impact on recrystallisation in IN738LC processed by selective laser melting,” *Addit. Manuf.*, vol. 22, no. November 2017, pp. 394–404, 2018.

[122] Tucho, Wakshum M, Vidar Hansen, “Studies of Post-Fabrication Heat Treatment of L-PBF-Inconel 718: Effects of Hold Time on Microstructure, Annealing Twins, and Hardness,” *Metals (Basel).*, no. 11, p. 266, 2021.

[123] D. Zhang, W. Niu, X. Cao, and Z. Liu, “Effect of standard heat treatment on the microstructure and mechanical properties of selective laser melting manufactured Inconel,” *Mater. Sci. Eng. A*, vol. 644, pp. 32–40, 2015.

[124] X. Li *et al.*, “Effect of heat treatment on microstructure evolution of Inconel 718 alloy fabricated by selective laser melting,” *J. Alloys Compd.*, vol. 764, 2018.

[125] M. Ahmad Mostafa, Medraj, “Structure, Texture and Phases in 3D Printed IN718 Alloy Subjected to Homogenization and HIP Treatments,” *Metals (Basel).*, vol. 7, no. 196, pp. 1–23, 2017.

[126] T. Trosch, J. Strößner, R. Völkl, and U. Glatzel, “Microstructure and mechanical properties of selective laser melted Inconel 718 compared to forging and casting,” *Mater. Lett.*, vol. 164, pp. 428–431, 2016.

[127] X. Zhao, J. Chen, X. Lin, and W. Huang, “Study on microstructure and mechanical properties of laser rapid forming Inconel 718,” *Mater. Sci. Eng. A*, vol. 478, pp. 119–124, 2008.

[128] E. Chlebus, K. Gruber, B. Ku, J. Kurzac, and T. Kurzynowski, “Effect of heat treatment on the microstructure and mechanical prop- erties of Inconel 718 processed by selective laser

melting," *Mater. Sci. Eng. A*, vol. 639, pp. 647–655, 2015.

[129] F. Liu *et al.*, "The effect of laser scanning path on microstructures and mechanical properties of laser solid formed nickel-base superalloy Inconel 718," *J. Alloys Compd.*, vol. 509, no. 13, pp. 4505–4509, 2011.

[130] D. Deng, R. Lin, H. Brodin, and J. Moverare, "Microstructure and mechanical properties of Inconel 718 produced by selective laser melting : Sample orientation dependence and effects of post heat treatments," *Mater. Sci. Eng. A*, vol. 713, no. July 2017, pp. 294–306, 2018.

[131] P. Kanagarajah, F. Brenne, T. Niendorf, and H. J. Maier, "Inconel 939 processed by selective laser melting: Effect of microstructure and temperature on the mechanical properties under static and cyclic loading," *Mater. Sci. Eng. A*, vol. 588, pp. 188–195, 2013.

[132] P. Kanagarajah, F. Brenne, T. Niendorf, and H. J. Maier, "Inconel 939 processed by selective laser melting : Effect of microstructure and temperature on the mechanical properties under static and cyclic loading," *Mater. Sci. Eng. A*, vol. 588, pp. 188–195, 2013.

[133] S. Neumeier *et al.*, "Microstructural design of Ni-base alloys for high-temperature applications : impact of heat treatment on microstructure and mechanical properties after selective laser melting," *Prog Addit. Manuf.*, pp. 141–151, 2016.

[134] S. Sui, J. Chen, E. Fan, H. Yang, X. Lin, and W. Huang, "Materials Science & Engineering A The in fl uence of Laves phases on the high-cycle fatigue behavior of laser additive manufactured Inconel 718," *Mater. Sci. Eng. A*, vol. 695, no. February, pp. 6–13, 2017.

[135] L. Kunz, G. Nicoletto, and A. Bac, "Long fatigue crack growth in Inconel 718 produced by selective laser melting," *Int. J. Fatigue*, vol. 92, pp. 499–506, 2016.

[136] S. Kim, H. Choi, J. Lee, and S. Kim, "Room and elevated temperature fatigue crack propagation behavior of Inconel 718 alloy fabricated by laser powder bed fusion," *Int. J. Fatigue*, vol. 140, no. March, p. 105802, 2020.

[137] A. Bandyopadhyay and B. Heer, "Additive manufacturing of multi-material structures," *Mater. Sci. Eng. R Reports*, vol. 129, no. April, pp. 1–16, 2018.

[138] S. Hasanov, S. Alkunte, M. Rajeshirke, A. Gupta, O. Huseynov, and I. Fidan, "Review on Additive Manufacturing of Multi-Material Parts : Progress and Challenges," 2022.

[139] X. Yao, S. K. Moon, G. Bi, and J. Wei, "A multi-material part design framework in additive

manufacturing," *Int. J. Adv. Manuf. Technol.*, pp. 2111–2119, 2018.

[140] M. Soodi, S. H. Masood, and M. Brandt, "Tensile strength of functionally graded and wafer layered structures produced by direct metal deposition," *Rapid Prototyp. J.*, vol. 20, no. 5, pp. 360–368, 2014.

[141] T. Gualtieri and A. Bandyopadhyay, "Additive manufacturing of compositionally gradient metal-ceramic structures: Stainless steel to vanadium carbide," *Mater. Des.*, vol. 139, pp. 419–428, 2018.

[142] I. Shishkovsky, F. Missemer, and I. Smurov, "Metal matrix composites with ternary intermetallic inclusions fabricated by laser direct energy deposition," *Compos. Struct.*, vol. 183, no. 1, pp. 663–670, 2018.

[143] A. Hinojos *et al.*, "Joining of Inconel 718 and 316 Stainless Steel using electron beam melting additive manufacturing technology," *Mater. Des.*, vol. 94, pp. 17–27, 2016.

[144] S. Rzepa, J. Vav, D. Melzer, D. Jan, and M. Koukolíkov, "Structural integrity and mechanical properties of the functionally graded material based on 316L / IN718 processed by DED technology," *Mater. Sci. Eng. R*, vol. 811, no. March, 2021.

[145] A. Yadollahi and N. Shamsaei, "Additive manufacturing of fatigue resistant materials: Challenges and opportunities," *Int. J. Fatigue*, vol. 98, pp. 14–31, 2017.

[146] ASTM, "B822 - Standard Test Method for Particle Size Distribution of Metal Powders and Related Compounds by Light Scattering," 2020.

[147] B213-20, "Standard Test Methods for Flow Rate of Metal Powders Using the Hall Flowmeter Funnel," *ASTM Int.*, 2020.

[148] ASTM, "B212 - Standard Test Method for Apparent Density of Free-Flowing Metal Powders Using the Hall Flowmeter Funnel," 2021.

[149] ASTM, "B527-15 - Standard Test Method for Tap Density of Metal Powders and Compounds," 2015.

[150] G. Soundarapandiyan, M. E. Fitzpatrick, C. Johnston, and R. H. U. Khan, "A technical review of the challenges of powder recycling in the laser powder bed fusion additive manufacturing process," *J. Eng.*, no. August 2020, pp. 1–7, 2021.

[151] Sandmayer, "Specification Sheet : Alloy 316 / 316L," no. 1, pp. 9–11, 2014.

[152] Special metals, “INCONEL alloy 718,” *Spec. Met.*, 2007.

[153] Q. Jia and D. Gu, “Selective laser melting additive manufacturing of Inconel 718 superalloy parts : Densification , microstructure and properties,” *J. Alloys Compd.*, vol. 585, pp. 713–721, 2014.

[154] R. Saluja, “The emphasis of phase transformations and alloying constituents on hot cracking susceptibility of type 304L and 316L stainless steel welds,” *Int. Eng. Sci. Technol.*, vol. 4, no. 05, pp. 2206–2216, 2012.

[155] W. Zhou, R. P. Apkarian, and Z. L. Wang, “Fundamentals of Scanning Electron Microscopy,” *Scanning Microsc. Nanotechnol.*, 2006.

[156] BS EN ISO 6507, “Vickers hardness test.,” *Stand. Test Methods Met. Mater.*, 2018.

[157] ASTM, “E8/E8M A. Standard test Methods for Tension Testing of Metallic Materials,” *ASTM Int.*, vol. 16ae1.

[158] H. E. Boyer, “Fatigue Testing,” *Atlas fatigue curves, ASM Int.*, 1986.

[159] BS ISO 12108, “Metallic materials — Fatigue testing — Fatigue crack growth method,” *Int. Stand.*, 2012.

[160] M. Naebe and K. Shirvanimoghaddam, “Functionally graded materials: A review of fabrication and properties,” *Appl. Mater. Today*, vol. 5, pp. 223–245, 2016.

[161] B. E. Carroll *et al.*, “Acta Materialia Functionally graded material of 304L stainless steel and inconel 625 fabricated by directed energy deposition : Characterization and thermodynamic modeling,” *Acta Mater.*, vol. 108, pp. 46–54, 2016.

[162] S. J. Zinkle and G. S. Was, “Materials challenges in nuclear energy,” *Acta Mater.*, vol. 61, no. 3, pp. 735–758, 2013.

[163] C. Wei and E. T. Al, “Multiple-Material selective laser melting : a new approach :,” *laser user*, no. 89, pp. 18–19, 2018.

[164] O. Kolednik, J. Zechner, and J. Predan, “Scripta Materialia Improvement of fatigue life by compliant and soft interlayers,” *SMM*, vol. 113, pp. 1–5, 2016.

[165] T. Persenot, G. Martin, R. Dendievel, J. Bu, and E. Maire, “Materials Characterization Enhancing the tensile properties of EBM as-built thin parts : Effect of HIP and chemical etching,” *Mater. Characterisation*, vol. 143, no. November 2017, pp. 82–93, 2018.

[166] Y. M. Wang *et al.*, “Additively manufactured hierarchical stainless steels with high strength and ductility,” *Nat. Mater.*, vol. 17, no. 1, pp. 63–70, 2018.

[167] K. Saeidi, X. Gao, Y. Zhong, and Z. J. Shen, “Hardened austenite steel with columnar sub-grain structure formed by laser melting,” *Mater. Sci. Eng. A*, vol. 625, pp. 221–229, 2015.

[168] M.C.Flemings, “Solidification Processing,” *Metall. Trans.*, vol. 5, 1974.

[169] Z. W. Chen, M. A. L. Phan, and K. Darvish, “Grain growth during selective laser melting of a Co – Cr – Mo alloy,” *J. Mater. Sci.*, vol. 52, no. 12, pp. 7415–7427, 2017.

[170] G. Posch, R. Vallant, W. Klagges, and H. Cerjak, “Influence of Niobium on mechanical properties and hot crack susceptibility of Nickel-base cored-wire weld metal type 70 / 20 and 70 / 15 Cracking in Nickelbasis-weldments Solidification cracking,” *Proc.*, vol. 2000, 2000.

[171] S. Wen, K. Chen, and Y. Che, “Tailored microstructure and robust joint of Inconel 718 / 316L bimetallic multi-material fabricated by selective laser melting,” *Res. Sq. pre-prints*.

[172] Z. Jones, K. Cooper, and K. Chou, “Characterisation of Microstructure and Mechanical Property of Inconel 718 from Selective Laser Melting,” *Int. mafufacturing Sci. Eng.*, no. January 2015, 2017.

[173] P. Mercelis and J. Kruth, “Residual stresses in selective laser sintering and selective laser melting,” *Rapid Prototyp. J.*, vol. 5, no. June, pp. 254–265, 2006.

[174] Z. Wang, E. Denlinger, P. Michaleris, A. D. Stoica, D. Ma, and A. M. Beese, “Residual stress mapping in Inconel 625 fabricated through additive manufacturing : Method for neutron diffraction measurements to validate thermomechanical model predictions ☆,” *JMADE*, vol. 113, pp. 169–177, 2017.

[175] S. D. K. John N Dupont, John CLippold, *Welding Metallurgy and Weldalitity of Nickel-base alloys*. 2009.

[176] J. F. Radavich, “The physical metallurgy of cast and wrought alloy 718,” *Sch. Mater. Eng. Purdue Univ.*, 1989.

[177] T. Keil, E. Bruder, and K. Durst, “Exploring the compositional parameter space of high-entropy alloys using a diffusion couple approach,” *Mater. Des.*, vol. 176, p. 107816, 2019.

[178] R. J. Vikram, A. Singh, and S. Suwas, “Effect of heat treatment on the modification of microstructure of selective laser melted (SLM) IN718 and its consequences on mechanical

behavior," *J. Mater. Sci.*, no. June, 2020.

[179] ASTM F3055, "Standard Specification for Additive Manufacturing Nickel Alloy (UNS N07718) with Powder Bed Fusion," *ASTM Int.*, vol. 14a, 2021.

[180] M. S. Duval-chaneac *et al.*, "Fatigue crack growth in IN718 / 316L multi-materials layered structures fabricated by laser powder bed fusion," *Int. J. Fatigue*, vol. 152, no. April, p. 106454, 2021.

[181] X. Mei, X. Wang, Y. Peng, H. Gu, G. Zhong, and S. Yang, "Materials Science & Engineering A Interfacial characterization and mechanical properties of 316L stainless steel / inconel 718 manufactured by selective laser melting," *Mater. Sci. Eng. A*, vol. 758, no. January, pp. 185–191, 2019.

[182] D. Wang *et al.*, "Recent progress on additive manufacturing of multi-material structures with laser powder bed fusion," 2022.

[183] C. Wei and L. Li, "Recent progress and scientific challenges in multi- material additive manufacturing via laser-based powder bed fusion," 2021.

[184] G. Xu, R. Wu, K. Luo, and J. Lu, "Effects of heat treatment on hot corrosion behavior of directed energy deposited In718 / 316L functionally graded material," *Corros. Sci.*, vol. 197, no. July 2021, p. 110068, 2022.

[185] C. Mercer, A. B. O. Soboyejo, and W. O. Soboyejo, "Micromechanisms of fatigue crack growth in a single crystal Inconel 718 Nickel-based," *Acta Metall.*, vol. 47, no. 9, 1999.

[186] F. Jiang, Z. L. Deng, K. Zhao, and J. Sun, "Fatigue crack propagation normal to a plasticity mismatched bimaterial interface," vol. 356, pp. 258–266, 2003.

[187] H. A. Hassan, J. J. Lewandowski, M. H. A. B. D. El-latif, and A. Materials, "Effects of Lamination and Changes in Layer Thickness on Fatigue-Crack Propagation of Lightweight Laminated Metal Composites," *Metall. Mater. Trans. A*, vol. 35A, 2004.

[188] R. R. Adharapurapu, K. S. Vecchio, and F. Jiang, "Effects of Ductile Laminate Thickness , Volume Fraction , and Orientation on Fatigue-Crack Propagation in Ti-Al 3 Ti Metal-Intermetallic Laminate Composites," *Metall. Mater. Trans. A*, vol. 36, no. June, pp. 1595–1608, 2005.

[189] J. M. Yu, "Effects of build direction on tensile and creep properties of 316L stainless steel produced by selective laser melting," no. July, pp. 2623–2636, 2020.

[190] K. Wang, R. Bao, T. Zhang, B. Liu, Z. Yang, and B. Jiang, “Fatigue crack branching in laser melting deposited Ti – 55511 alloy,” *Int. J. Fatigue*, vol. 124, no. 37, pp. 217–226, 2019.

[191] Q. Zhang and X. Zhang, “The crack nature analysis of primary and secondary cracks : A numerical study based on moment tensors,” *Eng. Fract. Mech.*, vol. 210, no. May 2018, pp. 70–83, 2019.

[192] R. O. Ritchie, “Mechanisms of fatigue-crack propagation in ductile and brittle solids,” *Int. J. Fract.*, vol. 100, pp. 55–83, 2000.

[193] P. M. SCOTT and T. W. THORPE, “A critical review of crack tip stress intensity factors for semi-elliptic cracks,” *Fatigue Fract. Eng. Mater. Struct.*, vol. 4, no. 4, pp. 291–309, 1981.